Josephson effects and Cooper pair splitting in modern hybrid devices

Romain Jacquet

Centre de physique théorique
Aix-Marseille Université
ED 352 Physique et sciences de la matière

Specialité: Nanophysique

Thèse pour l'obtention du grade de docteur
présentée par

Romain JACQUET

Josephson effects and Cooper pair splitting in modern hybrid devices

Soutenance le 28 septembre 2018 devant le jury

Laurence Masson	Présidente
Reinhold Egger	Rapporteur
Fabio Pistolesi	Rapporteur
Christian Glattli	Examinateur
Thierry Martin	Directeur de thèse
Thibaut Jonckheere	Co-encadrant (invité)
Jérôme Rech	Co-encadrant (invité)

Acknowledgments

I would like to acknowledge the persons who have supervised my work: Thierry MARTIN, Thibaut JONCKHEERE, Jerome RECH. I am also grateful for fruitful discussions with Alex ZAZUNOV. There is no need to do the entire list of family members and friends who already know that their support was important throughout these years.

Contents

Nomenclature

AB	Aharonov-Bohm
AR	Andreev Reflection
BdG	Bogoliubov - de Gennes
BTK	Blonder, Tinkham and Klapwijk
CAR	Crossed Andreev Reflection
CP	Cooper Pair
DAR	Direct Andreev Reflection
EC	Electron Cotunneling
HBT	Hanbury Brown and Twiss
MAR	Multiple Andreev Reflection
MCPR	Multiple Cooper Pair Resonance
MPT	Multiple Particle Tunneling
QD	Quantum Dot
SEM	Scanning Electron Microscopy
SGS	Subhamonic Gap Structure
SQUID	Superconducting QUantum Interference Device
SWCNT	Single Wall Carbon NanoTube

Introduction

Mesoscopic physics aim at the description of solids which length scales are between those of the macroscopic world governed by classical physics and those of the microscopic world which requires quantum physics for its description. Looking at a solid at a macroscopic scale well defined by classical physics and progressively zooming on, the mesoscopic threshold is reached as soon as quantum fluctuations are required to correctly describe it (for example, concerning electronic transport, one can propose a definition of the mesoscopic scale by the failure of ohmic predictions [1]). Of course, there is no sharp transition nor fixed value. It depends on both the quantity which is considered and the accuracy which is expected. However, a common feature of mesoscopic systems can be proposed as follows: contrary to microscopic ones, they still contain a large number of particles so that the tools of statistical (quantum) physics can be used but contrary to macroscopic systems, they manifest quantum effects. In such systems either the quantum state randomization is not complete or the sample size probes the spatial extent of the constituent particles.

As quantum objects, the constituent particles of a mesoscopic system have a wave-like behavior encoded in their De Broglie wavelength. At low temperature, conduction is ensured by electrons near the Fermi level and a first key length scale is the Fermi wavelength λ_F. Indeed a constriction created by depletion of a two dimensional electron gas (formed in GaAs-AlGaAs heterostructures) can be pinched down to this length scale and the quantization of the conductance [2] which is observed requires the Landauer formalism [3] to be explained. Another key quantity is the phase-relaxation length L_ϕ, the distance along which a certain degree of coherence is maintained. If we imagine that we can interfere the wave with itself at two different times, the degree of coherence will be the visibility of the fringes which we would obtain. This is not just a thougth experiment: in a doubly connected wire designed in a loop geometry with a magnetic flux threading the area in between the two paths, the relative phase between the two

arms of this electronic interferometer acquire a flux dependence and, as a result, Aharonov-Bohm (AB) oscillations of electrical quantities are observed. The situation can be somewhat different from the early version of the AB experiment [4] which involves free particles (ballistic regime). The oscillations have been observed in samples with a size much larger than the mean free path L_m [5] so that the electrons undergo a random walk inside the arms of the AB interferometer (diffusive regime) but still interfere coherently. Different kinds of scattering occuring in a real crystal lead to different influences on momentum or phase randomization and depend on external parameters such as temperature or magnetic field. To summarize, different length scales have to be considered in a mesoscopic system:

- the Fermi wavelength λ_F, which gives the spatial extension of the conducting species,
- the mean free path L_m along which the momentum memory is lost,
- the phase-relaxation length L_ϕ along which the phase memory is lost,
- the typical size L of the sample.

Physics could be strongly affected by the effective dimensionality of the system. Considering a d-dimensional sample, if the typical size L_i along the dimension i is much smaller than λ_F, the system has to be considered as $(d-1)$-dimensional. This is the geometric way to reduce the dimensionality but mesoscopic physics could provide other possible realizations of low-dimensional systems, e.g. boundary helical 1D edge states which appears in a 2DEG in the Quantum Hall Effect [6] or the metallic surface states of a 3D topological insulator [7].

Concerning electronic transport, ohmic predictions fail as soon as λ_F, L_m or L_ϕ exceeds the sample size L. Quasi-classical theories of electronic transport, such as Drude model or Boltzmann transport equation can be considered as long as the sample size is large compared to the phase-relaxation length $L \gg L_\phi$ but the importance of disorder encoded in the mean free path L_m can be illustrated in localization phenomena (not quasi-classically explained) extendingly studied since the pioneering work of Anderson [8] in 1958.

Throughout this thesis which propose transport-based diagnoses, we will investigate devices that exhibit phase coherence: the sample size will always be of the order or smaller than the phase-relaxation length $L \sim L_\phi$ or $L < L_\phi$. Disorder problematics will not be investigated: the mean free path will satisfy $L_m \gg L, L_\phi$ (ballistic regime). We will also adress reduced dimensionality systems.

One of the hallmark of solid-state systems is the emergence of new states of matter. Among them, superconductivity is particularly fascinating since it displays remarkable features such as vanishing resistivity and perfect diamagnetism [9]. Microscopically, superconductivity relies on the possibility to pair electrons with opposite spins and momenta in so-called Cooper pairs [10]. A new length scale is then involved, namely the correlation length ξ which is the typical size of the Cooper pairs. This is the most relevant length scale in the hybrid devices that will be investigated in the first part of this thesis and typically, some dimensions of the order of ξ will be required for the observation of the nonlocal transport processes under study.

Entanglement is a specific feature of quantum mechanics [11] which has been experimentally proved in photonic systems [12] through the violation of Bell's inequalities [13]. Entanglement between electrons in solid-state systems remains a challenging task due to the interactions with the neighboring Fermi sea but superconductivity and its instrinsical entanglement between electrons can be conveniently involved in the design of an electron entangler. In **Chapter 1**, we briefly present the microscopic theory of superconductivity which describes a ground state made of an arbitrary number of Cooper pairs and quasiparticle excitations which are gapped. We also introduce the underlying process of these electron entangler proposals, namely the Andreev reflection [14] which takes place at the interface between a normal metal and a superconductor (N-S junction): a subgap current flows $I(e|V| < \Delta) \neq 0$ because an electron can be reflected as a hole provided the emission of a Cooper pair inside the superconductor (Fig. 1a). The transmission of a Cooper pair inside a normal metal can be viewed as an Andreev reflection process (a hole is reflected as an electron). Suppose that we can spatially separate the two particles, creating a nonlocal entangled state, then one deals with the so-called Cross Andreev Reflection (CAR) process that can be observed in a Cooper pair beam splitter which consists of a N-S junction with the N material designed in a fork geometry (Fig. 2a). Other processes rely on the Andreev reflection. In a Josephson junction between two superconductors bridged with a weak link such as a narrow metallic region (S-N-S junction) at equilibrium (no voltage drop), if Cooper pairs have different phases in the two reservoirs then a DC supercurrent (a current of Cooper pairs) flows [15] and it can be understood as the result of Andreev reflections at the two N-S interfaces (Fig. 1b). It is related to the existence of Andreev bound states inside the gap region. Then, if a voltage bias is applied accross a Josephson junction then an AC current arises at the Josephson frequency $\omega_J = eV/\hbar$ [15] and the Cooper pairs are oscillating from one reservoir to the other with no permanent transport. At first sight, one expects that no DC current flows until quasiparticles can tunnel which occurs for $e|V| > 2\Delta$. However, even at zero temperature,

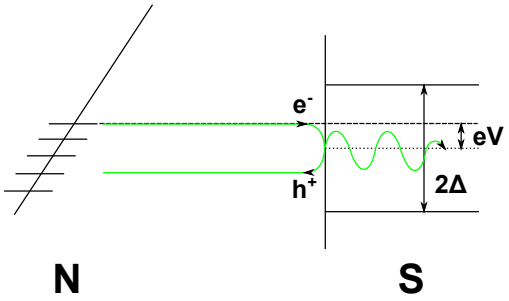

(a) Andreev reflection.

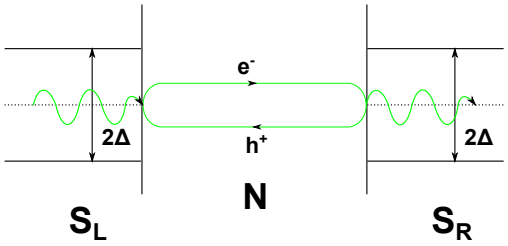

(b) Josephson current as a result of two Andreev reflections.

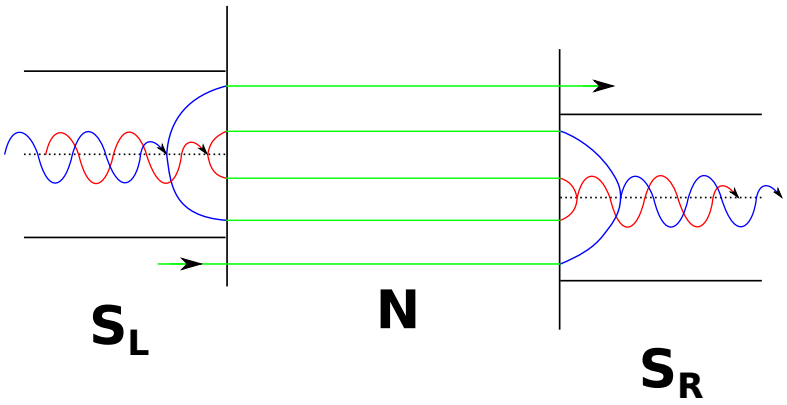

(c) Multiple Andreev Reflection (MAR) where a quasiparticle is transmitted together with the emission of two Cooper pairs.

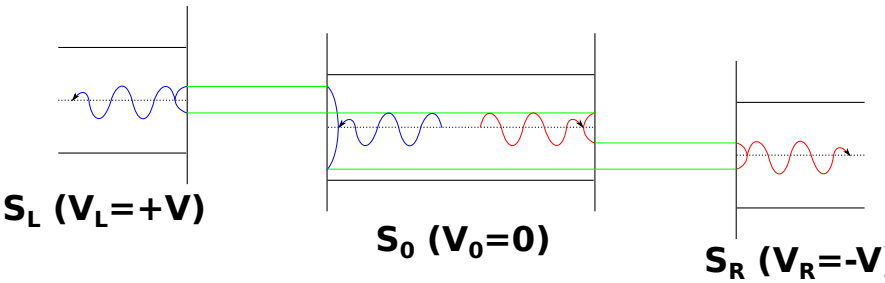

(d) Quartets process in a bijunction with $V_0 = 0$ and $V_L + V_R = 0$ where two Cooper pairs are split from the central superconductor and where recombinations in the lateral gates require an exchange of the constituent electrons.

Figure 1: Hybrid device phenomena relying on Andreev reflection processes. N stands for Normal metal and S for Superconductor.

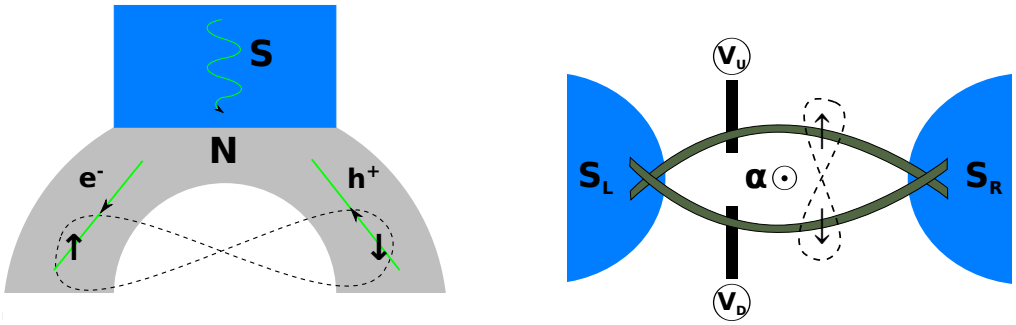

(a) Crossed Andreev Reflection at a N-S interface in a fork geometry.

(b) Josephson junction with nanowire/nanotube quantum dots (setup studied in Chapter 2).

Figure 2: Schematics of Cooper pair splitter devices.

a subgap structure can be noticed and explained in terms of Multiple Andreev Reflection (MAR) processes [16], *i.e* successions of Andreev reflections that result in the promotion of a quasiparticle from the valence band of one superconductor to the conduction band of the other, accompanied by Cooper pair transfers (Fig. 1c). Even more interesting, under specific voltage conditions, one can imagine nonlocal interferences between Andreev reflection processes at different interfaces of a multi-terminal all-superconducting junction. In a three-terminal junction, these interferences could lead to multipair productions [17] where an even number of Cooper pairs are split from the central electrode and recombined in the lateral leads (Fig. 1d).

In **Chapter 2**, we consider a Josephson junction with two quantum dots between the superconducting leads as an (equilibrium) alternative Cooper pair splitter [18]. It can meet a practical realization through the use of nanowires that bridge the two superconductors (Fig. 2b). The dots materialize two conduction channels for the electrons ejected from one superconductor and recombined (as Cooper pairs) on the other one. Among all processes that can occur in such a junction, the delocalization of the two electrons of a Cooper pair on the two quantum dots requires a CAR process (for Cooper pair splitting) at the boundary of the source superconductor followed by a reverse CAR process (for Cooper pair recombination) at the boundary of the drain superconductor. This Cooper pair splitting can be enhanced by varying the parameters of the quantum dots (experimentally the Coulomb repulsion is fixed but the energy levels can be monitored by gate voltages applied to the nanowires) such that realizing two parallel π junctions, *i.e.* singly occupied quantum dots [19]. The diagnosis relies on the Aharonov-Bohm oscillations of the critical current when a magnetic flux threads the area between the quantum dot nanowires.

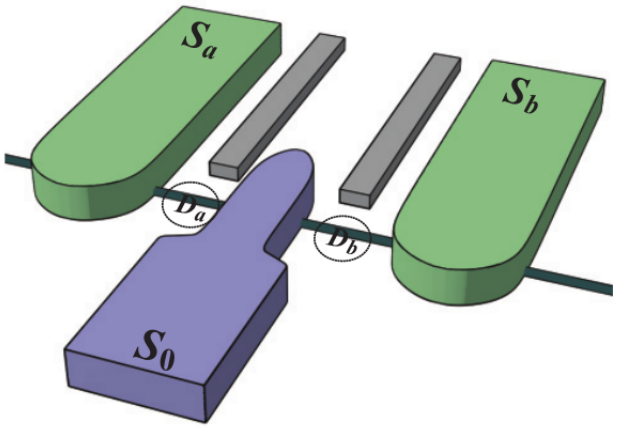

Figure 3: Josephson bijunction (setup studied in Chapter 3). Adapted from [17].

In **Chapter 3**, we consider an all-superconducting bijunction (Fig. 3): a central electrode (labeled 0) is connected to two lateral leads (labeled a and b) *via* quantum dots. If the central electrode is grounded ($V_0 = 0$), commensurate voltages applied to the lateral electrodes lead to multipair DC Josephson resonances: if $nV_a + mV_b = 0$ then n pairs are transfered from S_0 to S_a and m pairs from S_0 to S_b. Of particular interest is the case $n = m = 1$ called quartet resonance (Fig. 1d) which is a realization of an entanglement with four particles originated from a double CAR process. Their signature in the current-phase relations have already been investigated [17] but less is known about noise correlations. Here we investigate two regimes which bear strong differences. While in the metallic junction limit, noise correlations are vanishing for sufficiently low voltages, the resonant dots regime provide huge phase sensitive Fano factors. Moreover, positive noise crossed correlations are predicted in the latter regime.

Another hallmark of solid-state systems is the emergence of quasiparticles which are collective excitations of the quantum many-body state describing the interacting fermionic system. Among the exotic states which can be synthesized, particles which are their own antiparticles, the so-called Majorana quasiparticles have attracted a lot of attention, mostly because non-Abelian statistics could be achieved [20] providing new perspectives in quantum computation such as topological protection and hardware protection against decoherence [21]. **Chapter 4** is dedicated to the revival of this particle physics idea in the context of condensed matter physics and to the clever proposals [22–24] for the design of topological phases hosting Majorana modes using materials and technics which are commonly used in nanofabrication. Then **Chapter 5** partici-

pates in the recent search for convincing signatures of Majorana zero energy modes in condensed matter platforms. Current and noise in a junction between two topological superconductors are adressed and the calculations are performed within a framework which conveniently covers the case of a junction between two conventional superconductors. This unified treatment allows a systematic study of the two systems and some differences are ascribed to the eventual presence of Majorana modes.

Chapter 1

Conventional superconductors

Since superconductors will regularly be involved in the mesoscopic devices that will be presented throughout this thesis, this chapter is dedicated to the presentation of the microscopic theory of conventional superconductivity (Section 1.1) and to the presentation of the Andreev reflection (Section 1.2), this new conduction channel that emerges in the vicinity of a superconductor boundary and that is responsible for the formation of Andreev bound states in a normal region surrounded by superconductors as well as for the Josephson effects (Section 1.3) and the subgap MAR structure (Section 1.5). The occurence of negative Josephson critical current in the so-called π junctions is also discussed (Section 1.4). This chapter presents the minimal theoretical background essential for the comprehension of further discussions, especially emphasizing the microscopic processes underlying some non-local phenomena investigated in this thesis, including Cooper pair splitting in a junction between a grounded superconductor and two voltage biased normal leads or in the equilibrium setup with two superconductors bridged by two quantum dot nanowires (Chapter 2) and multipair production in an all-superconducting three-terminal junction (Chapter 3). In this chapter, we consider units in which Planck constant is unity $\hbar = 1$.

1.1 Microscopic description of s-wave superconductivity

Standard superconductivity textbooks [9, 25] have been used.

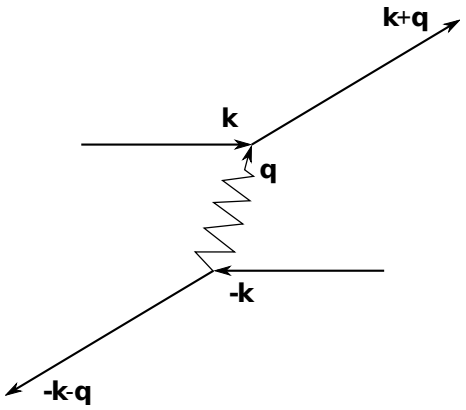

Figure 1.1: Illustration of the attractive interaction between two opposite spin and opposite momentum electrons that occurs inside a superconductor. A phonon (momentum $\mathbf{q}$) is exchanged, resulting in the scattering from state $(\mathbf{k}, -\mathbf{k})$ to state $(\mathbf{k}', -\mathbf{k}')$ with $\mathbf{k}' = \mathbf{k} + \mathbf{q}$.

1.1.1 BCS variational method

The BCS (for Bardeen Cooper Schrieffer) theory [10] followed the discovery by Cooper [26] that an arbitrarily small attractive interaction can bind two electrons with opposite spins and momenta above the Fermi sea. These are the so-called Cooper pairs and such an attractive interaction was ascribed to phonons because of the isotope effect (transition temperature dependence with isotopic constitution of the superconducting crystal). The exchange of phonons, illustrated in Fig 1.1, is responsible for an attractive interaction who wins compared to the (screened) repulsive interaction between electrons. An intuitive picture could be that an electron propagating in a solid deforms the lattice by displacing the constituent ions so that another electron can experience this distorsion with some delay due to the larger inertia of ions. Despite the fact that this interaction is weak, the number of states available for a Cooper pair can be important so that the energy of a sea of Cooper pairs can be considerably lowered compared to a classical Fermi sea of unpaired electrons. Cooper pairs are entangled systems in both momentum and spin space. Such a state is a tensorial product $|\Psi\rangle_{\mathbf{k}} = |\phi\rangle_{\mathbf{k}} \otimes |\chi\rangle$ of an antisymmetric spin state (spin singlet)

$$|\chi\rangle = \frac{|\uparrow\downarrow\rangle - |\downarrow\uparrow\rangle}{\sqrt{2}} \tag{1.1.1}$$

and a symmetric orbital state which associated spatial wavefunction is the following symmetric superposition of products of single electron wavefunctions

$$\langle \mathbf{r}_1, \mathbf{r}_2 \, |\phi\rangle_{\mathbf{k}} = \phi_{\mathbf{k}}(\mathbf{r_1})\phi_{-\mathbf{k}}(\mathbf{r_2}) + \phi_{\mathbf{k}}(\mathbf{r_2})\phi_{-\mathbf{k}}(\mathbf{r_1}) \ . \tag{1.1.2}$$

The ground state of the system was proposed as constituted by such Cooper pairs

$$|\Psi_{\rm BCS}\rangle = \prod_{\mathbf{k}} \left(u_{\mathbf{k}} + v_{\mathbf{k}} c^{\dagger}_{\mathbf{k}\uparrow} c^{\dagger}_{-\mathbf{k}\downarrow} \right) |0\rangle \ . \tag{1.1.3}$$

To impose normalization $\langle \Psi_{\rm BCS} \, | \Psi_{\rm BCS} \rangle = 1$, one must require that $|u_{\mathbf{k}}|^2 + |v_{\mathbf{k}}|^2 = 1$ for all $\mathbf{k}$, so that angles can be introduced according to (for the sake of simplicity, $u_{\mathbf{k}}$ and $v_{\mathbf{k}}$ are supposed to be real)

$$u_{\mathbf{k}} = \cos\theta_{\mathbf{k}} \quad \text{and} \quad v_{\mathbf{k}} = \sin\theta_{\mathbf{k}} \ . \tag{1.1.4}$$

Then the variational principle of quantum mechanics was employed to minimize the energy of the system described by the Hamiltonian

$$H = \sum_{\mathbf{k}\sigma} \frac{k^2}{2m} c^{\dagger}_{\mathbf{k}\sigma} c_{\mathbf{k}\sigma} + H_{\rm int} \ , \tag{1.1.5}$$

featuring the attractive interaction which connects two Cooper pair states according to

$$H_{\rm int} = \sum_{\mathbf{k},\mathbf{k}'} V_{\mathbf{k}\mathbf{k}'} \, c^{\dagger}_{\mathbf{k}'\uparrow} c^{\dagger}_{-\mathbf{k}'\downarrow} c_{-\mathbf{k}\downarrow} c_{\mathbf{k}\uparrow} \ . \tag{1.1.6}$$

The minimization has to be performed under the constraint that the mean number of particles should be fixed as the number operator is not a conserved quantity in the ground state given by Eq. (1.1.3). Introducing the chemical potential μ (which is the Lagrange multiplier of the minimization under constraint), the variational method leads to the equations

$$\frac{\partial}{\partial \theta_{\mathbf{k}}} \langle \Psi_{\rm BCS} | \sum_{\mathbf{k}\sigma} \xi_{\mathbf{k}} c^{\dagger}_{\mathbf{k}\sigma} c_{\mathbf{k}\sigma} + H_{\rm int} \, | \Psi_{\rm BCS} \rangle = 0 \quad \text{where} \quad \xi_{\mathbf{k}} = \frac{\mathbf{k}^2}{2m} - \mu \ . \tag{1.1.7}$$

An energy parameter called the gap function $\Delta_{\mathbf{k}} = -\sum_{\mathbf{k}'} V_{\mathbf{k}\mathbf{k}'} u_{\mathbf{k}'} v_{\mathbf{k}'}$ appears during calculations and verifies a self-consistency condition which is crudely evaluated in the Cooper model where the attractive potential is assumed to be constant under a cut-off determined by single-particle energies reaching the Debye energy ω_D, that is

$$V_{\mathbf{k}\mathbf{k}'} = \begin{cases} -V & \text{if } |\xi_{\mathbf{k}}|, |\xi_{\mathbf{k}'}| < \omega_D \ , \\ 0 & \text{otherwise} \ . \end{cases} \tag{1.1.8}$$

Introducing the normal density of states at the Fermi level $\nu(0)$ and under the assumption $V\nu(0) \ll 1$, the gap function is given by the non-analytical expression (in terms of potential magnitude)

$$\Delta = 2\omega_D \, \mathrm{e}^{-\frac{1}{V\nu(0)}} \ . \tag{1.1.9}$$

Note that the dependence of Δ as a function of V prohibits a perturbative treatment of (1.1.6) to find superconductivity at low V. This constitutes an "essential singularity" (at $V = 0$ all derivatives of Δ vanish so a Taylor expansion in V does not yield any information). Then, one can easily obtain

$$u_{\mathbf{k}}^2 = \frac{E_{\mathbf{k}} + \xi_{\mathbf{k}}}{2E_{\mathbf{k}}} \quad \text{and} \quad v_{\mathbf{k}}^2 = \frac{E_{\mathbf{k}} - \xi_{\mathbf{k}}}{2E_{\mathbf{k}}} \tag{1.1.10}$$

where the energies are gapped according to

$$E_{\mathbf{k}}^2 = \xi_{\mathbf{k}}^2 + \Delta^2 \ . \tag{1.1.11}$$

1.1.2 Bogoliubov mean-field method

The mean-field treatment consists in neglecting terms which appear in the interaction term (1.1.6) and which are quadratic in the operators

$$c_{-\mathbf{k}\downarrow} c_{\mathbf{k}\uparrow} - \langle c_{-\mathbf{k}\downarrow} c_{\mathbf{k}\uparrow} \rangle \quad \text{and} \quad c^\dagger_{\mathbf{k}'\uparrow} c^\dagger_{-\mathbf{k}'\downarrow} - \left\langle c^\dagger_{\mathbf{k}'\uparrow} c^\dagger_{-\mathbf{k}'\downarrow} \right\rangle \ . \tag{1.1.12}$$

The resulting mean field Hamiltonian which involves the gap function $\Delta_{\mathbf{k}} = -\sum_{\mathbf{k}'} V_{\mathbf{k}\mathbf{k}'} \langle c_{-\mathbf{k}'\downarrow} c_{\mathbf{k}'\uparrow} \rangle$ is then diagonalized by the following transformation which was proposed by Bogoliubov [27] and Valatin [28]

$$\gamma_{\mathbf{k}\sigma} = u_{\mathbf{k}} c_{\mathbf{k}\sigma} - \sigma v_{\mathbf{k}} c^\dagger_{-\mathbf{k}-\sigma} \ . \tag{1.1.13}$$

The quantities $u_{\mathbf{k}}$, $v_{\mathbf{k}}$ are then given by (1.1.10) and one can easily verify that the BCS ground state (1.1.3) is the vaccum for the operator $\gamma_{\mathbf{k}\sigma}$, meaning that $\gamma_{\mathbf{k}\sigma} |\Psi_{\mathrm{BCS}}\rangle = 0$. The excitations $\gamma^\dagger_{\mathbf{k}\sigma} |\Psi_{\mathrm{BCS}}\rangle$ raise the energy of the system by an amount E_k given in (1.1.11). The occupation of the state $\mathbf{k}$ prevents the pairing state $(\mathbf{k}, -\mathbf{k})$ to be available for Cooper pairs so that their delocalization energy is lowered (in absolute value) and the energy is raised.

Excitation picture

A one-dimensional free gas of electrons has a dispersion relation given by $\epsilon(k) = \frac{k^2}{2m}$ and, at zero temperature, these energy levels are filled up to the chemical potential $\mu = \frac{k_F^2}{2m}$: this is the so-called Fermi sea constituted by electrons with momenta k in the interval $[-k_F, k_F]$. An excited state is a promotion of an electron in state $0 < q < k_F$ such that $\epsilon(q) < \mu$ to the state $p > k_F$ such that $\epsilon(p) > \mu$. The difference in energy reads $\epsilon(p) - \epsilon(q)$ and, defining the quasiparticle excitation energy $E^0(k) = |\epsilon(k) - \mu| = |\xi_k|$, can be written as $E^0(p) + E^0(-q)$. The difference in momentum reads $p - q = p + (-q)$. Consequently, an excitation in a free gas of electrons

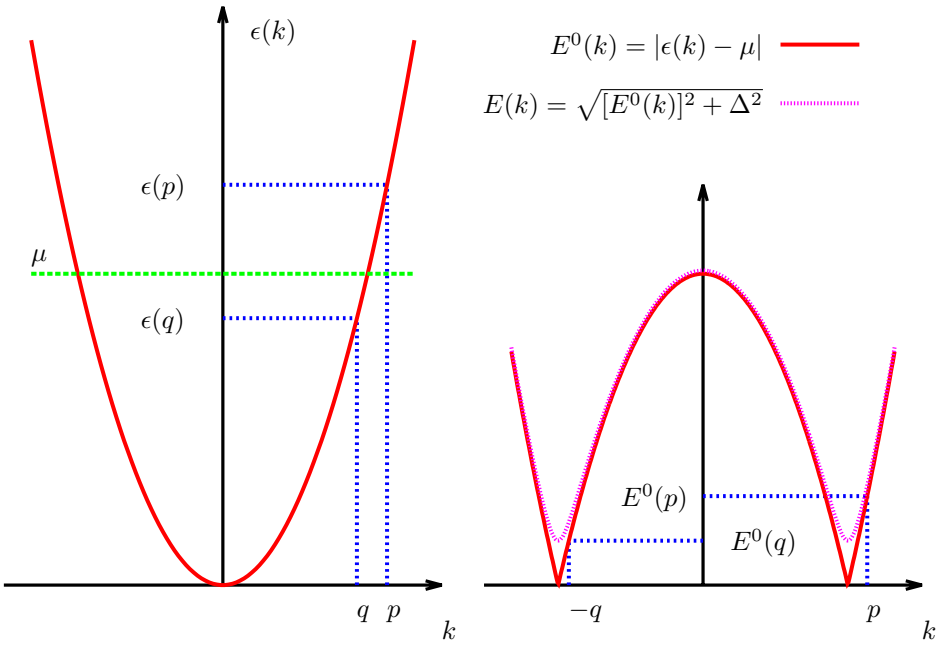

Figure 1.2: Excitation picture in a gas of free electrons: the promotion of an electron from the Fermi sea to an energy above the chemical potential (left) can be viewed as the creation of a pair of electron-like and hole-like quasiparticles (right). In a superconductor, the quasiparticles have gapped energies and the cusps at Fermi momenta $\pm k_F$ are rounded.

results in the creation of a pair of electron-like (momentum p and energy $E^0(p)$) and hole-like (momentum $-q$ and energy $E^0(-q)$) quasiparticles. A superconductor is a material where the excitations are gapped according to $E(k) = \sqrt{[E^0(k)]^2 + \Delta^2}$. The excitation spectrum is given in Fig 1.2. The semiconductor model [29] consists in duplicating this spectrum by introducing the negative branches which are symmetric with respect to the horizontal axis $E = 0$. This proves to be convenient for the study of single-charge transfer processes.

Bogoliubov - de Gennes equations

The Bogoliubov procedure can be conveniently applied to non-uniform superconductors where the momentum $\mathbf{k}$ is no longer a good quantum number [30]. The effective mean field Hamiltonian is written as

$$H_{\rm MF} = \int \mathrm{d}\mathbf{r} \left\{ \sum_\sigma \Psi^\dagger_\sigma(\mathbf{r}) \mathcal{H}_0(\mathbf{r}, \partial_\mathbf{r}) \Psi_\sigma(\mathbf{r}) + \Delta(\mathbf{r}) \Psi^\dagger_\uparrow(\mathbf{r}) \Psi^\dagger_\downarrow(\mathbf{r}) + \Delta^*(\mathbf{r}) \Psi_\downarrow(\mathbf{r}) \Psi_\uparrow(\mathbf{r}) \right\} , \quad (1.1.14)$$

where the single-particle Hamiltonian reads

$$\mathcal{H}_0(\mathbf{r}, \partial_\mathbf{r}) = \frac{\left[-i\partial_\mathbf{r} - e\mathbf{A}(\mathbf{r})\right]^2}{2m} + U(\mathbf{r}) - \mu \ . \tag{1.1.15}$$

It can be diagonalized as

$$H_{\mathrm{MF}} = \sum_{n\sigma} E_n \gamma^\dagger_{n\sigma}\gamma_{n\sigma} \ , \tag{1.1.16}$$

using the generalized Bogoliubov-Valatin transformation

$$\Psi_\sigma(\mathbf{r}) = \sum_n \left(u_n(\mathbf{r})\gamma_{n\sigma} - \sigma v_n^*(\mathbf{r})\gamma^\dagger_{n-\sigma} \right) \tag{1.1.17}$$

yielding the so-called Bogoliubov - de Gennes (BdG) equations [31]

$$\begin{cases} \mathcal{H}_0 u_n(\mathbf{r}) + \Delta(\mathbf{r}) v_n(\mathbf{r}) = E_n u_n(\mathbf{r}) \ , \\ \Delta^*(\mathbf{r}) u_n(\mathbf{r}) - \mathcal{H}_0^* v_n(\mathbf{r}) = E_n v_n(\mathbf{r}) \ . \end{cases} \tag{1.1.18}$$

Note that $\mathcal{H}_0^*$ denotes the complex conjugate (not the hermitian conjugate $\mathcal{H}_0^\dagger = \mathcal{H}_0$) and could be different from $\mathcal{H}_0$ in presence of an electromagnetic field. Going back to the one-dimensional homogeneous case, the two-vector $\Phi(x) = (u(x), v(x))^T$, which collects electron and hole amplitudes, verifies the following BdG problem

$$\left\{H_{\mathrm{BdG}}(\partial_x) - E\right\}\Phi(x) = 0 \quad \text{with} \quad H_{\mathrm{BdG}}(\partial_x) = \begin{pmatrix} -\frac{\partial_x^2}{2m} - \mu & \Delta \\ \Delta^* & \frac{\partial_x^2}{2m} + \mu \end{pmatrix} \ . \tag{1.1.19}$$

Solutions can be searched as $\mathrm{e}^{ikx}\Phi_0$ with dispersion relation

$$k_\pm^2 = 2m\left(\mu \pm \sqrt{E^2 - |\Delta|^2}\right) \ . \tag{1.1.20}$$

The sign $\pm$ corresponds to electron-like $(+)$ or hole-like $(-)$ excitations. For $|\Delta| < |E| < \sqrt{\mu^2 + \Delta^2}$, we recover the plane wave states with gapped energies (1.1.11) and otherwise (e.g for for $|E| < |\Delta|$), interestingly, we get evanescent waves.

1.2 A new conduction channel: Andreev Reflection

In the last section, we have exposed the key features of superconductivity: a ground state formed by a condensate of Cooper pairs and quasiparticles as coherent superpositions of electron-like and hole-like excitations. As a result a new conduction channel is available for an electron originated from a normal metal and meeting an interface with a superconductor: it can be reflected as a hole. This process is known as Andreev reflection and is illustrated in Fig. 1.3 in the semiconductor

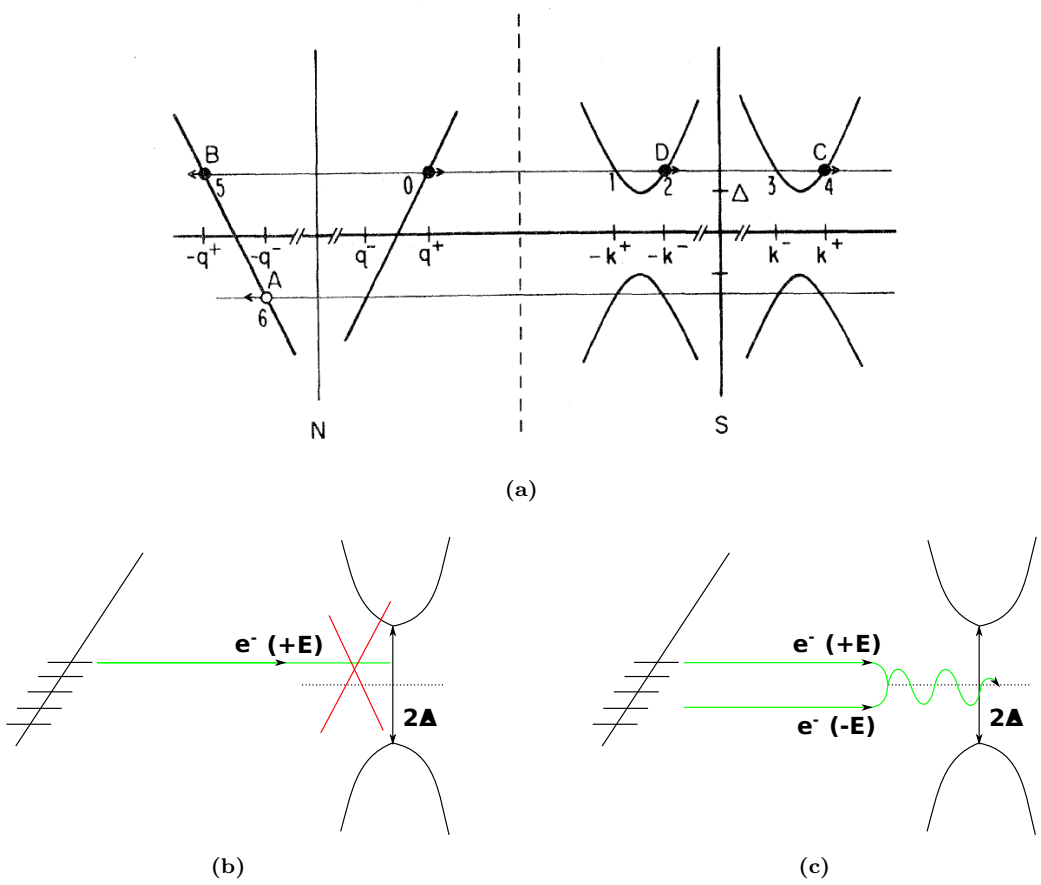

Figure 1.3: (a) Semiconductor model for a N-S interface. Closed (open) circles denote electron-like (hole-like) particles and arrows indicate the group velocity. The electron 5 is produced through normal reflection while the hole 6 is produced through Andreev reflection. Adapted from [29]. (b) A subgap electron ($0 < E < \Delta$) from the normal metal cannot enter the superconductor. (c) If it is accompanied by a partner at energy $-E$ then the tunneling is possible and this pair of electrons enter the superconductor as a Cooper pair.

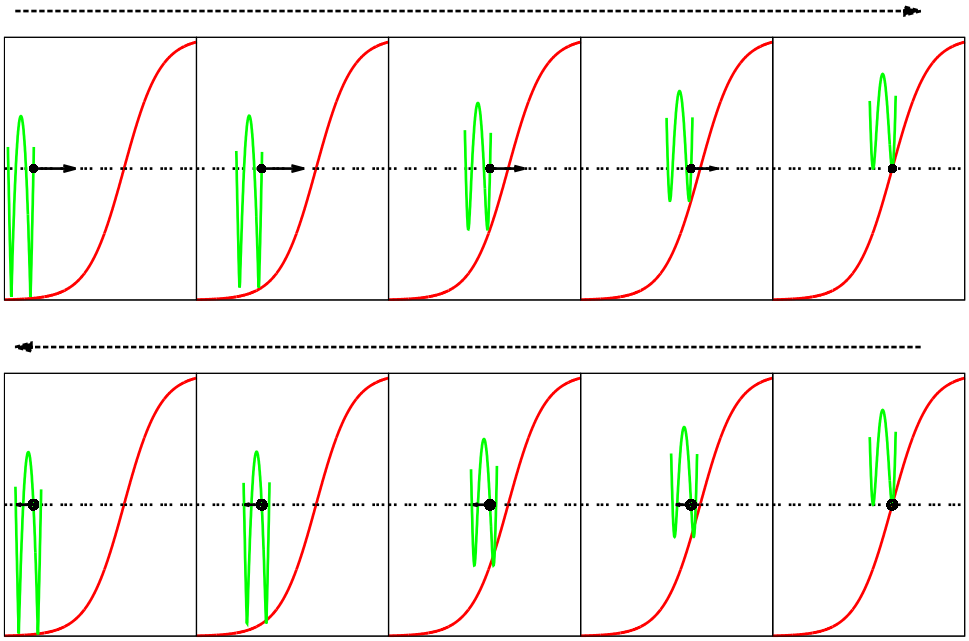

Figure 1.4: Quasi-classical explanation of Andreev reflection in the excitation picture (cf. Fig. 1.2): $E(k,z) = \sqrt{[E^0(k)]^2 + \Delta^2(z)}$ where $\Delta(z)$ (red profile) undergoes a smooth transition at a N-S interface, from 0 in the normal lead to $\Delta_0 > 0$ deep inside the superconductor. In the top panels (from left to right), a subgap electron-like quasiparticle ($E < \Delta_0$) propagates towards the N-S interface. The arrow from the quasiparticle indicates the group velocity $v = \frac{\partial E}{\partial k}$. During this forward propagation, the quasiparticle climbs down the electron-like branch of the excitation spectrum to finally reaches its minimum where its group velocity vanishes (classical turning point). Then its velocity is reversed, it propagates backward (bottom panels from right to left) as a hole-like quasiparticle climbing up the hole-like branch of the excitation spectrum.

model proposed in [29]. Remark that the difference of charge can be absorbed through the formation of a Cooper pair inside the superconductor. The reverse process of the reflection of a hole into an electron involves the destruction of a Cooper pair. For an experimental detection of Andreev reflection, see for example Ref. [32] which is an interferometric experiment where a normal metal wire contacts a superconducting fork electrode.

The problem was first tackled by Andreev in the seminal paper [14] in the quasi-classical limit of $\Delta/\mu \ll 1$ where the BdG problem (1.1.18), with $U(\mathbf{r}) = 0$ and $\mathbf{A}(\mathbf{r}) = 0$ in (1.1.15), can be rewritten in terms of slow varying amplitudes

$$u(\mathbf{r}) = \mathrm{e}^{ik_F \mathbf{n}.\mathbf{r}} \eta(\mathbf{r}) \quad \text{and} \quad v(\mathbf{r}) = \mathrm{e}^{ik_F \mathbf{n}.\mathbf{r}} \chi(\mathbf{r}) \ , \tag{1.2.1}$$

according to

$$\begin{cases} -\left[iv_F\mathbf{n}.\partial_{\mathbf{r}} + E\right]\eta(\mathbf{r}) + \Delta(\mathbf{r})\chi(\mathbf{r}) = 0 \ , \\ \Delta^*(\mathbf{r})\eta(\mathbf{r}) + \left[iv_F\mathbf{n}.\partial_{\mathbf{r}} - E\right]\chi(\mathbf{r}) = 0 \ , \end{cases} \tag{1.2.2}$$

where the Fermi velocity is defined as $v_F = k_F/m$. Andreev considered the limiting cases corresponding to normal bulk where $\Delta(\mathbf{r}) = 0$ and superconducting bulk where $\Delta(\mathbf{r}) = \Delta_0$ is constant. Rather considering a slow-varying gap on the Fermi wavelength scale $\lambda_F = 2\pi/k_F$, a Schrödinger equation can be obtained for χ (and also for η) [33]

$$\left\{-v_F^2\left(\mathbf{n}.\partial_{\mathbf{r}}\right)^2 - \left(E^2 - |\Delta(\mathbf{r})|^2\right)\right\}\chi(\mathbf{r}) = 0 \ . \tag{1.2.3}$$

Choosing the z axis along the direction of space variation of the gap function $\Delta(\mathbf{r}) = \Delta(z)$ and considering a unit vector $\mathbf{n}$ orthogonal to the transverse momentum, we get a one-dimensional equation and a WKB (for Wentzel-Kramers-Brillouin) quasi-classical approximation [34] yields the general solution as $\chi \propto (\chi_+ + r\chi_-)$, which is a superposition of electron-like (χ_+) and hole-like (χ_-) wave packets

$$\chi_\pm(z) \propto \frac{1}{\sqrt{|k(z)|}}\,\mathrm{e}^{\pm i\int^z \mathrm{d}z'\,k(z')} \quad \text{where} \quad k(z) = \frac{1}{v_F n_z}\sqrt{E^2 - |\Delta(z)|^2} \ . \tag{1.2.4}$$

Consider now a Normal metal - Superconductor (N-S) interface. The pairing potential $\Delta(z)$ will be a smooth and increasing function that vanishes inside the normal metal $\Delta(-\infty) = 0$ and takes a finite value inside the superconductor $\Delta(+\infty) = \Delta_0$ which is supposed to be real. For $E < \Delta_0$, an electron-like wave packet propagating from left to right will reach a classical turning point z_0 such that $\Delta(z_0) = E$ (where the quasi-classical approximation breaks down) and will be reflected as a hole-like wave packet. The energy can be considered as a function of k and z [33]

$$E(k,z) = \sqrt{(v_F n_z k)^2 + \Delta^2(z)} \tag{1.2.5}$$

and semi-classical (Hamilton) equations read

$$\begin{cases} \dfrac{\mathrm{d}z}{\mathrm{d}t} = \dfrac{\partial E}{\partial k} = \dfrac{(v_F n_z)^2}{E}\,k(t) \ , \\ \dfrac{\mathrm{d}k}{\mathrm{d}t} = -\dfrac{\partial E}{\partial z} = -\dfrac{\Delta(z)}{E}\,\dfrac{\partial \Delta}{\partial z} \ . \end{cases} \tag{1.2.6}$$

The particle has a momentum $k(t)$ that decreases with time then vanishes at time t_0 when reaching the turning point such that $z(t_0) = z_0$ (and $\Delta(z_0) = E$). For $t > t_0$, the momentum still decreases becoming negative such that the group velocity $\frac{\partial E}{\partial k} = \frac{\mathrm{d}z}{\mathrm{d}t}$ becomes negative. Such a quasi-classical picture of Andreev reflection can be adopted when looking at the excitation

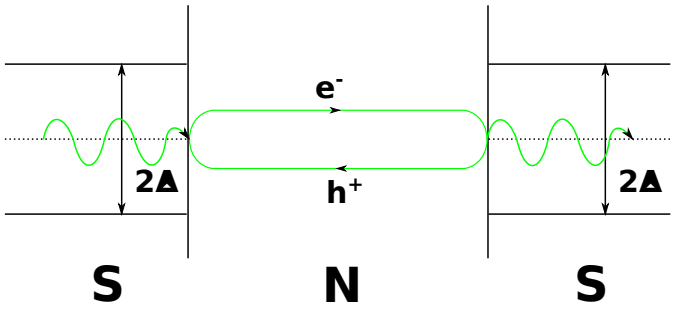

Figure 1.5: Andreev bound state as a result of constructive interferences between Andreev reflections on both N-S and S-N interfaces of a short S-N-S junction. At the N-S interface, the electron is reflected into a hole and charge conservation requires a Cooper pair to be created inside the right superconductor while at the S-N interface, the hole is reflected back as an electron and a Cooper pair must be removed from the ground state of the left superconductor. As a result, Cooper pairs are transfered from left to right. The other Andreev bound state would involve reverse propagations for the quasiparticles (electron going from right to left) so that Cooper pairs would be transfered from right to left. Consequently Andreev bound states carry opposite current.

spectrum along the propagation of an electron-like excitation [35] as illustrated in Fig. 1.4. In the forward motion (from left to right) the quasiparticle progressively climbs down the electron branch with a decreasing velocity $\frac{\partial E}{\partial k}$ and reaches the turning point where the velocity vanishes. Then, it goes backward (negative velocity) and climbs up the hole branch.

In a S-N-S junction designed by adding a superconductor on the left of the N-S junction, there are two turning points for carriers with energies smaller than both gaps, leading to a succession of Andreev reflections that can interfere coherently requiring a quantization of the phase acquired along a round trip (Bohr-Sommerfeld quantization [34]) so that bound states can exist. A little more detailed description of the emergence of these so-called Andreev bound states is presented in the following section.

1.3 Andreev bound states and Josephson current

Considering the simple one-dimensional problem [36] with a step gap function $\Delta(x) = \Delta_0 e^{i\varphi}\Theta(x)$, an incident electron with subgap energy $E < \Delta_0$ and wavevector $k_+^{(0)} = \sqrt{2m(\mu + E)}$ can be reflected into a hole with wavevector $k_-^{(0)} = \sqrt{2m(\mu - E)}$. This Andreev reflection process goes with some penetration inside the superconductor as an evanescent wave with wavevector

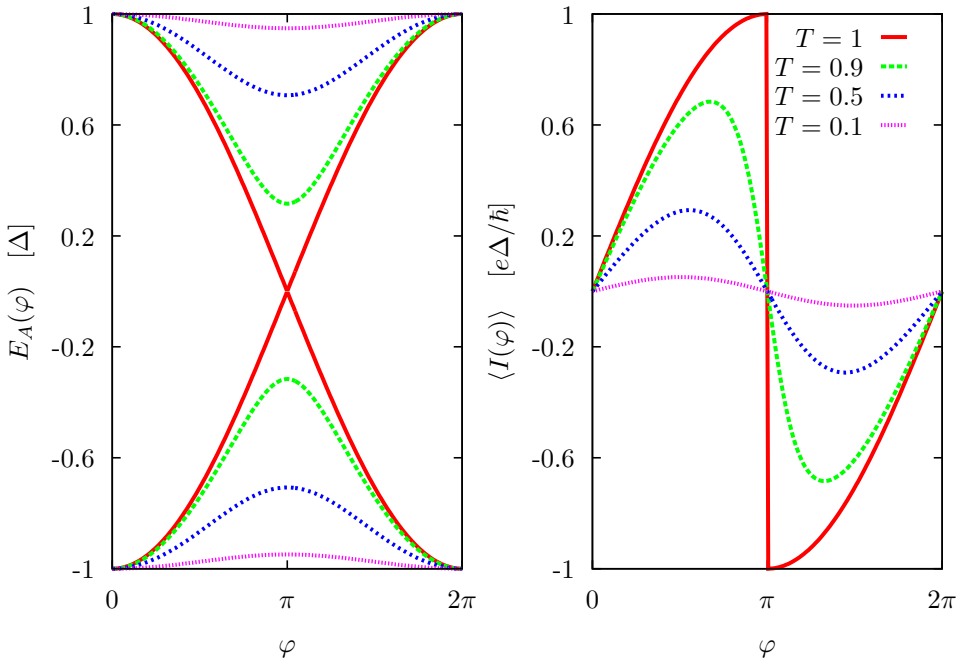

Figure 1.6: Andreev energy and Josephson current in a short superconducting constriction for different transmissions T (key given in the right panel).

$k_+^{(1)} = \sqrt{2m\left(\mu + i\sqrt{\Delta_0^2 - E^2}\right)}$ according to

$$\Psi(x) = \Theta(-x)\left[e^{ik_+^{(0)}x}\begin{pmatrix}1\\0\end{pmatrix} + re^{ik_-^{(0)}x}\begin{pmatrix}0\\1\end{pmatrix}\right] + \Theta(x)\,te^{ik_+^{(1)}x}\begin{pmatrix}1\\\gamma\end{pmatrix} \quad \text{where} \quad \gamma = e^{-i\text{acos}\frac{E}{\Delta_0}-i\varphi}\ . \tag{1.3.1}$$

The continuity around $z = 0$ gives $r = \gamma$. Remark that, in the limit $E/\mu \ll 1$, the change in momentum is $k_+^{(0)} - k_-^{(0)} \sim \frac{2E}{v_F}$ so that dephasing occurs over distances $\sim v_F/E$ (the coherence length $\xi \propto v_F/\Delta$ gives a lower bound). To maintain coherence in a ballistic S-N-S junction, the length L of the normal region should not exceed the characteristic length of dephasing $L < v_F/E$ or alternatively the energy should remain lower than the Thouless energy $E < E_{\text{Th}} = v_F/L$. In a diffusive S-N-S junction (coefficient D), the mean free path substitutes to the coherence length and the Thouless energy, not to exceed in order to maintain coherence, reads $E_{\text{Th}} = D/L^2$. Then in a short enough S-N-S junction, an electron can be reflected into a hole which can be reflected back into an electron, as schematized in Fig 1.5, leading to a bound state, providing constructive interferences (leading to discrete levels). In the short junction limit $L\Delta/v_F \ll 1$,

one can neglect propagation in the normal region and obtain a pair of Andreev bounds states

$$|\gamma|^2 \mathrm{e}^{\pm i\delta\varphi} = 1 \quad \Rightarrow \quad E_\pm^0(\delta\varphi) = \pm\Delta \cos\frac{\delta\varphi}{2} \ , \tag{1.3.2}$$

which oscillates as a function of the phase difference $\delta\varphi = \varphi_R - \varphi_L$ between right and left superconductors. In the general case, a transcendental equation has to be solved [36] and a set of pairs of bound states is obtained with a low-energy level spacing $\propto v_F/d$ between these pairs, where d is the length of the normal region. In Eq. (1.3.1), backscattering due to normal reflection has been neglected in the limit $\Delta/\mu \ll 1$. A full treatment which takes into account finite transmission $T < 1$ would lead to a coupling of the two perfect transmission states with energies $E_\pm^0$ and to an avoided crossing at $\delta\varphi = \pi$, according to

$$E_\pm(\delta\varphi) = \pm E_A(\delta\varphi) \quad \text{with} \quad E_A(\delta\varphi) = \Delta\sqrt{1 - T\sin^2\frac{\delta\varphi}{2}} \ . \tag{1.3.3}$$

It is displayed in Fig. 1.6. In Chapter 5, we will calculate the Andreev bound states around a Dirac delta scatterer in a superconducting wire. We will recover the last result.

As mentioned earlier, due to charge conservation, an Andreev reflection should be accompanied with the creation or a destruction of a Cooper pair from the BCS ground state of the superconducting material. As a result, a bound state is formed providing Cooper pairs are transmitted from one superconductor to the other as illustrated in Fig. 1.5. This equilibrium (phase-driven) DC supercurrent was predicted within the BCS framework by Josephson in his seminal work [15]. In Chapter 5, we will also provide an expression for the Josephson current: bound states carry opposite currents $I_\pm(\delta\varphi) \propto \frac{\partial E_\pm}{\partial(\delta\varphi)}$ so that the average current at zero temperature reads (in such a limit only the lowest Andreev state is occupied, for finite temperature the difference of Fermi factors is involved as a prefactor)

$$\langle I(\delta\varphi)\rangle = -e\,\frac{\partial E_A}{\partial(\delta\varphi/2)} = \frac{T}{2}\,\frac{\sin\delta\varphi}{\sqrt{1 - T\sin^2\frac{\delta\varphi}{2}}}\,e\Delta \ . \tag{1.3.4}$$

It is also displayed in Fig. 1.6. Remark that in the limit of low transmission $T \ll 1$ (tunnel regime), we recover the phenomenological prediction $\langle I(\delta\varphi)\rangle = I_c \sin\delta\varphi$ [37], established using the pseudowavefunction $\Psi_j = \sqrt{n_j}\,\mathrm{e}^{i\varphi_j}$ (where n_j is the number of Cooper pairs in the superconductor S_j and φ_j is their phase) introduced as an order parameter in the Ginzburg-Landau formalism [9]. Josephson current is indeed a phenomenon which occurs in a great variety of weak links between superconductors. It is a macroscopic manifestation of quantum coherence which has been observed soon after its prediction [38]. The study of these different kinds of junction supporting a supercurrent include the computation of the critical current I_c following the work by Ambegaokar and Baratoff [39, 40].

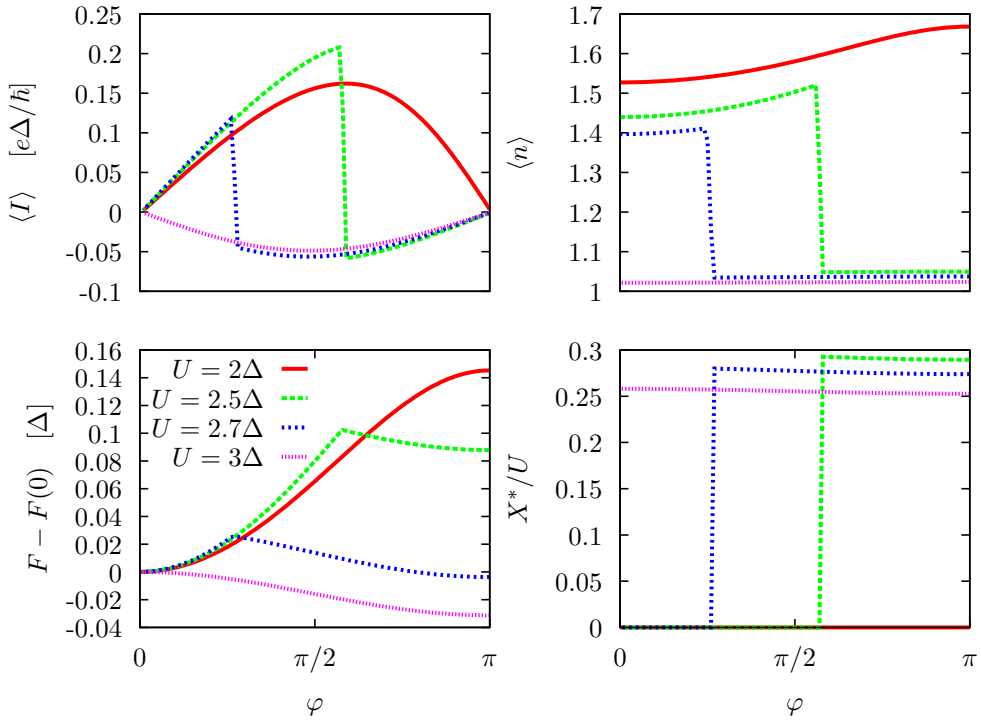

Figure 1.7: First order phase transition in a S-QD-S junction (the key is given in the bottom left panel). The energy level $\varepsilon = -2\Delta$ is negative so that the π phase is achievable. Other parameters are $\gamma = 0$, $\Gamma = \Delta$, $\beta^{-1} = 0.01\Delta$.

1.4 π junction

Interestingly, the critical current could be negative [41, 42] in the so-called π junctions where the Josephson current reads $I_c \sin\varphi = |I_c| \sin(\varphi + \pi)$. A derivation for such a negative coupling was proposed for a magnetic impurity localized between two superconducting grains [43]. This argument used perturbation theory in the coupling between the impurity and the grains. Nevertheless it was confirmed by a non-perturbative treatment of a single dot embedded in a Josephson junction (S-QD-S junction) followed by a numerical investigation of the phase transition which occurs in such a system [44]. We do not enter into the details because it will be further done in Chapter 3 when modelizing a SQUID experiment where two S-QD-S junctions will enclose a magnetic flux as a probe for Cooper pair splitting [19]. A path integral formulation of the partition function Z is used and a free energy is defined as $F = \beta^{-1} \ln Z$ where β^{-1} is the temperature (if Boltzmann constant is taken as unity $k_B = 1$). To include Coulomb interaction, a Hubbard-Stratonovich transformation is employed and a auxiliary parameter X^* is then in-

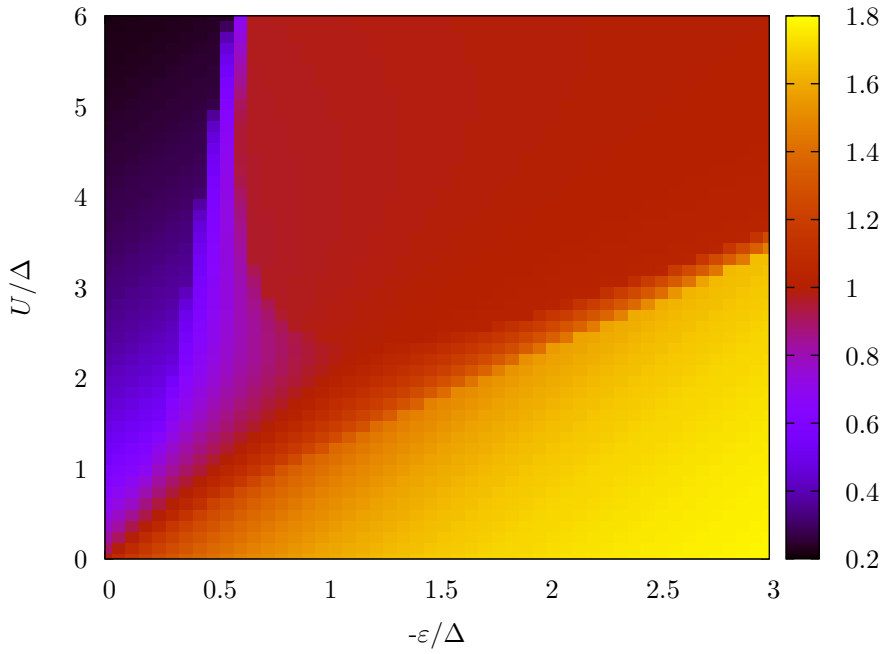

Figure 1.8: Mean occupation number diagram of the quantum dot in a S-QD-S junction for symmetric couplings ($\gamma = 0$) and for $\Gamma = \Delta$, $\beta^{-1} = 0.02\Delta$.

troduced. Two parameters characterize the isolated level of the quantum dot, namely its energy ε and the on-site Coulomb interaction U. Coupling parameters between the superconducting leads and the quantum dot also enter the description of the S-QD-S junction and can be recast into two quantities which are the decay rate Γ of the quantum dot and the asymmetry γ of the junction.

The phase in which standard positive critical current (positive Josephson current for $\varphi \in [0, \pi]$) is recovered is denoted as the 0 phase. It can be further separated between a $0^{(0)}$ phase where the dot is almost empty and a $0^{(2)}$ phase where the mean occupation number of the dot is almost 2. The π phase is associated with an anomalous negative critical current (negative Josephson current for $\varphi \in [0, \pi]$) and corresponds to a singly occupied dot.

Both the Josephson current and the mean occupation number can be written as first order derivatives of the free energy, $\langle I \rangle = 2e\frac{\partial F}{\partial \varphi}$ and $\langle n \rangle = \frac{\partial F}{\partial \tilde{\varepsilon}}$ where $\tilde{\varepsilon} = \varepsilon + U/2$, so that both quantities undergo a discontinuity at the (first order) phase transition. This is illustrated in Fig 1.7 where the Coulomb interaction U is tuned across the critical point U_c (all other parameters are fixed) so that the system originally in the $0^{(2)}$ phase evolves into a π phase: in the intermediate regime,

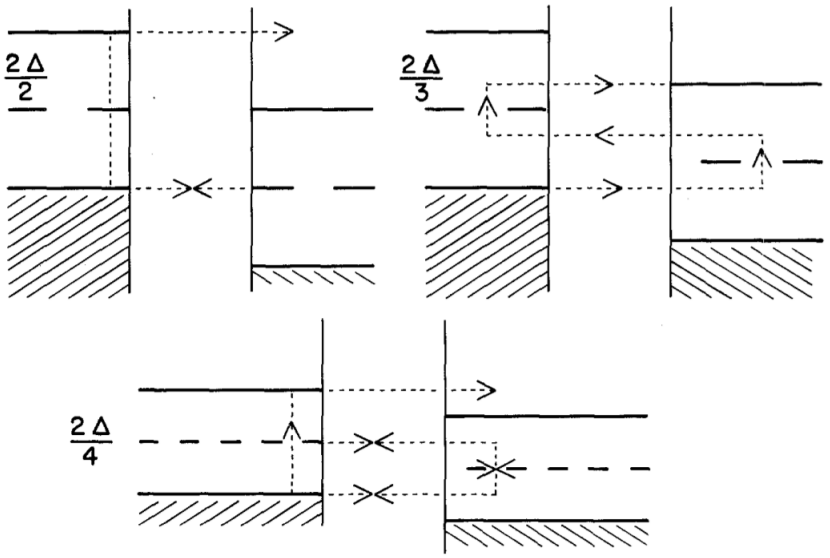

Figure 1.9: Three lowest order MAR. Adapated from [46]

the discontinuities are visible. In the same figure, we also provide the evolution of the free energy and of the magnetization X^*/U. While the free energy displays a single local minimum in the 0 phase (located in $\varphi = 0$) and in the π phase (located in $\varphi = \pi$), two local minima are encountered in the intermediate regime. The magnetization takes no vanishing values as soon as the 0 phase is exited. Computing the mean occupation number on the quantum dot in the $(-\varepsilon, U)$ plane reveals the presence of all three phases, as shown in Fig. 1.8, where the π phase, which lies around the line $\tilde{\varepsilon} = 0$, separates the $0^{(0)}$ and $0^{(2)}$ phases. These predictions have been verified experimentally a decade ago [45].

1.5 MAR processes

When a voltage is applied between the two superconductors of a Josephson junction, the phase difference becomes time-dependent as described by the Josephson relation

$$\frac{\mathrm{d}\delta\varphi}{\mathrm{d}t} = 2eV \ , \tag{1.5.1}$$

so that a constant voltage drop leads to the Josephson AC effect $\langle I(\varphi)\rangle = I_c \sin(\varphi_0 + 2eVt)$ as predicted by Josephson [15]. Consequently, as soon as the voltage does not exceed the sum of the gaps, above which quasiparticle tunneling dissipative current is expected, the (time-averaged) current should vanish as no Cooper pairs are (permanently) transported from one superconductor

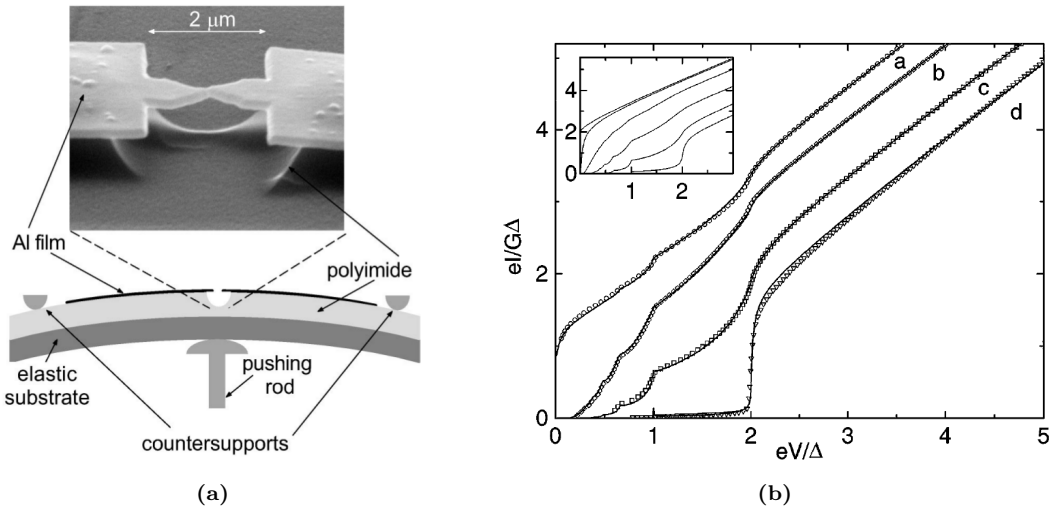

Figure 1.10: (a) Al quantum point contact realized with the break-junction technique which consists in bending the substrate in a controlled way [47]. (b) $I-V$ curves (the labels a-d correspond to different channel transmissions) obtained in Ref. [47] displaying the MAR onsets in agreement with the tunnel Hamiltonian approach of Ref. [48].

to the other. However, first evidences for subgap transport in a S_a-N-S_b junction beyond single particle tunneling emerge in experimental I-V characteristics [49]: onsets in the excess current at voltages Δ_a and Δ_b can be explained by taking into account double particle tunneling [50] possible by involving Cooper pair transfer. This idea was precised in the so-called BTK (for Blonder, Tinkham and Klapwijk) mechanism [16] by involving the process at the origin of Cooper pair generation/destruction at N-S interfaces, namely Andreev reflection [14]. This approach relies on the generalized semiconductor scheme for superconducting leads, that is a trajectory technique considering that the only relevant factor is the density of states as a function of the energy.

A Multiple Andreev Reflection (MAR) is responsible for the promotion of a quasiparticle just below the gap of lead a into the conduction band of lead b if $V_a > V_b$. Let us suppose $\Delta_a = \Delta_b \equiv \Delta$ for simplicity. If $V_a - V_b > 2\Delta/n$, the incident quasiparticle can undergo $2 \times \text{floor}(n/2)$ Andreev reflections involving the transfer of $\text{floor}(n/2)$ Cooper pairs. The three lowest order MAR processes are illustrated in Fig. 1.9. MAR processes explain the Subhamonic Gap Structure (SGS) of I-V curves where onsets are visible at voltages $2\Delta/n$.

Normal scattering was neglected in [16] and was later included in another approach, based on the resolution of Boltzmann equations [51] that simply reduces to the KBT model in the limit of no normal scattering. This last model (extended to include heating effects) was used to

successfully describe I-V experimental curves [52].

The original idea [50] of Multiple Particle Tunneling (MPT) relies on a tunneling Hamiltonian approach and faces some technical issues (divergences due to finite order perturbation theory). A nonequilibrium Green's function formalism was used to circumvent these difficulties [46]. In this last work, the AC components of the Josephson current are also investigated and they exhibit structures at the MAR thresholds. A scattering matrix approach recovering these results [53] further investigates the low voltage regime in connection with the quasistationary Josephson current carried by the subgap Andreev levels. Another scattering approach [54] in single channel tunnel junctions was motivated by experimental results on break junctions [55]. Let us also mention the study of low voltages in Ref. [56].

The Hamiltonian approach (and the original MPT idea) finally proved to be efficient when treated in a non-perturbative way [48] and these single conduction channel results were used in order to fit experimental data [47]. In the last Al quantum point contact experiment with several conduction channels, the fit allows to extract the set of channel transmissions (Fig. 1.10). Shot noise is also calculated in [57] and Fano factor effectively gives the effective transported charge in a MAR.

Chapter 2

Cooper pair splitting in a Josephson junction geometry

In this chapter, we are interested in the enhancement of Cooper Pair (CP) splitting in a double Josephson junction where two superconducting leads are bridged by two Quantum Dot (QD) nanotubes/nanowires, as illustrated in Fig. 2.1. When used as a Superconducting QUantum Interference Device (SQUID), a magnetic flux is inserted inside the area enclosed by the two nanotubes/nanowires and the measurement of the Aharonov-Bohm (AB) oscillations of the critical current can give quantitative information about the nonlocal conduction processes which can occur in this so-called nanoSQUID CP splitter [19].

The proposed diagnosis is a convenient alternative to the early proposals of CP splitters which require out-of-equilibrium measurements which are difficult to achieve experimentally (Section 2.1). The improvement in contacting QD nanotubes/nanowires to superconductors together with the achievement of large QD charging energies [58, 59] motivated a theoretical approach going beyond previous descriptions of the double Josephson junction [18, 60, 61] and early qualitative evidences for CP splitting [59] motivated the search for a quantitative measurement of the efficiency of this setup when used in a SQUID operation (Section 2.2). The path integral formulation of the partition function (Section 2.3) allows to treat non-pertubatively the couplings between superconductors and QDs, and a Hubbard-Stratonovich transformation followed by a saddle-point approximation is used to deal with Coulomb on-site repulsion terms [44] (Section 2.4). A systematic study of all possible phase associations for the QDs (0 or π junctions) reveals that monitoring the energy levels of the QDs through gate voltages to impose single oc-

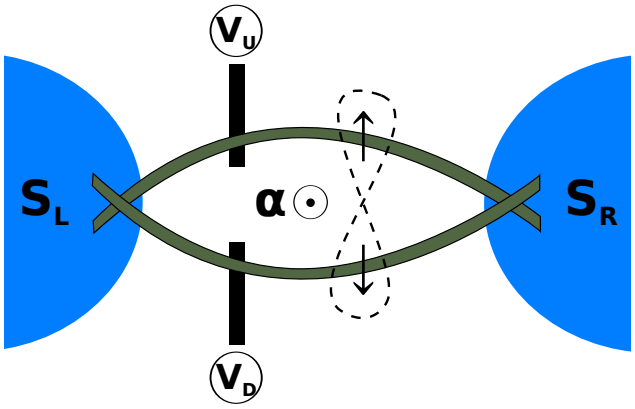

Figure 2.1: NanoSQUID CP splitter practical realization: nanotube/nanowire QDs which energies can be varied with gate voltages bridge two superconducting contacts.

cupancy (π phase) enhances the CP splitting (Section 2.5). Several limitations of the theoretical approach developped here are mentioned and some ways to overcome them are envisaged as possible extensions of this work (Section 2.6).

2.1 First proposals of Cooper pair splitters

The process of Andreev Reflection (AR) has already been introduced in Section 1.2 of Chapter 1. When a superconductor is connected to a normal metal, the constituent electrons of a CP can be transmitted through AR: a hole from the normal metal incident on the superconductor is reflected as an electron in this same metal. If now two metallic contacts are connected to a superconductor, the reflection can occur accross the two contacts if they are separated by a distance smaller than the superconducting coherence length (Fig. 2.2a). This process called Crossed AR (CAR) is responsible for CP splitting: the pair exits the superconductor and its two constituent electrons propagate in two different metallic leads forming a nonlocal state with spin and orbital degrees of freedom which are entangled. Evidently the local AR refered as Direct AR (DAR) can still occur inside each metallic lead (Fig. 2.2b) and spoils the efficiency of the device operating as a CP splitter. Another competing nonlocal process will occur in such a three-terminal device: Electron Cotunneling (EC) [62] refers to the transmission of an electron from one metallic lead to the other through the superconductor (Fig. 2.2c). EC is not based on AR and therefore no real CP production/destruction is involved in this tunnel effect but it requires a virtual excited quasi-particle state in the superconductor. EC is reminiscent of the normal behavior of the injecting

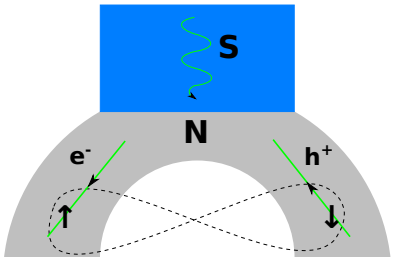

(a) CAR process.

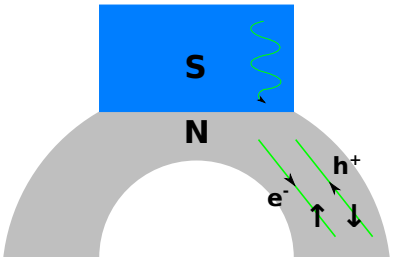

(b) DAR process.

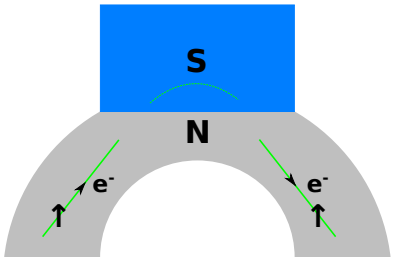

(c) EC process.

Figure 2.2: Elementary processes which can happen when two metallic leads are contacted to a superconductor. Two processes are based on AR: DAR occurs inside a single contact (local) while CAR occurs across the two contacts (nonlocal). EC is a tunneling process across the two contacts (nonlocal) which involves a virtual excited quasi-particle state in the superconductor.

material (when superconductivity is quenched by temperature or magnetic field) and spoils the efficiency of the device operating as an electron entangler. Let us emphasize that the transmission of the electrons originated from CPs inside the superconductor to the normal material, through AR processes, is driven here by voltage biases (non-equilibrium setup) and CAR signatures are expected in nonlocal/cross-junction (linear or differential) conductance measurements as well as in the cross correlations of the currents flowing in the two outgoing leads.

An early theoretical proposal [63] for the manifestation of CAR relies on the measurement of nonlocal current in a nanoscale two-contact tunneling device (Fig. 2.3a). Ferromagnets with opposite polarizations (spin filtering for CAR enhancement to the detriment of EC) as contacts were proposed [64] and a first experimental CP splitting signature was obtained in an aluminium sample [65] (Fig. 2.3b). Nonlocal linear conductance $G^{\sigma}_{\rm cross}$ is different between parallel ($\sigma = +$) and antiparallel ($\sigma = -$) alignement configurations of the spin valve. Below the critical

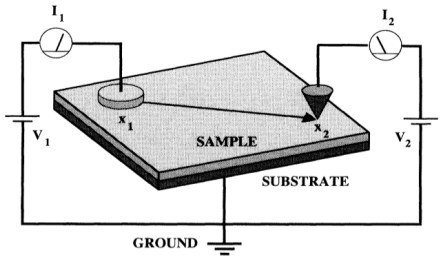

(a) The cross-junction differential conductance $\frac{\partial I_1}{\partial V_2}(V_2, |\mathbf{x_1} - \mathbf{x_2}|)$ measurement of a superconducting sample should reveal CAR process [63].

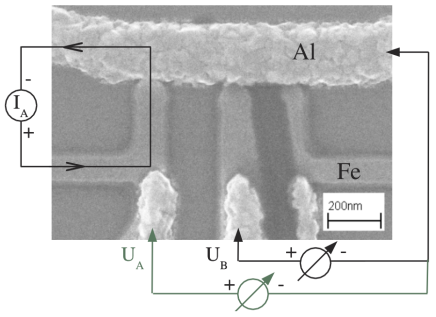

(b) SEM image of a sample used in [65]. The Aluminium sample is connected to ferromagnetic iron contacts. Nonlocal linear conductance $G_{\text{cross}} = I_A/U_B$ is different between parallel and antiparallel alignement configurations of the spin valve and this difference in the superconducting state is explained by EC and CAR nonlocal processes.

Figure 2.3: Nonlocal conductance as a probe of CP splitting [63, 65].

temperature, the spatial dependance of this difference $\Delta G_{\text{cross}} = G^{+}_{\text{cross}} - G^{-}_{\text{cross}}$ is in agreement with a theory describing both CAR and EC processes in a dirty superconductor [62, 66, 67]. The first CAR evidence in a device with normal leads was claimed later on [68]. In this N-S-N multilayer setup, a current is injected inside one of the N-S junctions and the voltage response across the second one is measured has a function of the energy of the injected electrons. The sign change in samples with a sufficiently thin superconducting layer proves that CAR and EC processes (responsible for opposite sign contributions) have energy dependences that can be exploited in order to build an efficient electron entangler (where CP splitting is favored). Multiple parallel normal leads were coupled across a superconducting lead and allow spatial dependence analysis [69] in agreement with theoretical predictions in the extended contact limit [66]. The experimental works [65, 69] agree with the theoretical exponential supressions of EC and CAR effects on a length scale given by coherence requirements (BCS coherence length ξ_0 in a clean superconductor or dirty coherence length $\tilde{\xi} = \sqrt{l\xi_0}$ in a diffusive superconductor with mean free path l) with eventual algebraic prefactors ($1/r^2$ in the clean limit and $1/r$ in the dirty limit and none for extended contacts which width is much larger than coherence length) [66]. The oscillating behavior on the Fermi wavelength scale obtained for ponctual contacts, reminiscent

of the surprising result that the entanglement length in the BCS ground state is given by Fermi wavelength and not coherence length [70], is averaged by integration over the finite size of the injection regions [62, 66].

The study of the noise in mesoscopic devices is a powerful tool to probe the statistics of the charge carriers [71]. In a "Y"-shaped structure, the nature of the injecting branch is important for the prediction of the cross correlations $\langle \Delta I_1 \Delta I_2 \rangle$ between the currents I_1 and I_2 flowing in the two outgoing normal branches. An all-normal fork will lead to negative correlations as a consequence of Fermi statistics: this is the fermionic version of the Hanbury Brown and Twiss (HBT) experiment [72] that displays antibunching effect. However, if the injecting material is superconducting then the question of the sign of these correlations remains open [73]. Assuming the spin singlet nature reminiscent of Cooper pairing in the injector to be preserved in the vicinity of the N-S interface, one expects bunching effect [74] and eventually positive correlations. This bunching effect originates in the injection of the constituent electrons of CPs from the superconductor to the normal metal or alternatively in the CAR of a hole into an electron in the normal metal. In the generalization of the Landauer-Buttiker scattering theory of transport for multiterminal mesoscopic normal devices [75] to include a superconducting region, one prescription was to add an index representing the conducting species (e for electron and h for hole) to every contact in order to take into account the AR processes responsible for electron to hole (and *vice versa*) conversions [76]. In the calculation of the noise cross correlations between contacts i and j of an hybrid device, *i.e.* including superconducting material, the anomalous positive components $\langle \Delta I_{ie} \Delta I_{jh} \rangle + \langle \Delta I_{ih} \Delta I_{je} \rangle$ add to the standard normal scattering negative components $\langle \Delta I_{ie} \Delta I_{je} \rangle + \langle \Delta I_{ih} \Delta I_{jh} \rangle$ and while the resulting sign is generally undetermined, an Andreev interferometer setup was proposed to obtain positive correlations (Fig. 2.4). The possibility to achieve positive correlations in a HBT experiment in the vicinity of a N-S interface has been confirmed in a theoretical work based on the same scattering approach [77]. Considering the original proposal for CAR manifestation [63], that is two normal biased leads weakly coupled to a grounded superconducting sample, the lowest order of perturbation theory in the subgap regime (voltages and temperature much smaller than the gap energy) involves nonlocal CAR and EC as well as DAR on each lead [78]. Current cross correlations in this regime are only due to nonlocal processes which contribute with opposite signs: CAR leads to a positive contribution contrary to EC.

In order to characterize the entanglement in the vicinity of a N-S junction, a fork geometry for the normal lead associated to spin-selective or energy-selective filters inside the leads

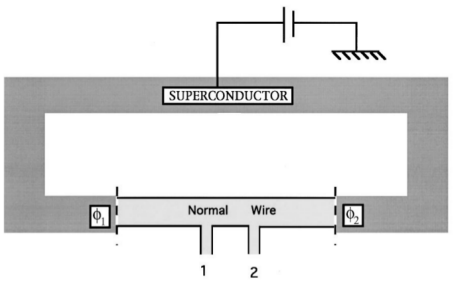

(a) Andreev interferometer.

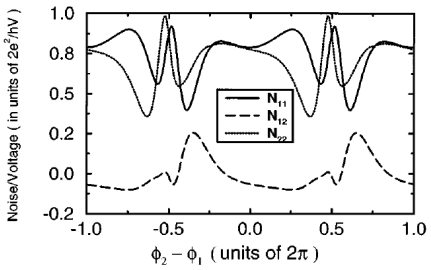

(b) The noise cross correlations N_{12} can either be positive or negative depending on the phase difference $\phi_2 - \phi_1$.

Figure 2.4: Bunching effect between electrons in hybrid mesoscopic devices can be evidenced in noise measurements [76].

were considered [79] in order to enhance the CAR process and quantify the efficiency of the entanglement in the selected degree of freedom by measuring (positive) noise cross correlations. Energy filtering is commonly retained and as a result spin is the degree of freedom which entanglement is measured. Bell Inequality (BI) tests involve the measurement of particle number correlators but in the limit of a large counting time BI can be reformulated in terms of current cross correlators and potentially violated in a "Y"-shaped N-S tunnel junction with energy filters (spin entanglement) and ferromagnets as spin polarizers [80]. In order to supress DAR processes and therefore favor nonlocal processes, electron-electron interactions can be used. QDs in the Coulomb blockade regime between the injecting superconductor and the normal metal leads were proposed in order to enhance the CP splitting [81] (see Fig. 2.5a for the proposed QD CP splitter setup). T matrix calculations were performed to compute separately the currents due to lowest order perturbation processes that lead to the transport of a CP in such a device. The parasitic tunneling processes through a single QD which involve either direct AR on the QD with a resulting double occupancy or sequential tunneling are suppressed (with respect to the CAR process) respectively by large Coulomb on-site repulsion and large superconducting gap energy. Interestingly the CAR process features a resonance for opposite QD energies and it was stressed that the electron constituents of the spin singlet delocalized on the two QDs can achieve a degeneracy of orbital energies crucial for bunching effect. The working regime of this entangler (when CAR is enhanced) has been further studied by the use of a density matrix formalism that describes the mixing of theses processes (through EC) and the derivation of quantum master

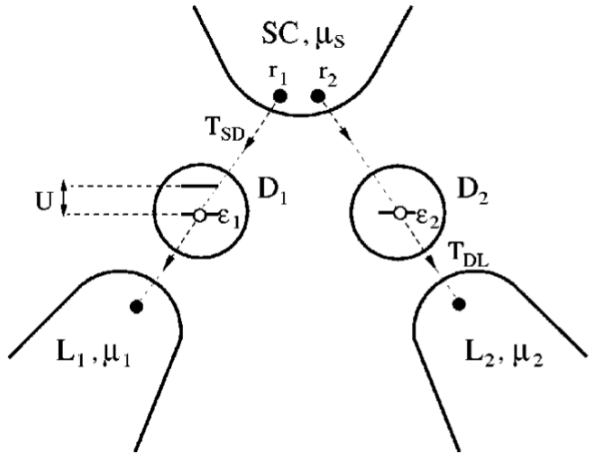

(a) Theoretical proposal [81].

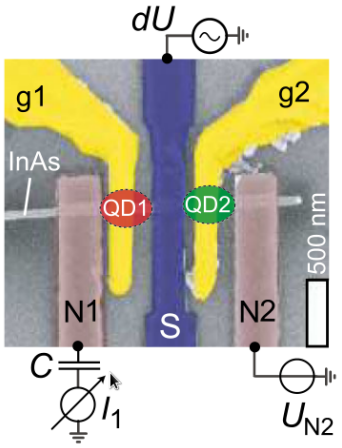

(b) Colored SEM image of the device used in [86,87].

Figure 2.5: Theoretical proposal [81] and first experimental implementation [86] of the QD CP splitter.

equations [82]. The same formalism was used in order to compute spin current ($I_i^{\text{spin}} = I_i^{\uparrow} - I_i^{\downarrow}$) noise and the associated Fano factor which was proposed as an alternative tool to probe the efficiency of the entangler, the ultimate characterization remaining the BI tests [83]. The same setup was studied later on and the current correlations were expressed in terms of two-particle Green's functions of the QD electrons [84]. It was confirmed that opposite QD energy levels favors the CAR process and that the associated positive noise cross correlations are enhanced by on-site Coulomb repulsion [85]. This setup has raised a lot of interest since its practical realization has been achieved using an InAs semiconducting nanowire realizing a double QD connecting an Aluminium superconducting source to two metallic drain contacts [86, 87]. Fig. 2.5b is a Scanning Electron Microscopy (SEM) image of the device. Evidence for CP splitting in linear conductance measurements was claimed [86] (Fig. 2.6a) and further investigations, albeit in a different measuring scheme, adress the competition between CAR and EC processes while tuning through a QD resonance [87]. CAR manifestations were also reported in [88] where differential conductances were measured through anticrossings of the "honeycomb" stability diagram of a double QD engineered in a Single Wall Carbon NanoTube (SWCNT). The efficiency of CP splitting was estimated in a similar experiment [89] to a value close to BI violation requirement. A further step towards a quantitative measure of the entanglement in such a geometry has been achieved by the measurement of positive noise cross correlations [90]. In this InAs nanowire QD

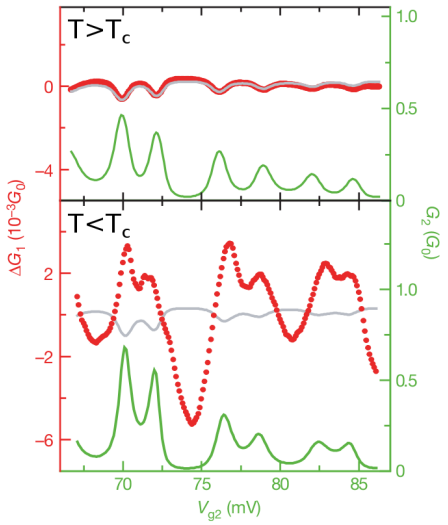

(a) Nonlocal conductance signature of CP splitting [86]. When the source is superconducting ($T < T_c$) $\Delta G_1(V_{g2})$ (red dots) strongly differs from the classical expectation (grey curve) and is positive at Coulomb peaks (maxima of the green curve $G_2(V_{g2})$).

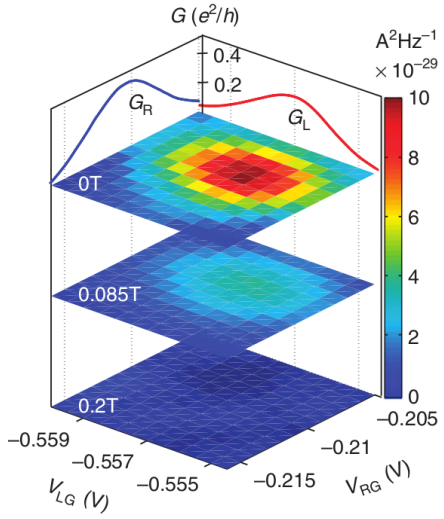

(b) Noise cross correlations are maximally positive at a resonance for both QDs and are suppressed when a magnetic flux quenches superconductivity [90]. This bunching effect originates in the CP splitting operating in the device.

Figure 2.6: CAR manifestations in a QD CP splitter [86, 90].

CP splitter, below the critical temperature of the Aluminium injector, positive correlations are obtained around a resonance for both QDs and they vanish as soon as a magnetic flux quenches superconductivity (Fig. 2.6b). Let us mention that a less convincing claim (a simpler geometry without filtering for CAR enhancement is used) was communicated earlier [91]. An alternative to QDs was proposed in the use of Luttinger liquid nanowires [92, 93] but to our knowledge it has not met experimental implementations yet.

Let us emphasize that CAR processes are intimately related to entanglement, which constitutes yet another motivation for perfecting our understanding of such processes. Indeed, when the two electrons of a CP are separated in two different normal metal electrodes, one expects that the entanglement of the spin degrees of freedom is preserved because the tunneling processes are spin-preserving. CAR processes thus create pairs of spatially separated entangled electrons. We have already mentioned that tests of quantum entanglement, based on BI violation, could be implemented *via* noise cross correlation measurements [80, 83]. Moreover, these ideas can be extended to quantum information and computation problematics. They have been applied for

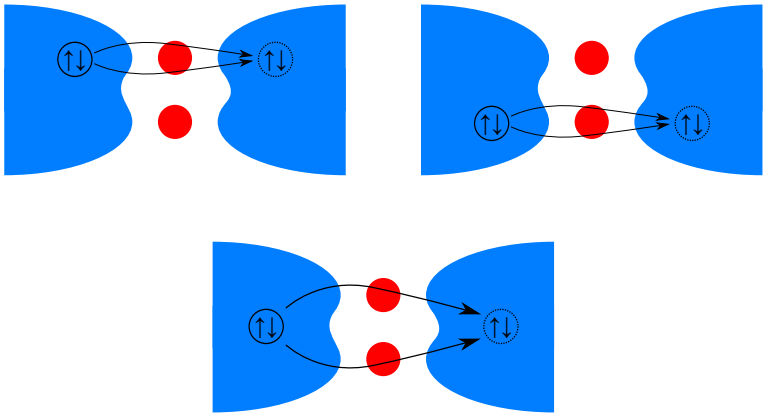

Figure 2.7: The three different processes involved in the transmission of a CP in the nanoSQUID CP splitter: the two electrons can either be both transmitted through the upper QD (top left), through the lower QD (top right), or the CP can be split with one electron transmitted through each QD (bottom).

example to the paradigm of quantum teleportation [94, 95].

2.2 Cooper pair splitting in an equilibrium setup

All the experimental works highlighted in Section 2.1 rely on non-equilibrium measurements. Noise cross correlation measurements achieved in [90] represent a considerable ordeal due to the poor signal to noise ratio, and no attempt has been made so far to reproduce them. In order to circumvent these difficulties a Josephson (equilibrium) geometry was proposed [18]: two QDs are placed between two superconductors and materialize two spatially separated conduction channels for the constituent electrons of a CP which can tunnel from one superconductor to the other driven by an applied phase difference. Fig. 2.7 illustrates the different possible processes: the two electrons can either pass both through a given QD or they can transit through different QDs and realize CP splitting through a CAR process at the boundary of the superconducting source (the recombination on the superconducting drain involves a second CAR process). This double Josephson junction with embedded QDs realizes an AB interferometer and we will refer to this setup as the nanoSQUID CP splitter [19]. In the presence of a magnetic flux $\Phi = \frac{\alpha}{2\pi}\Phi_0$ ($\Phi_0 = h/e$ is the flux quantum), electrons experience a path dependent phase shift. When a CP tunnels as a whole through a single QD, it accumulates a phase shift $\pm\alpha$ ($\pm$ depending on which QD) in addition to the phase difference ϕ between the two superconductors. However, when the Cooper pair is delocalized on the two QDs, one electron gets a phase shift $+\frac{\alpha}{2}$ while

the other one gets a phase shift $-\frac{\alpha}{2}$, the pair accumulating as a result no additional phase shift. The Josephson current at the lowest order in the transmission probabilities (where only the three processes illustrated in Fig. 2.7 are relevant) can be written as

$$J(\phi,\alpha) = I_1 \sin(\phi+\alpha) + I_2 \sin(\phi-\alpha) + I_{\rm CAR} \sin\phi \ . \tag{2.2.1}$$

The associated critical current then reads

$$J_c(\alpha) = \max_\phi |J(\phi,\alpha)| = I_0\sqrt{1 + a\,\cos\alpha + b\,\cos 2\alpha} \tag{2.2.2}$$

where we define

$$I_0 = \sqrt{I_1^2 + I_2^2 + I_{\rm CAR}^2}\ , \quad I_0^2\, a = 2I_{\rm CAR}\,(I_1+I_2) \quad \text{and} \quad I_0^2\, b = 2I_1 I_2\ . \tag{2.2.3}$$

The critical current as a function of the AB flux should be π periodic if electrons are not split between the two QDs (if $I_{\rm CAR} = 0 \Rightarrow a = 0$) and 2π periodic if CP splitting is effective (as soon as $I_{\rm CAR} \neq 0$) [60]. Each of the three processes illustrated in Fig. 2.7 can be uncovered with different successions of elementary tunneling processes. The original proposal [18] which focuses on a configuration with singly occupied QDs (negative QD energy levels and infinite on-site repulsion) identifies these successions (see Fig. 2.8) in their perturbative calculations. Some of them can be suppressed if they involve intermediate virtual states with large energy deviation from the ground state energy. Diagnoses to probe the spin state (singlet or triplet) of the electrons on the QDs were proposed [18, 60] in the limit $\epsilon/\Delta \ll 1$ where all processes involving multiple quasi-particle excitations in the superconductors are suppressed (processes (a) and (b) in Fig. 2.8 for instance), in particular AB flux-dependent processes. The effective Hamiltonian can be expressed in terms of the spin operators $\mathbf{S}_a$ $(a = 1, 2)$ of the dots

$$H_{\rm eff} \propto \mathbf{S}_1.\mathbf{S}_2 - \frac{1}{4} = \begin{cases} -1 & \text{for a singlet state,} \\ 0 & \text{for a triplet state.} \end{cases} \tag{2.2.4}$$

The process (c) in Fig. 2.8 will contribute to the current if the QD electrons initially in a singlet state could be combined as a CP in one superconductor and could be regenerated by CP splitting from the other superconductor. Remark that these diagnoses rely on the single occupancy of the QDs. In a configuration with empty QDs (positive QD energy levels) for instance, the AB flux-dependent processes do not necessary involve multiple quasi-particle excitation virtual states. Let us mention the complementary perturbative calculations [60] of the currents in such a configuration with finite on-site Coulomb repulsion. Proposing a more general diagnosis, in

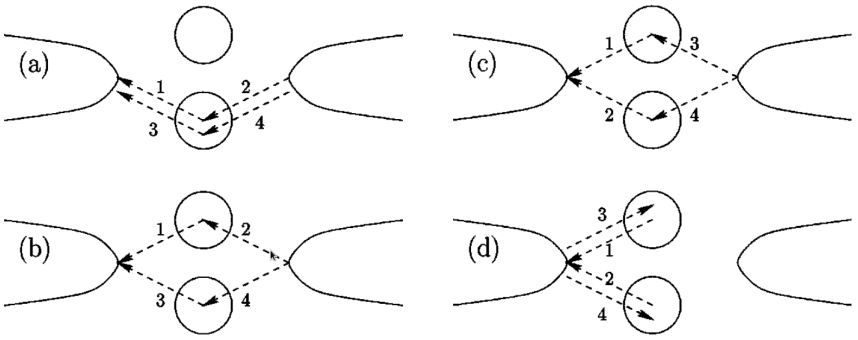

Figure 2.8: Some of the fourth order (in the tunneling amplitudes) processes which can occur in the nanoSQUID CP splitter in a configuration with singly occupied QDs [18]. In process (a) the two constituent electrons of a CP tunnel through a single QD and it involves a virtual state with two quasi-particle excitations. Processes (b), (c) and (d) involve CP splitting. Process (b) involves a virtual state with two quasi-particle excitations contrary to processes (c) and (d) with at most one quasi-particle excitation. Remark that process (d) does not lead to effective charge transport and therefore does not contribute to the current.

particular independent of the occupancy of the QDs in the ground state of the system, is a first motivation for the present work. Analysing the AB flux dependence of the critical current could give quantitative information about CP splitting based nonlocal phenomena in the whole parameter space.

First we have to define a CP splitting efficiency in terms of AB oscillation measurements. We need a way to quantify contributions to the Josephson current which involve CP splitting. For that, we start by discussing the case of low electron transmission, where intuition can be gained from simple perturbation theory. We have already introduce the three lowest order processes (illustrated in Fig. 2.7) that contribute to the transmission of a CP, which is the elementary supercurrent charge. If we are able to extract the three associated amplitudes I_1, I_2 and I_{CAR} that enter the expression (2.2.1) of the Josephson current, e.g. from a fit of the AB critical current (2.2.2), we can calculate the quantity

$$r_t = \frac{I_{\mathrm{CAR}}^2}{I_1^2 + I_2^2 + I_{\mathrm{CAR}}^2} \tag{2.2.5}$$

which encodes the splitting efficiency of the double Josephson junction. It varies between 0 and 1 and $r_t = 1$ ($\Leftrightarrow I_1, I_2 \ll I_{\mathrm{CAR}}$) is obtained when the spatial delocalization of the two electrons of the transmitted CP (CAR process or CP splitting) is much more favored than the tunneling processes of the whole CP through a single QD, contrary to the case $r_t = 0$

($\Leftrightarrow I_{\rm CAR} \ll I_1, I_2$). The CAR process is suppressed by a large separation of the injection points in the superconductors, compared to the superconducting coherence length, and such a configuration can be used as a benchmark for an estimation of local processes. On the contrary, it is maximally favored when the contacts are brought together within a distance much smaller than the superconducting coherence length. A parameter $\eta \in [0, 1]$ will be introduced in Section 2.4 to tune the prominence of CAR processes in a phenomenological way. Its extremal values encode the two cases we have just mentioned:

- $\eta = 0$ for infinitely distant injection points, *i.e.* much more separated than the superconducting coherence length,
- $\eta = 1$ for coinciding injection points, *i.e.* much closer than the superconducting coherence length.

An alternative way to obtain the quantity (2.2.5) involves the mean powers of the critical current obtained in these two cases $\eta = 0$ and $\eta = 1$:

$$r = \frac{|\mathcal{P}_{\eta=1} - \mathcal{P}_{\eta=0}|}{\mathcal{P}_{\eta=1}} \quad \text{with} \quad \mathcal{P}_\eta = \int_0^{2\pi} \mathrm{d}\alpha \, [J_c^\eta(\alpha)]^2 \ . \tag{2.2.6}$$

This quantity which can be computed regardless of the strength of the coupling between the superconductors and the QDs, generalizes the concept of splitting efficiency to the case of arbitrary transmission, and coincides with the definition (2.2.5) of r_t in the tunneling regime.

Let us discuss now the feasibility of such an experiment. For CP splitting to be efficient, the distance between the injection points to the QDs on both superconductors must not exceed the superconducting coherence length ($\xi_{\rm Al} = 1.6\,\mu$m, $\xi_{\rm Nb} = 38$ nm [96]), which constrains the area threaded by the AB flux. If the applied magnetic field required to apply a few flux quanta becomes larger than the critical field of the superconductors ($H^c_{\rm Al} = 10^{-2}$ Teslas, $H^c_{\rm Nb} = 0.2$ Teslas [97, 98]), the whole diagnosis breaks down. Working with SWCNT [99] or nanowire QDs could be a good option. Indeed their large aspect ratio ($\sim$ micrometer length for $\sim$ nanometer diameter [99]) can optimize the area: one can imagine to bend the wires so that the connections on each superconductor are separated by a distance smaller than the superconducting coherence length (Fig. 2.1) and expect an area of the order of the μm^2. Imposing two magnetic flux quanta within such an area requires a magnetic field of 8×10^{-3} Tesla, which is still smaller than the critical fields of Aluminium and Niobium. A charging energy $E_c = 2.6$ meV has been measured in SWCNTs [99] and it has to be compared with typical gap energies ($2\Delta_{\rm Nb} = 3.05$ meV, $2\Delta_{\rm Al} = 0.34$ meV [96]). Despite the fact that Aluminum has a lower critical temperature

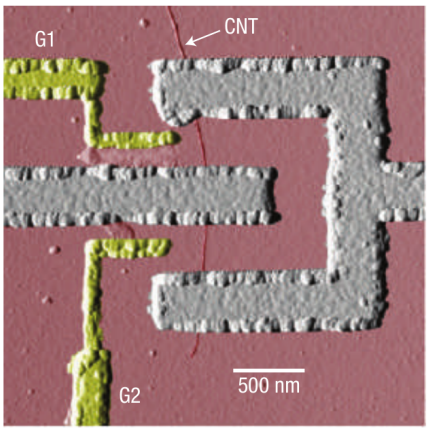

(a) Atomic Force Microscope image of the CNT SQUID device.

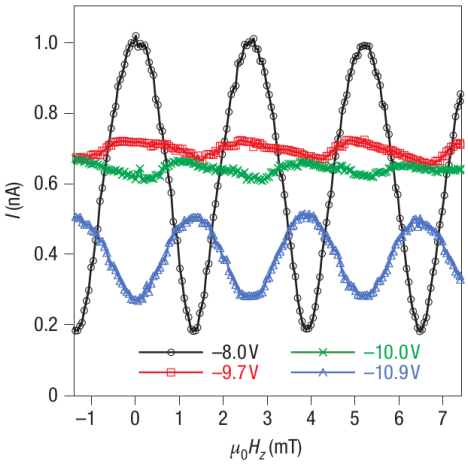

(b) AB flux dependence of the switching current. One of the two Josephson junctions is in a π phase while the other one is tuned (*via* a gate voltage monitoring the QD energy level) through a transition from 0 (black curve) to a π (blue curve) phase.

Figure 2.9: CNT SQUID experiment [58].

and lower critical field than Niobium, this material is probably more suitable for the realization of the nanoSQUID CP splitter due to its small enough gap energy (so that large enough charging energies are available $\Delta_{\mathrm{Al}} \ll E_c$) and its long coherence length (so that CP splitting can be optimized).

Previous descriptions [18, 60] using lowest order perturbation theory in the tunneling Hamiltonian turn out to be insufficient considering progress in the improvement of the contact of SWCNTs to superconducting electrodes and consequently, the achivement of large transmission between the resulting QDs and the leads. In the first experimental realization of a CNT SQUID [58], the superconducting material (Pd/Al bilayer) of the SQUID loop was deposited by electron-beam lithography on the SWCNT (see Fig. 2.9a) and a tunnel rate $h\Gamma = 1$ meV was measured which is not negligible compared to gap energy $2\Delta = 0.12$ meV and Coulomb energy $E_c = 6$ meV. In parallel InAs QD Josephson junctions [59] (see Fig. 2.10a), high charging energies ($U \sim 2 - 5$ meV) and QD-lead tunnel couplings $\Gamma \sim 0.1 - 1.5$ meV (to be compared with the gap energy $\Delta \sim 130\,\mu$m) have been reported.

Let us precise that CP splitting is not efficient in the CNT SQUID experiment [58]: only

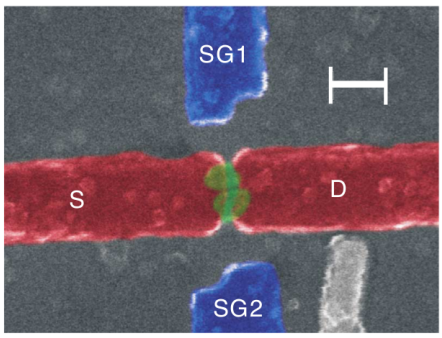

(a) SEM image of the device.

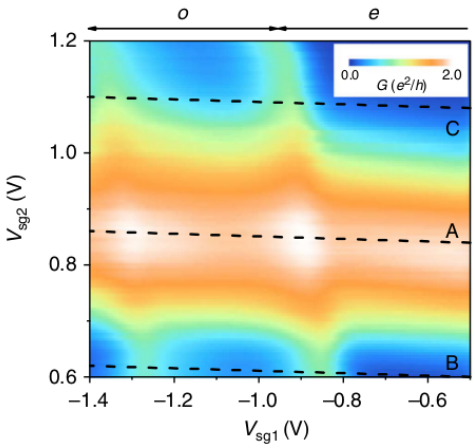

(b) Differential conductance as a function of gate voltages $\frac{\mathrm{d}I}{\mathrm{d}V_{SD}}(V_{sg1}, V_{sg2})$ displaying a Coulomb blockade diamond diagram. Traces A and C give respectively the ON and OFF resonance signals for QD 2 in Fig. 2.10c.

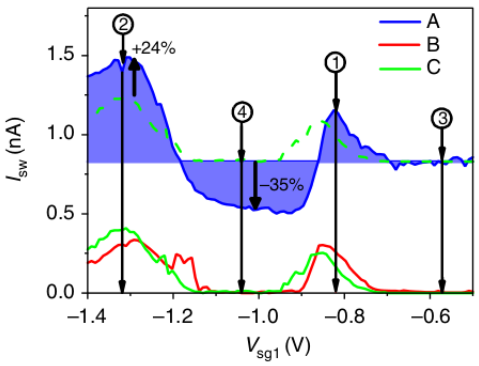

(c) Switching current signals. Points 3 and 4 correspond respectively to even (e) and odd (o) parity for the occupation number of QD 1 (see Fig. 2.10b). Point 3 is taken as a reference level and the 35% difference at point 4 between traces A and C gives an estimate for the contribution of nonlocal transport processes.

Figure 2.10: Parallel InAs QD Josephson junctions [59].

the normal SQUID $\Phi_0/2 = h/(2e)$ periodicity of the switching current (which can be considered as equivalent of the critical current in the present discussion) as a function of the AB flux was observed (no doubling of periodicity as a result of CP splitting). The two parallel Josephson junctions are independent and CPs tunnel from one superconductor to the other through a single QD as CAR processes responsible for CP splitting are prohibited by a too large separation of the CNT contacts. This is the case $\eta = 0$ which is used as a benchmark to estimate local transport phenomena in the diagnosis of CP splitting we propose. An interesting result concerns the influence of the parity of the number of electrons on each CNT arm of the SQUID device. While the parity of one of the arms is fixed, the parity of the other one is changed and consequently the switching current undergoes a $\Phi_0/4$ phase-shift which is attributed to the reversal of the sign of the Josephson current through the junction which is tuned accross a $0-\pi$ transition (see Fig. 2.9b).

Let us mention that the experiment [59] with parallel InAs QD Josephson junctions was not studied in a SQUID operation because of a too small enclosed area. Nevertheless, CP splitting demonstration was claimed in measurements of switching currents $I_{\rm sw}$. Gate voltages V_{sg1} and V_{sg2} allow to monitor the energy levels of the QDs 1 and 2 and displace in the Coulomb blockade diamond diagram (see Fig. 2.10b). A reference signal $I_{\rm sw}^{QD2=OFF}(V_{sg1})$ is taken when QD2 is OFF resonance so that it mostly originates from local transport through QD1 and then an ON resonance signal $I_{\rm sw}^{QD2=ON}(V_{sg1})$ is recorded (see Fig. 2.10c). The difference $\Delta I_{\rm sw} = I_{\rm sw}^{QD2=ON} - I_{\rm sw}^{QD2=OFF}$ is studied as a function of V_{sg1} on a range which extends over two different parity states of QD 1 on each side of a resonance. When QD1 is OFF resonance, $\Delta I_{\rm sw} = \Delta I_{\rm sw}^{(2)} + \Delta I_{\rm sw}^{(12)}$ has a contribution $\Delta I_{\rm sw}^{(2)}$ from local processes through QD2 and a contribution $\Delta I_{\rm sw}^{(12)}$ from nonlocal processes. The first contribution does not depend on the parity of QD1 (the interdot coupling is proved to be negligible), so that taking the difference of the signals for two different parity states of QD1 gives an estimate of the (parity-dependent) nonlocal contribution.

A formalism based on nonequilibrium Green's functions was used in [61] to deal with arbitrary coupling strengths between the superconducting leads and the QDs but CP splitting is clearly not a motivation of this study since Coulomb repulsion on the QDs is neglected. Motivated by the experimental realizations [58, 59], the present work aims at adressing arbitrary transmissions at the contacts of the nanotube/nanowire QDs on the superconductors and at taking into account the QD Coulomb charging energies. For that, we use a path integral formulation of the partition function of the system. A Hubbard-Stratonovich transformation is performed in order to deal with the Coulomb interaction (non quadratic) term that enters the Euclidean action and a saddle-

point approximation is used to obtain numerical results. This is a generalization to two QDs of the formalism developed in [44] which was sufficient to study the 0-π transition of a single QD embedded in a Josephson junction. It has already been introduced in Section 1.4 of Chapter 1, that depending on its energy level position, on its on-site Coulomb repulsion and on its decay rate to the leads, three phases can be distinguished:

- the π phase where the QD is singly occupied,
- the $0^{(0)}$ phase where the QD is empty,
- the $0^{(2)}$ phase where the QD is doubly occupied.

A goal of the present work is to propose a comparative study specifying which combination of the QD phases may enhance the CP splitting signature in the AB signal.

2.3 Path integral formulation of the partition function

In the following $\hbar = k_B = e = 1$. The device is illustrated in Fig. 2.1. For simplicity, the two leads (labeled $j = L, R$) consist of the same superconducting material with chemical potential μ and gap energy Δ. $\hat{\psi}^\dagger_{jk\sigma}$ denotes the creation operator for an electron with momentum k and spin $\sigma =\uparrow,\downarrow$ in the superconductor j. We introduce the Nambu spinors

$$\hat{\psi}_{jk} = \begin{pmatrix} \hat{\psi}_{jk,\uparrow} \\ \hat{\psi}^\dagger_{j(-k),\downarrow} \end{pmatrix} \tag{2.3.1}$$

and the Pauli matrices σ_i $(i = x, y, z)$ that act in Nambu space, useful to write the BCS Hamiltonian of the lead j as

$$\hat{H}_j = \sum_k \hat{\psi}^\dagger_{jk} \left\{ \left(\frac{k^2}{2m} - \mu \right) \sigma_z + \Delta\, \sigma_x \right\} \hat{\psi}_{jk} \ . \tag{2.3.2}$$

The two nanotube/nanowire QDs (labeled $a = U, D$) are placed in the nanogap between the two electrodes. The energies ε_a of the QDs can be monitored *via* gate voltages. Non zero charging energies of these QDs originate in Coulomb on-site repulsions U_a. $\hat{d}^\dagger_{a\sigma}$ denotes the creation operator for an electron with spin $\sigma =\uparrow,\downarrow$ on the QD a. It is convenient to conserve the Nambu structure and we introduce then

$$\hat{d}_a = \begin{pmatrix} \hat{d}_{a\uparrow} \\ \hat{d}^\dagger_{a\downarrow} \end{pmatrix} \tag{2.3.3}$$

so that the Hamiltonian of the QD a (Anderson-type impurity model) reads

$$\hat{H}_a = \varepsilon_a \sum_{\sigma=\uparrow,\downarrow} \hat{d}^\dagger_{a\sigma}\hat{d}_{a\sigma} + U_a \hat{n}_{a\uparrow}\hat{n}_{a\downarrow} \quad \text{where} \quad \hat{n}_{a\sigma} = \hat{d}^\dagger_{a\sigma}\hat{d}_{a\sigma} \ . \tag{2.3.4}$$

By adjusting the QD energy levels ε_a and the Coulomb interaction parameters U_a, we expect to filter the constituent electrons of CPs orginating from the superconducting source. Indeed, negative energies favor occupation of the QDs while on-site Coulomb repulsion prohibits their saturation (double occupation). The regime $U_a \gg \Delta > -\varepsilon_a > 0$ is expected to favor CP splitting. Another crucial requiremement for CP splitting observation resides in the separation between injection points. It must not be much larger than the superconducting coherence length so that the two electrons of a CP can travel through opposite QDs, realizing a CAR process on the superconducting source, followed by an "inverse" CAR process on the superconducting drain: this is the process of CP splitting and recombination with effective charge transport we want to favor. The diagnosis presented in Section. 2.2 will involve two extreme cases. In the first one, the injection points are infinitely distant, nonlocal CAR process is completely suppressed and only local DAR processes occur: the constituent electrons of a CP both pass by a given single QD as in the work [58]. In the second one, the injection points are considered as coinciding, CP splitting is maximally favored (for given QD parameters) and DARs on a single QD are processes that spoil the CP splitting efficiency. The main goal of the present study is to find QD parameters which minimize these spoiling processes.

For given tunneling amplitudes t_{ja} between lead j and QD a, by adjusting the QD free parameters, energy levels ε_a and Coulomb repulsions U_a (in practice only the energy levels can be conveniently varied by additional gates), one can monitor the phases of the two single parallel junctions: 0 phase with even occupancy and positive critical current or π phase with odd occupancy and negative critical current [44]. For that a controllable phase difference ϕ must be imposed accross the junction and it can be achieved by embedding the device in a macroscopic SQUID [18]. This phase difference can be gauged out so that we can conserve the Hamiltonian (2.3.2) (with Δ real). Nevertheless, it will result in the appearance of Peierls factors in the tunneling Hamiltonian. The diagnosis proposed in Section. 2.2 relies on the measurement of the AB oscillations of the system: a magnetic flux $\Phi = \frac{\alpha}{2\pi}\Phi_0$ ($\Phi_0 = h/e$ is the flux quantum), which is in principle independent from the one imposed to trigger a DC Josephson signal between the electrodes, threads the area enclosed by the nanotubes/nanowires. Another change of gauge allows to conserve the Hamiltonian (2.3.2) and leads to additional phase shifts which are different between the two paths that an electron can follow to reach the drain electrode (AB effect). The

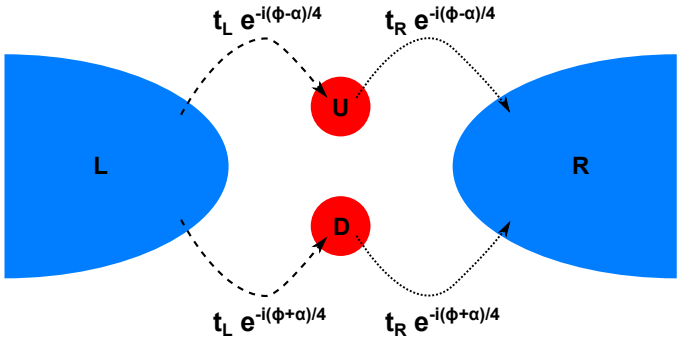

Figure 2.11: Path dependent phase shifts.

resulting tunneling amplitudes are given in Fig. 2.11. If we denote by $\mathbf{r_{ja}}$ the location of the injection point from lead j to QD a, the tunneling Hamiltonian H_t reads

$$\hat{H}_t = \sum_{jka} \mathrm{e}^{i\mathbf{k}.\mathbf{r_{ja}}}\, \hat{\psi}^\dagger_{jk}\, \mathcal{T}_{ja}\, \hat{d}_a + \mathrm{h.c.} \tag{2.3.5}$$

where the tunneling matrices $\mathcal{T}_{ja}$ are given by

$$\mathcal{T}_{LU} = t_L\, \sigma_z\, \mathrm{e}^{+i\frac{\phi-\alpha}{4}\sigma_z} \;, \quad \mathcal{T}_{RU} = t_R\, \sigma_z\, \mathrm{e}^{-i\frac{\phi-\alpha}{4}\sigma_z} \;, \tag{2.3.6a}$$

$$\mathcal{T}_{LD} = t_L\, \sigma_z\, \mathrm{e}^{+i\frac{\phi+\alpha}{4}\sigma_z} \;, \quad \mathcal{T}_{RD} = t_R\, \sigma_z\, \mathrm{e}^{-i\frac{\phi+\alpha}{4}\sigma_z} \;. \tag{2.3.6b}$$

The Hamiltonian of the nanoSQUID CP splitter reads

$$\hat{\mathcal{H}} = \sum_{a=U,D} \hat{H}_a + \sum_{j=L,R} \hat{H}_j + \hat{H}_t \;. \tag{2.3.7}$$

In the path integral formulation of statistical mechanics, the partition function is expressed as a coherent state functional integral [100]. A coherent state $|\xi_\alpha\rangle$ is the eigenstate of an annihilation operator $\hat{a}_\alpha$. The associated eigenvalue a_α ($\hat{a}_\alpha\,|\xi_\alpha\rangle = a_\alpha\,|\xi_\alpha\rangle$) is a Grassmann variable in the case of a fermionic sytem, *i.e.*

$$[a_\alpha, a_{\alpha'}]_+ = 0 \;. \tag{2.3.8}$$

Conjugated variables $\overline{a}_\alpha$ are also defined and the generators $\{a_\alpha, \overline{a}_\alpha\}_\alpha$ form a Grassmann algebra. The handling of Grassmann variables is explained with details in [101]. The collections of the Grassmann variables $d_{a\sigma}$, $\psi_{jk\sigma}$ and their conjugates in Nambu spinors d_a and ψ_{jk} are defined in the same way as (2.3.1) and (2.3.3). The partition function is given by a functional integration over paths that are β (β^{-1} is the temperature) antiperiodic [100]

$$Z = \int\limits_{\substack{d_a(\beta)=-d_a(0)\\ \psi_{jk}(\beta)=-\psi_{jk}(0)}} \mathcal{D}\left[\overline{d}, d, \overline{\psi}, \psi\right] \exp\left[-S_E\left(\overline{d}, d, \overline{\psi}, \psi\right)\right] \;. \tag{2.3.9}$$

The Euclidean action S_E reads

$$S_E\left(\overline{d},d,\overline{\psi},\psi\right)=\int_0^\beta \mathrm{d}\tau\left\{\mathcal{H}\left(\overline{d},d,\overline{\psi},\psi\right)+\sum_a \overline{d}_a\partial_\tau d_a+\sum_{jk}\overline{\psi}_{jk}\,\partial_\tau\psi_{jk}\right\} \tag{2.3.10}$$

and the matrix elements of the Hamiltonian can be written as

$$\mathcal{H}\left(\overline{d},d,\overline{\psi},\psi\right)=\sum_a H_a\left(\overline{d}_a,d_a\right)+\sum_{jk}H_{jk}\left(\overline{\psi}_{jk},\psi_{jk}\right)+\sum_{jka}H_{t,jka}\left(\overline{d}_a,d_a,\overline{\psi}_{jk},\psi_{jk}\right)\ . \tag{2.3.11}$$

The expressions of H_{jk} and $H_{t,jka}$ are readily obtained from (2.3.2) and (2.3.5) respectively by substituting the annihilation operators $\hat{a}$ by their eigenvalues a and the corresponding creation operators $a^\dagger$ by the conjugate Grassmann variables $\overline{a}$. For the QDs, we can also find an expression in terms of Nambu spinors as follows

$$H_a\left(\overline{d}_a,d_a\right)=\tilde{\varepsilon}_a+\tilde{\varepsilon}_a\,\overline{d}_a\,\sigma_z\,d_a-\frac{U_a}{2}\left(\overline{d}_a d_a\right)^2\quad\text{with}\quad\tilde{\varepsilon}_a=\varepsilon_a+\frac{U_a}{2}\ . \tag{2.3.12}$$

2.4 Free energy and Josephson current

As the lead degrees of freedom are quadratic in the Hamiltonian, they can be easily integrated out [100] and after this partial trace, the partition function is expressed as a functional integral only over the QD Grassmann variables:

$$Z=c_1\int\limits_{d_a(\beta)=-d_a(0)}\prod_a\mathcal{D}\left[\overline{d}_a,d_a\right]\exp\left[-S_{\text{eff}}\left(\overline{d},d\right)\right] \tag{2.4.1}$$

where c_1 is a quantity independent of ϕ and α. The effective action

$$S_{\text{eff}}\left(\overline{d},d\right)=\sum_a\int_0^\beta \mathrm{d}\tau\left\{\tilde{\varepsilon}_a+\overline{d}_a(\tau)\left[\partial_\tau+\tilde{\varepsilon}_a\,\sigma_z\right]d_a(\tau)-\frac{U_a}{2}\Big(\overline{d}_a(\tau)\,d_a(\tau)\Big)^2\right\}-\sum_{a,b}\int_0^\beta \mathrm{d}\tau\int_0^\beta \mathrm{d}\tau'\ \overline{d}_a(\tau)\,\Sigma^{ab}(\tau-\tau')\,d_b(\tau') \tag{2.4.2}$$

contains a non trivial term called self-energy (originated from the tunnel Hamiltonian (2.3.5) which couples QD and lead degrees of freedom)

$$\Sigma^{ab}(\tau)=\sum_{jk}\mathrm{e}^{i\mathbf{k}.(\mathbf{r_{jb}}-\mathbf{r_{ja}})}\mathcal{T}_{ja}^\dagger G_k(\tau)\mathcal{T}_{jb}\ . \tag{2.4.3}$$

It involves the Green function of the leads $G_k(\tau)$ solution of

$$\left\{\partial_\tau+\left(\frac{k^2}{2m}-\mu\right)\sigma_z+\Delta\sigma_x\right\}G_k(\tau)=\delta(\tau)\ . \tag{2.4.4}$$

Rather than keeping track of a cumbersome device-specific position dependence of the self-energy, we choose to introduce a phenomenological parameter η. It extrapolates between two relevant cases for which the calculations can be performed in a non-device-specific way ($[\delta r]_j \equiv |\mathbf{r_{jU}} - \mathbf{r_{jD}}|$ is the distance between injection points in lead j and ξ is the superconducting coherence length):

- $\eta = 0$ for infinitely distant injection points ($[\delta r]_j \gg \xi$),
- $\eta = 1$ for coinciding injection points ($[\delta r]_j \ll \xi$).

The quartic terms $(\overline{d}_a d_a)^2$ in (2.4.2) prohibit an exact computation of the partition function. We use a Hubbard-Stratonovich transformation to treat these terms and we neglect the temporal fluctuations of the auxiliary fields X_a which are introduced [44]

$$\mathrm{e}^{\frac{U_a}{2}\int_0^\beta \mathrm{d}\tau \left(\overline{d}_a d_a\right)^2} \approx \sqrt{\frac{\beta}{2\pi U_a}} \int_{-\infty}^{+\infty} \mathrm{d}X_a \, \mathrm{e}^{-\frac{\beta}{2U_a}X_a^2 + X_a \int_0^\beta \mathrm{d}\tau \, \overline{d}_a d_a} \; . \tag{2.4.5}$$

Because both the Green functions G_k and the Nambu spinor components $d_{a\sigma}$ are β antiperiodic, we use Matsubara series expansions

$$\begin{cases} G_k(\tau) = \displaystyle\sum_{p\in\mathbb{Z}} \mathrm{e}^{-i\omega_p \tau} G_k(\omega_p) \\ d_{a\sigma}(\tau) = \displaystyle\sum_{p\in\mathbb{Z}} \mathrm{e}^{-i\omega_p \tau} d_{a\sigma}(\omega_p) \end{cases} \quad \text{with} \quad \omega_p = \left(p + \frac{1}{2}\right)\frac{2\pi}{\beta} \; . \tag{2.4.6}$$

The QD degrees of freedom are now integrated out and the partition function becomes

$$Z^\eta(\phi, \alpha) = c_1 c_2 \int_{-\infty}^{+\infty} \mathrm{d}X_U \int_{-\infty}^{+\infty} \mathrm{d}X_D \exp\left[-S_{\mathrm{eff}}^{\mathrm{HS},\eta}\left(X_U, X_D, \phi, \alpha\right)\right] \; . \tag{2.4.7}$$

c_2 is also a quantity independent of ϕ and α. The effective action

$$S_{\mathrm{eff}}^{\mathrm{HS},\eta}\left(X_U, X_D, \phi, \alpha\right) = \sum_a \left(\beta\, \tilde{\varepsilon}_a + \frac{\beta}{2U_a} X_a^2\right) - 2\sum_{p\in\mathbb{N}} \ln\Big(\beta^4 \Big| \det\left[\mathcal{M}_p^\eta\left(X_U, X_D, \phi, \alpha\right)\right] \Big|\Big) \tag{2.4.8}$$

contains a Matsubara series expansion which terms involve determinants of (4x4) matrices written in QD space (each entry is a 2x2 matrix in Nambu space) as

$$\mathcal{M}_p^\eta\left(X_U, X_D, \phi, \alpha\right) = \begin{bmatrix} -\left(i\omega_p + X_U\right) + \tilde{\varepsilon}_U\, \sigma_z - \mathcal{A}_p(\phi - \alpha) & -\mathcal{B}_p^\eta(\phi, +\alpha) \\ -\mathcal{B}_p^\eta(\phi, -\alpha) & -\left(i\omega_p + X_D\right) + \tilde{\varepsilon}_D\, \sigma_z - \mathcal{A}_p(\phi + \alpha) \end{bmatrix} . \tag{2.4.9}$$

The Nambu matrices $\mathcal{A}_p$ and $\mathcal{B}_p^\eta$ originate from the self-energy term (2.4.3). We define the decay rate (of the two QDs)

$$\Gamma = \pi\, \nu(0)(t_L^2 + t_R^2) \tag{2.4.10}$$

where $\nu(0)$ is the density of states of the leads at the Fermi level as well as the contact asymmetry

$$\gamma = \frac{t_L^2 - t_R^2}{t_L^2 + t_R^2} \ . \tag{2.4.11}$$

The matrix involved in block diagonal terms reads

$$\mathcal{A}_p(\phi) = \frac{\Gamma}{\sqrt{\Delta^2 + \omega_p^2}} \left[i\omega_p - \Delta \left(\cos\frac{\phi}{2}\,\sigma_x + \gamma \sin\frac{\phi}{2}\,\sigma_y \right) \right] \tag{2.4.12}$$

while the block off-diagonal terms read

$$\mathcal{B}_p^{\eta}(\phi,\alpha) = \eta\,\frac{\Gamma}{\sqrt{\Delta^2 + \omega_p^2}} \left[i\omega_p \left(\cos\frac{\alpha}{2} + i\gamma \sin\frac{\alpha}{2}\,\sigma_z \right) - \Delta \left(\cos\frac{\phi}{2}\,\sigma_x + \gamma \sin\frac{\phi}{2}\,\sigma_y \right) \right] . \tag{2.4.13}$$

The CAR process is due to these last terms. We have done separately the calculations for inifinitely distant injection points (for which they vanish) and for coinciding injection points (for which they are given by $\mathcal{B}_p^{\eta=1}$) and then introduce the multiplicative phenomenological parameter η to extrapolate between the first case $\eta = 0$ and the second one $\eta = 1$ in a non-device-specific way. In practice, there is an explicit dependence on the separation between injection points δr. An exponential decay on the scale of the superconducting coherence length is expected requiring contacts within a smaller distance. Fast oscillations on the Fermi wavelength scale and power low decay originate from the microscopic tunneling Hamiltonian formulation used here: $\eta(\delta r) = (\sin k_F \delta r)/(k_F \delta r)$ for 3D clean superconductors [18, 102] (consistent with our limits $\eta = 0$ for $\delta r \to 0$ and $\eta = 1$ for $\delta r \to \infty$) and no power law decay for quasi-one-dimensional clean superconductors [103]. To justify abnormally strong nonlocal signal compared to the prediction of a dirty 3D superconductor contacted with nanowire QDs to two metallic leads, geometry-specific arguments were proposed [86]. The issue is indeed quite complex and a lot of device-specific effects must be taken into account, e.g. proximity effect from the bulk superconductors on the nanowires used in three-terminal CP splitters [86–90]. Note that the spatial dependence of CAR process was also studied in [65, 69] (as a diagnosis of CAR manifestation): the oscillations were not observed due to finite size contacting regions [66] but exponential decay together with eventual power law decay were proved to be consistent with the device geometry. In the present work, we use $\eta \in [0, 1]$ as a phenomenological parameter (with two meaningful limits) used to turn nonlocal effects on in a non-device-specific way. We also avoid the pathologic limit $\delta r \to 0^+$ of the cotunneling process that occurs at finite $0 < \delta r < \infty$ [102].

To evaluate the partition function (2.4.7), we use a saddle-point method [44]. The effective action (2.4.8) is computed numerically by summing over Matsubara frequencies (up to a cut-off

much larger than the superconducting gap). Its minimum, located in $[X_U^*(\phi,\alpha), X_D^*(\phi,\alpha)]$, is obtained with a gradient descent method for fixed ϕ and α. The less symmetric this function is the more starting points are required. The free energy is then defined from this minimum value as

$$F^\eta(\phi,\alpha) = \beta^{-1} S_{\text{eff}}^{\text{HS},\eta}\left[X_U^*(\phi,\alpha), X_D^*(\phi,\alpha), \phi, \alpha\right] \ . \tag{2.4.14}$$

The current is finally obtained by differentiating the free energy with respect to the phase difference ϕ

$$J^\eta(\phi,\alpha) = 2\,\partial_\phi F^\eta(\phi,\alpha) \ . \tag{2.4.15}$$

The critical current, function of the AB flux α, is defined as

$$J_c^\eta(\alpha) = \max_\phi \left|J^\eta(\phi,\alpha)\right| \ . \tag{2.4.16}$$

It is quite easy to show that, as expected, the critical current is π periodic in the case $\eta = 0$, contrary to the case $\eta = 1$ where off-diagonal terms in (2.4.9) are responsible for 2π periodicity [19]. This is a signature for the emergence of CAR process. Our proposition (2.2.6) to evaluate the efficiency of CP splitting requires the calculation of the critical current in these two cases. By adjusting the parameters of the QDs, different possible phase associations are achievable and the present work is a proposition to predict which one is the more favorable for CP splitting observation.

2.5 Numerical results

The results were obtained for symmetric couplings $\gamma = 0$, at low temperature $\beta^{-1} \ll \Delta$. Two regimes of transparency are investigated (tunneling regime with $\Gamma \ll \Delta$ and high transparency regime with $\Gamma \sim \Delta$) and QD energy levels are chosen to place them in definite phases according to

	Γ/Δ	$\varepsilon[\pi]/\Delta$	$\varepsilon[0^{(0)}]/\Delta$	$\varepsilon[0^{(2)}]/\Delta$
tunneling	0.01	-0.3	0.3	-0.9
high transparency	2	-4	4	-12

Table 2.1

The critical current curves for the different QD phase associations, in the two transparency regimes and for several values of the Coulomb on-site repulsion strength U, chosen to be the same

for the two QDs (and varied within a specific range such as staying in the considered phases), are given in Figs. 2.12 and 2.13. The associated splitting efficiencies calculated with (2.2.6) are displayed in Fig. 2.14. The particle-hole symmetry ensures that the current is invariant under the change $(\tilde{\varepsilon}_U, \tilde{\varepsilon}_D) \to (-\tilde{\varepsilon}_U, -\tilde{\varepsilon}_D)$ responsible for some redundancy in the results [19].

Let us first mention, considering the left panels of Figs 2.12 and 2.13, *i.e* the case of independent Josephson junction $\eta = 0$, that a $\pi/2$ phase shift occurs as soon as the parity of one of the QDs is changed. Indeed, the maximum of these π periodic curves is located in $\alpha = 0$ when the QDs have the same parity ($0 - 0$ or $\pi - \pi$) while it is displaced in $\alpha = \pi/2$ when the QDs have different parity ($0 - \pi$). It can be easily explained in the tunneling regime [19] considering lowest order perturbative expectations. Let us emphasize that it is still noticeable in the high transparency regime we have considered, in agreement with the experimental observation [58].

Comparing the left panels of Figs 2.12 and 2.13 to the right ones, *i.e.* the case $\eta = 0$ to $\eta = 1$, we immediately obtain evidence of the cross-talk between the two single Josephson junctions: as expected, the period of the critical current doubles as a result of the emergence of the CAR process. Some of the phase associations are very sensitive to the switching from $\eta = 0$ to $\eta = 1$. A phenomenological approach consisting in progressively turning on the parameter η can be found in [19].

In the tunneling regime we can fit the critical current curves with the theoretical expectation (2.2.2). For identical parameters for the two QDs, we must add the constraint $I_1 = I_2 \equiv I/2$ to the fit procedure, so that the critical current reads

$$\frac{J_c(\alpha)}{|I|} = \left| \frac{I_{\mathrm{CAR}}}{I} + \cos\alpha \right| \ . \tag{2.5.1}$$

From the top right panel of Fig. 2.13, *i.e* considering the $\pi - \pi$ association for $\eta = 1$, it is then clear that a decay rate $\Gamma \sim \Delta$ leads to transport properties beyond tunneling expectations.

The sensitivity to the switching from $\eta = 0$ to $\eta = 1$ somehow manifests itself in the splitting efficiency value. The symmetric associations of 0 phases (middle and bottom panels of Figs. 2.12a and 2.13a) are quite sensitive: the maximum at $\alpha = \pi$ for $\eta = 0$ becomes a zero for $\eta = 1$. It is expected in the tunneling regime with high Coulomb on-site repulsion. Indeed, the splitting of a CP is expected to be twice more likely than the cotunneling of the two constituent electrons through a single QD so that the critical current is simply given by $J_c(\alpha) \propto |\cos\alpha/2|$. Remark that this expectation leads to a theoretical splitting efficiency $r = 2/3$ which is effectively obtained in the tunneling regime (cf Fig. 2.14a). In the high transparency regime, the splitting efficiency is lowered but still significant (cf Fig. 2.14b). The $\pi - \pi$ association (top panels of Figs. 2.12a

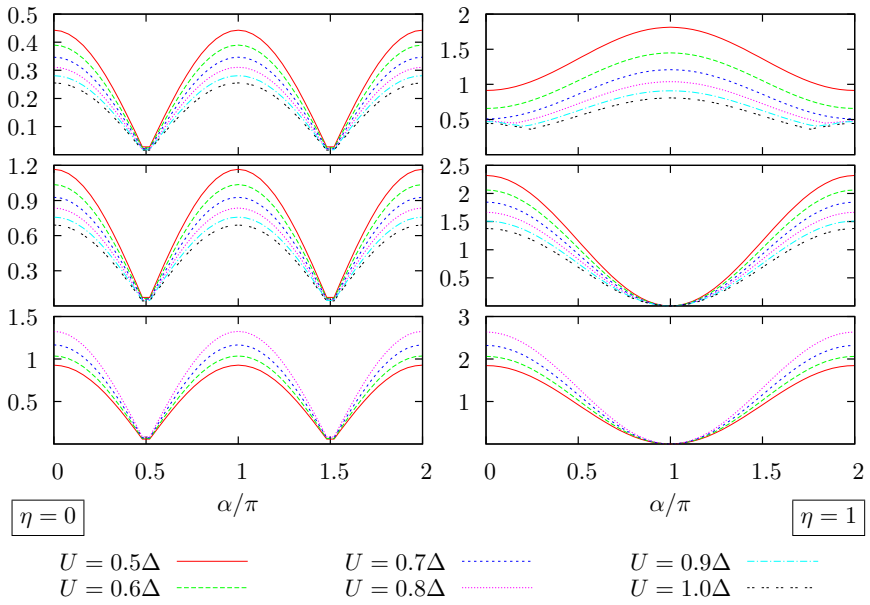

(a) symmetric associations of QDs: $\pi{-}\pi$ (top panel), $0^{(0)}{-}0^{(0)}$ (middle panel), $0^{(2)}{-}0^{(2)}$ (bottom panel).

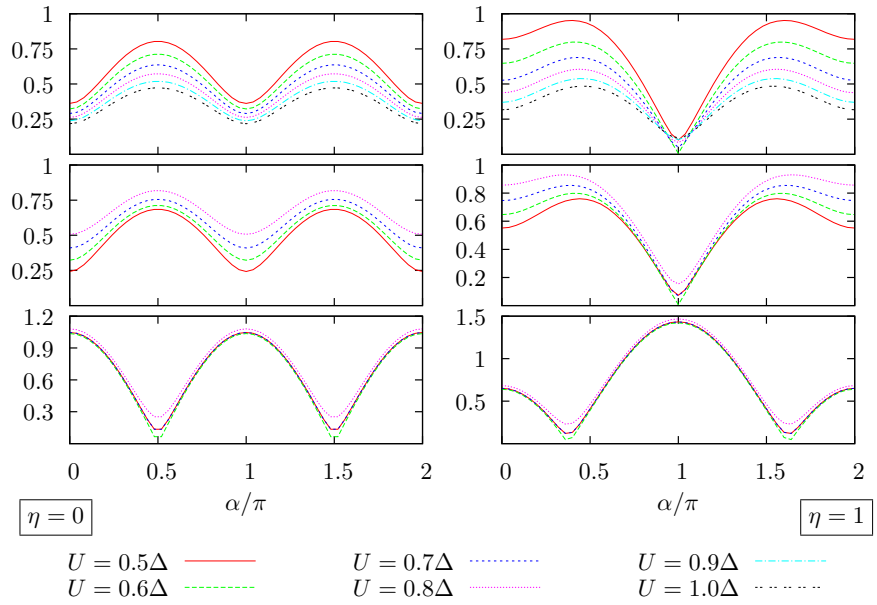

(b) asymmetric associations of QDs: $0^{(0)} - \pi$ (top panel), $0^{(2)} - \pi$ (middle panel), $0^{(0)} - 0^{(2)}$ (bottom panel).

Figure 2.12: Critical current (in units of $10^4 e\Delta/\hbar$) curves in the tunneling regime (parameters given in Table 2.1).

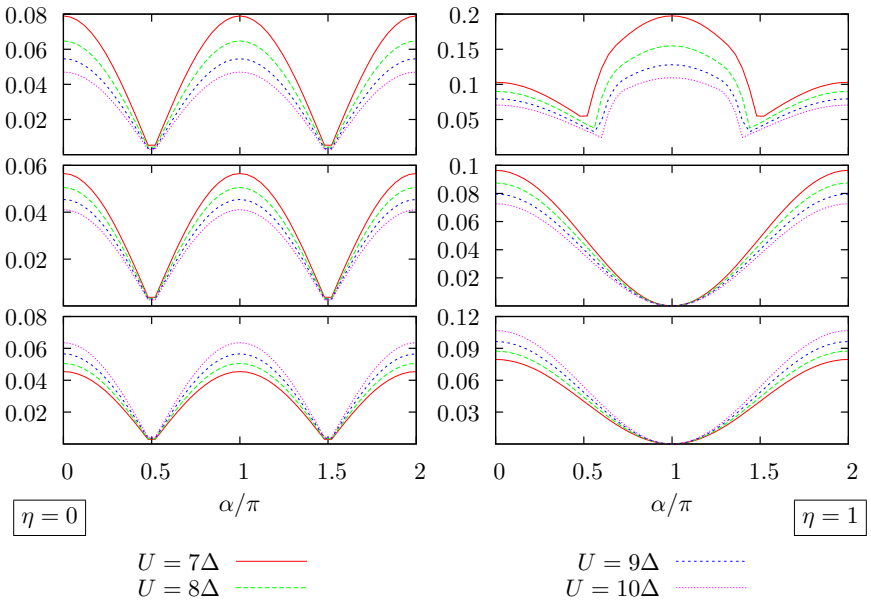

(a) symmetric associations of QDs: $\pi-\pi$ (top panel), $0^{(0)}-0^{(0)}$ (middle panel), $0^{(2)}-0^{(2)}$ (bottom panel).

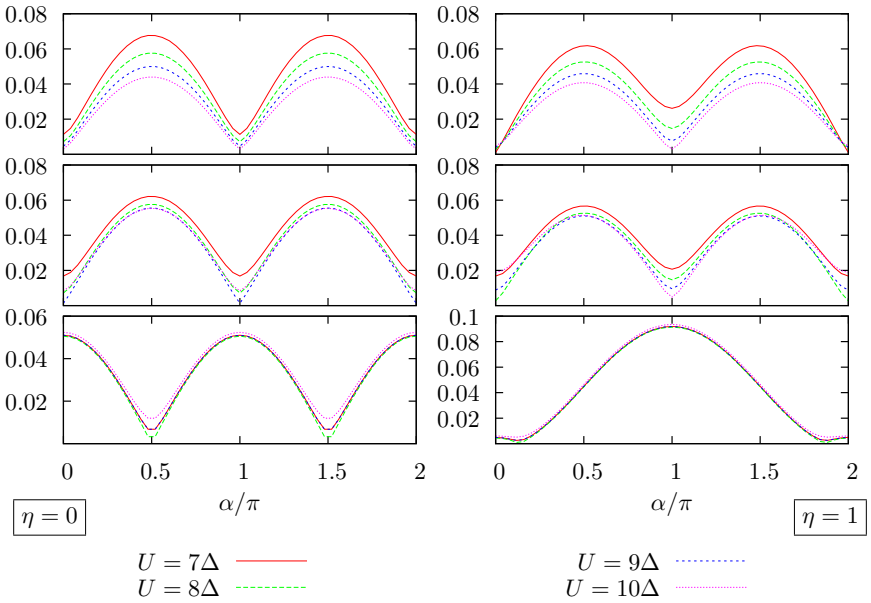

(b) asymmetric associations of QDs: $0^{(0)} - \pi$ (top panel), $0^{(2)} - \pi$ (middle panel), $0^{(0)} - 0^{(2)}$ (bottom panel).

Figure 2.13: Critical current (in units of $e\Delta/\hbar$) curves in the high transparency regime (parameters given in Table 2.1).

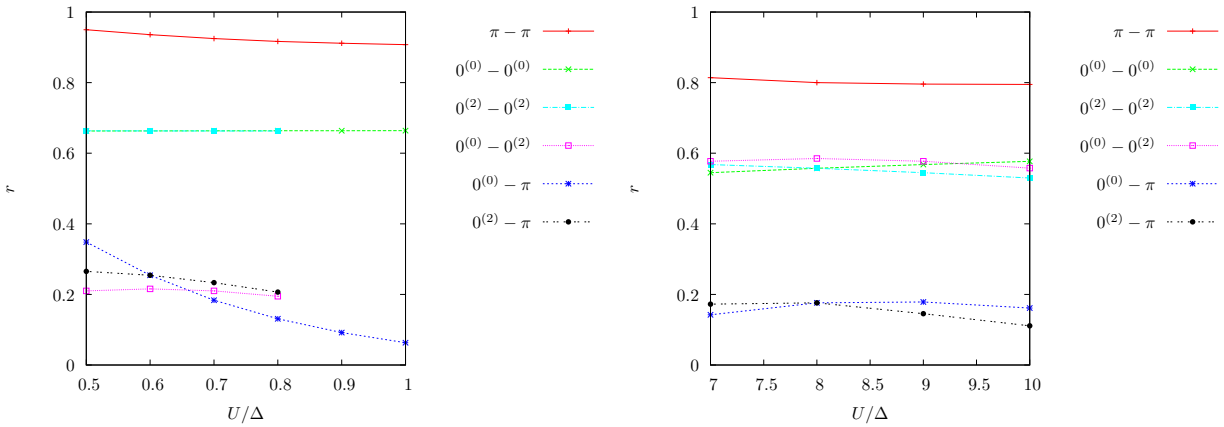

(a) Tunneling regime.

(b) High transparency regime.

Figure 2.14: Splitting efficiency r given by (2.2.6) (parameters given in Table 2.1).

and 2.13a) is also very sensitive to the switching of η and the splitting efficiency is indeed high, in fact the largest value which we have obtained in our comparison of QD phase associations: as expected, ensuring a single mean occupancy on each QD favors the CAR process. Beyond 0.9 in the tunneling regime (cf Fig. 2.14a), it is lowered in the high transparency regime around 0.8 (cf Fig. 2.14b). Concerning the asymmetric associations (Figs. 2.12b and 2.13b), the critical current curves for $\eta = 1$ somehow look like those obtained for $\eta = 0$: the positions of the maxima and minima are mostly preserved for all phase associations, only their local or global character changes when tuning η. However, for the $0^{(0)} - 0^{(2)}$ association in the high transparency regime (bottom panel of Fig. 2.13b), the maximum in $\alpha = 0$ is considerably lowered from $\eta = 0$ to $\eta = 1$ leading to a high value of the splitting efficiency, in fact similar to other associations of 0 phases (cf Fig. 2.14b). The other asymmetric phase associations lead to low splitting efficiency values.

Increasing U results in a more pronounced filtering as the processes where the QDs are doubly occupied are less favored. This explains the observed decrease in critical current for the $0^{(0)} - 0^{(0)}$, $\pi - \pi$ (top and middle panels of Figs. 2.12a and 2.13a) and $0^{(0)} - \pi$ (top panels of Figs. 2.12b and 2.13b) phase associations. The opposite behavior is observed for the $0^{(2)} - 0^{(2)}$ phase association. There, increasing U favors processes where the occupation of the QDs is lowered, since approaching the π transition results in the decrease of the mean occupation number on the QD. The opposite U-dependences while tuning U for $0^{(0)} - 0^{(0)}$ and $0^{(2)} - 0^{(2)}$ phase associations can be seen as a consequence of particle-hole symmetry. The U-dependence in the case of the $0^{(2)} - \pi$ phase association is more subtle [19]. Interestingly, the interaction has no noticeable

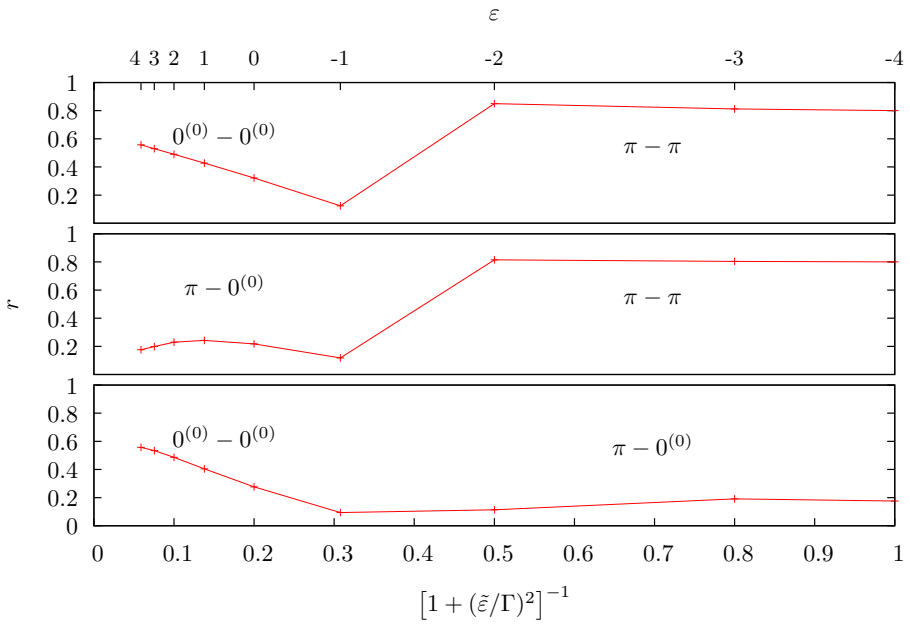

Figure 2.15: Evolution of the splitting efficiency as a function of the effective transparency $D(\varepsilon)$ given by (2.5.2), for fixed $\Gamma = 2\Delta$ and $U = 8\Delta$. *Top:* The energy levels of both QDs are taken to be identical and varied simultaneously ($\varepsilon_U = \varepsilon_D \equiv \varepsilon$). *Middle:* the U QD is taken in the π phase ($\varepsilon_U = -4\Delta$) while the energy of the D QD is varied ($\varepsilon_D \equiv \varepsilon$). *Bottom:* the D QD is taken in the $0^{(0)}$ phase ($\varepsilon_D = 4\Delta$) while the energy of the U QD is varied ($\varepsilon_U \equiv \varepsilon$).

effect in the case of the $0^{(0)} - 0^{(2)}$ phase association. In the studied domain for Coulomb repulsion parameter U, we do not observe noticeable evolutions of the splitting efficiency r except for the $0^{(0)} - \pi$ association in the tunneling regime for which we see a clear decrease (cf Fig. 2.14a). At high transparency, the nanotubes consitute "open QDs" and the quantization of the charge is ineffective due to large fluctuations of their populations: the interation U has little influence on the competition between electronic transport processes as soon as a phase transition for one of the QDs is not crossed (cf Fig. 2.14b).

While the coupling strengths between the superconductors and the nanotube QDs, and the Coulomb charging energies of the latters are in practice fixed by nanofabrication, their energy levels are free parameters which can be easily varied experimentally using electrostatic gates. At fixed decay rate Γ and Coulomb on-site interaction U, changing the energy ε of a QD allows to monitor its mean occupation number (placing it in a given phase) while tuning its effective

transparency defined as

$$D(\varepsilon) = \frac{\Gamma^2}{\Gamma^2 + \left(\varepsilon + \frac{U}{2}\right)^2} \ . \tag{2.5.2}$$

By varying the energy levels of the two QDs, we can optimize the splitting efficiency by reaching the $\pi - \pi$ phase at high effective transparency. Fig. 2.15 displays splitting efficiency crossovers when the energy level, and consequently the effective transparency, of one QD or both QDs is varied.

2.6 Conclusion and perspectives

We have studied a double Josephson junction consisting of two nanowire/nanotube QDs bridging two superconductors as a tool to probe CP splitting. When the two single Josephson junctions which constitute the device are coupled to each other via CAR processes, the doubling of the period of AB oscillations of the critical current measured in a nanoSQUID experiment [18] provides a proof that CP splitting and recombination operates. One of the key results of the work [19] resides in defining the degree of efficiency of CP splitting, the prominence of nonlocal phenomena among all processes contributed to the equilibrium electronic transport in this double Josephson junction. We insist on the fact that CP splitting is uncovered using a current measurement at equilibrium unlike early propositions for CP splitters which involve a superconducting source of electrons, two normal drain leads and QDs in the Coulomb blockade regime as filters [81] and which require the measurement of either nonlocal conductance signal [86] or noise cross-correlations [90]. The measurement of positive noise cross correlations which are undeniable evidences for CP splitting in these three-terminal junctions are difficult to achieve but constitute a preliminary for the measurement of the degree of entanglement of the emitted electrons *via* BIs [80]. The AB diagnosis for CP splitting efficiency in a double Josephson junction may prove more convenient. Nevertheless, recombination is crucial in such a setup so that it cannot be used as a source of entangled electrons nor provide a measurement of the degree of entanglement of the QD electrons.

Some existing double Josephson junction experiments have been presented. In the SQUID experiment [58], the two SWCNT QDs were too spaced out to allow some cross-talk contrary to the CP splitting experiment [59] where the two InAs nanowire QDs were too close to each other to allow the recording of AB oscillations (an alternative CP splitting diagnosis is proposed therein) but we have discussed the practical feasibility of such an experiment taking into account recent progress achieved in nanofabrication techniques.

A theoretical approach going beyond existing studies led in the context of perturbation theory in the tunneling Hamiltonian [18, 60] may prove essential, considering the experimental improvement in contacting nanotube/nanowire QDs to superconductors [58, 59]. The treatment of Coulomb interaction is also crucial since high charging energies can be achieved on the QDs. Coupling strength to the leads, Coulomb on-site repulsion and energy level (which can be monitored thanks to an electrostatic gate) monitors the mean occupation number on the QD, placing it in one of the three phases $0^{(0)}$ (empty QD), π (singly occupied QD), $0^{(2)}$ (doubly occupied QD), which have been numerically investigated in [44]. The path integral approach with a Hubbard-Stratonovich treatment of the Coulomb interaction followed by a saddle point approximation developped in this latter work is adapted to our device and meet the requirements to treat arbitrary transmissions and Coulomb interactions. We thus studied the prominence of nonlocal phenomena depending on the phases of the QDs and found that the $\pi - \pi$ association optimizes the splitting of the CPs that are emitted from one superconductor and recombined on the other one. Yet, our analysis shows that the $0^{(0)} - 0^{(0)}$ and $0^{(2)} - 0^{(2)}$ combinations also provide robust CP splitting signals. Within each of these combinations of phases, we see for the most part that variations of the Coulomb repulsion parameter has little influence on the CP splitting efficiency.

Some restrictions of our treatment together with hints to overcome them are listed below:

- A phenomenological CAR coupling parameter η has been introduced to avoid device-specific dependence on the geometry of the contacting regions in the superconductors. Nevertheless, additional information on the contacts (separation, extent, dimensionality...) could be incorporated in our theoretical model in order to explain experimental data.

- The present project relies on a Hubbard-Stratonovich treatment of the Coulomb interactions on the QDs, involving auxiliary fields, which is exact if the path integral over the latter is performed. Within the mean field approximation used here following [44], we cannot access the Kondo regime occuring for $T_K > \Delta$. For a Josephson junction containing a single QD, with energy ε_0, on-site Coulomb interaction parameter U and decay rate Γ, the Kondo temperature [104] is given by $T_K = \frac{\sqrt{\Gamma U}}{2}\, \mathrm{e}^{\pi\varepsilon_0(\varepsilon_0+U)/(\Gamma U)}$ and evaluated at most at $T_K = 0.13\Delta$ in our numerical study. The Kondo regime in a single Josephson junction has been studied either with a Hubbard-Stratonovich transformation approach followed by a Monte Carlo numerical treatment of the auxiliary field [105] or by an exact numerical renormalization group approach [106]. Extensions of our treatment of the double Josephson junction could be envisioned by following one of the latter approaches. At any rate,

even if $T_K > \Delta$, the Kondo regime could be avoided altogether by working with QD gate voltages such that only the $0^{(0)} - 0^{(0)}$ combination of phases occurs for which a sizable splitting efficiency has been found.

- Direct interdot tunneling and interdot Coulomb interaction are absent of our treatment but they could be incorporated. The issue of interdot tunneling was adressed in the double-dot CP splitter [84, 85]: the positive noise cross correlations, due to CP splitting, are spoiled when interdot coupling becomes large compared to the other couplings. In the nanoSQUID CP splitter, we also expect a decrease of the splitting efficiency with increasing coupling between the QDs, but as long as it is small compared to the other couplings, the results we have presented should remain valid. Nonetheless, this interdot tunneling will be responsible for the formation of two AB subrings in the nanoSQUID setup and we could add our treatment of Coulomb interaction to generalize the existing study [61]. A Coulomb interaction term between the QDs might render the operation of our device in the π-π phase, which is our optimal candidate for large splitting efficiency, less efficient.

Chapter 3

Current and noise characteristics of multiple Cooper pair resonances

In this chapter, we consider a hybrid Quantum Dots (QDs) / superconductors three-terminal device, as illustrated in Fig. 3.1. The system consists of a (grounded) superconducting finger which distributes the constituent electrons of Cooper Pairs (CPs) on either QD, before such electrons are absorbed, by recombination as CPs, in the two (biased) remaining leads. When Crossed Andreev Reflection (CAR) processes are operating on the central superconductor and when the voltages of the lateral leads are commensurate, the partial currents are known to depend on the bare superconducting phases differences, leading to a Josephson-like signature, albeit in off-equilibrium conditions [17, 107] which has been confirmed by experimental signatures [108]. Such a phenomenon is refered as a Multiple Cooper Pair Resonance (MCPR) as the underlying explanation involves the correlated motion of several CPs between the three superconducting reservoirs (Section 3.1). Within the out-of-equilibrium Keldysh formalism we use a path integral technique to produce a Dyson equation for the dressed QD Green's function which accounts for the coupling to superconductors in a nonperturbative way (Section 3.2) and counting fields are introduced in order to compute the current statistics (Section 3.3). Numerical results for Josephson current and noise correlations are given (Section 3.4) and some perspectives are presented (Section 3.5).

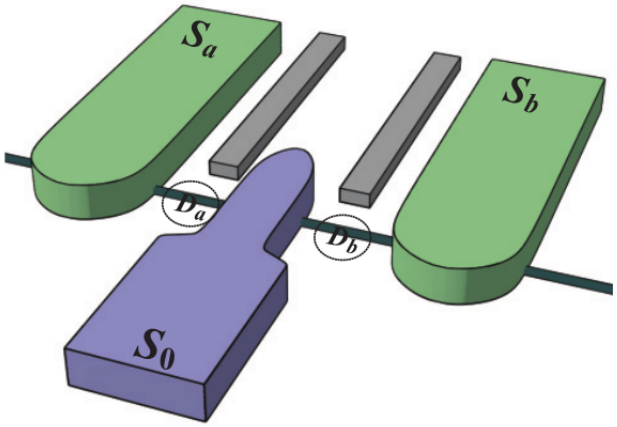

Figure 3.1: Three superconductors designed in a Josephson bijunction. The central electrode S_0 is grounded while the lateral ones S_a and S_b are biased with voltages V_a and V_b. Two quantum dot nanowires D_a and D_b, with energies ε_a and ε_b which can be monitored by gates (in grey), bridge the central superconductor to the two lateral ones. The distance between the two dots is comparable to the coherence length. Adapted from [17].

3.1 Multipair production in superconducting bijunctions

We have already introduced transport phenomena in a Josephson junction (Chapter 1) including

- the DC Josephson supercurrent which depends on the CP phase difference between the two superconducting reservoirs, which is an equilibrium (no voltage is applied) dissipationless phenomenon,
- the AC Josephson effect which depends on the voltage applied across the junction,
- the pair-assisted quasiparticle transport for subgap voltages, which is a phase insensitive nonequilibrium dissipative phenomenon.

We have highlighted the underlying process for such phenomena, namely the Andreev Reflection (AR). The last enumerated phenomenon is often refered as a Multiple Andreev Reflection (MAR) process, which clarifies its microscopic origin. In a superconducting bijunction, two phase differences and two voltages are involved, providing richer physics, as explained in the following.

Early works [109–111] attempting to describe transport in three-terminal all-superconducting junctions have focused on the incoherent regime [112], where quasiparticles experience MAR

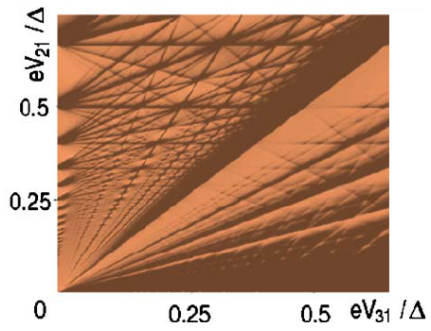

(a) The differential conductance presents SGS features at voltages V_{21}, V_{31} satisfying $pV_{21} + qV_{31} = 0$ or $pV_{21} + qV_{31} = 2\Delta/e$ with p, q integers. Adapted from [110].

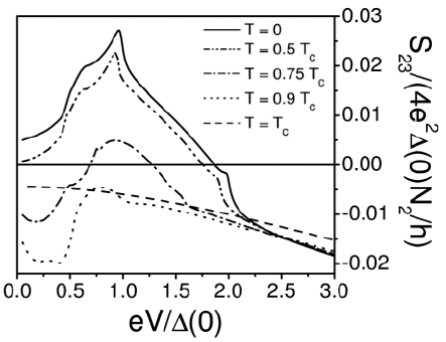

(b) Noise cross correlations negative in the normal state ($T = T_c$) are driven positive in the superconducting state ($T < T_c$). Adapted from [109].

Figure 3.2: MAR manifestations in a device which consists of a metallic island connected to three superconducting electrodes in the incoherent regime.

processes which do not interfere. The Subharmonic Gap Structure (SGS) becomes richer due to mechanisms which couple altogether the three superconductors as emphasized in Ref. [110]. In the latter work, the nonlocal currents inside a device consisted of three superconducting leads contacted to a metallic island are computed in presence of two voltages V_{21}, V_{31}. Interestingly, they predict SGS features for commensurate voltages $pV_{21} + qV_{31} = 0$ with p, q integers, as illustrated in Fig. 3.2a. Let us also mention the previous work of Ref. [109] which studies a similar device but in a presence of a single voltage. As discussed in Chapter 2, the correlations between currents flowing in two different leads (noise cross correlations) of a multiterminal mesoscopic hybrid device can be measured in order to probe eventual entanglement. While negative correlations are expected in a Y-shaped normal conductor, recall that positive noise cross correlations have been proposed as a signature for the production of split Cooper pairs in N-S-N junctions. In the three-terminal all-superconducting junction studied in Ref. [109], the noise cross correlations between the two grounded superconducting leads are investigated and interestingly, it is established that the MAR processes could possibly drive these correlations to be positive, as illustrated in Fig. 3.2b. However, only negative cross correlations were reported in a S-N-S-N-S junction [113].

In the coherent regime however, correlated motion of CPs originated from the three superconductors can be envisioned [114] and interestingly, looking to subgap transport, some

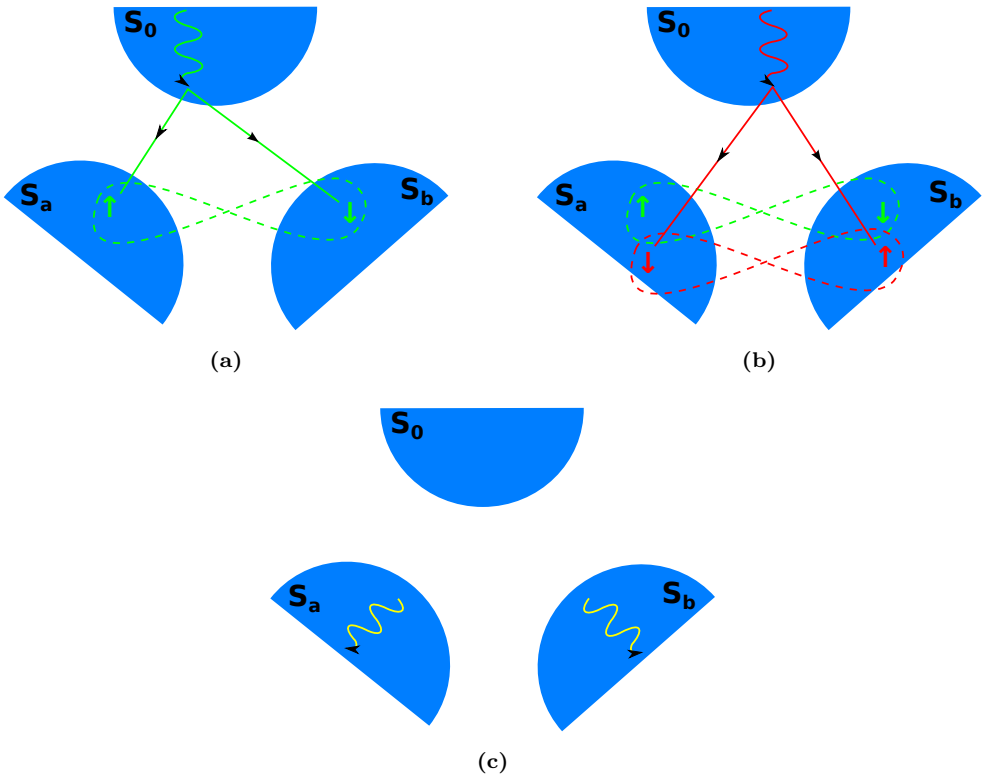

Figure 3.3: Quartet production as double CP splitting (followed by recombinations). Through CAR a first CP is split with spin up on the left and spin down on the right (a) and a second CP is split with spin down on the left and spin up on the right (b). Then, recombination is possible in each lead and two CPs exit (c).

nonequilibrium dissipationless current associated with MCPR together with some phase sensitive dissipative transport (phase-sensitive MAR) are expected [17]. The lowest order MCPR results in the entanglement of two CPs, a process refered as quartet and first envisioned (at least in these terms) in the equilibrium calculations of Ref. [107]. In an other formulation, these resonances were earlier predicted as voltage-induced (fractional) Shapiro steps [115]. The usual Shapiro steps [116] in an irradiated Josephson junction are due to the synchronization between the AC Josephson frequency and one of the harmonics of the radiation [9], which is responsible for a DC current. Here, due to the presence of two voltages, there are two Josephson frequencies, and one of them can be thought of as a "radiation source" for the other. The synchronization requires commensurate voltages which is the condition for MCPR as explained further.

We have already described a three-terminal device with a superconducting (S) source connected to two normal (N) leads, refered as the N-S-N CP splitter (cf. Chapter 2). ARs at N-S interfaces are responsible for new conduction channels including the CAR which is the underlying process for CP splitting. Now imagine the two normal leads are replaced by superconducting materials where the transport properties are given by CP and quasiparticle (with gapped energy) tunnelings. CAR processes are still operating but for subgap voltages single-particle conduction inside the outgoing leads is prohibited. Nevertheless, imagine the process is duplicated then two electrons exit in each lead and possibly can recombine as CPs: this is the quartet process. Remark that this correlated nonlocal four fermion state requires that the two split CPs exchange their constituent electrons. This sequential picture is illustrated in Fig 3.3. Actually, an even number of CAR processes is the key requirement for recombination of electrons, originating from the splitting of CPs of the central electrode, as CPs in the two lateral superconductors, so that higher order processes can be imagined. Note that these CP-splitting-based processes are not the only supercurrent channels: CPs can cross one of the two junctions as a whole through a (double) Direct Andreev Reflection (DAR) or CPs can be transfered through the central superconductor *via* a (double) electron cotunneling (EC) process. Note also that CP splitting is efficient provided a separation between lateral reservoirs smaller that the coherence length of the superconducting material.

A simple argument which yields the MCPR condition for voltages has been proposed in Ref. [17]. If one assumes that the superconductors S_0, S_a and S_b have respective (time dependent) phases $\phi_0(t) = 0$, $\phi_a(t) = \phi_a + \frac{2e}{\hbar} V_a t$, and $\phi_b(t) = \phi_b + \frac{2e}{\hbar} V_b t$ (V_a and V_b are the bias voltages on superconductors a and b), the phenomenological approach of Josephson type effects suggests that the current in lead $j = a, b$ has the form:

$$I_j(t) = \sum_{n,m\in\mathbb{Z}} I_{j,nm} \sin\left[n\phi_a(t) + m\phi_b(t)\right] \ . \tag{3.1.1}$$

- $m = 1,\ n = 0$ and $m = 0,\ n = 1$ correspond to the usual Josephson effects between S_0 and $S_a,\ S_b$.
- $m > 1,\ n = 0$ and $m = 0,\ n > 1$ describe higher harmonics of the Josephson current.
- $nV_a + mV_b = 0$ is the condition for MCPR.

Under the MCPR condition $nV_a + mV_b = 0$, the phase of the sine in Eq. (3.1.1) ceases to have a time dependence, and the currents I_a and I_b have a pure DC component which depends on the combination of the bare phases $n\phi_a + m\phi_b$. The lowest order MCPR is the quartet which

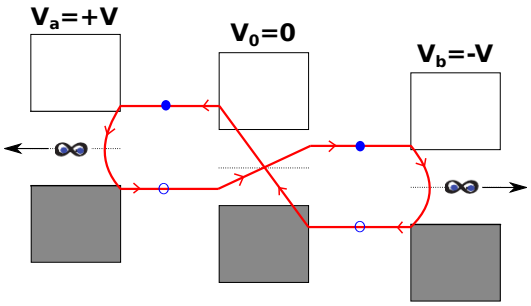

(a) Quartet process $V_a = -V_b$.

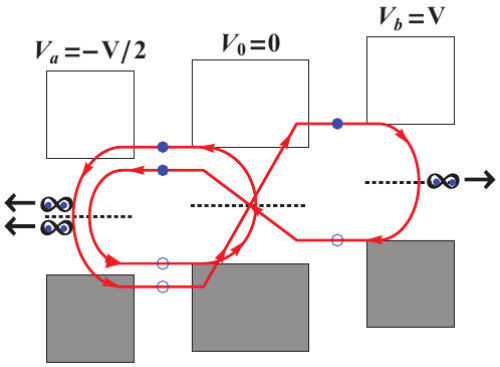

(b) Sextet process $V_a = -V_b/2$. Adapted from [17].

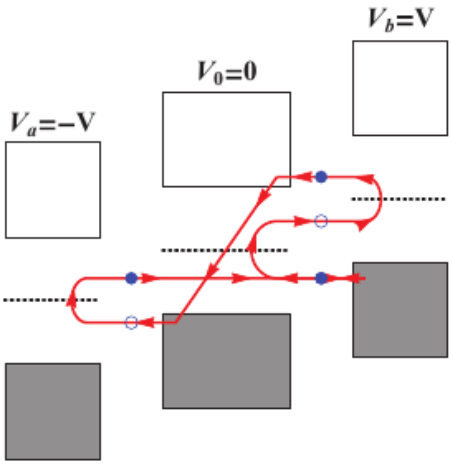

(c) Lowest order phase-sensitive MAR process in the quartet configuration $V_a = -V_b$ with threshold $2\Delta/3$. Adapted from [17].

Figure 3.4: Energy diagrams of the two lowest order MCPR (quartet et sextet) and of the lowest order phase-sensitive MAR process in the quartet configuration.

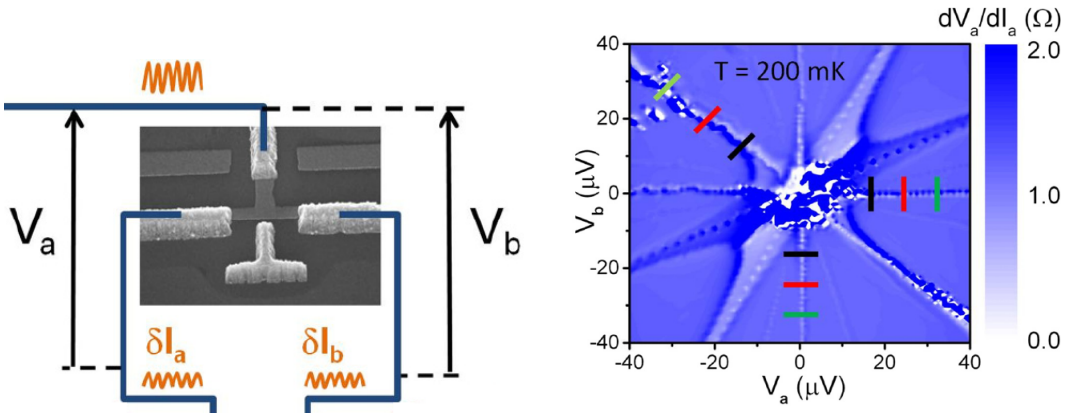

(a) SEM image of the device: a T-shape copper conductor is connected to three aluminium electrodes.

(b) Differential resistance displaying anomalies along lines $V_a + V_b = 0$, $V_b - 2V_a = 0$ and $V_a - 2V_b = 0$ ascribed to quartet productions from each superconductor.

Figure 3.5: An experimental claim for quartet signatures. Adapted from [108].

corresponds to $n = m = 1$ and a similar argument had been earlier proposed in this special case [107]. An energy diagram for this current is given in Fig. 3.4a. Remark that it realizes an energy-conserving channel. More generally, a couple (n, m) which satisfies the MCPR condition $nV_a + mV_b = 0$ corresponds to the transfer of $n + m$ CPs from S_0 as n outgoing CPs in S_a and m outgoing CPs in S_b. A second-order process (sextet) is given in Fig. 3.4b.

Anomalies in the electronic subgap transport of an all-superconducting bijunction [108] could meet an interpretation in terms of quartet resonances. The differential resistance measured as a function of both voltages V_a and V_b is displayed in Fig. 3.5. The anomalies along the axes are ascribed to usual (single junction) Josephson effects between S_0 and one of the lateral electrodes S_a or S_b. More interestingly, the anomaly which is noticeable along the diagonal line $V_a + V_b = 0$ can be attributed to quartets originating from S_0. Note that this resonance for the emission of quartets from S_0 (which is grounded $V_0 = 0$) reads $(V_a - V_0) + (V_b - V_0) = 0$. Similar processes occur for $(V_b - V_a) + (V_0 - V_a) = 0$ (emission of quartets from S_a) and for $(V_a - V_b) + (V_0 - V_b) = 0$ (emission of quartets from S_b) which explain the anomalies along the lines $V_b - 2V_a = 0$ and $V_a - 2V_b = 0$ respectively.

Still in Ref. [17], the phenomenological description presented above is confirmed by a microscopic calculation (which is reported in the next sections) performed on a system consisting of two QDs placed in between the three superconductors S_a, S_0, S_b (cf Fig. 3.1). Most of the

numerical investigations presented in this work concern the quartet configuration $V_a + V_b = 0$. It was shown that at low voltages the current phase relation $I_a(\phi_b)$ is that of a π junction and it deviates from that form when the voltage is increased. For sufficiently low voltages, the currents in the two leads coincide $I_a(\phi_b) \simeq I_b(\phi_b)$, and then, increasing the voltage, the two currents deviate strongly from each other as the novel phase-sensitive MAR processes (which involve continuum states and which depend on the bare phases of the superconductors) enter the game. The energy diagram of the lowest order of these processes is given in Fig. 3.4c.

The study of out-of-equilibrium noise in such devices is particularly interesting. Indeed, if the subgap low bias behavior of electronic transport between these superconductors involves uniquely the exchange of CPs rather than dissipative processes (such as MAR or quasiparticle tunneling) which involve the continuum spectrum of the superconductors, it bears strong similarities with Josephson physics, which in the limit of zero temperature and zero frequency yields vanishing current noise. Furthermore, there is also a need to quantify noise crossed correlations between different terminals, as a function of voltage bias, as these could have a positive or negative sign depending on which process, CAR or EC, operates on the central superconductor. In a setup where a single lead is biased, low voltage positive noise crossed correlations in the coherent regime were predicted and ascribed to MARs [117]. In a setup (closer to what we are interested in) consisted of a single quantum dot connected to three terminals noise crossed correlations were also investigated [118] and our results agree with the main message of this work, namely that quartets are noiseless for a non-resonant dot contrary to the resonant case where a phase-sensitive noise is predicted. These issues need to be tackled in view of potential experiments which could follow the early realizations of Cooper pair splitters (cf. Chapter 2).

3.2 Model

We introduce the Hamiltonian of an all superconducting three-terminal junction with two QDs that bridge a central electrode to two lateral ones (Section 3.2.1). Then we define the bare Green's function of the QDs as well as the Green's function dressed by the coupling with the leads (Section 3.2.2) and derive the expression for the tunneling self-energy of the QDs (Section 3.2.3). Finally, using a double Fourier representation under the MCPR condition, we give the Dyson equation in a matrix form (Section 3.2.4). In the following $\hbar = k_B = e = 1$.

3.2.1 Hamiltonian formulation

We consider a central superconducting electrode S_0 coupled to two lateral superconducting leads S_a and S_b *via* two QDs D_a and D_b as illustrated in Fig. 3.1. All superconductors labelled $j = 0, a, b$ are described by BCS theory with a gap energy Δ_j. Each QD labelled $\alpha = a, b$ characterized by an energy level ε_α is coupled to the central lead and to (only) one lateral superconductor: the tunneling amplitude between lead j and QD α is denoted as $t_{j\alpha}$ and $t_{ab} = t_{ba} = 0$. An interdot coupling t_d is also considered.

The two lateral leads are biased with a voltage V_j measured with respect to the chemical potential of the central superconducting electrode which is grounded $V_0 = 0$. The width of S_0 is assumed to be smaller than the superconducting coherence length, so that CAR and EC processes can operate: CAR is responsible for CP splitting from S_0 which distributes electrons on both QDs, EC can transfer an electron from one QD to another through S_0.

The Hamiltonian of the total system is the sum of the Hamiltonian of superconducting leads, of the Hamiltonian of the double QD (including interdot tunneling) and of the tunneling Hamiltonian between leads and QDs:

$$H = \sum_j H_j + H_D + H_T(t) \ . \tag{3.2.1}$$

- $\psi^\dagger_{jk\sigma}$ is the creation operator for an electron with momentum k and spin $\sigma = \uparrow, \downarrow$ in lead j. It is useful to introduce Nambu spinors

  $$\Psi_{jk} = \begin{pmatrix} \psi_{jk,\uparrow} \\ \psi^\dagger_{j(-k),\downarrow} \end{pmatrix} \tag{3.2.2}$$

  in order to conveniently write the BCS Hamiltonian of the lead j as

  $$H_j = \sum_k \Psi^\dagger_{jk} \left\{ \left(\frac{k^2}{2m} - \mu \right) \sigma_z + \Delta_j \sigma_x \right\} \Psi_{jk} \ , \tag{3.2.3}$$

  where the Pauli matrices σ_z and σ_x act in Nambu space.

- If $d^\dagger_{\alpha\sigma}$ is the creation operator for an electron with spin $\sigma = \uparrow, \downarrow$ on QD α, then the Hamiltonian H_{D_α} of the QD α reads

  $$H_{D_\alpha} = \varepsilon_\alpha \sum_\sigma d^\dagger_{\alpha\sigma} d_{\alpha\sigma} \tag{3.2.4}$$

  and the tunneling between the QDs reads

  $$H_{D_a D_b} = t_d \sum_\sigma d^\dagger_{a\sigma} d_{b\sigma} + \text{h.c.} \tag{3.2.5}$$

Introducing Nambu spinors

$$d_\alpha = \begin{pmatrix} d_{\alpha\uparrow} \\ d^\dagger_{\alpha\downarrow} \end{pmatrix} \tag{3.2.6}$$

and collecting them for $\alpha = a, b$ into a Nambu-Dot space spinor as

$$\tilde{d} = \begin{pmatrix} d_a \\ d_b \end{pmatrix} , \tag{3.2.7}$$

the Hamiltonian of the double QD can be conveniently written as

$$H_D = \sum_\alpha H_{D_\alpha} + H_{D_a D_b} = \tilde{d}^\dagger \, h_D \sigma_z \, \tilde{d} \tag{3.2.8}$$

where the Pauli matrix σ_z acts in Nambu space and the matrix

$$h_D = \begin{pmatrix} \varepsilon_a & t_d \\ t_d & \varepsilon_b \end{pmatrix} \tag{3.2.9}$$

acts in dot space.

- The tunneling Hamiltonian between leads and QDs is written in terms of Nambu spinors according to

$$H_T(t) = \sum_{jk\alpha} \Psi^\dagger_{jk} \, \mathcal{T}_{j\alpha}(t) \, d_\alpha + \text{h.c.} \quad \text{with} \quad \mathcal{T}_{j\alpha}(t) = t_{j\alpha} \, \sigma_z \, \mathrm{e}^{i\sigma_z \int V_j \mathrm{d}t} \tag{3.2.10}$$

where the Pauli matrix σ_z acts in Nambu space. As already mentioned, in our system $t_{ab} = t_{ba} = 0$.

3.2.2 Green's functions in the Keldysh formalism

In order to calculate average values of operators in an out-of-equilibrium system, the Keldysh time contour C has been introduced [119]: it goes from $-\infty$ to $+\infty$ (+ forward branch) and goes back to $-\infty$ (− backward branch). The time ordering operator along this contour is denoted as T_C. We introduce the Nambu-Dot-Keldysh spinors collecting Nambu-Dot spinors (3.2.7) evaluated on the two different branches of the Keldysh time contour

$$\check{d} = \begin{pmatrix} \tilde{d}^+ \\ \tilde{d}^- \end{pmatrix} . \tag{3.2.11}$$

The bare Green's functions of the QDs (in the absence of tunneling between QDs and superconducting leads) reads

$$\check{G}_0(t, t') = -i \left\langle T_C \left\{ \check{d}(t) \check{d}^\dagger(t') \right\} \right\rangle_0 . \tag{3.2.12}$$

The quantum mechanical averaging is performed with respect to the Hamiltonian without tunneling

$$\langle \dots \rangle_0 = \frac{\mathrm{Tr}\left\{e^{-\beta H_0} \dots\right\}}{\mathrm{Tr}\left\{e^{-\beta H_0}\right\}} \quad \text{where} \quad H_0 = \sum_j H_j + H_D \ . \tag{3.2.13}$$

QD and superconducting degrees of freedom are coupled with the time-dependent tunneling Hamiltonian $H_T(t)$ and the Green's function dressed by this tunneling reads

$$\check{G}(t,t') = -i \left\langle T_C \left\{ S(\infty)\, \check{d}(t) \check{d}^\dagger(t') \right\} \right\rangle_0 \ , \tag{3.2.14}$$

where $S(\infty)$ is the evolution operator along the Keldysh contour

$$S(\infty) = T_C \exp\left\{ -i \int_C \mathrm{d}t\, H_T(t) \right\} \ . \tag{3.2.15}$$

3.2.3 Self energy of the quantum dots

The evolution operator when averaged over the lead degrees of freedom

$$\langle S(\infty) \rangle_{\text{leads}} = T_C \exp\left[-i \int_{-\infty}^{+\infty} \mathrm{d}t_1 \int_{-\infty}^{+\infty} \mathrm{d}t_2 \ \check{d}^\dagger(t_1) \check{\Sigma}_T(t_1,t_2) \check{d}(t_2) \right] \ , \tag{3.2.16}$$

involves a total self-energy

$$\check{\Sigma}_T = \sum_j \check{\Sigma}_j \tag{3.2.17}$$

which has a structure in Nambu-Dot-Keldysh space. The Dot space matrix element of the lead self energy $\check{\Sigma}_j$ is given by a Nambu-Keldysh matrix according to

$$\left[\check{\Sigma}_j\right]_{\alpha\beta}(t_1,t_2) = \mathcal{T}^\dagger_{j\alpha}(t_1) \tau_z \hat{g}_j(t_1 - t_2) \tau_z \mathcal{T}_{j\beta}(t_2) \tag{3.2.18}$$

where the Pauli matrix τ_z acts in the Keldysh space and where

$$\hat{g}_j(t-t') = -i \sum_k \left\langle T_C \left\{ \hat{\Psi}_{jk}(t) \hat{\Psi}^\dagger_{jk}(t') \right\} \right\rangle \tag{3.2.19}$$

is the Green's function of the superconducting lead j. It involves the Nambu-Keldysh spinors which collect the Nambu spinors (3.2.2) evaluated on the two different branches of the Keldysh time contour

$$\hat{\Psi}_{jk} = \begin{pmatrix} \Psi^+_{jk} \\ \Psi^-_{jk} \end{pmatrix} \ . \tag{3.2.20}$$

It is useful to perform a rotation in Keldysh space (Pauli matrix τ_z and matrix L act in Keldysh space) according to

$$\begin{pmatrix} g^R_j & g^K_j \\ 0 & g^A_j \end{pmatrix} = L \tau_z \hat{g}_j L^{-1} \quad \text{with} \quad L = \frac{1}{\sqrt{2}} \begin{pmatrix} 1 & -1 \\ 1 & 1 \end{pmatrix} \tag{3.2.21}$$

to work with retarded (R), advanced (A) and Keldysh (K) Green functions. These components are given by

$$\begin{cases} g_j^{R,A}(\omega) = \pi\nu(0)\,\dfrac{\omega + \Delta_j\sigma_x}{i\zeta_j^{R,A}(\omega)}\ , \\ g_j^{K}(\omega) = [1-2f(\omega)]\left[g_j^{R}(\omega) - g_j^{A}(\omega)\right]\ , \end{cases} \tag{3.2.22}$$

where $\nu(0)$ is the density of states of the lead in the normal metal regime at the Fermi level, $f(\omega)$ is the Fermi distribution and where

$$\zeta_j^{R,A}(\omega) = \pm\mathrm{sign}(\omega)\sqrt{\omega^2-\Delta_j^2}\,\Theta\left(|\omega|-\Delta_j\right) + i\sqrt{\Delta_j^2-\omega^2}\,\Theta\left(\Delta_j-|\omega|\right)\ . \tag{3.2.23}$$

3.2.4 Double Fourier representation and Dyson equation

When arbitrary voltages V_a and V_b are applied to the lateral superconducting leads while the central superconducting electrode is grounded, two Josephson frequencies $2|V_a|$ and $2|V_b|$ govern the system. In general, they are independent and there is no periodicity, the QD Green's function is a function of two times t_1 and t_2 or alternatively of $\tau = t_1 - t_2$ and $t = (t_1+t_2)/2$. However, under the MCPR condition (comensurate voltages) $nV_a + mV_b = 0$ with n, m integers, a periodicity $T = \pi|m/V_a| = \pi|n/V_b| \equiv 2\pi/V$ in the variable t is recovered. It is then convenient to introduce the double Fourier transformation of the bare and dressed QD Green's functions, $\check{G}_0$ and $\check{G}$ respectively, and of the self energy terms $\check{\Sigma}_j$. Now, when the frequency variable ω is specified, the concerned matrices have an additional frequency structure. For example, the (n,m) frequency elements of $\check{G}(\omega)$ defined *via*

$$\check{G}\left(t_1,t_2\right) = \sum_{n,m\in\mathbb{Z}}\int_0^V \frac{\mathrm{d}\omega}{2\pi}\,\mathrm{e}^{-i(\omega+nV)t_1}\,\mathrm{e}^{i(\omega+mV)t_2}\check{G}_{nm}\left(\omega\right) \tag{3.2.24}$$

$$\Leftrightarrow\quad \check{G}_{nm}\left(\omega\right) = \frac{V}{2\pi}\int_{-\infty}^{+\infty}\mathrm{d}t_1\int_{-\infty}^{+\infty}\mathrm{d}t_2\,\mathrm{e}^{i(\omega+nV)t_1}\,\mathrm{e}^{-i(\omega+mV)t_2}\check{G}\left(t_1,t_2\right) \tag{3.2.25}$$

have a Nambu-Dot-Keldysh structure. The Dyson equation takes the simple form of a matrix inversion

$$\check{G}(\omega)^{-1} = \check{G}_0(\omega)^{-1} - \check{\Sigma}_T(\omega)\ , \tag{3.2.26}$$

which is translated for RAK components into

$$\tilde{G}^{R/A}(\omega)^{-1} = \tilde{G}_0^{R/A}(\omega)^{-1} - \tilde{\Sigma}_T^{R/A}(\omega)\ , \tag{3.2.27}$$

$$\tilde{G}^{K}(\omega) = \tilde{G}_0^{K}(\omega) + \tilde{G}^{R}(\omega)\tilde{\Sigma}_T^{K}(\omega)\tilde{G}^{A}(\omega)\ . \tag{3.2.28}$$

The bare Green's function is diagonal in the RAK basis

$$\tilde{G}_0^K = 0 \tag{3.2.29}$$

and in frequency domain. These diagonal elements can be written in a Dot matrix form (where each entry is a Nambu matrix) as

$$\left[\tilde{G}_0^{R/A}(\omega)^{-1}\right]_{nm} = \delta_{nm}\begin{pmatrix} \omega + nV - \varepsilon_a\sigma_z & -t_d\sigma_z \\ -t_d\sigma_z & \omega + nV - \varepsilon_b\sigma_z \end{pmatrix} . \tag{3.2.30}$$

The frequency matrix elements of the lead self-energy are given by [120]:

$$\left[\check{\Sigma}_j(\omega)\right]_{nm} = \Gamma_j \begin{pmatrix} \delta_{n,m}\,\hat{X}_j(\omega + nV - V_j) & \delta_{n-2V_j/V,m}\,\hat{Y}_j(\omega + nV - V_j) \\ \delta_{n+2V_j/V,m}\,\hat{Y}_j(\omega + nV + V_j) & \delta_{n,m}\,\hat{X}_j(\omega + nV + V_j) \end{pmatrix} \quad \text{with} \quad \hat{Y}_j(\omega) = -\Delta_j\,\frac{\hat{X}_j(\omega)}{\omega} , \tag{3.2.31}$$

where Γ_j is a matrix in Dot space with matrix elements

$$\Gamma_{j\alpha\beta} = \pi\nu(0)t_{j\alpha}^* t_{j\beta} , \tag{3.2.32}$$

and where the Keldysh matrix $\hat{X}_j$ which is involved in the entries of the Nambu matrix in (3.2.31) have RAK components given by

$$\begin{cases} X_j^{R/A}(\omega) = -\dfrac{\Theta(\Delta_j - |\omega|)\,\omega}{\sqrt{\Delta_j^2 - \omega^2}} \mp i\,\dfrac{\Theta\left(|\omega| - \Delta_j\right)|\omega|}{\sqrt{\omega^2 - \Delta_j^2}} , \\ X_j^K(\omega) = -2i\,\dfrac{\Theta\left(|\omega| - \Delta_j\right)|\omega|}{\sqrt{\omega^2 - \Delta_j^2}}\tanh\dfrac{\beta\omega}{2} . \end{cases} \tag{3.2.33}$$

The dressed Green's function is obtained numerically through the handling of finite size matrices including inversions (3.2.27) which can be potentially time-consuming. The Fourier transformations are limited to a cut-off energy E_c, which has to be large compared to all the relevant energies of the problem. It defines a finite number N of useful frequency domains with width V so that $N \sim E_c/V$. At small voltages, one needs to sum on a very large number of Andreev reflections.

3.3 Current correlations

The Josephson current in this device has been derived in a previous work [17]. We recall this result (Section 3.3.1) since the current will be useful as a normalization for noise (Fano factors). The time dependent current correlations (correlations in each lead and crossed correlations between different leads) are computed using counting fields (Section 3.3.2) and these results are expressed in frequency domain under the MCPR condition (Section 3.3.3).

3.3.1 Current operator and its average value

The current operator from QD α into the lead j reads

$$I_{j\alpha}(t) = i \sum_k \Psi^\dagger_{jk}\, \sigma_z \mathcal{T}_{j\alpha}(t)\, d_\alpha + \text{h.c.} \tag{3.3.1}$$

As the average current does not depent on the branch of the Keldysh contour, it is convenient to introduce counting fields $\eta_{j\alpha}(t)$ in the tunneling amplitudes according to

$$\mathcal{T}_{j\alpha}(t) \to \mathcal{T}_{j\alpha}(t)\, \mathrm{e}^{i\sigma_z\tau_z\eta_{j\alpha}(t)/2}\ , \tag{3.3.2}$$

so that the evolution operator becomes $S(\infty) \to S(\infty,\eta)$ and that the average current can be computed through the functional differentiation

$$\langle I_{j\alpha}\rangle(t) = i\,\frac{1}{Z[0]}\,\frac{\delta Z[\eta]}{\delta\eta_{j\alpha}(t)}\bigg|_{\eta=0} \quad \text{where} \quad Z[\eta] = \langle S(\infty,\eta)\rangle_0\ . \tag{3.3.3}$$

After performing the differentiation we obtain the average current as the following $\alpha\alpha$ diagonal element in Dot space

$$\langle I_{j\alpha}\rangle(t) = \frac{1}{2}\,\mathrm{Tr}^{(NK)}\left\{\sigma_z\tau_z\int_{-\infty}^{+\infty}\mathrm{d}t'\,\left[\check{G}(t,t')\check{\Sigma}_j(t',t) - \check{\Sigma}_j(t,t')\check{G}(t',t)\right]^{\alpha\alpha}\right\}\ , \tag{3.3.4}$$

where $\mathrm{Tr}^{(NK)}$ denotes the trace in Nambu-Keldysh space.

3.3.2 Current correlations

In full generality, we need to compute the unsymmetrized current-current correlator. A convenient way consists, as in the work [84], in introducing new counting fields $\eta_{j\alpha s}(t)$ where $s = \pm$ specifies the branch of the Keldysh contour. We define the following matrices in Keldysh space

$$\pi_+ = \frac{\tau_z+1}{2} = \begin{pmatrix} 1 & 0 \\ 0 & 0 \end{pmatrix}\ , \quad \pi_- = \frac{\tau_z-1}{2} = \begin{pmatrix} 0 & 0 \\ 0 & -1 \end{pmatrix}\ . \tag{3.3.5}$$

The tunneling amplitudes are then redefined as

$$\mathcal{T}_{j\alpha}(t) \to \mathcal{T}_{j\alpha}(t)\, \mathrm{e}^{i\sigma_z\sum_s \pi_s\eta_{j\alpha s}(t)}\ , \tag{3.3.6}$$

so that the evolution operator becomes $S(\infty) \to S(\infty,\eta)$ and that the current correlations can be computed through the second order functional differentiation

$$\left\langle I^-_{i\alpha}(t)\, I^+_{j\beta}(t')\right\rangle = -\frac{1}{Z[0]}\,\frac{\delta^2 Z[\eta]}{\delta\eta_{i\alpha-}(t)\,\delta\eta_{j\beta+}(t')}\bigg|_{\eta=0} \quad \text{where} \quad Z[\eta] = \langle S(\infty,\eta)\rangle_0\ . \tag{3.3.7}$$

Performing this differentiation, we obtain

$$\left\langle I^-_{i\alpha}(t) I^+_{j\beta}(t') \right\rangle = \int \mathrm{d}t_1 \int \mathrm{d}t_2 \sum_{\gamma\delta} \sum_{ss'} \sum_{\sigma\sigma'\sigma_1\sigma_2} \sigma\sigma'$$
$$\times \Bigg(\left[\check{\Sigma}_i\right]^{-s}_{\substack{\alpha\gamma \\ \sigma\sigma_1}} (t,t_1) \left[\check{\Sigma}_j\right]^{+s'}_{\substack{\beta\delta \\ \sigma'\sigma_2}} (t',t_2) \check{K}^{ss'-+}_{\substack{\gamma\delta\alpha\beta \\ \sigma_1\sigma_2\sigma\sigma'}} (t_1,t_2,t,t') - \left[\check{\Sigma}_i\right]^{-s}_{\substack{\alpha\gamma \\ \sigma\sigma_1}} (t,t_1) \left[\check{\Sigma}_j\right]^{s'+}_{\substack{\delta\beta \\ \sigma_2\sigma'}} (t_2,t') \check{K}^{s+-s'}_{\substack{\gamma\beta\alpha\delta \\ \sigma_1\sigma'\sigma\sigma_2}} (t_1,t',t,t_2)$$
$$- \left[\check{\Sigma}_i\right]^{s-}_{\substack{\gamma\alpha \\ \sigma_1\sigma}} (t_1,t) \left[\check{\Sigma}_j\right]^{+s'}_{\substack{\beta\delta \\ \sigma'\sigma_2}} (t',t_2) \check{K}^{-s's+}_{\substack{\alpha\delta\gamma\beta \\ \sigma\sigma_2\sigma_1\sigma'}} (t,t_2,t_1,t') + \left[\check{\Sigma}_i\right]^{s-}_{\substack{\gamma\alpha \\ \sigma_1\sigma}} (t_1,t) \left[\check{\Sigma}_j\right]^{s'+}_{\substack{\delta\beta \\ \sigma_2\sigma'}} (t_2,t') \check{K}^{-+ss'}_{\substack{\alpha\beta\gamma\delta \\ \sigma\sigma'\sigma_1\sigma_2}} (t,t',t_1,t_2) \Bigg) \tag{3.3.8}$$

where the matrix/tensor elements have indices listed in three lines, corresponding from top to bottom to Keldysh, Dot and Nambu spaces. The 4-indices tensor

$$\check{K}^{s_1s_2s_3s_4}_{\substack{\alpha_1\alpha_2\alpha_3\alpha_4 \\ \sigma_1\sigma_2\sigma_3\sigma_4}}(t_1,t_2,t_3,t_4) = -\left\langle T_C \left\{ \check{d}^{s_1}_{\alpha_1\sigma_1}(t_1) \check{d}^{s_2}_{\alpha_2\sigma_2}(t_2) \check{d}^{\dagger s_3}_{\alpha_3\sigma_3}(t_3) \check{d}^{\dagger s_4}_{\alpha_4\sigma_4}(t_4) \right\} \right\rangle \tag{3.3.9}$$

is the two particle Green's function of the dot electrons. As the Hamiltonian is quadratic in both lead and QD degrees of freedom, it can be expressed in terms of products of single particle Green's functions, according to Wick's theorem:

$$\check{K}^{s_1s_2s_3s_4}_{\substack{\alpha_1\alpha_2\alpha_3\alpha_4 \\ \sigma_1\sigma_2\sigma_3\sigma_4}}(t_1,t_2,t_3,t_4) = \check{G}^{s_1s_4}_{\substack{\alpha_1\alpha_4 \\ \sigma_1\sigma_4}}(t_1,t_4) \check{G}^{s_2s_3}_{\substack{\alpha_2\alpha_3 \\ \sigma_2\sigma_3}}(t_2,t_3) - \check{G}^{s_1s_3}_{\substack{\alpha_1\alpha_3 \\ \sigma_1\sigma_3}}(t_1,t_3) \check{G}^{s_2s_4}_{\substack{\alpha_2\alpha_4 \\ \sigma_2\sigma_4}}(t_2,t_4) \ . \tag{3.3.10}$$

Substituting this last result into (3.3.8), we obtain the irreducible part of the current-current correlator

$$\begin{aligned} S_{i\alpha,j\beta}(t,t') &= \langle I_{i\alpha}(t) I_{j\beta}(t') \rangle - \langle I_{i\alpha}(t) \rangle \langle I_{j\beta}(t') \rangle \\ &= -\int_{-\infty}^{+\infty} \mathrm{d}t_1 \int_{-\infty}^{+\infty} \mathrm{d}t_2 \, \mathrm{Tr}^{(NK)} \Big\{ \pi_- \sigma_z \Big([\check{\Sigma}_i(t,t_1)\check{G}(t_1,t')]^{\alpha\beta} \, \pi_+ \sigma_z \, [\check{\Sigma}_j(t',t_2)\check{G}(t_2,t)]^{\beta\alpha} \\ &\qquad + [\check{G}(t,t_1)\check{\Sigma}_j(t_1,t')]^{\alpha\beta} \, \pi_+ \sigma_z \, [\check{G}(t',t_2)\check{\Sigma}_i(t_2,t)]^{\beta\alpha} \\ &\qquad - [\check{\Sigma}_i(t,t_1)\check{G}(t_1,t_2)\check{\Sigma}_j(t_2,t')]^{\alpha\beta} \, \pi_+ \sigma_z \, \check{G}^{\beta\alpha}(t',t) \\ &\qquad - \check{G}^{\alpha\beta}(t,t') \, \pi_+ \sigma_z \, [\check{\Sigma}_j(t',t_1)\check{G}(t_1,t_2)\check{\Sigma}_i(t_2,t)]^{\beta\alpha} \Big) \Big\} \ . \end{aligned} \tag{3.3.11}$$

Performing the partial trace over Keldysh space, it can be expressed in terms of RAK components

$$S_{i\alpha,j\beta}(t,t') = -\frac{1}{2} \, \mathrm{Re} \int_{-\infty}^{+\infty} \mathrm{d}t_1 \int_{-\infty}^{+\infty} \mathrm{d}t_2$$
$$\times \, \mathrm{Tr}^{(N)} \Bigg\{ \sigma_z \left(\tilde{\Sigma}^K_i \tilde{G}^A + \tilde{\Sigma}^R_i \tilde{G}^K - \tilde{\Sigma}^A_i \tilde{G}^A + \tilde{\Sigma}^R_i \tilde{G}^R \right)^{\alpha\beta}_{(t,t_1)\circ(t_1,t')} \sigma_z \left(\tilde{\Sigma}^K_j \tilde{G}^A + \tilde{\Sigma}^R_j \tilde{G}^K + \tilde{\Sigma}^A_j \tilde{G}^A - \tilde{\Sigma}^R_j \tilde{G}^R \right)^{\beta\alpha}_{(t',t_2)\circ(t_2,t)}$$
$$- \sigma_z \left(\tilde{\Sigma}^R_i \tilde{G}^R \tilde{\Sigma}^K_j + \tilde{\Sigma}^K_i \tilde{G}^A \tilde{\Sigma}^A_j + \tilde{\Sigma}^R_i \tilde{G}^K \tilde{\Sigma}^A_j - \tilde{\Sigma}^A_i \tilde{G}^A \tilde{\Sigma}^A_j + \tilde{\Sigma}^R_i \tilde{G}^R \tilde{\Sigma}^R_j \right)^{\alpha\beta}_{(t,t_1)\circ(t_1,t_2)\circ(t_2,t')} \sigma_z \left(\tilde{G}^K + \tilde{G}^A - \tilde{G}^R \right)^{\beta\alpha}_{(t',t)} \Bigg\} \ . \tag{3.3.12}$$

3.3.3 Josephson current and noise at a MCPR

As already explained in Section 3.2.4, the MCPR condition is responsible for commensurate voltages and the recovery of a single Josephson frequency (instead of two). As a result, a periodicity $T = 2\pi/V$ is restored, where V is the lowest common multiple of lateral gate voltages. The current admits a Fourier series expansion according to

$$\langle I_{j\alpha}\rangle(t) = \sum_{p\in\mathbb{Z}} \mathrm{e}^{-ipVt}\,\mathcal{I}^p_{j\alpha} \tag{3.3.13}$$

with Fourier coefficients given by

$$\mathcal{I}^p_{j\alpha} = \frac{1}{2}\,\mathrm{Tr}^{(NK)}\left\{\sigma_z\tau_z\int_0^V \frac{\mathrm{d}\omega}{2\pi}\sum_n \left[\hat{G}(\omega)\hat{\Sigma}_j(\omega) - \hat{\Sigma}_j(\omega)\hat{G}(\omega)\right]^{\alpha\alpha}_{n,n-p}\right\}\,. \tag{3.3.14}$$

Performing the partial trace over Keldysh space, it can be expressed in terms of RAK components

$$\mathcal{I}^p_{j\alpha} = \frac{1}{2}\,\mathrm{Tr}^{(N)}\left\{\sigma_z\int_0^V \frac{\mathrm{d}\omega}{2\pi}\sum_n \left[\tilde{G}^R(\omega)\tilde{\Sigma}^K_j(\omega) + \tilde{G}^K(\omega)\tilde{\Sigma}^A_j(\omega) - \tilde{\Sigma}^R_j(\omega)\tilde{G}^K(\omega) - \tilde{\Sigma}^K_j(\omega)\tilde{G}^A(\omega)\right]^{\alpha\alpha}_{n,n-p}\right\}\,. \tag{3.3.15}$$

Concerning the noise, typically one introduces a measuring frequency by calculating the Fourier transforms of the correlators:

$$S_{i\alpha,j\beta}(\omega,t) \equiv \int_{-\infty}^{+\infty}\mathrm{d}t'\,\mathrm{e}^{i\omega t'}\,S_{i\alpha,j\beta}(t+t',t)\,, \tag{3.3.16}$$

$$S'_{i\alpha,j\beta}(\omega,t) \equiv \int_{-\infty}^{+\infty}\mathrm{d}t'\,\mathrm{e}^{i\omega t'}\,S_{i\alpha,j\beta}(t,t+t')\,. \tag{3.3.17}$$

Under the MCPR condition these Fourier-transformed correlators, like the currents, contain all harmonics of the Josephson frequency, which motivates the computation of the averages:

$$\bar{S}_{i\alpha,j\beta}(\omega) \equiv \frac{V}{2\pi}\int_0^{2\pi/V}\mathrm{d}t\,S_{i\alpha,j\beta}(\omega,t)\,, \tag{3.3.18a}$$

$$\bar{S}'_{i\alpha,j\beta}(\omega) \equiv \frac{V}{2\pi}\int_0^{2\pi/V}\mathrm{d}t\,S'_{i\alpha,j\beta}(\omega,t)\,. \tag{3.3.18b}$$

In Eq.(3.3.12), we can express the self energy and the Green's function elements using the double Fourier transform with summation over finite domains of energy. At zero frequency, performing all 4 time integrations, this gives the result:

$$\bar{S}_{i\alpha,j\beta}(\omega=0) = -\frac{(2\pi)^3}{2}\mathrm{Re}\sum_{mnpq=-\infty}^{+\infty}\int_0^V \mathrm{d}\omega'$$

$$\times\,\mathrm{tr}\left\{\sigma_z\left(\tilde{\Sigma}^K_{imn}\tilde{G}^A_{np} + \tilde{\Sigma}^R_{imn}\tilde{G}^K_{np} - \tilde{\Sigma}^A_{imn}\tilde{G}^A_{np} + \tilde{\Sigma}^R_{imn}\tilde{G}^R_{np}\right)^{\alpha\beta}_{\omega'}\sigma_z\left(\tilde{\Sigma}^K_{jpq}\tilde{G}^A_{qm} + \tilde{\Sigma}^R_{jpq}\tilde{G}^K_{qm} + \tilde{\Sigma}^A_{jpq}\tilde{G}^A_{qm} - \tilde{\Sigma}^R_{jpq}\tilde{G}^R_{qm}\right)^{\beta\alpha}_{\omega'}\right.$$

$$\left.-\sigma_z\left(\tilde{\Sigma}^R_{imn}\tilde{G}^R_{np}\tilde{\Sigma}^K_{jpq} + \tilde{\Sigma}^K_{imn}\tilde{G}^A_{np}\tilde{\Sigma}^A_{jpq} + \tilde{\Sigma}^R_{imn}\tilde{G}^K_{np}\tilde{\Sigma}^A_{jpq} - \tilde{\Sigma}^A_{imn}\tilde{G}^A_{np}\tilde{\Sigma}^A_{jpq} + \tilde{\Sigma}^R_{imn}\tilde{G}^R_{np}\tilde{\Sigma}^R_{jpq}\right)^{\alpha\beta}_{\omega'}\sigma_z\left(\tilde{G}^K_{qm} + \tilde{G}^A_{qm} - \tilde{G}^R_{qm}\right)^{\beta\alpha}_{\omega'}\right\}\,. \tag{3.3.19}$$

We obtain the same expression when calculating $\bar{S}'_{i\alpha,j\beta}(\omega = 0)$. It is also possible to obtain compact expressions when the noise is evaluated at harmonics lV (l integer) of the Josephson frequency :

$$\bar{S}_{i\alpha,j\beta}(lV) = -\frac{(2\pi)^3}{2}\mathrm{Re}\sum_{mnpq=-\infty}^{+\infty}\int_0^V d\omega'$$

$$\times \mathrm{tr}\Big\{\sigma_z\left(\tilde{\Sigma}^K_{imn}\tilde{G}^A_{np+l} + \tilde{\Sigma}^R_{imn}\tilde{G}^K_{np+l} - \tilde{\Sigma}^A_{imn}\tilde{G}^A_{np+l} + \tilde{\Sigma}^R_{imn}\tilde{G}^R_{np+l}\right)^{\alpha\beta}_{\omega'}\sigma_z\left(\tilde{\Sigma}^K_{jpq}\tilde{G}^A_{qm-l} + \tilde{\Sigma}^R_{jpq}\tilde{G}^K_{qm-l} + \tilde{\Sigma}^A_{jpq}\tilde{G}^A_{qm-l} - \tilde{\Sigma}^R_{jpq}\tilde{G}^R_{qm-l}\right)^{\beta\alpha}_{\omega'}$$

$$-\sigma_z\left(\tilde{\Sigma}^R_{imn}\tilde{G}^R_{np}\tilde{\Sigma}^K_{jpq+l} + \tilde{\Sigma}^K_{imn}\tilde{G}^A_{np}\tilde{\Sigma}^A_{jpq+l} + \tilde{\Sigma}^R_{imn}\tilde{G}^K_{np}\tilde{\Sigma}^A_{jpq+l} - \tilde{\Sigma}^A_{imn}\tilde{G}^A_{np}\tilde{\Sigma}^A_{jpq+l} + \tilde{\Sigma}^R_{imn}\tilde{G}^R_{np}\tilde{\Sigma}^R_{jpq+l}\right)^{\alpha\beta}_{\omega'}\sigma_z\left(\tilde{G}^K_{qm-l} + \tilde{G}^A_{qm-l} - \tilde{G}^R_{qm-l}\right)^{\beta\alpha}_{\omega'}\Big\} \tag{3.3.20}$$

The other non symmetrized correlator reads

$$\bar{S}'_{i\alpha,j\beta}(lV) = -\frac{(2\pi)^3}{2}\mathrm{Re}\sum_{mnpq=-\infty}^{+\infty}\int_0^V d\omega'$$

$$\times \mathrm{tr}\Big\{\sigma_z\left(\tilde{\Sigma}^K_{imn}\tilde{G}^A_{np-l} + \tilde{\Sigma}^R_{imn}\tilde{G}^K_{np-l} - \tilde{\Sigma}^A_{imn}\tilde{G}^A_{np-l} + \tilde{\Sigma}^R_{imn}\tilde{G}^R_{np-l}\right)^{\alpha\beta}_{\omega'}\sigma_z\left(\tilde{\Sigma}^K_{jpq}\tilde{G}^A_{qm+l} + \tilde{\Sigma}^R_{jpq}\tilde{G}^K_{qm+l} + \tilde{\Sigma}^A_{jpq}\tilde{G}^A_{qm+l} - \tilde{\Sigma}^R_{jpq}\tilde{G}^R_{qm+l}\right)^{\beta\alpha}_{\omega'}$$

$$-\sigma_z\left(\tilde{\Sigma}^R_{imn}\tilde{G}^R_{np}\tilde{\Sigma}^K_{jpq-l} + \tilde{\Sigma}^K_{imn}\tilde{G}^A_{np}\tilde{\Sigma}^A_{jpq-l} + \tilde{\Sigma}^R_{imn}\tilde{G}^K_{np}\tilde{\Sigma}^A_{jpq-l} - \tilde{\Sigma}^A_{imn}\tilde{G}^A_{np}\tilde{\Sigma}^A_{jpq-l} + \tilde{\Sigma}^R_{imn}\tilde{G}^R_{np}\tilde{\Sigma}^R_{jpq-l}\right)^{\alpha\beta}_{\omega'}\sigma_z\left(\tilde{G}^K_{qm+l} + \tilde{G}^A_{qm+l} - \tilde{G}^R_{qm+l}\right)^{\beta\alpha}_{\omega'}\Big\} \tag{3.3.21}$$

We note the symmetry property $\bar{S}'_{i\alpha,j\beta}(lV) = \bar{S}_{i\alpha,j\beta}(-lV)$.

3.4 Numerical results

The code which has been developped to investigate MCPR configurations allows the computation of the harmonics (3.3.15) of the Josephson current as well as the computation of the frequency unsymmetrized noise (3.3.20)-(3.3.21) for the harmonics of the Josephson frequency. It is versatile in the sense that various configurations (and phenomena) can be adressed and as benchmark tests, we have first recovered some well established results including

- the MAR onsets in a single voltage biased Josephson junction [121], obtained by desactivating the tunnel coupling between S_0 and S_b,
- the noise cross correlations in a N-S-N junction [84], obtained in the limit of vanishing lateral superconducting gaps.

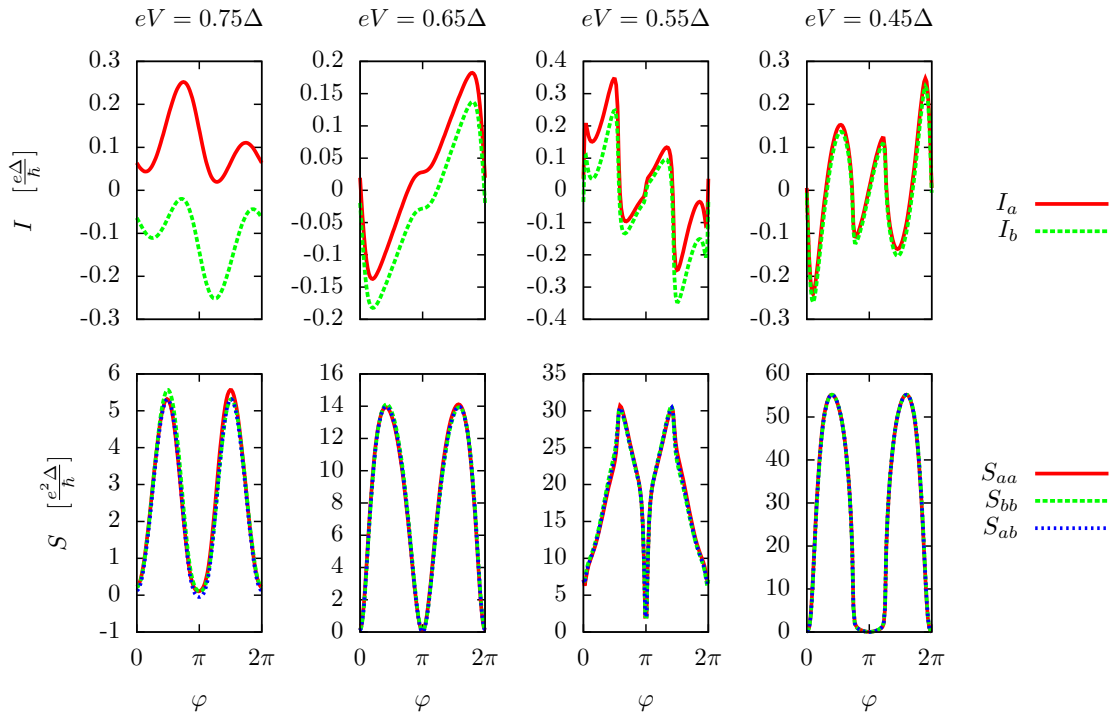

Figure 3.6: Current and noise correlations for a high (subgap) voltage in the resonant dots regime.

We will focus on the quartet resonance $V_a = -V_b = V > 0$. Moreover we will adopt an antisymmetric position for the dots $\varepsilon_a = -\varepsilon_b = \varepsilon > 0$ to optimize CP splitting [84]. We assume symmetric couplings between superconductors and dots $\Gamma_{j\alpha\beta} = \Gamma$. The quartet phase $\varphi_Q = \varphi_a + \varphi_b - 2\varphi_0$ is monitored through $\varphi_b = \varphi$, the two others being set to zero $\varphi_0 = \varphi_a = 0$. We will present results for the DC currents in the leads $I_a \equiv \mathcal{I}^0_{aa}$ and $I_b \equiv \mathcal{I}^0_{bb}$ (cf. Eq. (3.3.15)) as well as for the zero-frequency correlations of these currents $S_{aa} \equiv \bar{S}_{aa,aa}(\omega = 0)$, $S_{bb} \equiv \bar{S}_{bb,bb}(\omega = 0)$ and $S_{ab} \equiv \bar{S}_{aa,bb}(\omega = 0)$ (cf. Eq. (3.3.19)). S_{aa} and S_{bb} will be refered as noise autocorrelations whereas S_{ab} are the noise crossed correlations. Usual Fano factors in the leads are also given:

$$\mathcal{F}_j = \frac{S_{jj}}{2I_j} \quad \text{for} \quad j = a, b \ . \tag{3.4.1}$$

Another Fano factor is defined from the sum of the currents and gives information about noise crossed correlations

$$\mathcal{F}_0 = \frac{S_{aa} + S_{bb} + 2S_{ab}}{2(I_a + I_b)} \ . \tag{3.4.2}$$

Concerning the Josephson currents, investigated in Ref. [17], a remark is worthy: defining the vectors $\bar{I} = (I_a, I_b)$, $\bar{\varphi} = (\varphi_a, \varphi_b)$, $\bar{V} = (V_a, V_b)$ and $\bar{\varepsilon} = (\varepsilon_a, \varepsilon_b)$ which collect average currents,

phases, voltages and dot energies, particle-hole symmetry is responsible for

$$\bar{I}(-\bar{\varphi}, -\bar{V}, -\bar{\varepsilon}) = -\bar{I}(\bar{\varphi}, \bar{V}, \bar{\varepsilon}) \ . \tag{3.4.3}$$

In close connection to Josephson's original work [15], the authors of Ref. [17] postulate the following form for the current

$$\bar{I}(\bar{\varphi}, \bar{V}, \bar{\varepsilon}) = \bar{I}^{\mathrm{MP}}(\bar{\varphi}, \bar{V}, \bar{\varepsilon}) + \bar{I}^{\mathrm{phMAR}}(\bar{\varphi}, \bar{V}, \bar{\varepsilon}) + \bar{I}^{\mathrm{qp}}(\bar{V}, \bar{\varepsilon}) \tag{3.4.4}$$

as a sum of an usual phase insentive (odd in voltages) quasiparticle current $\bar{I}^{\mathrm{qp}}$ and a phase sensitive current which is further decomposed as a component $\bar{I}^{\mathrm{MP}}$ odd in phases and even in voltages ascribed to multipair production and a component $\bar{I}^{\mathrm{phMAR}}$ even in phases and odd in voltages due to nonlocal MAR processes. Within the symmetries that result from the choice of parameters we have done, we should recover $I_b(-\varphi) = -I_a(\varphi)$. For clarity and despite some redundancy, we will sometimes give the two currents to show eventual discrepancies or to make clear that both are equal and then odd in phases which is ascribed to quartets production as emphasized in Ref. [17]. Following the latter work, two different regimes will be investigated:

- the resonant dots regime is obtained for QD energy levels within the gap $\varepsilon < \Delta$ and not so large couplings $\Gamma < \Delta$,
- the metallic junction regime is obtained for energy levels out of resonance $\varepsilon > \Delta$ and large couplings $\Gamma > \Delta$.

3.4.1 Resonant dots regime

A common feature which emerges from all the investigations led in this regime is the presence of (very) phase sensitive and voltage sensitive giant Fano factors even when the Josephson current is fully ascribed to quartets production. Numerical issues in the computation of current correlations prevent to reach reliably the adiabatic regime where a sinusoidal (π-shifted) current-phase relation is recovered. Here we present results for $\varepsilon = 0.6\Delta$ and $\Gamma = 0.3\Delta$.

In Figs. 3.6, the phase dependences of the currents I_a and I_b as well as those of noise correlations S_{aa}, S_{bb} and S_{ab} are given for different voltages. While at voltages below $2\Delta/3$, the two currents in the lateral electrodes are identical, they become to move away from each other for higher voltages (we still have the symmetry $I_b(-\varphi) = -I_a(\varphi)$ which has been clarified in the beginning of this section). It has been ascribed to the emergence of phase-sensitive MAR processes (the lowest order process illustrated in Fig. 3.4c has a threshold $2\Delta/3$). Remark that

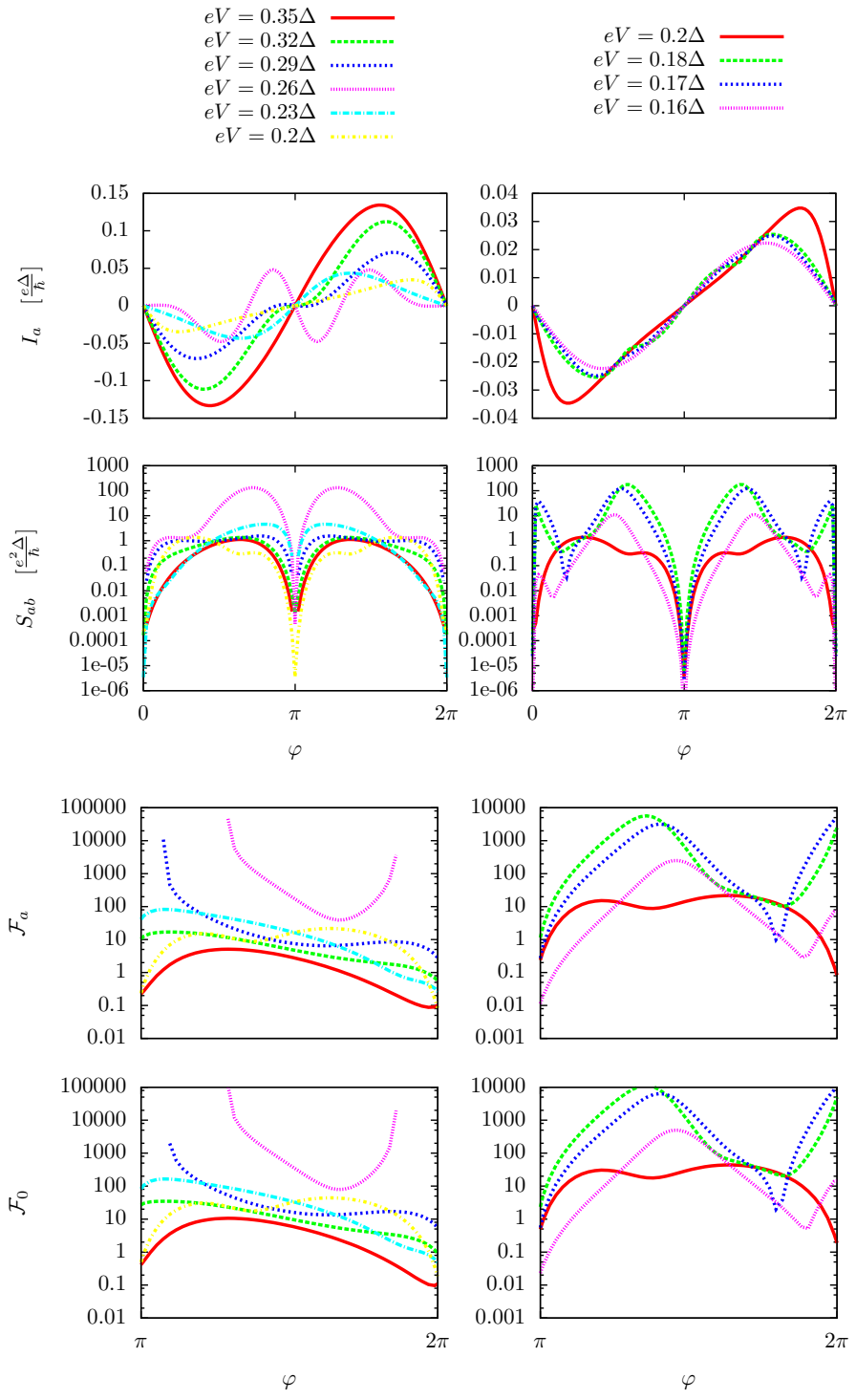

Figure 3.7: Current, noise crossed correlations and Fano factors for a low (subgap) voltage in the resonant dots regime. Note the logarithmic scale for noise crossed correlations and Fano factors.

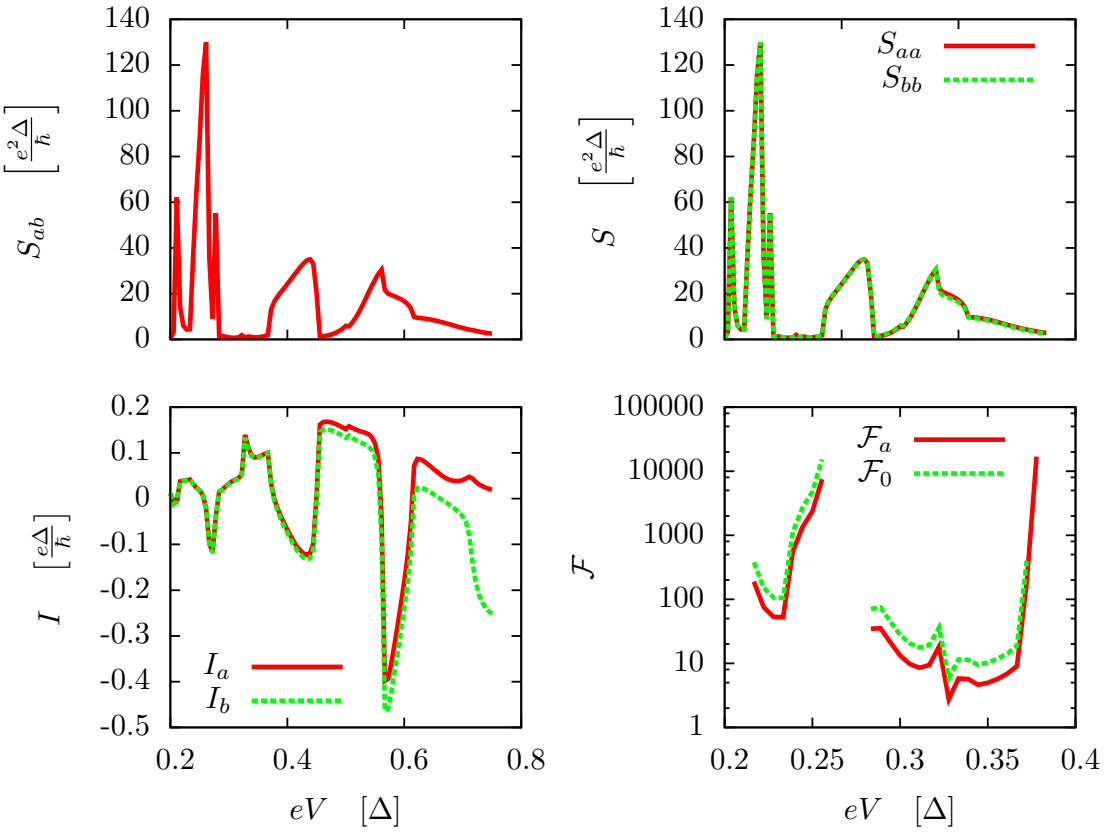

Figure 3.8: Current, noise correlations and Fano factors as a function of the voltage in the resonant dots regime, for $\varphi = 4$. Note the logarithmic scale for Fano factors. Note also that this quantity displayed in the bottom right panel is considered in the low voltage regime (the voltage range is different from other panels).

both autocorrelations in the two leads and the crossed correlations collapse on the same curve even if the two currents are well separated and an important consequence is that positive noise crossed correlations are obtained. This noise increases as the voltage is lowered in contradiction with the expectation one should have from the disappearance of a low order and possibly noisy phase sensitive MAR process.

Decreasing further the voltage leads to nontrivial evolutions for the current as shown in Fig. 3.7. Nevertheless, it tends to adopt a π-junction behavior which has been verified for lower voltages (the numerical issues are less stringent for current computation than for noise computations) in agreement with Ref. [17]. A very simple argument has been provided in the latter work in relation to the spin singlet nature of CP pairing. Indeed a nonlocal singlet delocalized on

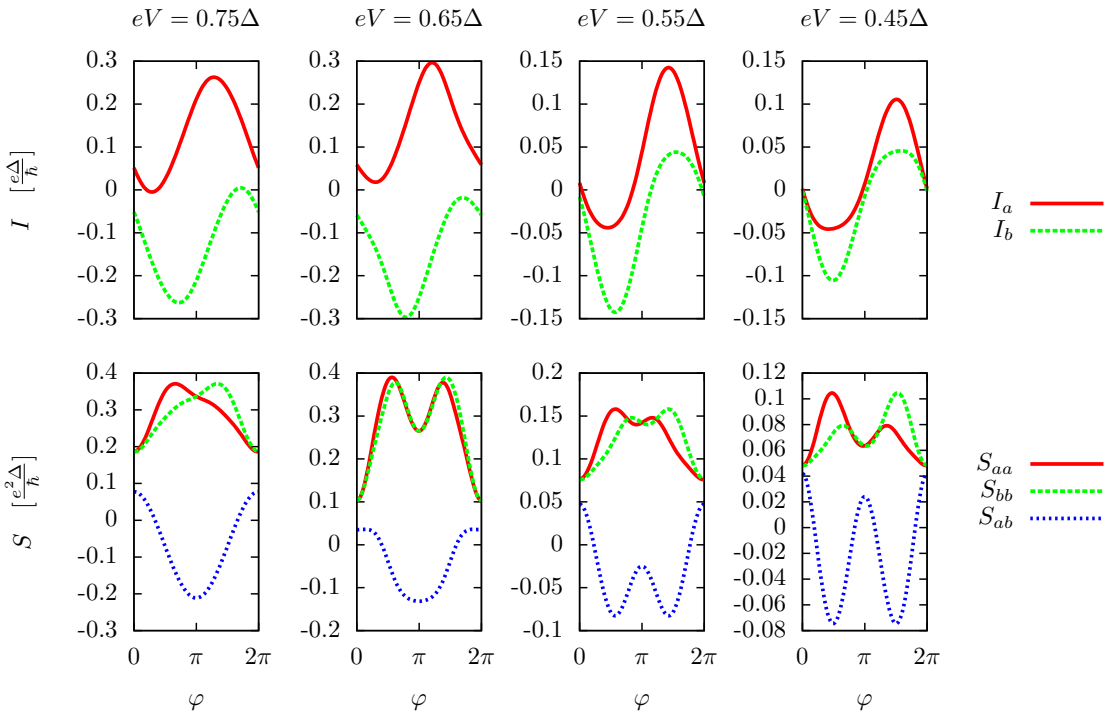

Figure 3.9: Current and noise correlations for a high (subgap) voltage in the metallic junction regime.

the QDs (CP splitting) is obtained by the operator $c_{ab} = (d^\dagger_{a\uparrow} d^\dagger_{b\downarrow} - d^\dagger_{a\downarrow} d^\dagger_{b\uparrow})/\sqrt{2}$ so that splitting two CPs on the QDs results in the state $c^2_{ab} \left|0\right\rangle_a \left|0\right\rangle_b = -\left|\uparrow\downarrow\right\rangle_a \left|\uparrow\downarrow\right\rangle_b$ and the minus sign which is obtained explains the anomalous sign of the Josephson supercurrent. The noise still presents high values compared to the current as the Fano factors reveal. The phase sensitivity of the noise is so huge (values ranging over 10 decades) that we have adopted a logarithmic scale. The Fano factors are represented for $\varphi \in [\pi, 2\pi]$ where the current is supposed to be positive for the expected π-junction behavior (remark that there are some voltages and phases for which the logarithm of the Fano factor is not defined as the current takes negative values). There are some voltages for which the phase sensitivity of the noise is attenuated ($eV/\Delta = 0.35$, 0.32, 0.23, 0.2 in Fig. 3.7) but Fano factors are still ranging between unity and some hundreds. Note that the voltages given are the lowest for which we have some confidence in the numerical convergences.

In Fig.3.8, we propose to investigate the dependence of currents and correlations on voltage V for a given phase ($\varphi = 4$). We notice a strong sensitivity with the presence of some resonances, the strongest corresponding to $V = \varepsilon$ for which the Fermi energies of both leads are at the level of QD energies. As already mentioned, the currents in both leads collapse on a single curve

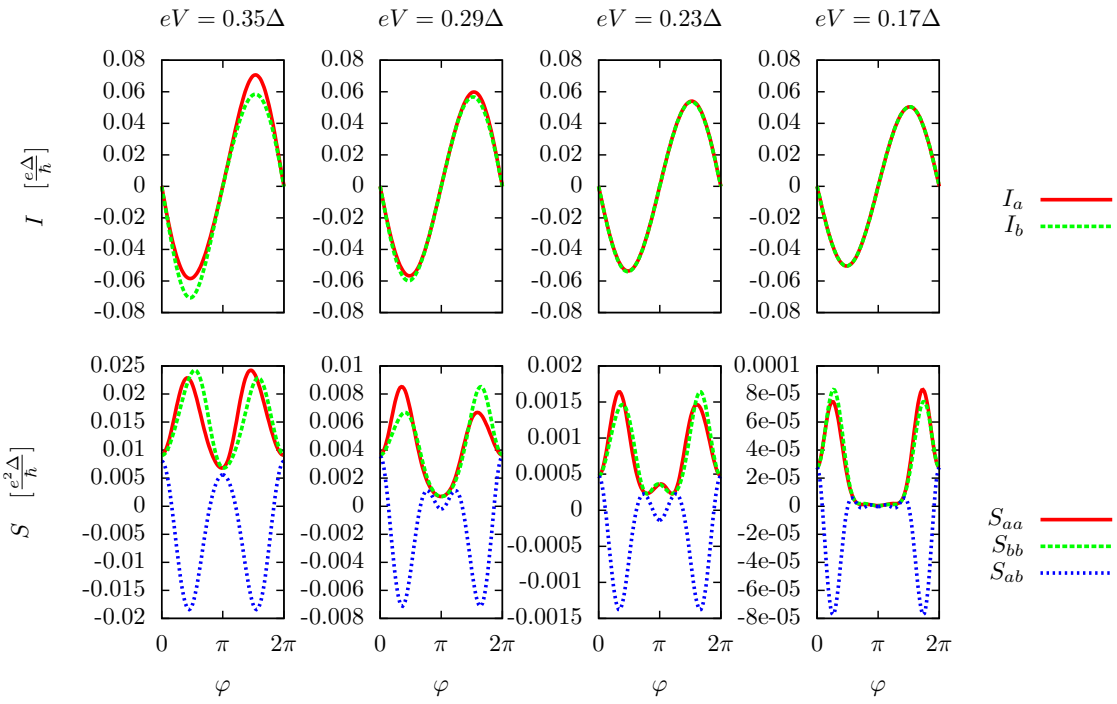

Figure 3.10: Current and noise correlations for a low (subgap) voltage in the metallic junction regime.

as soon as $V < 2\Delta/3$ while their associated autocorrelations coincide both with the crossed correlations for all subgap voltages investigated. As already stressed, Fano factors take high values (once again it is given using a logarithmic scale and there are some voltages for which it is not defined).

3.4.2 Metallic junction regime

Here we take $\varepsilon = 6\Delta$ and $\Gamma = 4\Delta$. In Figs. 3.9 and 3.10, the phase dependences of the currents I_a and I_b as well as those of noise correlations S_{aa}, S_{bb} and S_{ab} are given. We remark very different features as compared to the case of resonant QDs. First, considering the currents in the two leads, the coinciding of their average values is obtained for lower voltages and those of their autocorrelations for even lower voltages. Due to the large coupling, higher order phase sensitive MAR processes (higher than the lowest order process given in Fig. 3.4c) contribute to maintain this discrepancy. Second, noise crossed correlations strongly differ from autocorrelations in the leads and positive crossed correlations are obtained only in the neighboring of the quartet phase $\varphi = 0$ or π.

Very importantly, as shown in Fig. 3.11, as the voltage is lowered, the noise correlations de-

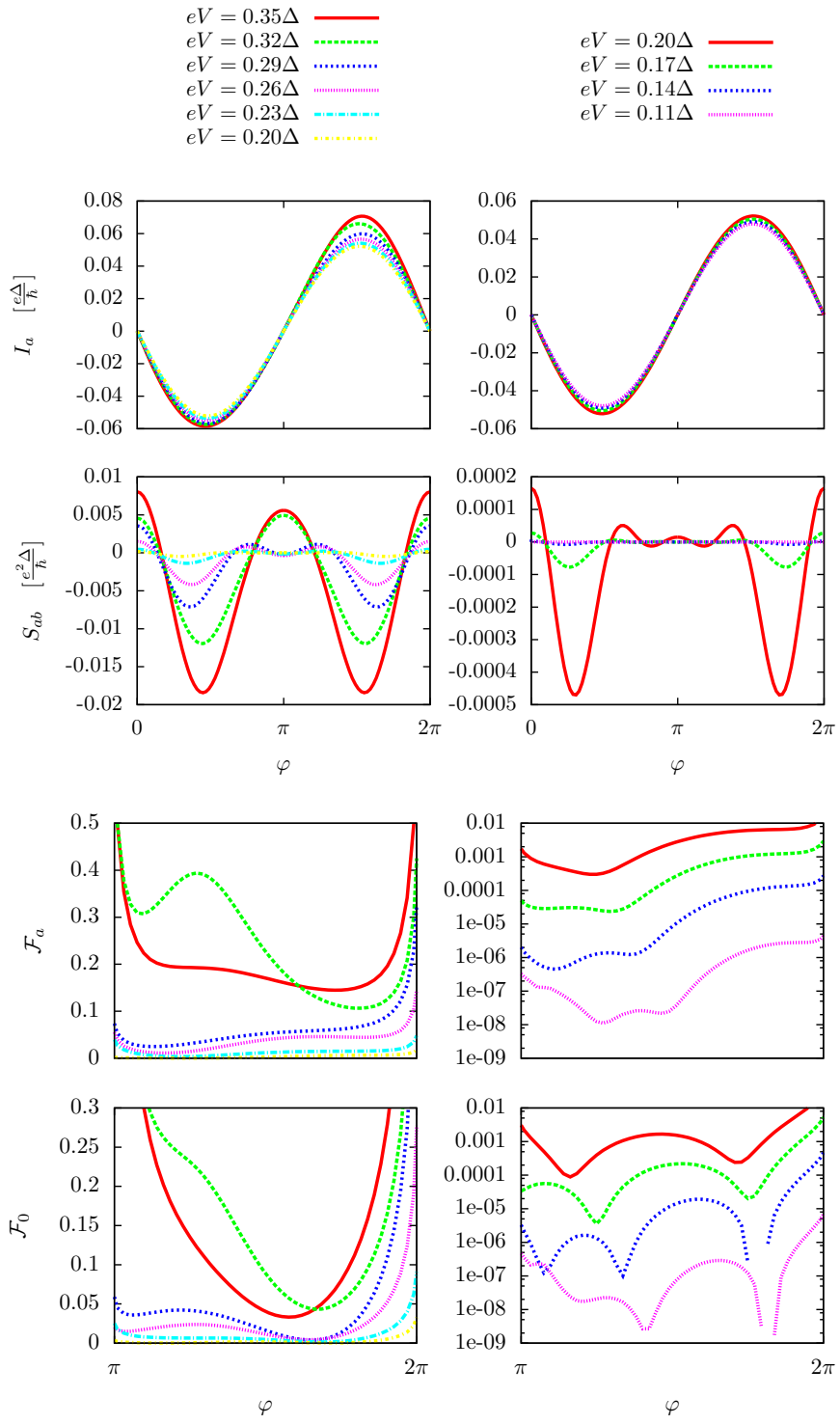

Figure 3.11: Current, noise crossed correlations and Fano factors for a low (subgap) voltage in the metallic junction regime. Note the logarithmic scale for Fano factors at low voltages (right column).

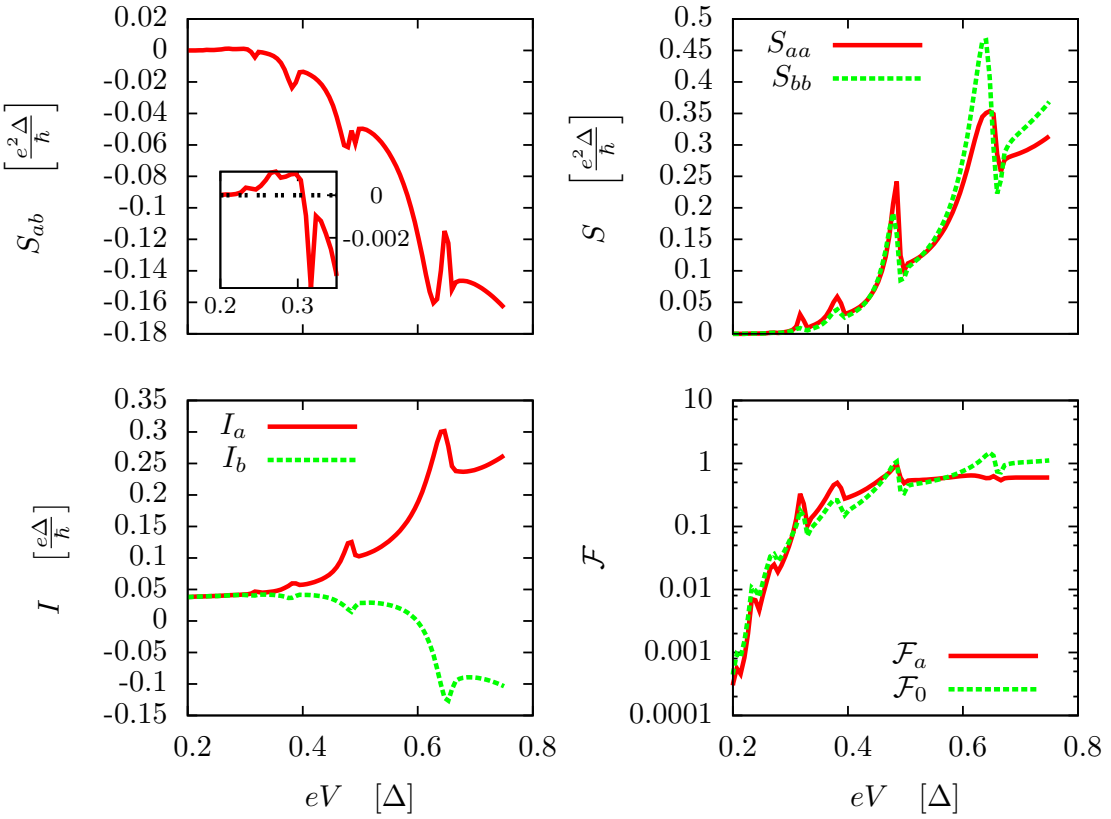

Figure 3.12: Current, noise correlations and Fano factors as a function of the voltage in the metallic junction regime, for $\varphi = 4$. Note the logarithmic scale for Fano factors.

crease whereas the Josephson current converges towards a given π-junction current-phase relation (which has already been explained in the last section). Note that the nontrivial oscillations of the noise crossed correlations lead to the appearance of positive values around fine-tuned quartet phases. Nevertheless, considering the amplitudes of noise correlations, they are considerably lowered and consequently, as the current converges, so do the Fano factors (note that a logarithmic scale has been adopted for the Fano factors at low voltages).

In Fig.3.12, the dependence of currents and correlations on voltage V for a given phase ($\varphi = 4$) is investigated. The currents in both leads both converge towards a finite value (the adiabatic limit) when the voltage is lowered. Autocorrelations and crossed correlations are different but both vanish in the limit of small voltages so do the Fano factors. Note that positive crossed correlations can be achieved as illustrated in the inset of the first panel.

3.5 Conclusion and perspectives

We have studied the noise correlations in a three-terminal all-superconducting device designed in a Josephson bijunction with a grounded electrode contacted *via* two QD nanowires to two lateral leads. When commensurate voltages are applied to these lateral electrodes, Josephson-like signatures are recovered and associated with MCPR.

Within the Keldysh framework, a path integral approach leads to a Dyson equation which relates bare and dressed (by interactions) QD Green's functions, introducing a self-energy term. The statistics of the current operator have been derived using counting fields. The commensurability of the voltages allows a (double) Fourier representation which is convenient for further numerical computations.

Two regimes have been numerically investigated. For resonant QDs, high values for the noise have been obtained together with a strong sensitivity on both phase and voltage. This regime supports (high) positive noise crossed correlations. In the metallic junction limit, we have found that the noise correlations decrease with voltage so that, when the adiabatic limit is reached, the Fano factors take very low values. Positive noise crossed correlations at a given voltage are obtained only for fine-tuned quartet phases.

Possible extensions of this work could follow several directions including

- the investigations of lower voltages in the resonant dots regime which would require more efficient integration tools,
- the influence of interdot tunneling,
- the influence of the QD Coulomb on-site energy which would require a Hubbard-Stratonovich treatment (cf. Chapter 2),
- the investigation of finite frequency noise at multiples of the Josephson frequency,
- the investigation of higher order multipair production processes.

The measurements of noise crossed correlations in three-terminal all-superconducting devices could follow from the progress achieved in N-S-N CP splitters, as presented in Chapter 2. A recent study [122] has reported such measurements. They have investigated the correlations between the two lateral electrodes labeled L, R accross the quartet line: V_R is fixed while V_L is monitored around V_R. The crossed correlations present a peak which coincide with the peak of

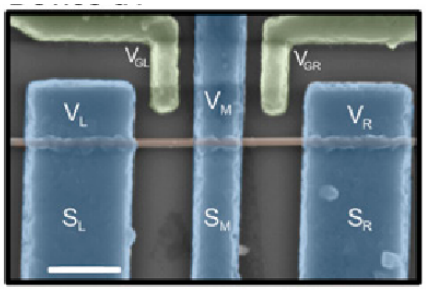

(a) SEM image of the three-terminal Josephson junction.

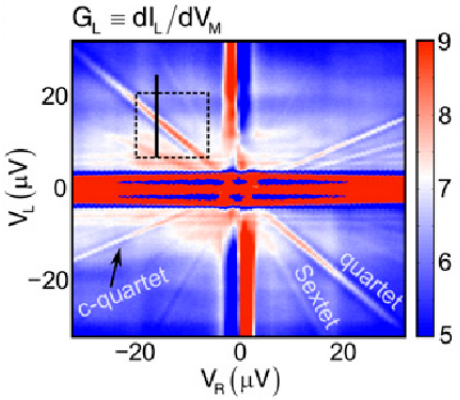

(b) Differential conductance displaying anomalies associated with MCPR.

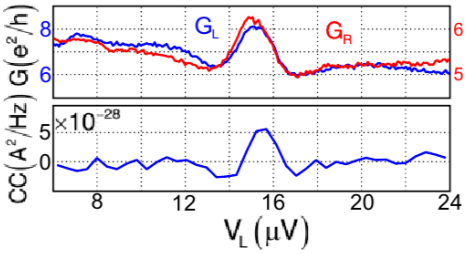

(c) Differential conductance (top) and cross correlations (bottom) along the line of (b).

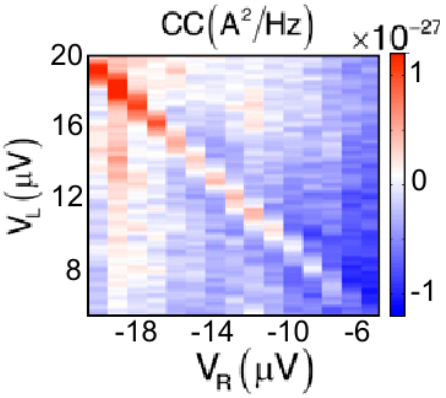

(d) Crossed correlations in the square of (b).

Figure 3.13: Measurements of crossed correlations in a three-terminal Josephson junction. Adapted from [122].

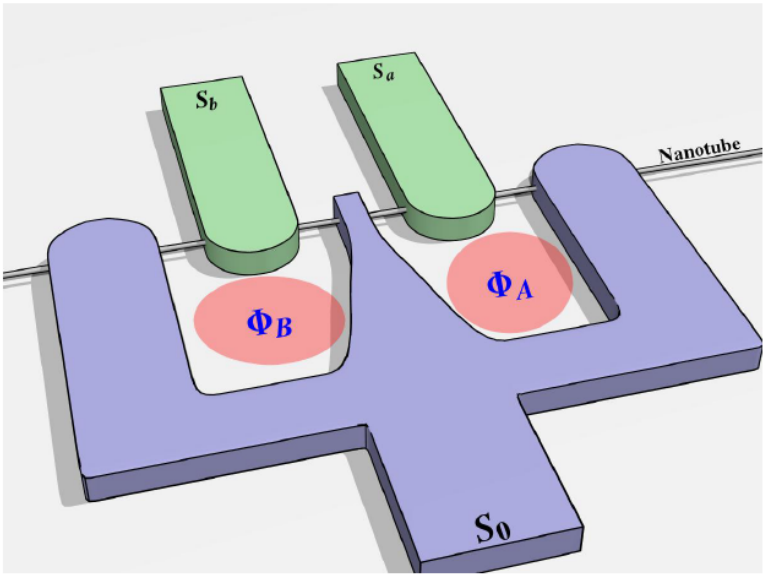

Figure 3.14: biSQUID proposal where a nanotube QD contact three different superconductors (S_0, S_a and S_b) such that two magnetic fluxes Φ_A and Φ_B can be enclosed. In such a device the measurement of the critical current as a function of these fluxes can probe nonlocal multipair production.

the differential conductance anomaly (Fig. 3.13). Measurements along the quartet line were also performed and present positive crossed correlations.

Remember that the SQUID-based CP splitter, studied in Chapter 2, was proposed as an equilibrium alternative to the (out-of-equilibrium) noise crossed correlation measurements required in earlier CP splitter proposals. In a very similar way, an equilibrium setup refered as biSQUID, and displayed in Fig. 3.14, has been proposed for nonlocal multipair production [103].

Chapter 4

Topological superconductors

In this chapter, we propose a brief introduction to Majorana quasiparticles in solid-state physics. The postulate for the existence of Majorana fermions originates in the context of high energy physics. The concept of an antiparticle emerged as an interpretation of negative energy solutions of the Dirac equation. Majorana proposed that some fermions could be indistinguishable from their antiparticle. While this possibility is actively pursued in some weak interaction mediated decays, the idea reappears in the context of condensed matter physics where collective excitations could exhibit the Majorana property (Section 4.1). Intuition can be gained by the study of the Kitaev toy model which describes spinless p-wave superconductivity in one-dimension (Section 4.2). Numerous are the proposals for practical realizations of topologically nontrivial phases hosting Majorana fermions which cleverly circumvent the problem of knowing whether the elusive p-wave superconductivity does exist or not in Nature. One-dimensional semiconducting wires on top of an s-wave supercondutor, the so-called Majorana wires, have received a lot of attention because strong Rashba spin-orbit coupling together with a Zeeman splitting for time-reversal symmetry breaking could be wisely used to create an isolated spin band inside which superconductivity can be proximity-induced (Section 4.3). The search for convincing signatures of Majorana zero-energy modes has been fueled by the promises of topologically protected fault-tolerant quantum computing schemes relying on the non-Abelian statistics that Majorana excitations exhibit in two-dimensional systems (Section 4.4). At the view of the growing interest rising in the condensed matter community about Majorana quasiparticles, some dedicated reviews have been published [123–128].

4.1 From particle physics to condensed matter physics

The Dirac equation is described with full details in standard particle physics textbooks, e.g. Ref [129]. One can also consult the early review [130] about relativistic field theories, including spin 1/2 Dirac theory and the Majorana viewpoint. The Dirac wave equation [131], which governs the dynamics of relativistic spin 1/2 particles, is the following first order partial differential equation

$$\{i\gamma^\mu\partial_\mu - m\}\,\Psi(\mathbf{r},t) = 0\ . \tag{4.1.1}$$

Dirac proposed this wave equation in 1928 in an attempt to conciliate quantum mechanics and special relativity, as an extension of Schrödinger equation [132]. The index μ covers time and space coordinates, $\mu = 0$ corresponding to time. The quantities γ^μ must verify the (Clifford algebra) defining relation $\gamma_\mu\gamma_\nu + \gamma_\nu\gamma_\mu = 2\eta_{\mu\nu}$ where $\eta_{\mu\nu}$ is the Minkowski metric so that a plane-wave state $\Psi(\mathbf{r},t) \propto \exp\left[i(\mathbf{p}.\mathbf{r} - Et)\right]$ solution of the Dirac equation provides the energy-momentum relation $E^2 = \mathbf{p}^2 + m^2$ as a result of squaring $\gamma^\mu p_\mu = m$ which gives the squared norm of the four-momentum $p_\mu = (E, \mathbf{p})$ (alternatively, squaring the differential operator $\gamma^\mu\partial_\mu$ yields the d'Alembert operator $\partial_\mu\partial^\mu$ and then a wavefunction $\Psi(\mathbf{r},t)$ which satisfies the Dirac equation also obeys the Klein Gordon equation). Hence the γ^μ must be matrices and one can show that representations are at least 4-dimensional. A spin 1/2 particle is then described by a wavefunction $\Psi(\mathbf{r},t)$ which is a bispinor (4-vector). Dirac proposed a set of gamma matrices which fulfills the requirement mentioned above and show that his wave equation is invariant under Lorentz tranformations. When solving this equation for stationary states and within his gamma matrix representation, negative energies emerged and were not ignored. These solutions were interpretated as antiparticles [133] and the discovery of the positron in 1932 was a considerable support for this theory. For a charged particle (with charge q), the coupling to an electromagnetic field (electromagnetic four-potential A_μ) is achieved *via* the so-called minimal coupling which consists in the substitution of the partial derivative ∂_μ by the covariant derivative $D_\mu = \partial_\mu - iqA_\mu$. If Ψ (describing a Dirac fermion f) satisfies the Dirac equation with charge q, its charge conjugate Ψ_C (describing the antiparticle $\bar{f}$) verifies the same equation with reversed charge $-q$ so that it can be related to the complex conjugate of Ψ through $\Psi_C = C\Psi^*$ where the matrix C is determined by solving $C\gamma_\mu^* C^{-1} = -\gamma_\mu$. Then to the stationary state $\Psi_E(\mathbf{r},t) = \mathrm{e}^{iEt}\Phi_E(\mathbf{r})$ at energy E corresponds another stationary state $C\Psi_E^*(\mathbf{r},t) = \mathrm{e}^{-iEt}C\Phi_E^*(\mathbf{r})$ at energy $-E$.

Majorana in his seminal last work [134] proposed a representation in terms of imaginary

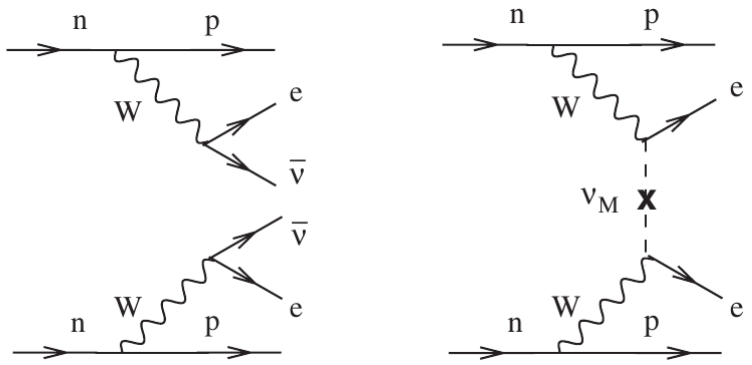

(a) $\beta\beta(2\nu)$ process. **(b)** $\beta\beta(0\nu)$ process.

Figure 4.1: Weak interaction mediated (W is the weak vector boson) double beta decay of two neutrons (n) into two protons (p) with emission of two electrons (e). The ordinary $\beta\beta(2\nu)$ process involves the emission of two antineutrinos ($\bar{\nu}$) and the neutrinoless $\beta\beta(0\nu)$ process can occur only if neutrinos are Majorana fermions. Extracted from [135].

gamma matrices, which allows for a real bispinor description

$$\Psi(\mathbf{r}, t) = \Psi^*(\mathbf{r}, t) \ . \tag{4.1.2}$$

This last equality is known as reality condition. Majorana provides a potential physical meaning for this purely formal mathematical operation, namely the existence of particles which are their own antiparticles, the so-called Majorana fermions. When expressed in other gamma matrix representation, this statement of identifying a field (describing the particle) with its charge conjugate (describing the antiparticle) results in the so-called pseudo-reality condition

$$\Psi(\mathbf{r}, t) = C\Psi^*(\mathbf{r}, t) \ . \tag{4.1.3}$$

An important point is that both conditions (4.1.2) and (4.1.3) involve the time-dependent field $\Psi^*(\mathbf{r}, t)$. Looking into energy domain, an energy eigenstate could not describe a Majorana fermion except at zero energy. Indeed, for $E \neq 0$, the charge conjugate $C\Phi_E \propto \Phi_{-E}$ is orthogonal to Φ_E.

The neutrinos which had been postulated to explain the continuous spectrum of beta decay were proposed as candidates and the double beta decay as a benchmark test since a neutrinoless disintegration could be envisioned if neutrinos are indeed Majorana fermions [136]. While the ordinary double beta decay with emission of two neutrinos $\beta\beta(2\nu)$ has been observed [137], the neutrinoless analogous $\beta\beta(0\nu)$ is yet to be detected and has motivated an international program

research [135]. The Feynman diagrams of these two processes are given in Fig. 4.1. If the neutrinoless decay is identified, it would not only contribute to the understanding of neutrino physics reinforcing the seesaw mechanism as an explanation for the lightness of neutrinos but also potentially give insight in possible mechanisms for the matter-antimatter asymmetry, since it would be the first example of a lepton number violating process. To a certain extent, it would also give some support for the supersymmetry theory which was proposed as an extension of the standard model and which postulates the existence of particles with Majorana properties.

A formal operation consists in writing a Dirac fermionic operator c as the linear combination of two Majorana fermionic operators γ_A and γ_B according to

$$c = \frac{\gamma_A + i\gamma_B}{2} \quad \text{and} \quad c^\dagger = \frac{\gamma_A - i\gamma_B}{2} \ , \tag{4.1.4}$$

so that inverting

$$\gamma_A = c + c^\dagger \quad \text{and} \quad \gamma_B = -i\left(c - c^\dagger\right) \ . \tag{4.1.5}$$

From the fermionic anticommutation relation satisfied by c ($\{c, c^\dagger\} = 1$), we deduce the relations for Majorana fermions

$$\{\gamma_X, \gamma_Y\} = 2\delta_{XY} \quad \text{for} \quad X, Y \in \{A, B\} \ . \tag{4.1.6}$$

In particular, $\gamma_X^2 = 1$. In a metal, electron and hole excitations created respectively with Dirac fermion operators $c_\sigma^\dagger$ and c_σ (σ is the spin projection) are distinct quasiparticles because they carry opposite charge. Superconductivity (cf. Chapter 1) could provide the fertile ground for the emergence of Majorana quasiparticles since Bogoliubov quasiparticles $\gamma_{k\sigma} = u_k c_{k\sigma} - \sigma v_k c_{-k-\sigma}^\dagger$ involve superpositions of electron and hole excitations owing to the intrinsic charge non-conserving BCS ground state. But, although one can expect adress zero momentum ($k = 0$) excitations with equal weight superpositions ($u_0 = v_0$), the spin issue prevents such quasiparticles to have Majorana properties. However, while BCS superconductivity describes s-wave spin singlet pairing, other pairing symmetries can be envisioned. Parallel spins can be paired if the two electrons form a triplet spin state. Note that the spatial wavefunction must then be antisymmetric and one talks about p-wave pairing [138, 139]. Freezing one of the two projections, the system is effectively spinless and one can expect midgap excitations with Majorana properties.

Actually, the Majorana nature of Bogoliubov quasiparticles is more general when looking into time domain (following original Majorana proposal) and it was realized first for p-wave superconductors [20, 140] then surprisingly, for standard s-wave superconductors [141]. The Bogoliubov - de Gennes (BdG) wave equation, which governs the dynamics of quasiparticle excitations, written as Nambu bispinors (the analogues of Dirac bispinors), presents a lot of

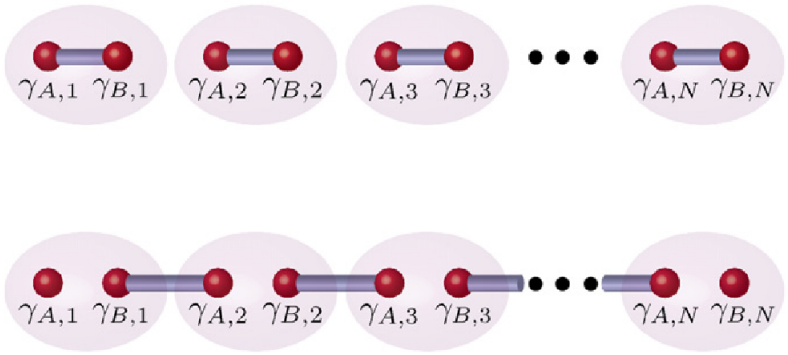

Figure 4.2: Different possible pairings of Majorana fermions which diagonalize Kitaev chain problem: the trivial phase contains the set of parameters such that the fermionic operators $c_j = \frac{\gamma_{A,j}+i\gamma_{B,j}}{2}$ (top: on-site Majorana operators are paired) diagonalize the problem while the topological phase contains the set of parameters such that the fermionic operators $\tilde{c}_j = \frac{\gamma_{B,j}+i\gamma_{A,j+1}}{2}$ (bottom: adjacent site Majorana operators are paired) diagonalize the problem. Remark that for the second set of parameters (in the topological phase), two Majorana fermions remain unpaired and do no enter the Hamiltonian meaning that it forms a highly nonlocal fermionic state $\tilde{c} = \frac{\gamma_{A,1}+i\gamma_{B,N}}{2}$ leading to a ground state degeneracy (corresponding to the different occupation numbers 0 or 1 of this state). Adapated from [123].

similarities with Dirac equation and by an unitary transformation the Hamiltonian can be put into a real form so that the total time-dependent field can be a Majorana fermion. Moreover, it can be tested in a very similar way to what is done in high energy physics, *i.e.* by collision and subsequent annihilation of a Majorana pair [142]. This interferometric proposal could benefit from the recent achievements in electronic quantum optics experiments [143, 144]. Nevertheless theoretical proposals for Majorana realizations have mainly focused on zero-energy (stationary) states.

A toy model was proposed by Kitaev to modelize a 1D p-wave superconductor [145]. It is a lattice model of spinless fermions with hopping amplitude and p-wave superconducting pairing between nearest neighbor sites. Depending on the parameters of the system, the formal expansion of the Dirac fermions into their Majorana components (4.1.4) can get some physical meaning and an alternative pairing of these Majorana fermions could lead to the emergence of unpaired Majorana end states which form an highly nonlocal fermion with zero-energy leading to a two-fold degenerate ground state, as illustrated in Fig 4.2 and further explained in Section 4.2. The

emergence of such unpaired Majorana fermions has a topological origin which will be discussed. Their presence is then robust as long as the topologically nontrivial phase is not escaped and one talks about topological protection. The phase transition is monitored by a single parameter which is the ratio of the chemical potential and the hopping amplitude.

The question of knowing whether materials can support p-wave pairing as a ground state is still under debate, the most serious candidate being Sr_2RuO_4 [146]. Another platform which could support Majorana quasiparticles is the 5/2 fractional quantum Hall state which has been related (through topological classes) to p-wave superconductivity [20] suggesting that non-Abelian statistics first proposed in the Moore-Read Pfaffian state [147] could be a robust property for Majorana quasiparticles bound to vortices in a 2D $p + ip$ superconductor [148]. The idea of fault-tolerant quantum computation originates in the discovery for the possibility of such exotic statistics [21, 149] which are briefly discussed in Section 4.4. Let us also mention the A phase of superfluid He^3 where zero modes supported by vortices were first calculated by Kopnin and Saloma [150] and which topological nature was elucidated by Volovik [151].

The proposal by Fu and Kane [22] constitutes a considerable breakthrough in the pursuit of Majorana emergent collective excitations in condensed matter as the idea was to mimick p-wave pairing by proximity-inducing conventional (s-wave) superconductivity on the helical edge states at the boundary of a 3D topological insulator [7]. It was understood that spin-orbit coupling is the key ingredient and alternative semiconductor-superconductor hybrid systems were proposed [153, 154] and a further simplification in the design results in the proposal of the so-called Majorana wires [23, 24]. In these 1D semiconducting wires with strong Rashba spin-orbit coupling, a Zeeman field is applied for time-reversal symmetry breaking and for the creation of an isolated spin band inside which superconductivity can be proximity-induced using a conventional s-wave superconductor. Such a proposal, further presented in Section 4.3, has received a lot of attention because of its feasibility since the materials and technics which are involved are commonly used in nanofabrication and because it allows for a control of the topological phase which can be conveniently monitored with the chemical potential set by gate voltages along the wire. Possibly remaining scepticism raised by the apparent triviality of 1D systems has been erased by a seminal work by Alicea [152] in which braiding of non-Abelian anyons has been proved to be achievable in an effective 2D network of Majorana wires as illustrated in Fig 4.3. Then such setups can be considered as solid candidates for future topological quantum computation schemes.

Other potential platforms for the emergence of Majorana quasiparticles that will not be fur-

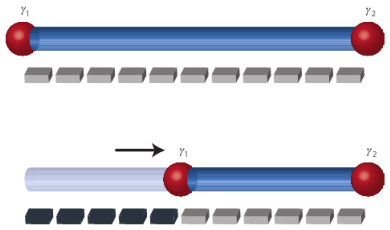

(a) A keyboard of gate voltages can be used to control the chemical potential along the wire and move a Majorana state which is bound to the interface of a topological (dark blue) and a trivial phase (light blue).

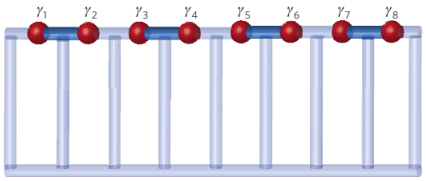

(c) The exchange of many Majorana fermions can be achieved in such a geometry. Indeed, any Majorana pair can be moved to the lower wire to be exchanged using a T-junction experiment.

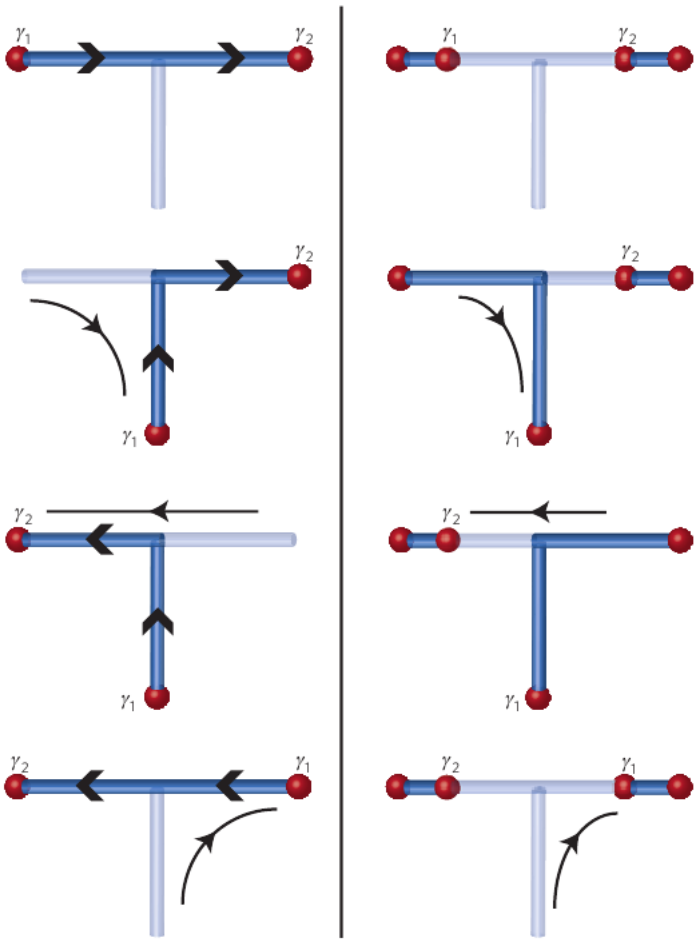

(b) In a T-junction, the exchange of Majorana fermions can be achieved. Two cases can be distinguished: end states of a topological phase (left) or a trivial phase (right) can be exchanged.

Figure 4.3: The braiding of Majorana fermions can be achieved using 1D p-wave superconducting wires. Adapted from [152].

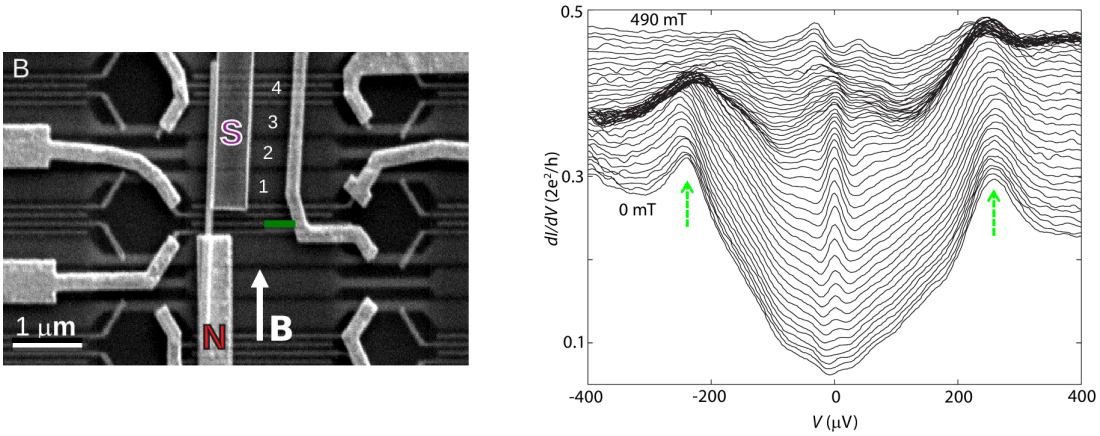

(a) SEM image of an InSb wire covered by normal and superconducting contacts. A Zeeman magnetic field is applied parallel to the wire.

(b) Differential conductance shows the developement of a zero-bias peak with increasing magnetic field. Green arrows show the proximity-induced gap.

Figure 4.4: One of the first experimental claim for a zero-bias conductance peak compatible with the presence of a Majorana fermion [155].

ther discussed in this thesis include the edge of a 2D topological insulator [156], 3D topological insulator nanowires [157], helical spin chains [158] and electrostatic line defects in a 2D semiconductor [159].

Several experiments have implemented Majorana wire proposals and have quite rapidly reported a zero-bias conductance peak [155, 160–163] compatible with the presence of Majorana zero-energy modes (see Fig. 4.4). Fractional 4π periodic Josephson current [22, 145, 156] has also been observed [164] but does not give decisive evidence for Majorana fermions neither. Potential non-topological origins for such signatures have to be ruled out. In particular, discriminating features in conductance measurements have motivated a lot of works. For example, recent theoretical predictions [165, 166] have followed the experimental study in Ref. [167] which has reported exponential suppression of energy splitting with wire length compatible with the hybridization of Majorana end states in a Coulomb blockaded nanowire. At the cutting edge of experimental progress in the search for Majorana fermions, a proper quantization of zero-bias conductance has recently been reported [168, 169]. Non-Abelian exchange statistics would be the ultimate compelling proof for the observation of Majorana fermions but before the implementation of T-junctions [152] for braiding experiments, quantum transport in systems supporting Majorana states can be investigated in the aim to propose other kinds of signature for the presence of Ma-

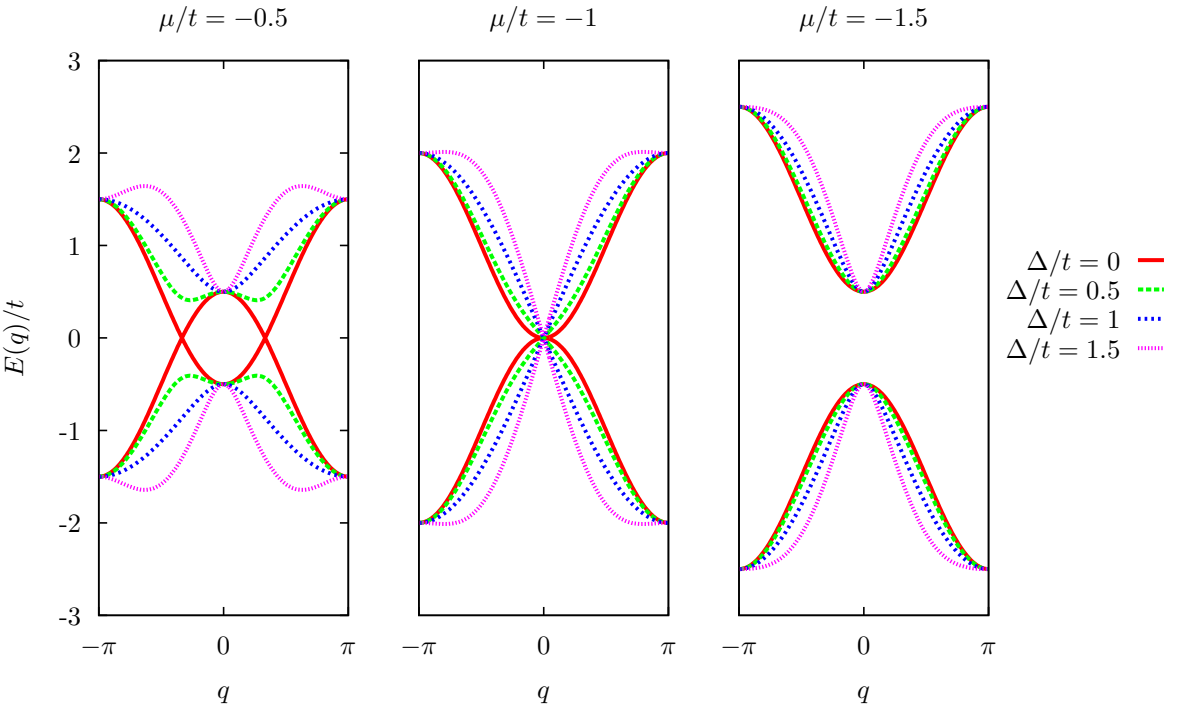

Figure 4.5: Spectrum in the Kitaev model. Depending on the ratio $|\mu|/t$, we have different bulk properties.

jorana fermions. The study of a junction between two p-wave superconductors in a topologically nontrivial phase (TS-TS junction) reported in Chapter 5 contributes to this program.

4.2 Kitaev modelization of p-wave superconductivity

Bulk properties are investigated in Section 4.2.1 and topologically different phases are identified in Section 4.2.2. We perform the formal expansion of Dirac fermions into Majorana fermions (cf. Eq (4.1.4)) in Section 4.2.3 and by focusing on two special sets of parameters lying on each side of the topological phase transition, we show that (topologically protected) bound states are supported in one of these phases. The emergence of Majorana zero-energy fermions is ascribed to the gap closure at a domain wall between two topologically distinct phases as argued in Section 4.2.4.

4.2.1 Bulk properties of the Kitaev model

To describe spinless fermions which can hop between nearest-neighbor sites of a 1D chain and which exhibit superconducting pairing, one can write the following toy model [145] in terms of position fermionic operators c_j ($c_j^\dagger$ creates a fermion on site j)

$$H = -\mu \sum_{j=1}^{N} c_j^\dagger c_j + \sum_{j=1}^{N-1} \left\{ -\frac{t}{2} \left(c_j^\dagger c_{j+1} + c_{j+1}^\dagger c_j \right) + \frac{1}{2} \left(\Delta\, c_j c_{j+1} + \Delta^* c_{j+1}^\dagger c_j^\dagger \right) \right\} , \tag{4.2.1}$$

where μ is the chemical potential, t is the (real) hopping amplitude and Δ is the (complex) superconducting gap. By coupling c_N with c_1 and imposing periodic boundary conditions $c_{N+1} = c_1$, one can change the chain into a loop and adress bulk properties

$$H_{\text{loop}} = \sum_{j=1}^{N} \left\{ -\mu\, c_j^\dagger c_j - \frac{t}{2} \left(c_j^\dagger c_{j+1} + c_{j+1}^\dagger c_j \right) + \frac{1}{2} \left(\Delta\, c_j c_{j+1} + \Delta^* c_{j+1}^\dagger c_j^\dagger \right) \right\} . \tag{4.2.2}$$

We introduce fermionic momentum space operators c_ν according to the discrete Fourier transform

$$c_j = \sum_{\nu=1}^{N} \frac{\mathrm{e}^{2i\pi \frac{\nu j}{N}}}{\sqrt{N}}\, c_\nu \ . \tag{4.2.3}$$

The Hamiltonian can be rewritten in momentum space as

$$H_{\text{loop}} = \sum_{\nu=1}^{N} \varepsilon \left(\frac{2\pi\nu}{N} \right) c_\nu^\dagger c_\nu - \sum_{\nu=1}^{N-1} \left\{ \frac{\tilde{\Delta} \left(\frac{2\pi\nu}{N} \right)}{2}\, c_\nu c_{N-\nu} + \frac{\tilde{\Delta}^* \left(\frac{2\pi\nu}{N} \right)}{2}\, c_{N-\nu}^\dagger c_\nu^\dagger \right\} , \tag{4.2.4}$$

where $\varepsilon(q) = -t\cos q - \mu$ and $\tilde{\Delta}(q) = i\Delta \sin q$. If a denotes the lattice spacing, we can have an expression in terms of momenta k in the Brillouin zone $BZ = [-\pi/a, \pi/a]$

$$H_{\text{loop}} = \sum_{k \in BZ} \left\{ \varepsilon\,(ka)\; c_k^\dagger c_k - \frac{\tilde{\Delta}\,(ka)}{2}\, c_k c_{-k} - \frac{\tilde{\Delta}^*\,(ka)}{2}\, c_{-k}^\dagger c_k^\dagger \right\} . \tag{4.2.5}$$

The pairing at $k = 0$ (or $\nu = N$) is forbidden (Pauli exclusion principle) because of the odd form of the pairing $\tilde{\Delta}$. It can be easily rewritten as (constant terms originated from anticommutation relations can be ignored)

$$H_{\text{loop}} = \frac{1}{2} \sum_{k \in BZ} \mathcal{C}_k^\dagger\, \mathcal{H}(ka)\, \mathcal{C}_k \quad \text{where} \quad \mathcal{C}_k = \begin{pmatrix} c_k \\ c_{-k}^\dagger \end{pmatrix} \quad \text{and} \quad \mathcal{H} = \begin{pmatrix} \varepsilon & \tilde{\Delta}^* \\ \tilde{\Delta} & -\varepsilon \end{pmatrix} . \tag{4.2.6}$$

We can decompose the $\mathcal{H}$ matrix thanks to Pauli matrices $\vec{\sigma} = (\sigma_x, \sigma_y, \sigma_z)^T$ according to

$$\mathcal{H} = \mathbf{h}.\vec{\sigma} \quad \text{where} \quad \begin{cases} h_x = \mathcal{R}(\tilde{\Delta})\,, \\ h_y = \mathcal{I}(\tilde{\Delta})\,, \\ h_z = \varepsilon\,. \end{cases} \tag{4.2.7}$$

This matrix can be easily diagonalized. Its eigenvalues are given by

$$E_{\pm}(q) = \pm E(q) \quad \text{with} \quad E(q) = \|\mathbf{h}(q)\| = \sqrt{\varepsilon^2(q) + |\tilde{\Delta}(q)|^2} = \sqrt{(\mu + t\cos q)^2 + (|\Delta|\sin q)^2} \ . \tag{4.2.8}$$

It is displayed in Fig 4.5. Depending on the value of $|\mu|/t$ (the sign of μ does not matter since $E_{\pm}(q)|_{\mu\to-\mu} = E_{\pm}(\pi - q)$), we have different bulk properties: for $|\mu|/t > 1$, we have no gapless points, for $|\mu|/t < 1$, gapless points for $\Delta = 0$ are opened as soon as $\Delta \neq 0$. A fine tuning to $|\mu|/t = 1$ leads to gapless points (for $ka = 0$ or π) whatever the value of Δ. We will consider two limiting cases to further investigate these different bulk properties:

- case 1: $|\mu|/t = +\infty$ with $\mu < 0$, $t = 0$ and $|\Delta| \ll |\mu|$,
- case 2: $|\mu|/t = 0$ with $\mu = 0$, $t = |\Delta| \neq 0$.

We introduce the angle θ defined as

$$\sin[\theta(q)] = \frac{|\Delta|\sin q}{E(q)} \quad \text{and} \quad \cos[\theta(q)] = \frac{\varepsilon(q)}{E(q)} \ . \tag{4.2.9}$$

We denote φ the phase of the superconducting gap, *i.e*

$$\Delta = |\Delta| e^{i\varphi} \quad \text{and} \quad \psi = \frac{\pi}{2} + \varphi \ . \tag{4.2.10}$$

Then introducing the coefficients

$$u(q) = e^{i\frac{\psi}{2}} \cos\frac{\theta(q)}{2} \ , \tag{4.2.11}$$

$$v(q) = -e^{-i\frac{\psi}{2}} \sin\frac{\theta(q)}{2} \ , \tag{4.2.12}$$

we can easily diagonalize the problem thanks to the definition of the following fermionic operators through the Bogoliubov - Valatin transformation (cf Chapter 1)

$$a_k = u(ka)\, c_k - v(ka)\, c_{-k}^{\dagger} \ . \tag{4.2.13}$$

Indeed, the diagonalization reads

$$\mathcal{H} = P \begin{pmatrix} E & 0 \\ 0 & -E \end{pmatrix} P^{\dagger} \quad \text{with} \quad P = \begin{pmatrix} u^* & v \\ -v^* & u \end{pmatrix} \ . \tag{4.2.14}$$

Then we have

$$P^{\dagger}(ka)\, \mathcal{C}_k = \begin{pmatrix} a_k \\ \sigma(ka)\, a_{-k}^{\dagger} \end{pmatrix} \quad \text{where} \quad \sigma(q) = \text{sign}\left[\cos\frac{\theta(q)}{2}\cos\frac{\theta(-q)}{2}\right] \tag{4.2.15}$$

so that

$$H_{\text{loop}} = \sum_{k\in BZ} E(ka)\, a_k^\dagger a_k \ , \tag{4.2.16}$$

where $E(q)$ is given in Eq. (4.2.8). The following (BCS-like) wavefunction (cf Chapter 1)

$$|\text{g.s.}\rangle \propto \exp\left[\sum_{0<k<\frac{\pi}{a}} g(ka)\, c_k^\dagger c_{-k}^\dagger\right]|0\rangle \quad \text{with} \quad g(q) = \frac{v(q)}{u(q)} = \mathrm{e}^{-i\Psi}\,\tan\frac{\theta(q)}{2} = \frac{E(q)-\varepsilon(q)}{\tilde{\Delta}(q)} \tag{4.2.17}$$

satisfies $a_k\,|\text{g.s.}\rangle = 0$. Normalizing it (adapt the calculation in Appendix B of [25]), we find the ground state

$$|\text{g.s.}\rangle = \prod_{0<k<\frac{\pi}{a}} \left[u(ka) + v(ka)\, c_k^\dagger c_{-k}^\dagger\right]|0\rangle \ . \tag{4.2.18}$$

We can rewrite the argument of the exponential (4.2.17) in terms of position operators as follows

$$\sum_{0<k<\frac{\pi}{a}} g(ka)\, c_k^\dagger c_{-k}^\dagger = \frac{1}{2}\sum_{\nu=1}^{N-1} g\left(\frac{2\pi\nu}{N}\right) c_\nu^\dagger c_{N-\nu}^\dagger = \frac{1}{2}\sum_{j,j'=1}^{N-1} \gamma_{jj'}\, c_j^\dagger c_{j'}^\dagger \ , \tag{4.2.19}$$

where we introduce the Fourier transform of the g function according to

$$\gamma_{jj'} = \frac{1}{N}\sum_{\nu=1}^{N-1} g\left(\frac{2\pi\nu}{N}\right)\mathrm{e}^{2i\pi\frac{j-j'}{N}\nu} = -\gamma_{j'j} \ . \tag{4.2.20}$$

We compute this quantity in the two cases.

- <u>case 1:</u> we have $\theta(q) = 0$ and we get (at first order in $|\Delta/\mu|$) a nearest-neighbor pairing term

$$\mathrm{e}^{i\varphi}\gamma_{jj'} = \frac{1}{4}\left|\frac{\Delta}{\mu}\right|(\delta_{j,j'-1} - \delta_{j,j'+1}) \ . \tag{4.2.21}$$

- <u>case 2:</u> we have $\theta(q) = \pi - q$ and if we define

$$\eta_\nu = \mathrm{e}^{\frac{2i\pi\nu}{N}} \quad \text{and} \quad S_N(m) = \sum_{\nu=1}^{N-1}\frac{\eta_\nu^m}{\eta_\nu - 1} = \frac{N+1}{2} - m \quad \text{for} \quad 1 \leqslant m \leqslant N \ , \tag{4.2.22}$$

  we get a long range pairing term [170]

$$\mathrm{e}^{i\varphi}\gamma_{jj'} = -\frac{S_N(j-j') + S_N(j-j'+1)}{N} = -\left(1 - 2\,\frac{j-j'}{N}\right) \quad \text{for} \quad j > j' \ . \tag{4.2.23}$$

It constitutes a hint (but not a decisive evidence) that $|\mu|/t > 1$ and $|\mu|/t < 1$ would correspond to different phases.

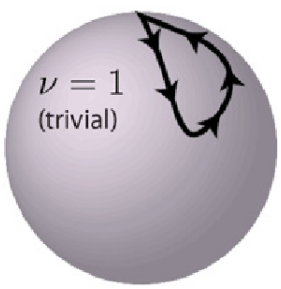

(a) Trivial phase: $\mathbf{h}(0) = \mathbf{h}(\pi)$ is on the same pole of the Bloch sphere and a close loop is drawn in the half Brillouin zone.

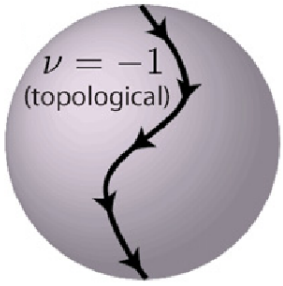

(b) Topological phase: $\mathbf{h}(0) = -\mathbf{h}(\pi)$ and the path in the half Brillouin zone joins the two poles of the Bloch sphere.

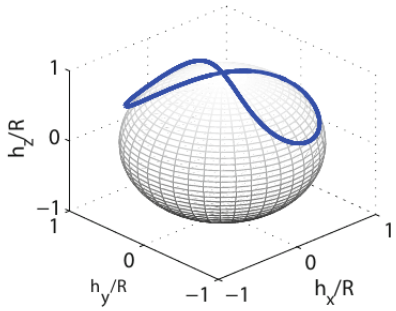

(c) Trivial phase: the two close loops (drawn in the two half Brillouin zones) subtend opposite fluxes resulting in a trivial Berry phase: $\gamma_- = 0$.

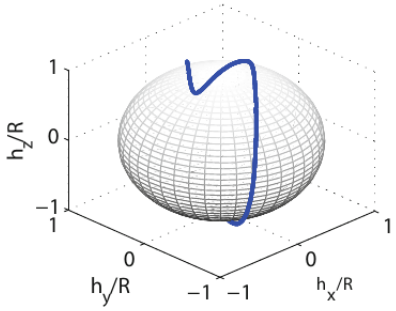

(d) Topological phase: in the second half of the Brillouin zone, the path is closed and the resulting flux is half the total solid angle so that the Berry phase is $\gamma_- = \pi$.

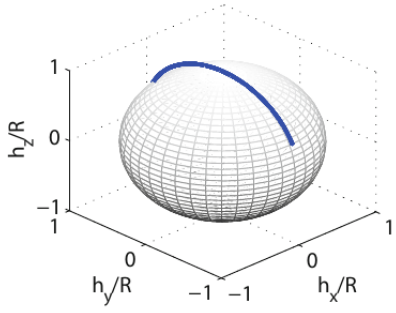

(e) Particular case of Kitaev Hamiltonian in the trivial phase. The curve follows a portion along a great circle.

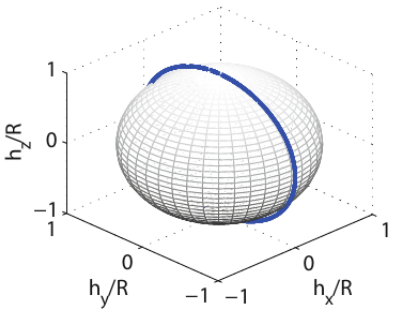

(f) Particular case of Kitaev Hamiltonian in the topological phase. The curve follows entirely a great circle.

Figure 4.6: Adapted from [123] for subfigures (a)-(b) and [171] for subfigures (c)-(e) ($R = \|\mathbf{h}\|$).

4.2.2 Topological phase transition

When k goes from $-\pi/a$ to π/a, the unit vector $\hat{\mathbf{h}}(ka) = \mathbf{h}(ka)/\|\mathbf{h}(ka)\|$ rotates on the Bloch sphere along a closed loop. This vector is parametrized thanks to spherical coordinates as

$$\hat{\mathbf{h}} = \begin{pmatrix} \sin\theta_1 \cos\Psi_1 \\ \sin\theta_1 \sin\Psi_1 \\ \cos\theta_1 \end{pmatrix} \quad \text{with} \quad \theta_1 \in [0,\pi] \ , \quad \Psi_1 \in [0,2\pi] \ . \tag{4.2.24}$$

In the Kitaev model case (cf Eqs. (4.2.7), (4.2.9) and (4.2.10)), θ_1 is defined as $\cos\theta_1 = \cos\theta$ and $\sin\theta_1 = |\sin\theta|$, and $\Psi_1(q) = \Psi$ if $q \geqslant 0$ or $\Psi_1(q) = \Psi \pm \pi$ otherwise. The path is then included on a great circle: we can indeed reduce the problem to 2 dimensions thanks to a rotation about the z-axis

$$\mathrm{e}^{i\frac{\Psi_1}{2}\sigma_z}[\mathbf{h}_{\text{Kitaev}}.\vec{\sigma}]\mathrm{e}^{-i\frac{\Psi_1}{2}\sigma_z} = \varepsilon\sigma_z + |\tilde{\Delta}|\sigma_x \ . \tag{4.2.25}$$

More generally, if we consider the class of Hamiltonians that can be written as

$$H_{\text{BdG}} = \frac{1}{2}\sum_{k\in BZ} \mathcal{C}_k^\dagger \left[\mathbf{h}(ka).\vec{\sigma}\right] \mathcal{C}_k \ , \tag{4.2.26}$$

we could have more complex paths on the Bloch sphere. But if we require particle-hole symmetry (as in the Kitaev model case) that is

$$\sigma_x \left[\mathcal{C}_k^\dagger\right]^T = \mathcal{C}_{-k} \quad \Rightarrow \quad \sigma_x\, h^T(ka)\, \sigma_x = -h(-ka) \ , \tag{4.2.27}$$

then we have the symmetries

$$\begin{cases} h_x(q) = -h_x(-q) \ , \\ h_y(q) = -h_y(-q) \ , \\ h_z(q) = h_z(-q) \ . \end{cases} \tag{4.2.28}$$

Because of that, the vectors $\hat{\mathbf{h}}(0)$ and $\hat{\mathbf{h}}(\pm\pi)$ are along the z-axis, and the path followed on one half part of the Brillouin zone can be deduced from the other half part. We can calculate the Berry phase [172]

$$\gamma_- = i\int_{-\frac{\pi}{a}}^{\frac{\pi}{a}} \mathrm{d}k \ \langle -,\mathbf{h}(ka)| \frac{\mathrm{d}}{\mathrm{d}k} |-,\mathbf{h}(ka)\rangle = \oint_{\mathcal{C}} \mathbf{A}_-(\mathbf{h}).\mathrm{d}\mathbf{h} = \int_S \mathbf{B}_-(\mathbf{h}).\mathrm{d}\mathbf{S} \tag{4.2.29}$$

where the Berry connexion $\mathbf{A}_-(\mathbf{h}) = i\langle -,\mathbf{h}|\nabla_{\mathbf{h}}|-,\mathbf{h}\rangle$ is integrated along the closed $\mathcal{C}$ path followed by the vector $\mathbf{h}$ (on the sphere of radius $|\mathbf{h}|$) and where the Berry curvature $\mathbf{B}_-(\mathbf{h}) = \nabla_{\mathbf{h}} \times \mathbf{A}_-(\mathbf{h})$ is integrated on a surface S which boundary is $\mathcal{C}$. Using the result

$$\mathbf{B}_-(\mathbf{h}) = -\frac{\mathcal{I}\left[\langle -,\mathbf{h}|\,\vec{\sigma}\,|+,\mathbf{h}\rangle \times \langle +,\mathbf{h}|\,\vec{\sigma}\,|-,\mathbf{h}\rangle\right]}{4|\mathbf{h}|^2} = \frac{\mathbf{h}}{2|\mathbf{h}|^3} \ , \tag{4.2.30}$$

we conclude that the Berry phase is simply half the solid angle subtented by the curve $\mathcal{C}$. Then depending on the respective positions of $\mathbf{h}(0)$ and $\mathbf{h}(\pi)$, we have 0 or π Berry phase. To distinguish between the two cases ($\mathbf{h}(0)$ and $\mathbf{h}(\pi)$ on the same pole, or $\mathbf{h}(0)$ and $\mathbf{h}(\pi)$ on different poles) the Majorana number (or $\mathbb{Z}_2$ topological invariant) first formulated by Kitaev [145] can be used and, for the class of Hamiltonians studied here, it reduces to [173]

$$\nu = \text{sign}\left[h_z(0)\right]\text{sign}\left[h_z(\pi)\right] \tag{4.2.31}$$

and we have

$$\nu = 1 \quad \Leftrightarrow \quad \gamma_- = 0 \ , \tag{4.2.32}$$

$$\nu = -1 \quad \Leftrightarrow \quad \gamma_- = \pi \ . \tag{4.2.33}$$

The two topologically distinct phases are illustrated in Fig. 4.6. A phase transition can occur only if the gap closes meaning $\mathbf{h}(\mathbf{k}) = 0$. In the Kitaev model case, $\nu = \text{sign}\left[\mu^2 - t^2\right]$ as foreseen, and the trivial phase obtained for $|\mu| > t$ is connected to vacuum $\mu \to -\infty$.

4.2.3 Majorana mode expansion in the Kitaev model

Let us investigate the consequences of the boundaries meaning let us go back to the finite size chain Hamiltonian (4.2.1). We introduce the following Majorana operators

$$\gamma_{A,j} = \mathrm{e}^{i\frac{\varphi}{2}} c_j + \mathrm{e}^{-i\frac{\varphi}{2}} c_j^\dagger = \gamma_{A,j}^\dagger \ , \tag{4.2.34}$$

$$\gamma_{B,j} = -i\mathrm{e}^{i\frac{\varphi}{2}} c_j + i\mathrm{e}^{-i\frac{\varphi}{2}} c_j^\dagger = \gamma_{B,j}^\dagger \ . \tag{4.2.35}$$

They can be viewed as half fermions in the sense that

$$c_j = \frac{\mathrm{e}^{-i\frac{\varphi}{2}}}{2}\left(\gamma_{A,j} + i\gamma_{B,j}\right) \ . \tag{4.2.36}$$

They obey Majorana fermion commutation relations

$$\{\gamma_{\alpha,j}, \gamma_{\alpha',j'}\} = 2\delta_{\alpha\alpha'}\delta_{jj'} \ . \tag{4.2.37}$$

The Hamiltonian (4.2.1) can then be written as

$$H = -i\,\frac{\mu}{2}\sum_{j=1}^{N}\gamma_{A,j}\gamma_{B,j} + \frac{i}{4}\sum_{j=1}^{N-1}\Big\{\left(|\Delta| + t\right)\gamma_{B,j}\gamma_{A,j+1} + \left(|\Delta| - t\right)\gamma_{A,j}\gamma_{B,j+1}\Big\} \ . \tag{4.2.38}$$

This can be easily diagonalized in the two cases defined in Section 4.2.1.

- case 1: we have interaction between the Majorana fermions of the same site (short-range pairing)

$$H = -\mu \sum_{j=1}^{N} c_j^\dagger c_j = -i \frac{\mu}{2} \sum_{j=1}^{N} \gamma_{A,j} \gamma_{B,j} \ . \tag{4.2.39}$$

- case 2: the interactions occur between Majorana fermions of different sites (long-range pairing)

$$H = i \frac{t}{2} \sum_{j=1}^{N-1} \gamma_{B,j} \gamma_{A,j+1} = t \sum_{j=1}^{N-1} \tilde{c}_j^\dagger \tilde{c}_j \ , \tag{4.2.40}$$

  where we define the fermionic operators

$$\tilde{c}_j = \frac{\gamma_{B,j} + i\gamma_{A,j+1}}{2} \tag{4.2.41}$$

  which are built with Majorana fermions localized on adjacent sites.

These different pairings are illustrated in Fig. 4.2. Despite the similarity of (4.2.39) and (4.2.40), the fact that the Majorana end states $\gamma_{A,1}$ and $\gamma_{B,N}$ do not enter explicitely the expression of the Hamiltonian (4.2.40) leads to a two-fold degeneracy of the ground state. Indeed, let us define the fermion

$$f = \frac{1}{2}(\gamma_{A,1} + i\gamma_{B,N}) \tag{4.2.42}$$

which can be populated without any energy cost. $|0\rangle$ and $|1\rangle = f^\dagger |0\rangle$ form degenerate ground states. Moreover from the highly non-local nature of the fermion f, one can expect a protection of this occupancy against decoherence.

The emergence of Majorana fermions is by no means a singular feature of this particular set of parameters, meaning that it does not require a fine tuning. Indeed one can see these boundary states as a consequence of a domain wall between the chain (in a topological phase) and vacuum (in a trivial phase) where the gap closes and reopens. This argument is developped in the next section.

4.2.4 Topological protection of Majorana end states

In the following, $\mu < 0$. Let us develop a low energy continuum theory of the Kitaev model analogous to what was done by Jackiw and Rebbi for the SSH model [174,175] and focus around the gap closure point $\mu = -t$. The Hamiltonian (4.2.25) at first order in ka reads

$$\mathcal{H}(ka) = m\,\sigma_z + v_F k\,\sigma_x \tag{4.2.43}$$

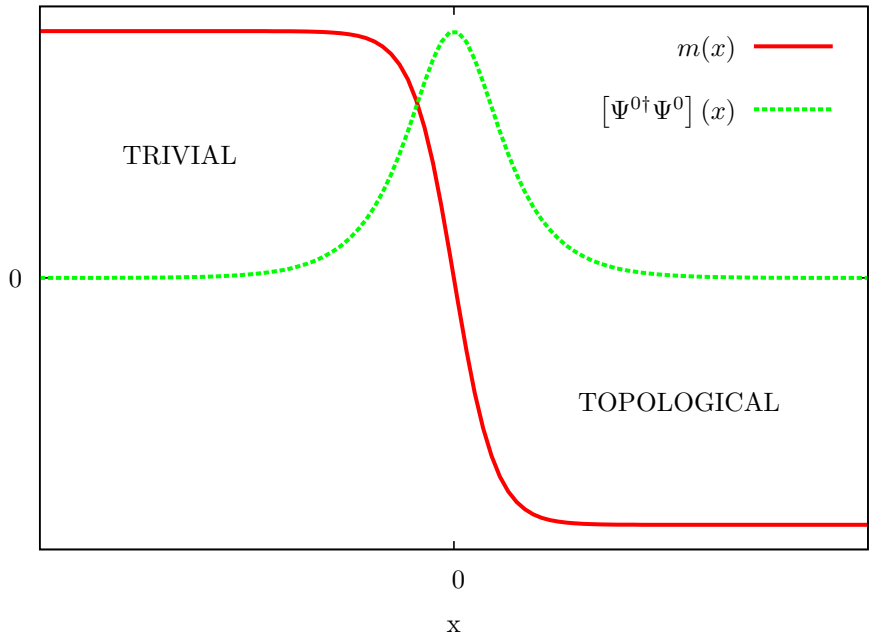

Figure 4.7: Domain wall materialized by a sign change of the Dirac mass $m(x)$ and Majorana state Ψ^0 associated.

with $m = -t - \mu$ and $v_F = |\Delta|a$. In real space, the low energy problem is described by the Dirac Hamiltonian

$$\mathcal{H}_{\text{low energy}}\left(\partial_x\right) = m\,\sigma_z - iv_F\,\partial_x\,\sigma_x\ . \tag{4.2.44}$$

Let us consider a domain wall between two topologically distinct regions, *i.e.* a change in the sign of the Dirac mass m as a function of x, separating a trivial region with $m > 0 \Leftrightarrow -\mu/t > 1$ and a topological region with $m < 0 \Leftrightarrow -\mu/t < 1$, and let us search for a zero-energy solution $\Psi^0(x)$ which is written in the basis of zero momentum operators $(c, c^\dagger)$ where $c \equiv c_{k=0}$ and which verifies

$$\left\{v_F\,\partial_x + m(x)\,\sigma_y\right\}\Psi^0(x) = 0\ . \tag{4.2.45}$$

We introduce the eigenvectors of the σ_y Pauli matrix

$$|y\pm\rangle = \mathrm{e}^{\mp i\frac{\pi}{4}}\begin{pmatrix}1\\ \pm i\end{pmatrix}\quad,\quad \sigma_y\,|y\pm\rangle = \pm\,|y\pm\rangle\ . \tag{4.2.46}$$

Expressed in the basis $(c, c^\dagger)$ they define majorana operators

$$\Psi_{y,\pm} = \mathrm{e}^{\mp i\frac{\pi}{4}}\left(c \pm ic^\dagger\right) = \Psi^\dagger_{y,\pm}\ . \tag{4.2.47}$$

Let us suppose that the topologically non-trivial phase lies on the right: the Dirac mass is positive for $x < 0$, vanishes for $x = 0$ and is negative for $x > 0$. We can easily write a zero energy solution as

$$\Psi^0_{\text{trivial}\to\text{topo}}(x) \propto \exp\left[\frac{1}{v_F}\int_0^x \mathrm{d}x'\, m(x')\right]\Psi_{y,-} \ . \tag{4.2.48}$$

The antikink in the mass m obtained by inverting the two phases will require the other Majorana operator

$$\Psi^0_{\text{topo}\to\text{trivial}}(x) \propto \exp\left[-\frac{1}{v_F}\int_0^x \mathrm{d}x'\, m(x')\right]\Psi_{y,+} \ . \tag{4.2.49}$$

If we take the simple example ($m_0 > 0$ for the kink trivial $\to$ topo and $m_0 < 0$ for the antikink topo $\to$ trivial)

$$m(x) = -m_0 \tanh\frac{x}{\xi} \quad \text{with} \quad \xi > 0 \ , \tag{4.2.50}$$

we find

$$\left[\Psi^{0\dagger}\Psi^0\right](x) \propto \frac{1}{\left[\cosh\frac{x}{\xi}\right]^{\frac{2|m_0|\xi}{v_F}}} \ . \tag{4.2.51}$$

This is illustrated in Fig. 4.7. This emergence of a Majorana zero mode at the gap closure point is quite general and one talks about topological protection.

4.3 Practical realization of p-wave superconductivity

Inspired by the seminal work by Fu and Kane [22], a lot of condensed matter platforms for the engineering of p-wave superconductivity were proposed. Among them, those based on 1D semiconducting wires [23, 24] are the most promising (emphasizing the relevance of the Kitaev model). Here we show that the gap in the energy spectrum can be closed as a consequence of the competition of Rashba spin-orbit interaction (with strength α) and Zeeman splitting (V_x). These are indeed the key ingredients that enter the Hamiltonian

$$H_0 = \int \mathrm{d}x\, \Psi^\dagger(x)\left\{-\frac{\partial_x^2}{2m} - \mu + i\alpha\partial_x\sigma_y + V_x\sigma_x\right\}\Psi(x) \ . \tag{4.3.1}$$

In momentum space $\Psi(x) = \sum_k \frac{\mathrm{e}^{-ikx}}{\sqrt{L}}\Psi(k)$, it becomes

$$H_0 = \sum_k \Psi^\dagger(k)\left\{\xi(k) + \alpha k\sigma_y + V_x\sigma_x\right\}\Psi(k) \quad \text{with} \quad \xi(k) = \frac{k^2}{2m} - \mu \ . \tag{4.3.2}$$

The eigenvalues are given by

$$\varepsilon_\pm(k) = \xi(k) \pm \sqrt{V_x^2 + \alpha^2 k^2} \tag{4.3.3}$$

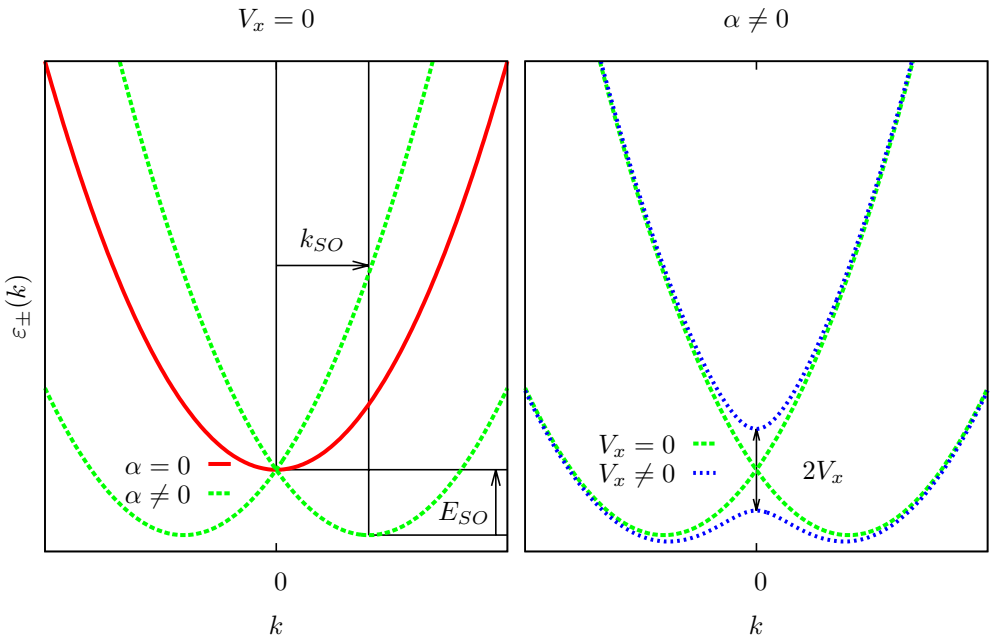

Figure 4.8: Spectrum of a semiconducting wire with Rashba spin-orbit (α) and in presence of a Zeeman field (V_x).

and the eigenvectors by

$$\Psi_\pm(k) = \frac{\mathrm{e}^{i\frac{\theta(k)}{2}}\Psi_\uparrow(k) \pm \mathrm{e}^{-i\frac{\theta(k)}{2}}\Psi_\downarrow(k)}{\sqrt{2}} \quad \text{where} \quad \mathrm{e}^{i\theta(k)} = \frac{V_x - i\alpha k}{\sqrt{V_x^2 + \alpha^2 k^2}} \,. \tag{4.3.4}$$

The spectrum is given in Fig. 4.8. Considering $V_x = 0$, the spin-orbit interaction is responsible for a splitting of the spin bands as two parabolas centered at $\pm k_{SO} = \pm m\alpha$ and a decreasing of the minimal energy by $E_{SO} = m\alpha^2/2$. Then turning on the Zeeman coupling, a gap is opened at $k = 0$. Interestingly, inside this gap a single Fermi point is available and this is crucial for the generation of spinless superconductivity. The proximity-induced superconductivity pairing reads

$$H_\Delta = \Delta \int \mathrm{d}x\, \Psi_\uparrow^\dagger(x)\Psi_\downarrow^\dagger(x) + \text{h.c.} = \Delta \sum_k \Psi_\uparrow^\dagger(k)\Psi_\downarrow^\dagger(-k) + \text{h.c.} \tag{4.3.5}$$

and it is instructive to write it in the basis of vectors $\Psi_{k\pm}$ according to

$$H_\Delta = \Delta \sum_k \left\{ \cos\left[\theta(k)\right] \Psi_-^\dagger(k)\Psi_+^\dagger(-k) + \sin\left[\theta(k)\right] \left(\Psi_+^\dagger(k)\Psi_+^\dagger(-k) - \Psi_-^\dagger(k)\Psi_-^\dagger(-k) \right) + \text{h.c.} \right\} \,. \tag{4.3.6}$$

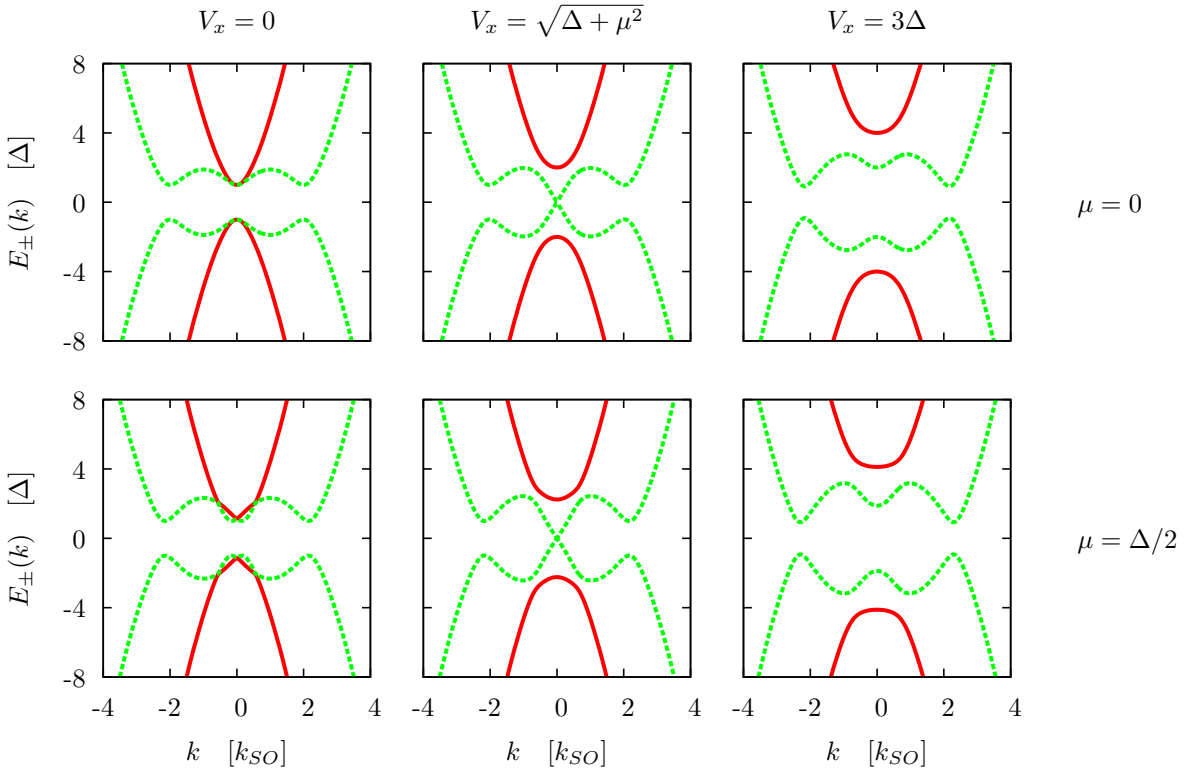

Figure 4.9: Spectrum of a semiconducting wire with Rashba spin-orbit (α), in presence of a Zeeman field (V_x) and where superconductivity (Δ) is induced by proximity effect. The gap closes for $V_x = \sqrt{\Delta^2 + \mu^2}$.

We denote interband and intraband pairing as $\Delta_s(k) = \Delta \cos[\theta(k)]$ and $\Delta_p(k) = \Delta \sin[\theta(k)]$ respectively. We consider the Nambu spinors

$$C(k) = \begin{pmatrix} \Psi_+(k) \\ \Psi_-^\dagger(-k) \end{pmatrix} \tag{4.3.7}$$

and the associated constrained bispinors

$$\mathcal{C}(k) = \begin{pmatrix} C(k) \\ [i\sigma_y C(-k)]^* \end{pmatrix} . \tag{4.3.8}$$

One can rewrite the total Hamiltonian in BdG form

$$H = H_0 + H_\Delta = \frac{1}{2} \sum_k \mathcal{C}(k)^\dagger \mathcal{H}(k) \mathcal{C}(k) \tag{4.3.9}$$

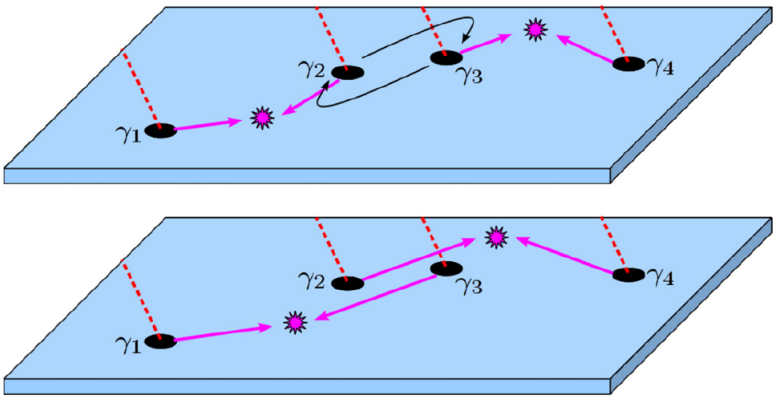

Figure 4.10: The exchange of two Majorana fermions results if the change of sign for one of them. Remark that the reading of the exchange supposes a measurement by fusion with other Majorana fermions. Exchanging the vortices then measuring (up) is equivalent to directly performing the proper measurements (bottom). Adapted from [124].

where

$$\mathcal{H} = \begin{pmatrix} \varepsilon_+ & \Delta_s & 0 & -\Delta_p \\ \Delta_s & -\varepsilon_- & \Delta_p & 0 \\ 0 & -\Delta_p & \varepsilon_- & \Delta_s \\ \Delta_p & 0 & \Delta_s & -\varepsilon_+ \end{pmatrix} \tag{4.3.10}$$

which yields the following BdG spectrum

$$E_\pm^2(k) = \xi^2(k) + V_x^2 + \alpha^2 k^2 + \Delta^2 \pm 2\sqrt{V_x^2\Delta^2 + \xi^2(k)(V_x^2 + \alpha^2 k^2)} \ . \tag{4.3.11}$$

This is displayed in Fig. 4.9. The gap closes for a Zeeman splitting verifying $V_x = \sqrt{\Delta^2 + \mu^2}$. For large V_x, a connection with a low-energy limit of Kitaev model can be made [152] so that the topological phase lies above

$$V_x > \sqrt{\Delta^2 + \alpha^2} \ . \tag{4.3.12}$$

Majorana zero-energy modes are expected to be bound to the ends of a topological region in such a 1D wire. The early claims for signatures compatible with the presence of Majorana quasiparticles have already been discussed in Section 4.1.

4.4 Non-Abelian statistics

The exchange of Majorana fermions bound to topological defects in a 2D system results in non-Abelian statistics [20,148] so that Majorana qubits can be used as a fault-tolerant building block for a universal quantum computer [21,149]. The nonlocal storage of the quantum information in such qubits adresses the issue of decoherence at the hardware level (contrary to error correction codes which act at the software level).

Closer to our presentation which emphasizes on the study of 1D p-wave superconductors, the non-Abelian braiding of Majorana fermions supported by semiconducting wires has been proved in Ref [152]. We would rather present here the original version of Majorana fermions bound to vortices in a $p+ip$ superconductor [148]. Considering vortices in a plane, one must define a branch cut which originates from each vortex. When crossing this branch cut the superconducting phase jumps by 2π but electron-like and hole-like components of a Majorana fermion acquires π and $-\pi$ phases so that the wavefunction changes sign. Then exchanging two neighboring Majorana fermions γ_i and γ_{i+1} results in the transformations

$$T_i(\gamma_i) = \gamma_{i+1} \ , \quad T_i(\gamma_{i+1}) = -\gamma_i \quad \text{and} \quad T_i(\gamma_j) = \gamma_j \quad \text{for} \quad j \notin \{i, i+1\} \ . \tag{4.4.1}$$

This is illustrated in Fig. 4.10. We easily check that braid group defining relations are verified

$$T_i T_j = T_j T_i \quad \text{for} \quad |i-j| > 1 \ , \tag{4.4.2}$$

$$T_i T_j T_i = T_j T_i T_j \quad \text{for} \quad |i-j| = 1 \ . \tag{4.4.3}$$

A projective representation is given by the action

$$T_i(\gamma_j) = \tau(T_i)\gamma_j[\tau(T_i)]^{-1} \quad \text{where} \quad \tau(T_i) = \exp\left[\frac{\pi}{4}\,\gamma_{i+1}\gamma_i\right] = \frac{1}{\sqrt{2}}\,(1+\gamma_{i+1}\gamma_i) \ . \tag{4.4.4}$$

If one considers a given parity sector, e.g. the two-dimensional state spanned by $|0\rangle$ and $f_1^\dagger f_2^\dagger\,|0\rangle$ where $f_1 = \frac{\gamma_1+i\gamma_2}{2}$ and $f_2 = \frac{\gamma_3+i\gamma_4}{2}$, these matrices read

$$\tau(T_1) = \exp\left[-i\frac{\pi}{4}\sigma_z\right] \ , \quad \tau(T_2) = \exp\left[-i\frac{\pi}{4}\sigma_x\right] \quad \text{and} \quad \tau(T_3) = \exp\left[-i\frac{\pi}{4}\sigma_z\right] \ . \tag{4.4.5}$$

The internal exchanges $\tau(T_1)$ (exchange of γ_1 and γ_2) and $\tau(T_3)$ (exchange of γ_3 and γ_4) produce non-trivial phase factors for the states $|0\rangle$ and $f_1^\dagger f_2^\dagger\,|0\rangle$. Even more interestingly, the exchange of γ_2 and γ_3, which are half fermions of f_1 and f_2 respectively, leads to a mixing of the states. The qubit rotations (4.4.5) are unitary tranformations which can be used for quantum computations taking advantage of the protection against decoherence (fault-tolerant quantum computing).

Chapter 5

Josephson current and thermal noise in a junction between two topological superconductors

The study of a junction between two p-wave superconductors in a topologically nontrivial phase (TS-TS junction) is motivated by the inherent presence of Majorana states at the interface [145]. We have already introduced in Chapter 4 the promises of Majorana physics in condensed matter platforms. Here is presented a calculation of Josephson current and thermal noise in a TS-TS junction in the aim to propose transport-based signatures for the presence of Majorana modes. Actually a unified approach to these transport quantities in BCS and topological superconducting junctions is proposed. It relies on an expansion over Bogoliubov - de Gennes (BdG) scattering states. This unified description of both types of junction is presented in Section 5.1 and the scattering states are given in Section 5.2. The Andreev sector is studied in Section 5.3. Then, the non-resonant noise which involves continuum states is computed in Section 5.4. Finally, we give some concluding remarks and propose some perspectives in Section 5.5.

Short BCS superconducting constrictions (junctions in which the contact length is much shorter than the superconducting coherence length) have extensively been studied in the litterature, including computations of Josephson current [176–178] and thermal noise [179] and here we recover some well established results. The Green's function based theoretical framework of Ref. [180] has been developped to analyze different kinds of hybrid quantum device including

TS-TS junction and has reported results in agreement with the study presented here.

5.1 Unified scattering approach to quantum transport in S-S and TS-TS junctions

Quasiclassical helical mode expansion and Dirac potential modelization for backscattering at the contact point between wires [181] are well suited to describe a junction between two BCS superconductors (S-S junction). This framework has been adopted to adress decoherence issues of the so-called Andreev level qubit [182], including interactions with acoustic phonons [183] and quasiparticle poisoning [184–186]. Here we recall this framework and extend it to include the description of a topological wire. (Section 5.1.1). Then we diagonalize the Hamiltonian by introducing the scattering eigenstates which would differ between the two types of junction through the matching equation (Section 5.1.2). Finally, we express the current statistics in terms of these scattering states (Section 5.1.3).

5.1.1 Unified Hamiltonian description of S-S and TS-TS junctions

We derive the BdG Hamiltonian written in terms of bispinors which collect the four kinds of movers (right or left movers with spin up or down). We show how a chiral TS wire can be described by the same Hamiltonian provided the use of constrained bispinors. Then, the modelization of backscattering at the junction is presented.

BdG Hamiltonian for a BCS superconducting wire

Let us consider the second-quantized Hamiltonian of a one-dimensional BCS superconductor [25] with Fermi energy E_F, gap energy Δ, potential phase drop $\phi(x)$

$$H_{\rm BCS} = \int \mathrm{d}x \left\{ \sum_{\sigma=\uparrow,\downarrow} \psi_\sigma^\dagger(x) \left[-\frac{\hbar^2}{2m}\,\partial_x^2 - E_F \right] \psi_\sigma(x) + \Delta\, \mathrm{e}^{i\phi(x)}\, \psi_\uparrow^\dagger(x)\psi_\downarrow^\dagger(x) + \mathrm{h.c.} \right\} , \quad (5.1.1)$$

where the field $\psi_\sigma^\dagger(x)$ denotes the fermionic creation operator for a particle with spin σ at position x. It is useful to search solutions in the form of right and left movers at the Fermi velocity $v_F = \frac{\hbar k_F}{m}$ by introducing envelope fermionic operators $\psi_{j\sigma}$ for $j = L, R$ and $\sigma = \uparrow, \downarrow$ according to

$$\psi_\sigma(x) = \mathrm{e}^{ik_F x}\psi_{R\sigma}(x) + \mathrm{e}^{-ik_F x}\psi_{L\sigma}(x) \quad \text{with} \quad k_F = \frac{\sqrt{2mE_F}}{\hbar} . \quad (5.1.2)$$

The so-called "Slowly Varying Envelope Approximation" (SVEA) consists in neglecting second order derivatives of the envelope operators. The Hamiltonian can be rewritten according to (the fast oscillating terms with wavevectors $\pm 2k_F$ in the integrand are suppressed)

$$H_{\mathrm{BCS}} = \int \mathrm{d}x \sum_{\sigma=\uparrow,\downarrow} \left\{ v_F \left(\psi^\dagger_{R\sigma}(x) \left[\frac{\hbar}{i} \partial_x \right] \psi_{R\sigma}(x) - \psi^\dagger_{L\sigma}(x) \left[\frac{\hbar}{i} \partial_x \right] \psi_{L\sigma}(x) \right) + \sigma \, \Delta \, \mathrm{e}^{i\phi(x)} \, \psi^\dagger_{R\sigma}(x) \psi^\dagger_{L-\sigma}(x) + \mathrm{h.c.} \right\} . \tag{5.1.3}$$

In the following, we express energies in units of the gap energy and lengths in units of the superconducting coherence length, which means doing the substitutions

$$H \leftarrow \frac{H}{\Delta} \quad \text{and} \quad x \leftarrow \frac{x}{\xi_0} , \quad \xi_0 = \frac{\hbar v_F}{\Delta} . \tag{5.1.4}$$

It leads to the adimensionnalized Hamiltonian

$$H_{\mathrm{BCS}} = \int \mathrm{d}x \sum_{\sigma=\uparrow,\downarrow} \left\{ -i \left(\psi^\dagger_{R\sigma}(x) \partial_x \psi_{R\sigma}(x) - \psi^\dagger_{L\sigma}(x) \partial_x \psi_{L\sigma}(x) \right) + \sigma \, \mathrm{e}^{i\phi(x)} \, \psi^\dagger_{R\sigma}(x) \psi^\dagger_{L-\sigma}(x) + \mathrm{h.c.} \right\} . \tag{5.1.5}$$

We introduce the following Nambu spinors

$$\psi_+ = \begin{pmatrix} \psi_{R\uparrow} \\ \psi^\dagger_{L\downarrow} \end{pmatrix} \quad \text{and} \quad \psi_- = \begin{pmatrix} \psi_{L\uparrow} \\ \psi^\dagger_{R\downarrow} \end{pmatrix} . \tag{5.1.6}$$

The helicity is defined as the sign of the product of spin projection and momentum: a given spin projection moving in a direction has the same helicity that the opposite spin projection moving in the other direction. The two Nambu spinors defined in the last equation have given $\pm$ helicity. We combine them into a bispinor according to

$$\Psi = \begin{pmatrix} \psi_+ \\ \psi_- \end{pmatrix} . \tag{5.1.7}$$

We define the Pauli matrices τ_i and σ_i $(i = x, y, z)$ which act respectively in Nambu and right/left-mover spaces so that the Hamiltonian can be written using this bispinor according to

$$H_{\mathrm{BCS}} = \int \mathrm{d}x \, \Psi^\dagger(x) \left[-i\partial_x \, \sigma_z \tau_z + \tau_x \, \mathrm{e}^{i\phi(x)\tau_z} \right] \Psi(x) . \tag{5.1.8}$$

If the phase is homogeneous accross the material, that is $\phi(x) = \varphi$, we can gauge it out with the substitution $\Psi \leftarrow \mathrm{e}^{i\frac{\varphi}{2}\tau_z} \Psi$, so that we obtain

$$H_{\mathrm{BCS}} = \int \mathrm{d}x \, \Psi^\dagger(x) \, \mathcal{H}_{\mathrm{BdG}} \left(\partial_x \right) \Psi(x) \quad \text{with} \quad \mathcal{H}_{\mathrm{BdG}} \left(\partial_x \right) = -i\partial_x \, \sigma_z \tau_z + \tau_x . \tag{5.1.9}$$

The BdG operator $\mathcal{H}_{\mathrm{BdG}}$ is diagonal in right/left-mover space:

$$\mathcal{H}_{\mathrm{BdG}} \left(\partial_x \right) = \begin{pmatrix} h(\partial_x) & 0 \\ 0 & \tau_x h(\partial_x) \tau_x \end{pmatrix} \quad \text{with} \quad h(\partial_x) = -i\partial_x \, \tau_z + \tau_x . \tag{5.1.10}$$

BdG Hamiltonian for a topological superconducting wire

Setting $\mu = 0$ in the Kitaev chain model leads to a topologically non-trivial phase (see Chapter 4 Section 4.2). Then linearizing (4.2.6) around Fermi points $k_F = \frac{\pi}{2a}$ [180], we get

$$H_{\mathrm{TS}} = \sum_q \Phi_q^\dagger \left[\hbar v_F q\, \tau_z + \Delta \mathrm{e}^{i\varphi\tau_z}\tau_x\right] \Phi_q \quad \text{with} \quad \Phi_q = \mathcal{C}_{k_F+q} = \begin{pmatrix} c_{k_F+q} \\ c^\dagger_{-k_F-q} \end{pmatrix} , \tag{5.1.11}$$

where $\hbar v_F = ta$. Performing the change of units (5.1.4), we get

$$H_{\mathrm{TS}} = \sum_q \Phi_q^\dagger \left[q\, \tau_z + \mathrm{e}^{i\varphi\tau_z}\tau_x\right] \Phi_q \ . \tag{5.1.12}$$

We introduce right and left movers ψ_j ($j = R, L$) by the following Fourier transforms (l is the wire length)

$$\begin{cases} c_{k_F+q} = \displaystyle\int \frac{\mathrm{d}x}{\sqrt{l}}\, \mathrm{e}^{-i(k_F+q)x}\psi_R(x) \ , \\ c_{-k_F-q} = \displaystyle\int \frac{\mathrm{d}x}{\sqrt{l}}\, \mathrm{e}^{i(k_F+q)x}\psi_L(x) \ , \end{cases} \tag{5.1.13}$$

and collect them into the Nambu spinor

$$\psi = \begin{pmatrix} \psi_R \\ \psi_L^\dagger \end{pmatrix} \ . \tag{5.1.14}$$

After gauging out the homogeneous phase φ with the transformation $\psi \leftarrow \mathrm{e}^{i\frac{\varphi}{2}\tau_z}\psi$, the Hamiltonian can be written as

$$H_{\mathrm{TS}} = \int \mathrm{d}x\, \psi^\dagger(x) h(\partial_x)\psi(x) \ , \tag{5.1.15}$$

where the operator h has been defined in (5.1.10). We introduce the Nambu spinor copy (the * operation consists in the hermitian conjugation of the components of the spinor)

$$\overline{\psi} = i\tau_y\psi^* = \begin{pmatrix} \psi_L \\ -\psi_R^\dagger \end{pmatrix} \tag{5.1.16}$$

which transforms in the same way under the phase gauging out $\overline{\psi} \leftarrow \mathrm{e}^{i\frac{\varphi}{2}\tau_z}\overline{\psi}$. It is useful to consider such a spinor copy because we easily verify that

$$-\psi^{*\dagger}\tau_x\psi^* = \psi^\dagger\tau_x\psi \quad \text{and} \quad \int \mathrm{d}x\, \psi^{*\dagger}(x)\, \partial_x\, \tau_z\, \psi^*(x) = \int \mathrm{d}x\, \psi^\dagger(x)\, \partial_x\, \tau_z\, \psi(x) \ . \tag{5.1.17}$$

Consequently, we get

$$\int \mathrm{d}x\, \overline{\psi}^\dagger(x)\, \tau_x h(\partial_x)\tau_x\, \overline{\psi}(x) = \int \mathrm{d}x\, \psi^{*\dagger}(x)\, \tau_z h(\partial_x)\tau_z\, \psi^*(x) = H_{\mathrm{TS}} \ . \tag{5.1.18}$$

Then, if we define the bispinor

$$\underline{\Psi} = \frac{1}{\sqrt{2}} \begin{pmatrix} \psi \\ \overline{\psi} \end{pmatrix} , \tag{5.1.19}$$

we can write the TS wire Hamiltonian in the same form than that of a BCS wire (5.1.9), that is

$$H_{\text{TS}} = \int \mathrm{d}x \, \underline{\Psi}^\dagger(x) \, \mathcal{H}_{\text{BdG}} \left(\partial_x\right) \underline{\Psi}(x) \ . \tag{5.1.20}$$

An important point is that the bispinors used in the description of a TS wire obey the pseudo-reality constraint

$$[C\underline{\Psi}]^* = \underline{\Psi} \quad \text{with} \quad C = \sigma_y \tau_y \ . \tag{5.1.21}$$

Remark: Guided by the previous result, we introduce the copies $\overline{\psi}_\zeta$ of the Nambu spinors ψ_ζ defined by (5.1.6) and the collecting constrained bispinors $\underline{\Psi}_\zeta$ according to

$$\overline{\psi}_\zeta = i\tau_y \psi_\zeta^* \quad \text{and} \quad \underline{\Psi}_\zeta = \frac{1}{\sqrt{2}} \begin{pmatrix} \psi_\zeta \\ \overline{\psi}_\zeta \end{pmatrix} \quad \text{for} \quad \zeta = \pm \ . \tag{5.1.22}$$

We can then rewrite (5.1.9) as

$$H_{\text{BCS}} = \sum_{\zeta=\pm} \int \mathrm{d}x \, \underline{\Psi}_\zeta^\dagger(x) \, \mathcal{H}_{\text{BdG}} \left(\zeta\partial_x\right) \underline{\Psi}_\zeta(x) \ . \tag{5.1.23}$$

A BCS 1D superconductor treated in the SVEA approximation can be seen as a superposition of two TS wires with opposite velocities $\pm v_F$ (and then opposite helicities).

Localized scatterer

We modelize a TS-TS junction by introducing a barrier at $x = 0$ that allows backscattering (right mover into a left mover or *vice versa*) which necessarily required spin flip (as a consequence of momentum-spin locking)

$$H_{\text{TS-TS}} = H_{\text{TS}} + \frac{g}{2} \left[\psi_L^\dagger(0^-)\psi_R(0^-) + \psi_R^\dagger(0^+)\psi_L(0^+) + \text{h.c.} \right] \ . \tag{5.1.24}$$

The interacting term can be written using a delta function[1] so that

$$H_{\text{TS-TS}} = \int \mathrm{d}x \, \underline{\Psi}^\dagger(x) \left\{ \mathcal{H}_{\text{BdG}}(\partial_x) + g\delta(x)\sigma_x \right\} \underline{\Psi}(x) \tag{5.1.25}$$

[1] In fact we use the distribution which gives the mean value of right and left limits in 0 of a function $\int \mathrm{d}x \, \delta(x) f(x) = \frac{f(0^-)+f(0^+)}{2}$.

with the constrained bispinor $\underline{\Psi}$ defined in (5.1.14), (5.1.16) and (5.1.19). In a S-S junction, we allow backscattering in a spin-preserving way

$$H_{\text{S-S}} = H_{\text{S}} + \frac{g}{2}\sum_{\sigma}\left[\psi^{\dagger}_{L\sigma}(0^{-})\psi_{R\sigma}(0^{-}) + \psi^{\dagger}_{R\sigma}(0^{+})\psi_{L\sigma}(0^{+}) + \text{h.c.}\right] \tag{5.1.26}$$

$$= \int \mathrm{d}x\, \Psi^{\dagger}(x)\left\{\mathcal{H}_{\text{BdG}}(\partial_x) + g\delta(x)\sigma_x\tau_z\right\}\Psi(x) \tag{5.1.27}$$

with the unconstrained bispinor Ψ defined in (5.1.6) and (5.1.7). Such a modelization of backscattering in a S-S junction is achieved in the litterature [181,183–185]. Both S-S and TS-TS junctions can be described by a second quantized Hamiltonian H written as

$$H = \int \mathrm{d}x\, \Phi^{\dagger}(x)\mathcal{H}(x,\partial_x)\Phi(x) \quad \text{with} \quad \mathcal{H}(x,\partial_x) = \mathcal{H}_{\text{BdG}}(\partial_x) + g\delta(x)\sigma_x\tau_z\tau_{\star} \tag{5.1.28}$$

where $\Phi(x)$ is a constrained bispinor only in the topological case and where we define

$$\tau_{\star} = \begin{cases} \tau_z & \text{in a TS-TS junction,} \\ 1 & \text{in a S-S junction.} \end{cases} \tag{5.1.29}$$

5.1.2 Hamiltonian diagonalization

The diagonalization of such the Hamiltonian (5.1.28) resides in the determination of the energies E_ν such that

$$H = \sum_{\nu} E_\nu c^{\dagger}_\nu c_\nu \ . \tag{5.1.30}$$

$c^{\dagger}_\nu$ is the fermionic creation operator for a particle in the energy state E_ν. This diagonalization can be performed using the ansatz

$$\Phi(x) = \sum_{\nu} \chi_\nu(x) c_\nu \ , \tag{5.1.31}$$

where the introduced 4-component wavefunctions satisfy

$$\begin{aligned} &\int \mathrm{d}x\, \chi^{\dagger}_\nu(x)\mathcal{H}(x,\partial_x)\chi_\nu(x) = E_\nu \ , \\ &\int \mathrm{d}x\, \left\{\chi^{\dagger}_\mu(x)\mathcal{H}(x,\partial_x)\chi_\nu(x) - \chi^{\dagger}_\nu(x)\mathcal{H}(x,\partial_x)\chi_\mu(x)\right\} = 0 \quad \text{for} \quad \mu \neq \nu \ . \end{aligned} \tag{5.1.32}$$

Assuming χ_ν to be normalized, *i.e.* $\int \mathrm{d}x\, \chi^{\dagger}_\nu(x)\chi_\nu(x) = 1$, we can rewrite the first equation of (5.1.32) as

$$\int \mathrm{d}x\, \chi^{\dagger}_\nu(x)\left\{\mathcal{H}(x,\partial_x) - E_\nu\right\}\chi_\nu(x) = 0 \ . \tag{5.1.33}$$

Solving the eigenvalue problem $\{\mathcal{H}(x,\partial_x)-E\}\,\chi(x)=0$ for the 4-component function $\chi(x)$ leads to the determination of the set of eigenvalues $\mathrm{Sp}(\mathcal{H})=\{E_\nu\}_\nu$ and an orthonormalized basis of eigenfunctions $\{\chi_\nu\}_\nu$

$$\{\mathcal{H}(x,\partial_x)-E_\nu\}\,\chi_\nu(x)=0 \quad \text{and} \quad \int \mathrm{d}x\,\chi_\mu^\dagger(x)\chi_\nu(x)=\delta_{\mu\nu}\ , \tag{5.1.34}$$

which satisfy (5.1.32) so that used in the ansatz (5.1.31) that is injected in (5.1.28), the diagnonalization (5.1.30) is effective. The interacting problem $\{\mathcal{H}(x,\partial_x)-E\}\,\chi(x)=0$ reduces to the free problem $\{\mathcal{H}_{\mathrm{BdG}}(\partial_x)-E\}\,\chi(x)=0$ for $x>0$ and $x<0$ and to the matching of the two solutions which is obtained by integrating the interacting eigenvalue problem around $x=0$ (which will lead to a case-dependent matching condition). Remark that we have

$$c_\nu=\int \mathrm{d}x\,\chi_\nu^\dagger(x)\Phi(x) \quad \text{and} \quad c_\nu^\dagger=\int \mathrm{d}x\,\chi_\nu^T(x)\Phi^*(x)\ . \tag{5.1.35}$$

In the case of constrained bispinors $\Phi=\underline{\Psi}$ with $[C\underline{\Psi}]^*=\underline{\Psi}$, we obtain

$$c_\nu^\dagger=\int \mathrm{d}x\ [C\chi_\nu(x)]^T\,\underline{\Psi}(x)\ . \tag{5.1.36}$$

Free problem

The free problem is the same in both S-S and TS-TS junctions and it reduces to the diagonalization of the BdG Hamiltonian $\mathcal{H}_{\mathrm{BdG}}$ given in (5.1.10). Its square is the scalar differential operator $\mathcal{H}_{\mathrm{BdG}}^2(\partial_x)=-\partial_x^2+1$. Then, we have continuum plane wave states $\propto \mathrm{e}^{ik_Ex}$ with dispersion relation $E^2=1+k_E^2$ and subgap (bound) states $\propto \mathrm{e}^{\kappa_Ex}$ with dispersion relation $E^2=1-\kappa_E^2$.

Continuum states ($|E|>1$)

In right/left-mover space, continuum states can be written as

$$\chi_E(x)=\mathrm{e}^{ik_Ex}\left\{\begin{pmatrix}\chi_E^{(1+)}\\0\end{pmatrix}+\begin{pmatrix}0\\\chi_E^{(2+)}\end{pmatrix}\right\}+\mathrm{e}^{-ik_Ex}\left\{\begin{pmatrix}\chi_E^{(1-)}\\0\end{pmatrix}+\begin{pmatrix}0\\\chi_E^{(2-)}\end{pmatrix}\right\}\ . \tag{5.1.37}$$

If we define $h_k=h(\partial_x)\,\mathrm{e}^{ikx}=k\tau_z+\tau_x$, the BdG equation written for this wavefunction gives

$$\begin{cases}\{h_{k_E}-E\}\,\chi_E^{(\alpha\rho)}=0 & \text{for} \quad (\alpha,\rho)=(1,+)\,\text{or}\,(2,-)\ ,\\ \{h_{-k_E}-E\}\,\chi_E^{(\alpha\rho)}=0 & \text{for} \quad (\alpha,\rho)=(1,-)\,\text{or}\,(2,+)\ .\end{cases} \tag{5.1.38}$$

It is convenient to introduce the angle θ_E defined as

$$\begin{cases}\cosh\theta_E=|E|\ ,\\ \sinh\theta_E=\sqrt{E^2-1}\ .\end{cases} \tag{5.1.39}$$

We have $\theta_{-E} = \theta_E$ and we link the signs of wavevector and energy as

$$\operatorname{sign} E = \operatorname{sign} k_E \equiv \eta_E \ . \tag{5.1.40}$$

Then we simply have

$$\begin{cases} \left\{\tau_x - \eta_E \, \mathrm{e}^{-\theta_E \tau_z}\right\} \chi_E^{(\alpha\rho)} = 0 & \text{for} \quad (\alpha,\rho) = (1,+) \text{ or } (2,-) \ , \\ \left\{\tau_x - \eta_E \, \mathrm{e}^{\theta_E \tau_z}\right\} \chi_E^{(\alpha\rho)} = 0 & \text{for} \quad (\alpha,\rho) = (1,-) \text{ or } (2,+) \ . \end{cases} \tag{5.1.41}$$

Now if we define

$$\tilde{\chi}_E^{(\alpha\rho)} = \begin{cases} \mathrm{e}^{-\frac{\theta_E}{2}\tau_z} \, \chi_E^{(\alpha\rho)} & \text{for} \quad (\alpha,\rho) = (1,+) \text{ or } (2,-) \ , \\ \mathrm{e}^{\frac{\theta_E}{2}\tau_z} \, \chi_E^{(\alpha\rho)} & \text{for} \quad (\alpha,\rho) = (1,-) \text{ or } (2,+) \ , \end{cases} \tag{5.1.42}$$

the equations (5.1.41) reduce to

$$\{1 - \eta_E \tau_x\} \, \tilde{\chi}_E^{(\alpha\rho)} = 0 \quad \Rightarrow \quad \tilde{\chi}_E^{(\alpha\rho)} \propto \begin{pmatrix} 1 \\ \eta_E \end{pmatrix} \ . \tag{5.1.43}$$

Two types of solutions are possible (depending on the value of (α,ρ)) and correspond to the two conducting species: electrons and holes. Then we define spinors describing electron (e) and hole (h) at energy E by (this is arbitrary and the roles of electrons and holes can be interchanged)

$$[\chi_e]_E = \chi(\theta_E, \eta_E) \quad \text{and} \quad [\chi_h]_E = \chi(-\theta_E, \eta_E) \ , \quad \text{where} \quad \chi(\theta,\eta) = \frac{\mathrm{e}^{\frac{\theta}{2}\tau_z}}{\sqrt{2\cosh\theta}} \begin{pmatrix} 1 \\ \eta \end{pmatrix} \ . \tag{5.1.44}$$

We have the following orthonormality conditions:

$$\begin{aligned} &\chi^\dagger(\theta,\eta)\chi(\theta,\eta) = 1 \quad \Rightarrow \quad [\chi_e]_E^\dagger [\chi_e]_E = [\chi_h]_E^\dagger [\chi_h]_E = 1 \ , \\ &\chi^\dagger(\theta,-\eta)\chi(-\theta,\eta) = 0 \quad \Rightarrow \quad [\chi_e]_{-E}^\dagger [\chi_h]_E = 0 \ . \end{aligned} \tag{5.1.45}$$

The incoming wave corresponding to an electron or a hole at energy E coming from the left ($x < 0$) or from the right ($x > 0$) is a particular solution of the BdG equation (l is the wire length)

$$\chi^{\text{in}}_{p=(E,s)}(x) = \Theta(-x) \, \frac{\mathrm{e}^{ik_E x}}{\sqrt{l}} \begin{pmatrix} \delta_{s,1}[\chi_e]_E \\ \delta_{s,2}[\chi_h]_E \end{pmatrix} + \Theta(x) \, \frac{\mathrm{e}^{-ik_E x}}{\sqrt{l}} \begin{pmatrix} \delta_{s,4}[\chi_h]_E \\ \delta_{s,3}[\chi_e]_E \end{pmatrix} \ . \tag{5.1.46}$$

An additionnal index $s = 1..4$ has been defined to distinguish between the four cases of incoming waves and p stands for the couple (E,s). This is not a solution of the interacting problem and the matching condition will lead to the emergence of an outgoing wave, which form is intuitively guessed to be

$$\chi^{\text{out}}_{p=(E,s)}(x;\varphi) = \Theta(-x) \, \frac{\mathrm{e}^{-ik_E x}}{\sqrt{l}} \begin{pmatrix} a_p(\varphi)[\chi_h]_E \\ b_p(\varphi)[\chi_e]_E \end{pmatrix} + \Theta(x) \, \frac{\mathrm{e}^{ik_E x}}{\sqrt{l}} \begin{pmatrix} c_p(\varphi)[\chi_e]_E \\ d_p(\varphi)[\chi_h]_E \end{pmatrix} \ , \tag{5.1.47}$$

so that a general solution could be written as

$$\chi_p(x;\varphi) = \chi_p^{\rm in}(x) + \chi_p^{\rm out}(x;\varphi) \ . \tag{5.1.48}$$

The coefficients a_p, b_p, c_p, d_p will depend on the phase difference φ between the two superconductors but also on the strength of the coupling g (through the transmission T to be defined later). It will be necessary to prove that the four solutions $s = 1..4$ at a given energy E form a basis for the solutions of the BdG equation.

Bound states ($|E| \leqslant 1$)

Physical solutions correspond to bound states with $\kappa_E = \sqrt{1-E^2} \geqslant 0$ written as

$$\chi_E(x) = {\rm e}^{-\kappa_E x}\,\Theta(x)\left\{\begin{pmatrix}\chi_E^{(1+)}\\0\end{pmatrix} + \begin{pmatrix}0\\\chi_E^{(2+)}\end{pmatrix}\right\} + {\rm e}^{\kappa_E x}\,\Theta(-x)\left\{\begin{pmatrix}\chi_E^{(1-)}\\0\end{pmatrix} + \begin{pmatrix}0\\\chi_E^{(2-)}\end{pmatrix}\right\} \ . \tag{5.1.49}$$

The BdG equation written for this wavefunction gives the same equations for the $\chi_{\alpha\rho}$ as in the previous case provided we substitute $i\kappa_E$ to k_E

$$\begin{cases} \{h_{i\kappa_E} - E\}\,\chi_E^{(\alpha\rho)} = 0 & \text{for} \quad (\alpha,\rho) = (1,+)\,\text{or}\,(2,-) \ , \\ \{h_{-i\kappa_E} - E\}\,\chi_E^{(\alpha\rho)} = 0 & \text{for} \quad (\alpha,\rho) = (1,-)\,\text{or}\,(2,+) \ . \end{cases} \tag{5.1.50}$$

The sign of the energy is denoted as $\sigma_E = {\rm sign}E$. The additional substitution $\theta_E \to i\gamma_E$ yields to the definition of the angle γ_E as

$$\begin{cases} \cos\gamma_E = |E| \ , \\ \sin\gamma_E = \sigma_E\kappa_E \ . \end{cases} \tag{5.1.51}$$

Without loss of generality we can choose $\gamma_{-E} = -\gamma_E$. Proceeding as previously, we have to define

$$[\tilde\chi_e]_E = \tilde\chi(\gamma_E,\sigma_E) \quad \text{and} \quad [\tilde\chi_h]_E = \tilde\chi(-\gamma_E,\sigma_E) \ , \quad \text{where} \quad \tilde\chi(\gamma,\sigma) = \frac{{\rm e}^{\frac{i\gamma}{2}\tau_z}}{\sqrt{2}}\begin{pmatrix}1\\\sigma\end{pmatrix} \ . \tag{5.1.52}$$

We have the following orthonormality conditions:

$$\begin{aligned} &\tilde\chi^\dagger(\gamma,\sigma)\tilde\chi(\gamma,\sigma) = 1 \quad \Rightarrow \quad [\tilde\chi_e]_E^\dagger[\tilde\chi_e]_E = [\tilde\chi_h]_E^\dagger[\tilde\chi_h]_E = 1 \ , \\ &\tilde\chi^\dagger(\gamma,-\sigma)\tilde\chi(\gamma,\sigma) = 0 \quad \Rightarrow \quad [\tilde\chi_h]_{-E}^\dagger[\tilde\chi_e]_E = 0 \ . \end{aligned} \tag{5.1.53}$$

Then we can write the general form for a bound state wavefunction as

$$\chi_E(x;\varphi) = {\rm e}^{-\kappa_E|x|}\left[\Theta(-x)\begin{pmatrix}a_E(\varphi)[\tilde\chi_h]_E\\b_E(\varphi)[\tilde\chi_e]_E\end{pmatrix} + \Theta(x)\begin{pmatrix}c_E(\varphi)[\tilde\chi_e]_E\\d_E(\varphi)[\tilde\chi_h]_E\end{pmatrix}\right] \ . \tag{5.1.54}$$

As in the previous case, the coefficients a_E, b_E, c_E, d_E will depend on the phase difference φ between the two superconductors but also on the strength of the coupling g.

Matching condition

Integrating the interacting eigenvalue problem $\{\mathcal{H}_{\rm BdG}(\partial_x) + g\delta(x)\sigma_x\tau_\star - E\}\,\chi(x) = 0$ around $x = 0$ provides

$$-i\sigma_z\tau_z\left[\chi(0^+) - \chi(0^-)\right] + \lambda\sigma_x\left[\chi(0^+) + \chi(0^-)\right] = 0 \quad \text{with} \quad \lambda = \frac{g}{2}\ . \tag{5.1.55}$$

Defining transmission and reflection coefficients

$$t = \frac{1-\lambda^2}{1+\lambda^2} = \sqrt{T} \quad \text{and} \quad r = \frac{2\lambda}{1+\lambda^2} = \sqrt{1-T}\ , \tag{5.1.56}$$

we can write

$$\chi(0^-) = \frac{1}{t}\left(1 - r\sigma_y\tau_\star\right)\chi(0^+)\ . \tag{5.1.57}$$

Remark that this equation matches solutions in the two half-spaces $x < 0$ and $x > 0$ which have not necessarily the same phase potential. It is then established before the gauge transformation

$$\chi(x) \leftarrow {\rm e}^{-i\frac{\varphi}{4}\,{\rm sign}(x)\tau_z}\chi(x) \tag{5.1.58}$$

where φ is the phase drop accross the junction. We also perform the following rotation

$$\chi(x) \leftarrow {\rm e}^{-i\frac{\pi}{4}\sigma_z}\chi(x)\ , \tag{5.1.59}$$

which transforms σ_y into $-\sigma_x$, for conventional reasons. We obtain

$$\chi(0^-) = \check{T}_\star\chi(0^+) \quad \text{with} \quad \check{T}_\star = \frac{{\rm e}^{i\frac{\varphi}{2}\tau_z}}{\sqrt{T}}\left(1 + \sqrt{1-T}\sigma_x\tau_\star\right)\ , \tag{5.1.60}$$

where $\tau_\star$ has been defined in (5.1.29).

Remarks:

- The transmission coefficient is independent of the energy so that the mode expansion (5.1.31) also satisfies the matching equation $\Phi(0^-) = \check{T}_\star\Phi(0^+)$.
- Importantly, the matching equation is the same for S-S and TS-TS junctions in the limit of perfect transparency $T = 1$ so that the BdG solutions must coincide.

5.1.3 Current operator and statistics

Moving to Heisenberg picture leads to time dependence for the operators. We express times in units of $\hbar/\Delta = \xi_0/v_F$ (which leads to $\hbar = 1$ in our system of units). The transformation between Schrödinger and Heisenberg pictures, for the field operators, reads

$$\Phi(x,t) = {\rm e}^{iHt}\,\Phi(x)\,{\rm e}^{-iHt} = \sum_{k\geqslant 0}\frac{(it)^k}{k!}Ad_H^k[\Phi(x)] \quad \text{with} \quad Ad_H[\Phi(x)] = [H,\Phi(x)]\ , \tag{5.1.61}$$

where we have used the Baker-Hausdorff lemma [187]. Since we have $[H, \Phi(x)] = -\mathcal{H}(x, \partial_x)\Phi(x)$, we get (using the decomposition (5.1.31) and the eigenvalue equation (5.1.34) verified by the functions χ_ν)

$$\Phi(x,t) = \sum_\nu \chi_\nu(x)\, \mathrm{e}^{-iE_\nu t} c_\nu \ . \tag{5.1.62}$$

An alternative proof consists in using first the decomposition (5.1.31) in order to write

$$\Phi(x,t) = \sum_\nu \chi_\nu(x) c_\nu(t) \quad \text{with} \quad c_\nu(t) = \mathrm{e}^{iHt}\, c_\nu\, \mathrm{e}^{-iHt} \ , \tag{5.1.63}$$

then still using the Baker identity and remarking that $[H, c_\nu] = -E_\nu c_\nu$, we recover the result.

Remarks:

- For continuum states, because of the sign choice (5.1.40), a plane wave $\mathrm{e}^{ik_E x}$ effectively propagates from left to right, whatever the sign of the energy E.
- The matching equation remains true in the Heisenberg picture

$$\Phi(x = 0^-, t) = \check{T}_\star \Phi(x = 0^+, t) \ . \tag{5.1.64}$$

Taking the electron charge e as charge unit, the current flowing through the junction (from left to right) is given by

$$I(t) = \Phi^\dagger(x = 0^+, t)\sigma_z \Phi(x = 0^+, t) = \Phi^\dagger(x = 0^-, t)\sigma_z \Phi(x = 0^-, t) \ . \tag{5.1.65}$$

The current conservation is provided by $T_\star^\dagger \sigma_z T_\star = \sigma_z$. Then, using the mode expansion (5.1.62), the current operator reads

$$I(t) = \sum_{\nu,\nu'} \mathcal{I}_{\nu\nu'} c_\nu^\dagger c_{\nu'} \mathrm{e}^{i(E_\nu - E_{\nu'})t} \quad \text{where} \quad \mathcal{I}_{\nu\nu'} = \chi_\nu^\dagger(0^+)\sigma_z \chi_{\nu'}(0^+) \ . \tag{5.1.66}$$

We introduce the Fermi occupation number

$$n(E) = \left(1 + \mathrm{e}^{\beta E}\right)^{-1} = \frac{1}{2}\left[1 - \tanh\frac{\beta E}{2}\right] \ . \tag{5.1.67}$$

The average value of the current operator (5.1.66) is given by

$$\langle I \rangle = \sum_\nu \mathcal{I}_{\nu\nu} n(E_\nu) \ , \tag{5.1.68}$$

while its fluctuations read (use Wick's theorem [188])

$$\langle \delta I(t) \delta I(t') \rangle = \langle I(t) I(t') \rangle - \langle I \rangle^2 = \sum_{\nu,\nu'} \left|\mathcal{I}_{\nu\nu'}\right|^2 n(E_\nu)\left[1 - n(E_{\nu'})\right] \mathrm{e}^{i(E_\nu - E_{\nu'})(t-t')} \ . \tag{5.1.69}$$

In the aim to provide a unified description of BCS and TS wires, we have artificially doubled the number of degrees of freedom for a TS wire and this issue has to be carefully considered when calculating expectation values. To avoid double counting (in the topological case), we introduce the prefactor $d_\star = 2$ in a TS-TS junction and $d_\star = 1$ in a S-S junction, so that the equilibrium Josephson current $\mathcal{I}$ and the unsymmetrized noise read

$$\mathcal{I} = \frac{1}{d_\star} \langle I \rangle \quad \text{and} \quad S(t,t') = \frac{1}{d_\star} \langle \delta I(t) \delta I(t') \rangle \ . \tag{5.1.70}$$

It is convenient to compute noise in frequency domain. After Fourier transform $S(t,t') = \int \frac{\mathrm{d}\omega}{2\pi} \mathrm{e}^{-i\omega(t-t')} S(\omega)$, we get

$$S(\omega) = \pi \sum_{\nu,\nu'} \left| \mathcal{I}_{\nu\nu'} \right|^2 n(E_\nu) \left[1 - n(E_{\nu'}) \right] \delta \left[\omega - (E_{\nu'} - E_\nu) \right] \ . \tag{5.1.71}$$

The finite frequency noise can be decomposed as the sum of contributions originated from transitions between Andreev levels (AA), between continuum states (CC) or between an Andreev level and a continuum state (AC), as follows

$$S(\omega \neq 0) = S_{AA}(\omega) + S_{CC}(\omega) + S_{AC}(\omega) \ . \tag{5.1.72}$$

5.2 Scattering states

Because the matching condition (5.1.60) just differs by the matrix $\tau_\star$ between BCS and topological cases, a unified treatment of S-S and TS-TS junctions can be envisaged and the energy dependent coefficients a, b, c, d which appear in both continuum (5.1.47) and bound state (5.1.54) wavefunctions will depend on a few case-dependent functions. However, as already stressed, the matching equation is the same for S-S and TS-TS junctions in the limit of perfect transparency $T = 1$ so that the BdG solutions must coincide. Note that the complete description in terms of scattering states has already been provided in Refs. [184, 185] in the S-S case. Still within our unified approach, we provide some first consequences of the matching condition, namely symmetries between continuum eigenstates and the quantization of Andreev levels (Section 5.2.1). Then, we give the expressions of wavefunctions (Sections 5.2.2 and 5.2.3). In the TS-TS case, a proper linear combination of zero-energy Andreev levels leads to the appearance of Majorana states (Section 5.2.4).

5.2.1 First consequences of the matching condition

Continuum states

At a given energy E, four possible scattering states are possible and they have been labeled by the index $s = 1..4$. p stands for the couple (E, s) and coeffcients a_p, b_p, c_p, d_p will acquire phase dependence through the matching condition (5.1.60). This relation yields the symmetries given in the following table

	$s=1$	$s=2$	$s=3$	$s=4$
$a_{(E,s)}(\varphi)$	$A(\theta_E,\varphi)$	$B(-\theta_E,\varphi)$	$-D(\theta_E,-\varphi)$	$C(-\theta_E,-\varphi)$
$b_{(E,s)}(\varphi)$	$B(\theta_E,\varphi)$	$A(-\theta_E,\varphi)$	$C(\theta_E,-\varphi)$	$-D(-\theta_E,-\varphi)$
$c_{(E,s)}(\varphi)$	$C(\theta_E,\varphi)$	$D(-\theta_E,\varphi)$	$-B(\theta_E,-\varphi)$	$A(-\theta_E,-\varphi)$
$d_{(E,s)}(\varphi)$	$D(\theta_E,\varphi)$	$C(-\theta_E,\varphi)$	$A(\theta_E,-\varphi)$	$-B(-\theta_E,-\varphi)$

Table 5.1: $a_{(E,s)}, b_{(E,s)}, c_{(E,s)}, d_{(E,s)}$ coefficients for $s = 1..4$ expressed thanks to four functions A, B, C, D.

Alternatively, if we define the wavefunction

$$\chi(x;\theta,\eta,\varphi) = \Theta(-x)\left\{\frac{\mathrm{e}^{ikx}}{\sqrt{l}}\begin{pmatrix}\chi(\theta,\eta)\\0\end{pmatrix} + \frac{\mathrm{e}^{-ikx}}{\sqrt{l}}\begin{pmatrix}A(\theta,\varphi)\,\chi(-\theta,\eta)\\B(\theta,\varphi)\,\chi(\theta,\eta)\end{pmatrix}\right\} + \Theta(x)\,\frac{\mathrm{e}^{ikx}}{\sqrt{l}}\begin{pmatrix}C(\theta,\varphi)\,\chi(\theta,\eta)\\D(\theta,\varphi)\,\chi(-\theta,\eta)\end{pmatrix}, \tag{5.2.1}$$

we have

$$\chi_{(E,1)}(x;\varphi) = \chi(x;\theta_E,\eta_E,\varphi)\ , \tag{5.2.2a}$$

$$\chi_{(E,2)}(x;\varphi) = \sigma_x\,\chi(x;-\theta_E,\eta_E,\varphi)\ , \tag{5.2.2b}$$

$$\chi_{(E,3)}(x;\varphi) = -i\sigma_y\,\chi(-x;\theta_E,\eta_E,-\varphi)\ , \tag{5.2.2c}$$

$$\chi_{(E,4)}(x;\varphi) = \sigma_z\chi(-x;-\theta_E,\eta_E,-\varphi)\ . \tag{5.2.2d}$$

We can then restrict the resolution to the case $s = 1$ and determine the functions A, B, C, D which respect the condition

$$\sqrt{T}\,[\chi(\theta,\eta) + A(\theta,\varphi)\chi(-\theta,\eta)] = \mathrm{e}^{i\frac{\varphi}{2}\tau_z}\left[C(\theta,\varphi)\chi(\theta,\eta) + \sqrt{1-T}\,\tau_\star D(\theta,\varphi)\chi(-\theta,\eta)\right]\ , \tag{5.2.3a}$$

$$\sqrt{T}B(\theta,\varphi)\chi(\theta,\eta) = \mathrm{e}^{i\frac{\varphi}{2}\tau_z}\left[D(\theta,\varphi)\chi(-\theta,\eta) + \sqrt{1-T}\,\tau_\star C(\theta,\varphi)\chi(\theta,\eta)\right]\ . \tag{5.2.3b}$$

An easy way to solve this system is to use the conditions (5.1.45). We define the two following

case-dependent quantities

$$\cosh\theta\left[\chi^\dagger(\theta,-\eta)\,\tau_\star\,\mathrm{e}^{i\frac{\varphi}{2}\tau_z}\chi(-\theta,\eta)\right]=f(\varphi)=\begin{cases}\cos\dfrac{\varphi}{2} & \text{in the topological case,}\\ i\sin\dfrac{\varphi}{2} & \text{in the BCS case.}\end{cases} \tag{5.2.4}$$

$$\cosh\theta\left[\chi^\dagger(\theta,-\eta)\,\tau_\star\,\chi(\theta,\eta)\right]=g(\theta)=\begin{cases}\cosh\theta & \text{in the topological case,}\\ \sinh\theta & \text{in the BCS case.}\end{cases} \tag{5.2.5}$$

Then we have the matrix equation $M\mathbf{V}=\mathbf{W}$ satisfied by the vectors

$$\mathbf{V}(\theta,\varphi)=\begin{pmatrix}A(\theta,\varphi)\\ B(\theta,\varphi)\\ C(\theta,\varphi)\\ D(\theta,\varphi)\end{pmatrix}\quad,\quad \mathbf{W}(\theta,\varphi)=\sqrt{T}\begin{pmatrix}\sinh\theta\\ 0\\ -i\sin\frac{\varphi}{2}\\ 0\end{pmatrix}\ . \tag{5.2.6}$$

The 4x4 matrix

$$M(\theta,\varphi)=\begin{pmatrix}0 & M_b(\theta,\varphi)\\ M_c(\theta,\varphi) & M_d(\theta,\varphi)\end{pmatrix}\ , \tag{5.2.7}$$

involves the 2x2 matrices M_i $(i=a,b,c,d)$ given by

$$M_b(\theta,\varphi)=\begin{pmatrix}\sinh\left(\theta+i\frac{\varphi}{2}\right) & \sqrt{1-T}\,f(\varphi)\\ \sqrt{1-T}\,f(\varphi) & -\sinh\left(\theta-i\frac{\varphi}{2}\right)\end{pmatrix}\ , \tag{5.2.8a}$$

$$M_c(\theta,\varphi)=\sqrt{T}\begin{pmatrix}\sinh\left(\theta+i\frac{\varphi}{2}\right) & 0\\ 0 & -\sinh\left(\theta-i\frac{\varphi}{2}\right)\end{pmatrix}\ , \tag{5.2.8b}$$

$$M_d(\theta,\varphi)=\sqrt{1-T}\begin{pmatrix}0 & g(-\theta)\\ g(\theta) & 0\end{pmatrix}\ . \tag{5.2.8c}$$

We define

$$Q^\star(\theta,\varphi)=\sinh\left(\theta-i\frac{\varphi}{2}\right)\sinh\left(\theta+i\frac{\varphi}{2}\right)=\sinh^2\theta+\sin^2\frac{\varphi}{2}=\cosh^2\theta-\cos^2\frac{\varphi}{2}\ . \tag{5.2.9}$$

This quantity can be expressed thanks to the case dependent functions g and f in a unified way

$$Q^\star(\theta,\varphi)=g^2(\theta)-f^2(\varphi)\ . \tag{5.2.10}$$

We also define

$$Q(\theta,\varphi)=Q^\star(\theta,\varphi)+(1-T)\,f^2(\varphi)=g^2(\theta)-Tf^2(\varphi)\ . \tag{5.2.11}$$

We have $\det M_b=-Q$, $\det M_c=-TQ^\star$ and $\det M=\det M_b\times\det M_c=TQQ^\star>0$ since $Q^\star>0$ and $Q>0$ in the case $|E|>1$ $(\theta>0)$. The matrix M is then invertible.

Andreev bound states

We can use the conditions (5.1.53) and proceed in the same way as done previously to obtain the matrix equation respected by the vector

$$\mathbf{V}_E(\varphi) = \begin{pmatrix} a_E(\varphi) \\ b_E(\varphi) \\ c_E(\varphi) \\ d_E(\varphi) \end{pmatrix} . \tag{5.2.12}$$

It is an homogeneous system $M(i\gamma_E, \varphi)\mathbf{V}_E(\varphi) = 0$ and to have non trivial solutions we must have

$$\det M(i\gamma_E, \varphi) = \det M_b(i\gamma_E, \varphi) \times \det M_c(i\gamma_E, \varphi) = 0 . \tag{5.2.13}$$

The matrix equation leads to

$$M_b\left[i\gamma_E, \varphi\right] \begin{pmatrix} c_E(\varphi) \\ d_E(\varphi) \end{pmatrix} = 0 , \tag{5.2.14}$$

$$M_c\left[i\gamma_E, \varphi\right] \begin{pmatrix} a_E(\varphi) \\ b_E(\varphi) \end{pmatrix} + M_d\left[i\gamma_E, \varphi\right] \begin{pmatrix} c_E(\varphi) \\ d_E(\varphi) \end{pmatrix} = 0 . \tag{5.2.15}$$

Let us search solutions that do not vanish in the right half space, *i.e.* $c_E \neq 0$ and $d_E \neq 0$. We must have

$$-\det M_b(i\gamma_E, \varphi) = Q(i\gamma_E, \varphi) = Q^\star(i\gamma_E, \varphi) + (1-T)f^2(\varphi) = 0 . \tag{5.2.16}$$

Then we have quantization of the bound states since

$$Q^\star(i\gamma_E, \varphi) = E^2 - \cos^2\frac{\varphi}{2} . \tag{5.2.17}$$

These are the so-called Andreev states which energies are given by

$$E_\sigma(\varphi) = \sigma E_A(\varphi) \quad \text{with} \quad E_A(\varphi) = \sqrt{\cos^2\frac{\varphi}{2} - (1-T)f^2(\varphi)} \quad \text{and} \quad \sigma = \pm 1 . \tag{5.2.18}$$

This two-level structure is crucial for interlevel transitions driven by an applied electromagnetic field [181]. In the following, all quantities indexed by E_σ ($a_{E_\sigma}, b_{E_\sigma}, c_{E_\sigma}, d_{E_\sigma}, \gamma_{E_\sigma}, [\tilde{\chi}_e]_{E_\sigma}, [\tilde{\chi}_h]_{E_\sigma}, \chi_{E_\sigma}$) are now just indexed by σ ($a_\sigma, b_\sigma, c_\sigma, d_\sigma, \gamma_\sigma, [\tilde{\chi}_e]_\sigma, [\tilde{\chi}_h]_\sigma, \chi_\sigma$). κ_{E_σ} does not depend on σ and is just replaced by κ

$$\kappa(\varphi) = \sqrt{1 - E_A^2(\varphi)} = \sqrt{\sin^2\frac{\varphi}{2} + (1-T)f^2(\varphi)} . \tag{5.2.19}$$

The φ dependence of Andreev states appears not only in coefficients $a_\sigma, b_\sigma, c_\sigma, d_\sigma$ but also in the damping coefficient κ and in the definition of the spinors $[\tilde{\chi}_e]_\sigma$ and $[\tilde{\chi}_h]_\sigma$ through γ_σ. The Andreev states $\sigma = \pm$ are written as

$$\chi_\sigma(x;\varphi) = \mathrm{e}^{-\kappa(\varphi)|x|}\left[\Theta(-x)\begin{pmatrix} a_\sigma(\varphi)[\tilde{\chi}_h]_\sigma(\varphi) \\ b_\sigma(\varphi)[\tilde{\chi}_e]_\sigma(\varphi)\end{pmatrix} + \Theta(x)\begin{pmatrix} c_\sigma(\varphi)[\tilde{\chi}_e]_\sigma(\varphi) \\ d_\sigma(\varphi)[\tilde{\chi}_h]_\sigma(\varphi)\end{pmatrix}\right] . \tag{5.2.20}$$

An important quantity will be the phase derivative of the Andreev energy

$$\delta_A(\varphi) = -\frac{\partial E_A}{\partial(\varphi/2)} . \tag{5.2.21}$$

It can be expressed in a unified way, since $-\frac{\partial}{\partial(\varphi/2)} f^2(\varphi) = \sin\varphi$ whatever the case considered, according to

$$\delta_A(\varphi) = \frac{T\sin\varphi}{2E_A(\varphi)} . \tag{5.2.22}$$

In the table below, we give the expressions of this last quantity together with those of Andreev energy and damping coefficient for both S-S and TS-TS junctions as well as the common limits $T \to 1$

	topological	BCS	limit $T \to 1$
$E_A(\varphi)$	$\sqrt{T}\left\lvert\cos\frac{\varphi}{2}\right\rvert$	$\sqrt{1 - T\sin^2\frac{\varphi}{2}}$	$\left\lvert\cos\frac{\varphi}{2}\right\rvert$
$\kappa(\varphi)$	$\sqrt{1 - T\cos^2\frac{\varphi}{2}}$	$\sqrt{T}\left\lvert\sin\frac{\varphi}{2}\right\rvert$	$\left\lvert\sin\frac{\varphi}{2}\right\rvert$
$\delta_A(\varphi)$	$\sqrt{T}\,\mathrm{sign}\left[\cos\frac{\varphi}{2}\right]\sin\frac{\varphi}{2}$	$\frac{T}{2}\dfrac{\sin\varphi}{\sqrt{1 - T\sin^2\frac{\varphi}{2}}}$	$\mathrm{sign}\left[\cos\frac{\varphi}{2}\right]\sin\frac{\varphi}{2}$

Table 5.2: Expressions of E_A, κ and δ_A.

These 2π-periodic quantities are displayed in Fig. 5.1. Several points are to be noticed:

- Andreev energy and damping length κ^{-1} are smaller in the topological case than in the BCS one. Consequently, the Andreev levels in a TS-TS junction reside more deeply inside the gap and their associated spatial wavefunctions are more strongly localized around the junction.

- In both cases, $\varphi = 0$ is the maximum of the Andreev energy and, consequently, a zero of the δ_A quantity and a maximum of the damping length. Zero phase difference is a peculiar point in a S-S junction: Andreev levels are ejected at the boundary of the gap and the damping length diverges.

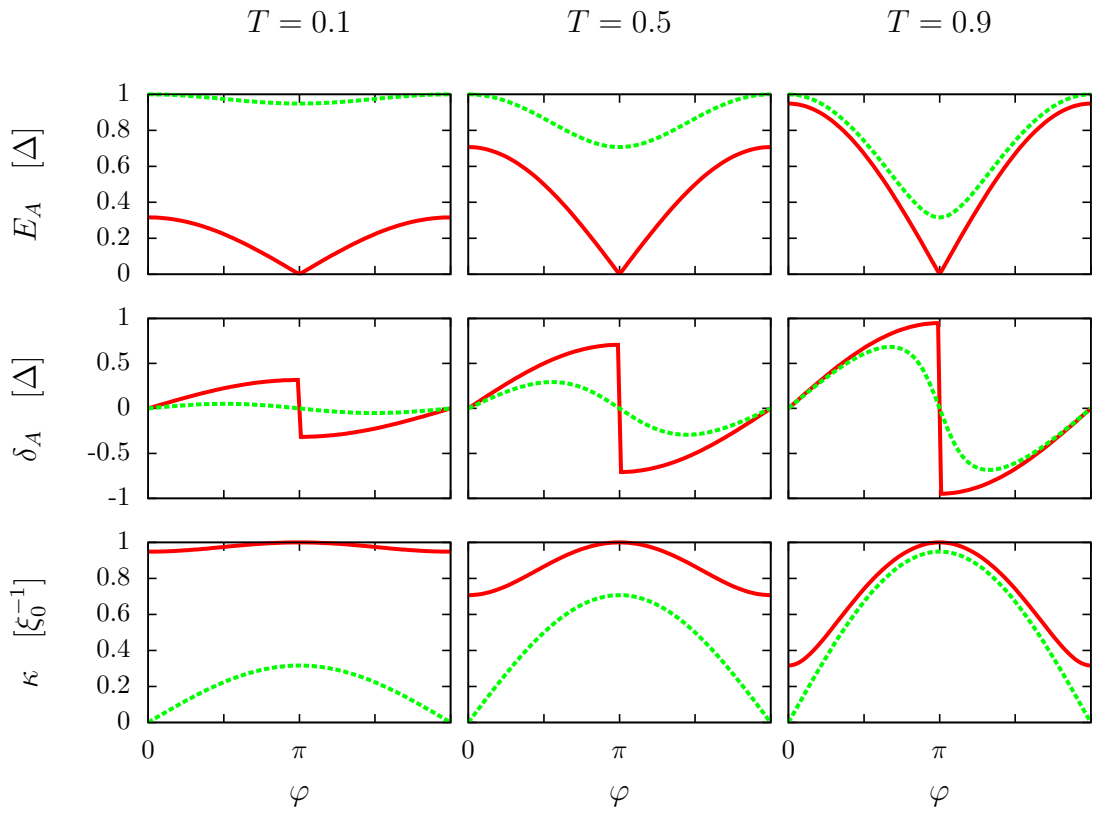

Figure 5.1: Andreev energy E_A, its phase derivative δ_A and damping parameter κ in TS-TS (full red) and S-S (dashed green) junctions, and for several transparencies.

- In the BCS case, the Andreev energy has a strictly positive minimum in $\varphi = \pi$ and consequenlty the δ_A quantity vanishes.
- In the topological case, the Andreev energy vanishes for $\varphi = \pi$ which goes with a discontinuity of the δ_A quantity.

The case $(\varphi = 0, E = 1)$ for BCS superconductors and the case $(\varphi = \pi, E = 0)$ for topological superconductors are pathological cases since the matrix M vanishes. Of particular interest will be the second case because of the emergence of Majorana fermions. To provide a good decoupling of the Andreev pair from continuum states, large transparency $T \sim 1$ and bias operating point $\varphi = \pi$ were envisioned in a S-S junction [182]. In a TS-TS junction, a good decoupling can always be achieved (whatever the transparency) around the zero $\varphi = \pi$ of the Andreev energy. Remark that, within our convention, see Eq. (5.2.18), in a TS-TS junction, the evolution with conserved fermion parity leads to a change from one Andreev level branch to the other $(E_\sigma \to E_{-\sigma})$ through

the crossing $\varphi = \pi$, at the origin of fractional (4π periodic) Josephson effect [145].

5.2.2 Continuum wavefunctions

We can invert $\mathbf{V} = M^{-1}\mathbf{W}$ and access the functions A, B, C, D :

$$\begin{cases} \tilde{A}(\theta,\varphi) = Q(\theta,\varphi)A(\theta,\varphi) = -\sinh\left(\theta - i\frac{\varphi}{2}\right)\left(iT\sin\frac{\varphi}{2} + \frac{(1-T)\,g(-\theta)}{Q^\star(\theta,\varphi)}\left[\sinh\theta\, f(\varphi) + i\sin\frac{\varphi}{2}\, g(-\theta)\right]\right) , \\ \tilde{B}(\theta,\varphi) = Q(\theta,\varphi)B(\theta,\varphi) = \sqrt{(1-T)}\sinh\theta\ g(\theta) , \\ \tilde{C}(\theta,\varphi) = Q(\theta,\varphi)C(\theta,\varphi) = \sqrt{T}\sinh\theta\sinh\left(\theta - i\frac{\varphi}{2}\right) , \\ \tilde{D}(\theta,\varphi) = Q(\theta,\varphi)D(\theta,\varphi) = \sqrt{T(1-T)}\sinh\theta\, f(\varphi) . \end{cases} \tag{5.2.23}$$

The $\tilde{C}$ function is the same in both cases. In order to write the $\tilde{B}$ and $\tilde{C}$ functions, the case-dependent functions f and g are used in a simple way. The expression of the $\tilde{A}$ function is more complicated. Nevertheless, it can be written in a unified way as

$$\tilde{A}(\theta,\varphi) = -\cosh\theta\,\kappa^2(\varphi) - i\sinh\theta\, E_A(\varphi)\delta_A(\varphi) . \tag{5.2.24}$$

Their expressions are given in the table below depending on the nature of the superconductors as well as the limits $T \to 1$.

	topological	BCS	limit $T \to 1$
$Q(\theta,\varphi)$	$\cosh^2\theta - T\cos^2\frac{\varphi}{2}$	$\sinh^2\theta + T\sin^2\frac{\varphi}{2}$	$Q^\star(\theta,\varphi)$
$\tilde{A}(\theta,\varphi)$	$-iT\sinh\left(\theta - i\frac{\varphi}{2}\right)\sin\frac{\varphi}{2} - (1-T)\cosh\theta$	$-iT\sinh\left(\theta - i\frac{\varphi}{2}\right)\sin\frac{\varphi}{2}$	$-i\sin\frac{\varphi}{2}\sinh\left(\theta - i\frac{\varphi}{2}\right)$
$\tilde{B}(\theta,\varphi)$	$\sqrt{1-T}\sinh\theta\cosh\theta$	$\sqrt{1-T}\sinh^2\theta$	0
$\tilde{C}(\theta,\varphi)$	$\sqrt{T}\sinh\theta\sinh\left(\theta - i\frac{\varphi}{2}\right)$	$\sqrt{T}\sinh\theta\sinh\left(\theta - i\frac{\varphi}{2}\right)$	$\sinh\theta\sinh\left(\theta - i\frac{\varphi}{2}\right)$
$\tilde{D}(\theta,\varphi)$	$\sqrt{T(1-T)}\sinh\theta\cos\frac{\varphi}{2}$	$i\sqrt{T(1-T)}\sinh\theta\sin\frac{\varphi}{2}$	0

Table 5.3: A, B, C, D functions in the two cases of junctions and their common limits $T \to 1$.

Their squared modulus are displayed in Figs. 5.2 and 5.3.

Single superconducting wire $T = 1$ and $\varphi = 0$

Only the C function remains so that

$$\chi_{(E,s)}(x) = \frac{\mathrm{e}^{ik_E x}}{\sqrt{l}}\begin{pmatrix}\delta_{s,1}[\chi_e]_E \\ \delta_{s,2}[\chi_h]_E\end{pmatrix} + \frac{\mathrm{e}^{-ik_E x}}{\sqrt{l}}\begin{pmatrix}\delta_{s,4}[\chi_h]_E \\ \delta_{s,3}[\chi_e]_E\end{pmatrix} . \tag{5.2.25}$$

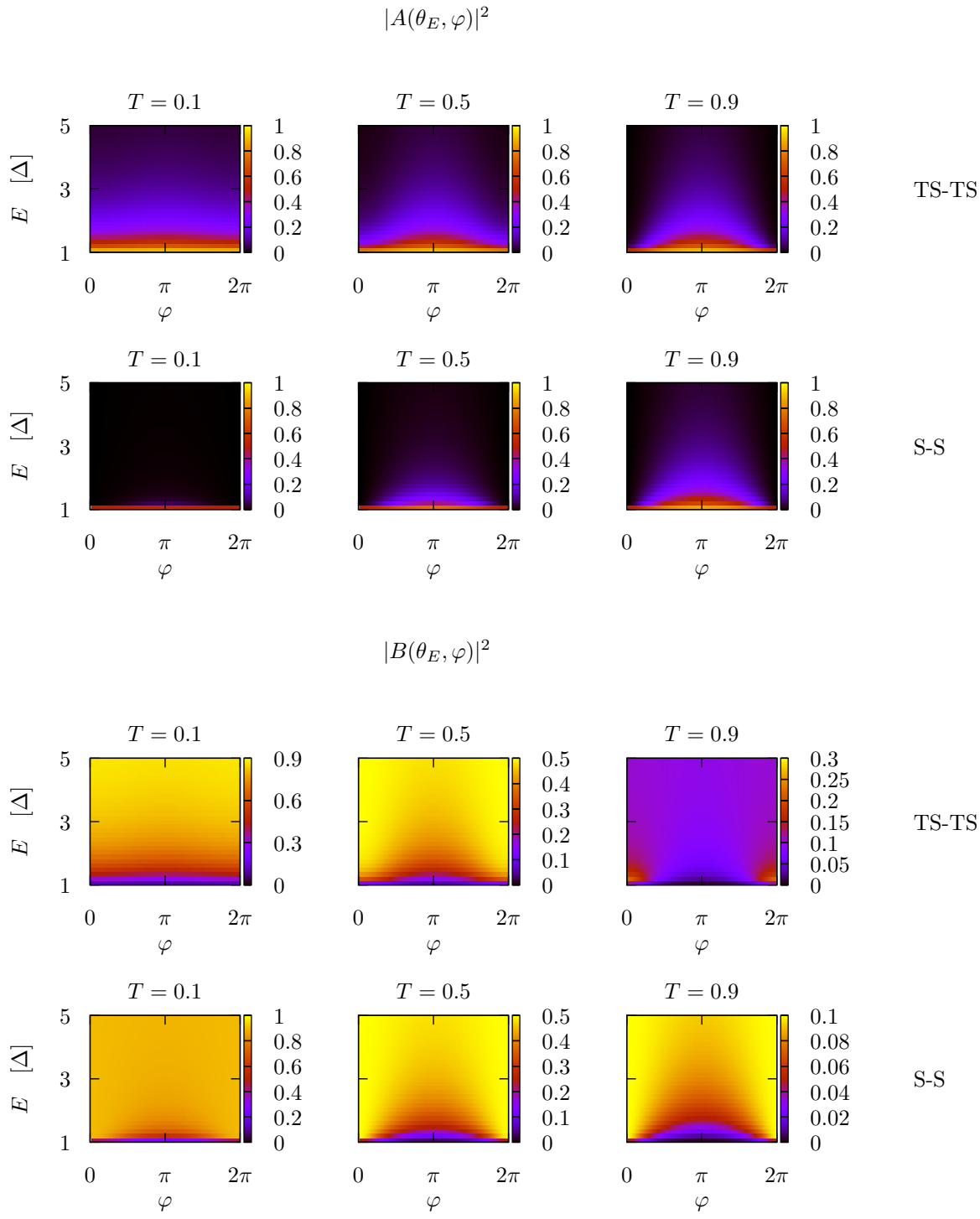

Figure 5.2: Squared modulus of A and B functions, given in table 5.3, in both TS-TS and S-S junctions, in the (φ, E) plane and for several transparencies T.

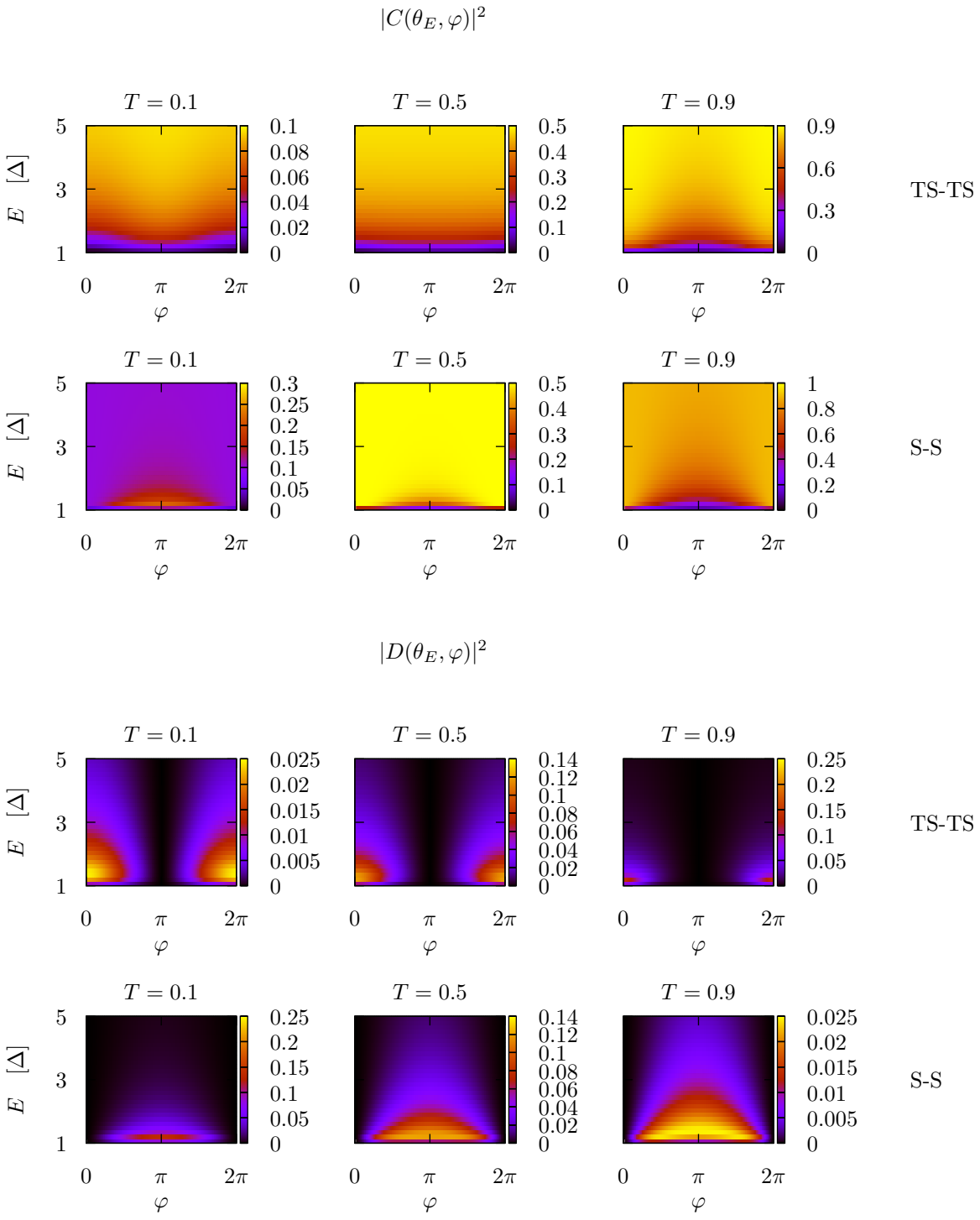

Figure 5.3: Squared modulus of C and D functions, given in table 5.3, in both TS-TS and S-S junctions, in the (φ, E) plane and for several transparencies T.

The case $s = 1$ ($s = 2$) corresponds to the propagation of an electron (hole) from left to right. The case $s = 3$ ($s = 4$) corresponds to the other propagation direction.

Broken junction $T = 0$

C and D functions vanish so that wavefunctions are localized in a single half space.

- In the BCS case, only the B function remains and we get reflection into the same channel. For example, an electron coming from the left is reflected as an electron going to the left, *i.e.*

$$\chi_{(E,s=1)}(x;\varphi) = \Theta(-x)\left[\frac{\mathrm{e}^{ik_E x}}{\sqrt{l}}\begin{pmatrix}[\chi_e]_E\\0\end{pmatrix} + \frac{\mathrm{e}^{-ik_E x}}{\sqrt{l}}\begin{pmatrix}0\\[\chi_e]_E\end{pmatrix}\right] . \tag{5.2.26}$$

- In a topological superconductor, because both A and B functions remain, we have an additional reflection channel. Taking the same example of an electron coming from the left, the reflected wavefunction contains a mixture of electron and hole going to the left, *i.e*

$$\chi_{(E,s=1)}(x;\varphi) = \Theta(-x)\left[\frac{\mathrm{e}^{ik_E x}}{\sqrt{l}}\begin{pmatrix}[\chi_e]_E\\0\end{pmatrix} + \frac{\mathrm{e}^{-ik_E x}}{\sqrt{l}}\tanh\theta\begin{pmatrix}\frac{1}{\sinh\theta}[\chi_h]_E\\[\chi_e]_E\end{pmatrix}\right] . \tag{5.2.27}$$

  Because the A function is inversely proportional to the energy, at high energies this additional reflection channel is suppressed.

High energies $|E| \gg 1$

In both BCS and topological cases

$$A(\theta,\varphi) \to 0\ , \quad B(\theta,\varphi) \to \sqrt{1-T}\ , \quad C(\theta,\varphi) \to \sqrt{T}\,\mathrm{e}^{-i\frac{\varphi}{2}}\ , \quad D(\theta,\varphi) \to 0\ . \tag{5.2.28}$$

An electron or a hole coming from the left ($s = 1$ or $s = 2$ respectively) is reflected with an amplitude $\sqrt{1-T}$ and transmitted with an amplitude $\sqrt{T}\,\mathrm{e}^{-i\frac{\varphi}{2}}$. An electron or a hole coming from the right ($s = 3$ or $s = 4$ respectively) is reflected with an amplitude $-\sqrt{1-T}$ and transmitted with an amplitude $\sqrt{T}\,\mathrm{e}^{i\frac{\varphi}{2}}$.

Continuum wavefunction basis

One can show that A, B, C, D functions are such that there is orthogonality between the columns of Table 5.1, *i.e.*

$$a^*_{(E,s)}a_{(E,s')} + b^*_{(E,s)}b_{(E,s')} + c^*_{(E,s)}c_{(E,s')} + d^*_{(E,s)}d_{(E,s')} = \delta_{ss'}\ , \tag{5.2.29}$$

so that, also using (5.1.45), we get

$$\int_{-l/2}^{+l/2} \mathrm{d}x\, \chi_p^\dagger(x;\varphi)\chi_{p'}(x;\varphi) = \delta_{pp'} \ . \tag{5.2.30}$$

This proves the independence of the four solutions $s = 1..4$. The four wavefunctions $\chi_{(E,s)}$ ($s = 1..4$) form a basis for the solutions of the BdG equation written for the energy E. The orthogonality between the lines of Table 5.1 can also be derived:

$$\sum_s \left|a_{(E,s)}\right|^2 = \sum_s \left|b_{(E,s)}\right|^2 = \sum_s \left|c_{(E,s)}\right|^2 = \sum_s \left|d_{(E,s)}\right|^2 = 1 \ , \tag{5.2.31a}$$

$$\sum_s a^*_{(E,s)}b_{(E,s)} = \sum_s a^*_{(E,s)}c_{(E,s)} = \sum_s a^*_{(E,s)}d_{(E,s)} = \sum_s b^*_{(E,s)}c_{(E,s)} = \sum_s b^*_{(E,s)}d_{(E,s)} = \sum_s c^*_{(E,s)}d_{(E,s)} = 0 \ . \tag{5.2.31b}$$

5.2.3 Andreev bound states

The expressions of the coefficients $a_\sigma, b_\sigma, c_\sigma, d_\sigma$ involve the quantity

$$\mathcal{R}_\sigma(\varphi) = \kappa(\varphi) - \sigma\,\delta_A(\varphi) \ , \tag{5.2.32}$$

and are given in the table below depending on the nature of the superconductors.

	topological	BCS
$\sigma(\varphi)$	$\mathrm{sign}\left[\cos\frac{\varphi}{2}\right]$	$\mathrm{sign}\left[\sin\frac{\varphi}{2}\right]$
$a_\sigma(\varphi)$	$\sigma(\varphi)\sqrt{\frac{\mathcal{R}_\sigma(\varphi)}{2}}$	$-\sigma\,\sigma(\varphi)\sqrt{\frac{\mathcal{R}_\sigma(\varphi)}{2}}$
$b_\sigma(\varphi)$	$-i\sigma\,\sigma(\varphi)\sqrt{\frac{\mathcal{R}_{-\sigma}(\varphi)}{2}}$	$-\sigma\,\sigma(\varphi)\sqrt{\frac{\mathcal{R}_{-\sigma}(\varphi)}{2}}$
$c_\sigma(\varphi)$	$\sqrt{\frac{\mathcal{R}_\sigma(\varphi)}{2}}$	$\sqrt{\frac{\mathcal{R}_\sigma(\varphi)}{2}}$
$d_\sigma(\varphi)$	$-i\sigma\sqrt{\frac{\mathcal{R}_{-\sigma}(\varphi)}{2}}$	$-\sqrt{\frac{\mathcal{R}_{-\sigma}(\varphi)}{2}}$

Table 5.4: Coefficients $a_\sigma, b_\sigma, c_\sigma, d_\sigma$ in the two cases of junctions.

All coefficients $a_\sigma, b_\sigma, c_\sigma, d_\sigma$ have squared modulus equal to $\frac{\mathcal{R}_\pm}{2}$. This last quantity is 2π-periodic. Since $\kappa(2\pi-\varphi) = \kappa(\varphi)$ and $\delta_A(2\pi-\varphi) = -\delta_A(\varphi)$ (cf. Table 5.2), we have $\mathcal{R}_-(\varphi) = \mathcal{R}_+(2\pi-\varphi)$. $\mathcal{R}_+$ is displayed in Fig. 5.4.

Orthogonality between Andreev states

To prove the orthogonality of two different Andreev states, we will use the following result

$$[\tilde{\chi}_e]^\dagger_\sigma[\tilde{\chi}_e]_{-\sigma} = -[\tilde{\chi}_h]^\dagger_\sigma[\tilde{\chi}_h]_{-\sigma} = -i\sigma\kappa \ , \tag{5.2.33}$$

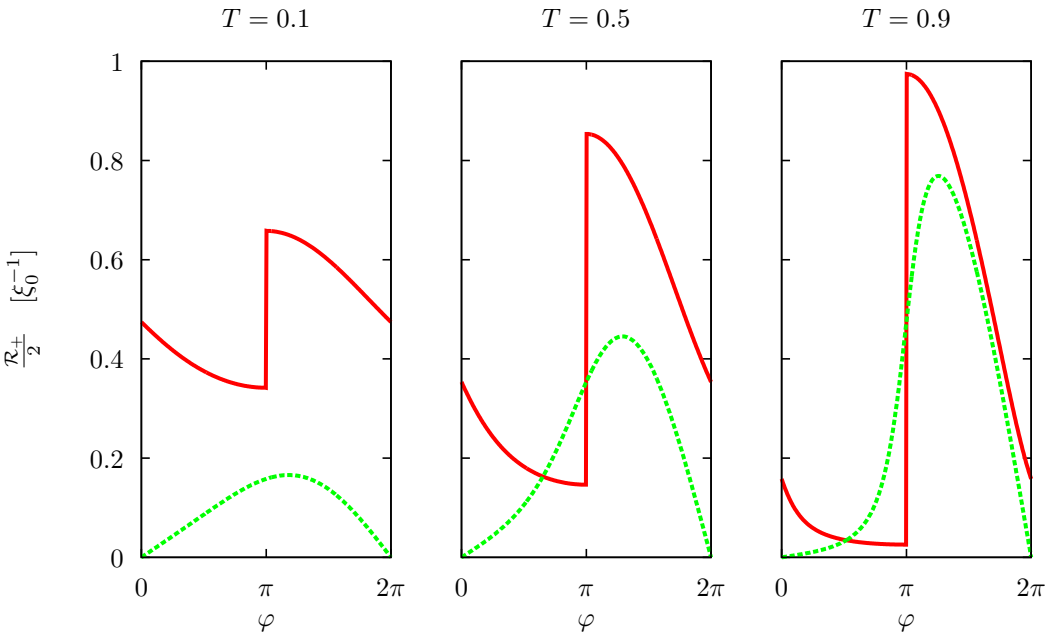

Figure 5.4: $\mathcal{R}_+/2$ in TS-TS (full red) and S-S (dashed green) junctions, and for several transparencies.

which implies that

$$\int_{-\infty}^{+\infty} \mathrm{d}x\, \chi_\sigma^\dagger(x;\varphi)\chi_{-\sigma}(x;\varphi) \propto a_\sigma^*(\varphi)a_{-\sigma}(\varphi) - c_\sigma^*(\varphi)c_{-\sigma}(\varphi) - b_\sigma^*(\varphi)b_{-\sigma}(\varphi) + d_\sigma^*(\varphi)d_{-\sigma}(\varphi)\ . \tag{5.2.34}$$

- In the topological case, we have

$$a_\sigma^* a_{-\sigma} - c_\sigma^* c_{-\sigma} = b_\sigma^* b_{-\sigma} - d_\sigma^* d_{-\sigma} = 0\ . \tag{5.2.35}$$

- In the BCS case, we have

$$d_\sigma = -c_{-\sigma} \in \mathbb{R} \quad \text{and} \quad b_\sigma = -a_{-\sigma} \in \mathbb{R} \quad \Rightarrow \quad a_\sigma^* a_{-\sigma} - b_\sigma^* b_{-\sigma} = c_\sigma^* c_{-\sigma} - d_\sigma^* d_{-\sigma} = 0\ . \tag{5.2.36}$$

Finally, the two Andreev states form a basis for subgap states

$$\int_{-\infty}^{+\infty} \mathrm{d}x\, \chi_\sigma^\dagger(x;\varphi)\chi_{\sigma'}(x;\varphi) = \delta_{\sigma\sigma'}\ . \tag{5.2.37}$$

An important relation in a TS-TS junction

For topological superconductors, we have the following relations

$$d_\sigma = -i\sigma\, c_{-\sigma} \quad \text{and} \quad b_\sigma = -i\sigma\, a_{-\sigma}\ , \tag{5.2.38}$$

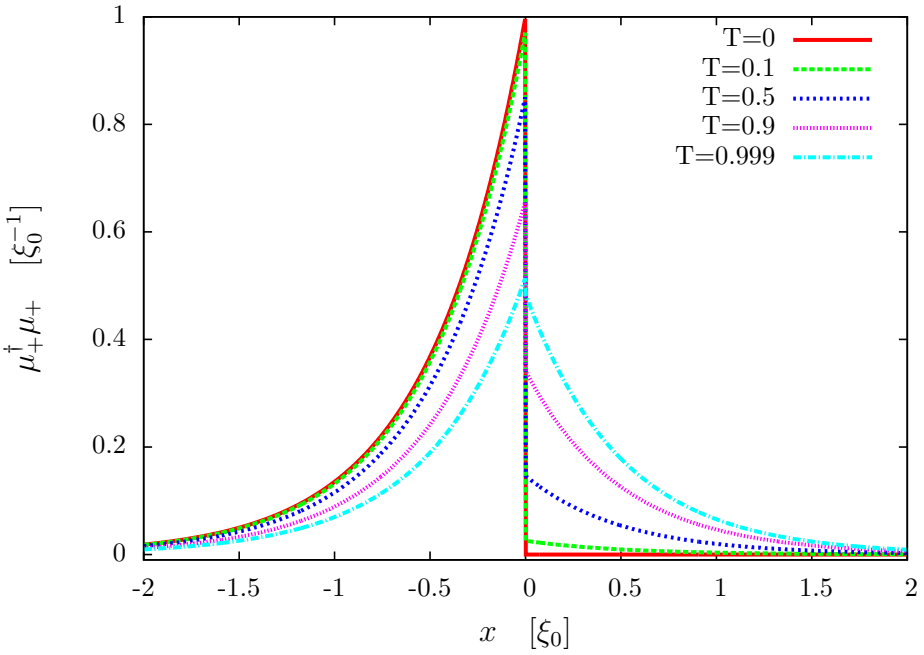

Figure 5.5: Majorana probability density ($\varphi = \pi$) around the junction position $x = 0$ for several transparencies.

that provide the important result

$$a_\sigma^* a_{-\sigma} + b_\sigma^* b_{-\sigma} = c_\sigma^* c_{-\sigma} + d_\sigma^* d_{-\sigma} = 0 \ . \tag{5.2.39}$$

5.2.4 Majorana states in a TS-TS junction

The annihilation operator c_σ for the quasiparticle with energy $E_\sigma = \sigma E_A$ is obtained through the projection

$$c_\sigma = \int \mathrm{d}x \, \chi_\sigma^\dagger(x) \underline{\Psi}(x) \ . \tag{5.2.40}$$

Because we have $[C\chi_\sigma]^* = -i\chi_{-\sigma}$ which originates from the relation (5.2.39), the pseudo-reality constraint $[C\underline{\Psi}]^* = \underline{\Psi}$ yields $c_\sigma^\dagger = ic_{-\sigma}$ (see Eq. (5.1.36)). Majorana wavefunctions are obtained as the following superpositions of zero-energy Andreev wavefunctions

$$\mu_\sigma(x) = \hat{\chi}_\sigma(x; \varphi = \pi) \quad \text{with} \quad \hat{\chi}_\sigma = \frac{\chi_\sigma - i\,\chi_{-\sigma}}{2} \ . \tag{5.2.41}$$

They verify the pseudo-reality constraint $[C\mu_\sigma]^* = \mu_\sigma$ so that the associated operators are Majorana fermions

$$\gamma^\sigma = 2 \int \mathrm{d}x \, \mu_\sigma^\dagger(x) \underline{\Psi}(x; \varphi = \pi) = (\gamma^\sigma)^\dagger \ , \quad (\gamma^\sigma)^2 = 1 \ . \tag{5.2.42}$$

These operators enter the definition of the Dirac fermion c_+ according to

$$c_+ = \frac{\gamma^+ - i\gamma^-}{2} \ . \tag{5.2.43}$$

The Majorana wavefunctions read

$$\mu_\sigma(x) = \frac{\mathrm{e}^{-|x|}}{4}\left(\sqrt{1-\sigma\sqrt{T}} - \sigma\ \mathrm{sign}(x)\sqrt{1+\sigma\sqrt{T}}\right)\mathrm{e}^{i\sigma\,\mathrm{sign}(x)\frac{\pi}{4}\tau_z}\begin{pmatrix}1\\ \sigma\\ \sigma\\ -1\end{pmatrix} \ . \tag{5.2.44}$$

The Majorana probability density functions are given by

$$\mu_\sigma^\dagger(x)\mu_\sigma(x) = \frac{\mathrm{e}^{-2|x|}}{2}\left[1 - \sigma\sqrt{1-T}\,\mathrm{sign}(x)\right] \ . \tag{5.2.45}$$

We display $\mu_+^\dagger\mu_+$ in Fig. 5.5 ($\mu_-^\dagger\mu_-$ is symmetric with respect to the junction position). For $T = 0$, each Majorana bound state localizes on a single side of the junction.

5.3 Andreev sector

At a given energy E, electron-like and hole-like excitations propagating in the same direction carry opposite currents so that the continuum contribution to the Josephson current vanishes

$$\left(\sum_s \mathcal{I}_{(E,s)(E,s)}\right) n(E) = 0 \ . \tag{5.3.1}$$

Then, the Josephson current is entirely carried by Andreev bound states, as expected in short constrictions [176–178]. Restricting to the Andreev subspace, in the basis $\sigma = (+,-)$, the current matrix is given by

	topological	BCS
$\frac{I_A(\varphi)}{\delta_A(\varphi)}$	$\begin{pmatrix}-1 & 0\\ 0 & 1\end{pmatrix}$	$\begin{pmatrix}-1 & -i\sqrt{1-T}\,\tan\frac{\varphi}{2}\\ i\sqrt{1-T}\,\tan\frac{\varphi}{2} & 1\end{pmatrix}$

Table 5.5

The Josephson current originates in diagonal elements of this matrix and reads

$$\mathcal{I}(\varphi) = \frac{\delta_A(\varphi)}{d_\star}\tanh\frac{\beta E_A(\varphi)}{2} \ . \tag{5.3.2}$$

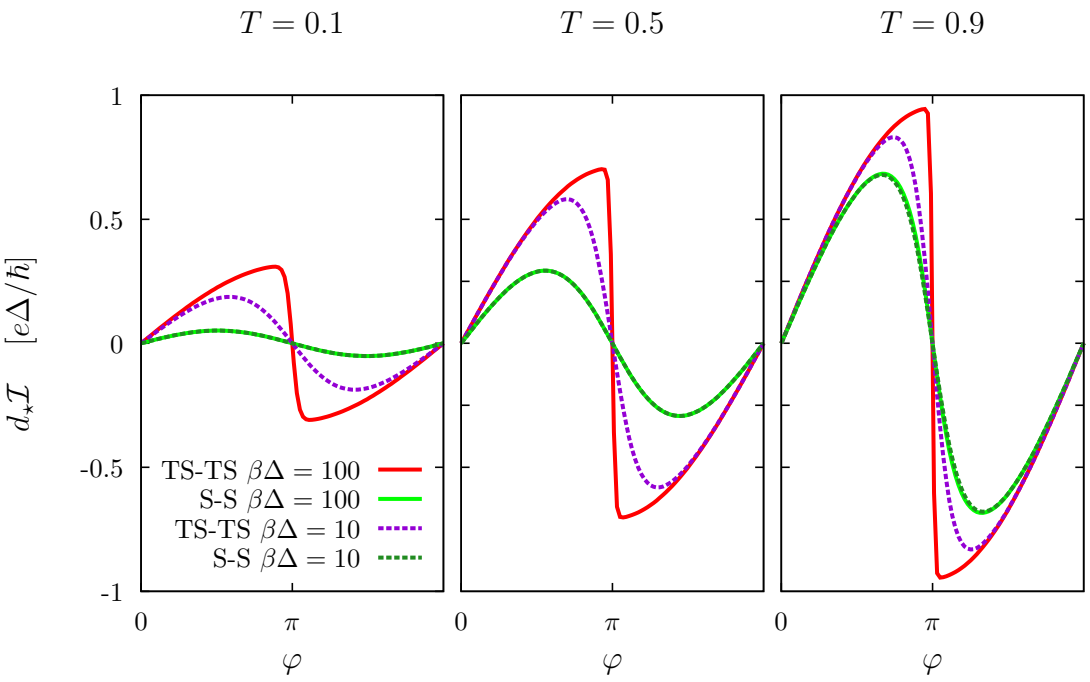

Figure 5.6: Josephson current in TS-TS and S-S junctions for several transparencies and two different temperatures.

This result is displayed in Fig. 5.6 for two different temperatures. For low temperatures, $d_\star\mathcal{I}$ is given by the function δ_A (given in Fig. 5.1) except around the vanishing point of the Andreev energy in a TS-TS junction (for $\varphi = \pi$) where finite temperature effects are noticeable. In the zero-temperature limit, the critical current scales as the "universal limit" $e\Delta/\hbar$ [177, 178]. It is multiplied by $\sqrt{T}/2$ in a TS-TS junction (the δ_A quantity is an increasing function on the interval $[0, \pi]$ reaching its maximum $\sqrt{T}$ in π) and by $\sqrt{-T\cos\varphi_0}$ in a S-S junction, where $\varphi_0 \in [\pi/2, \pi]$ is the position of the inflexion point of the BCS Andreev energy (maximum of the δ_A quantity). Although the current in a TS-TS junction is 4π periodic as long as fermion parity is conserved (fractional Josephson effect), the average (over all parity states) results in a 2π periodicity [156, 180]. Because current and Hamiltonian eigenstates are different in the BCS case, the currents carried by Andreev levels $\pm\delta_A(\varphi)$ do not coincide with the current operator eigenvalues $\pm T\Delta\sin\frac{\varphi}{2}$ [183]. Consequently, transitions between BCS Andreev levels give rise to a noise consisting in Dirac delta peaks at frequency $\omega = \pm 2E_A$

$$S_{AA}(\omega,\varphi) = \frac{2\pi}{d_\star}\left|\mathcal{I}_{+-}(\varphi)\right|^2\left\{\left(1-n[E_A(\varphi)]\right)^2\delta\left[\omega-2E_A(\varphi)\right] + \left(n[E_A(\varphi)]\right)^2\delta\left[\omega+2E_A(\varphi)\right]\right\}. \tag{5.3.3}$$

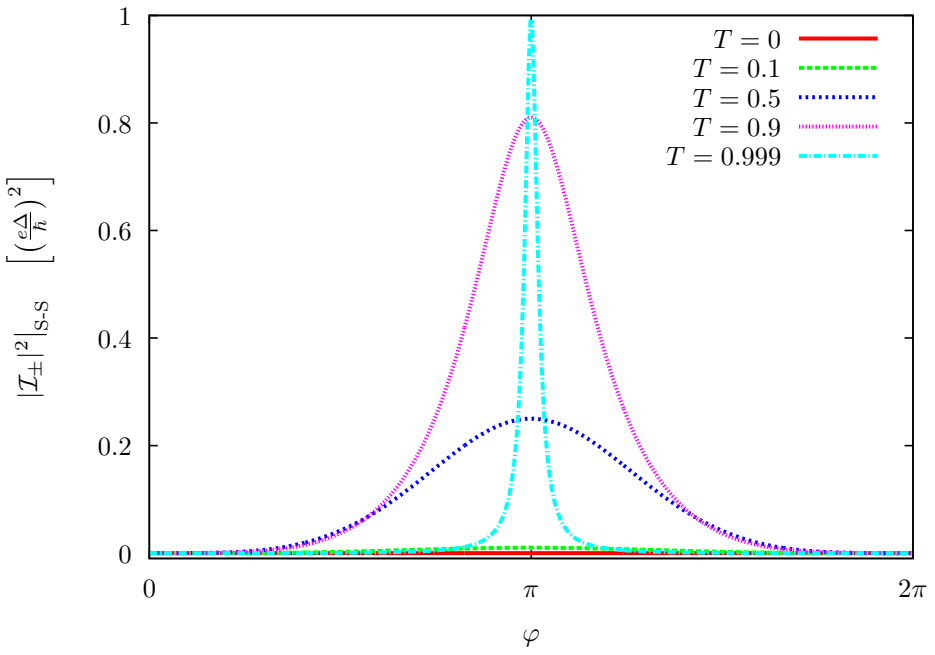

Figure 5.7: Phase dependence of the noise at $\omega = \pm 2E_A$ due to transitions between Andreev levels in a S-S junction, for several transparencies.

The (non-vanishing) squared modulus of the out-of-diagonal element reads

$$|\mathcal{I}_{+-}(\varphi)|^2\Big|_{\text{S-S}} = \frac{T^2(1-T)\sin^4\frac{\varphi}{2}}{1-T\sin^2\frac{\varphi}{2}} \ . \tag{5.3.4}$$

This result has been obtained in Ref. [179] and we display the phase dependence in Fig. 5.7. Remark that it vanishes for $\varphi = 0$ as a consequence of the expulsion of Andreev levels to the continuum and that it reaches a maximum $T^2\Delta^2$ in $\varphi = \pi$. In the topological case, the current matrix is diagonal in the basis of Andreev states so that there is no contribution to the noise at $\omega = \pm 2E_A$:

$$S_{AA}(\omega,\varphi)|_{\text{TS-TS}} = 0 \ . \tag{5.3.5}$$

This is closely related to the emergence of zero-energy Majorana modes. More precisely, the relation $[C\chi_\sigma]^* \propto \chi_{-\sigma}$ crucial in the construction of Majorana wavefunctions (cf. Section 5.2.4) and the result $\mathcal{I}_{+-} = 0$ both originate in the relation (5.2.39). Physically, the absence of direct transitions between Andreev levels in the topological case is related to fermion-parity conservation [156]. Let us conclude our study of the Andreev sector by giving the zero frequency

noise

$$S_A(\omega,\varphi) = \frac{4\pi\delta_A^2(\varphi)}{d_\star}\, n[E_A(\varphi)]\big(1-n[E_A(\varphi)]\big)\,\delta(\omega)\ . \tag{5.3.6}$$

This result has also been obtained in Ref. [179] for a S-S junction. In such a junction with transparency $T<1$, lowering temperature suppresses this noise resonance since the occupation factor $n(1-n)$ vanishes. This holds also in a TS-TS junction for all φ except $\varphi=\pi \bmod(2\pi)$. At the points of Andreev level crossings the zero-frequency noise (5.3.6) may be present at any low temperature provided that the junction is in a mixed parity state, with (temperature independent) $n(0)=1/2$.

5.4 Non-resonant frequency noise

Both Continuum-Continuum (CC) and Andreev-Continuum (AC) transitions contribute to the non-resonant noise. We examine both noise contributions separately (Sections 5.4.1 and 5.4.2) then we study their competition (Section 5.4.3). Note that in a TS-TS junction, the total non-resonant noise is the total finite frequency noise since transitions inside the Andreev sector are noiseless due to topological protection. In a S-S junction, two Dirac delta peaks at $\omega=\pm\omega_{AA}$, with $\omega_{AA}=2E_A$, emerge on top of that as a consequence of transitions between Andreev states. The sums over continuum indexes can be decomposed as $\sum_p=\sum_E\sum_s$ and we use the dispersion relation to perform the substitution $\sum_E\to\frac{l}{2\pi v_F}\int \mathrm{d}E\,\Theta\left(|E|-\Delta\right)\frac{|E|}{\sqrt{E^2-\Delta^2}}$. Except when mentioned (when investigating finite temperature effects at the end of this section), all figures which are presented in this section have been obtained with a small temperature $\beta^{-1}=0.01\,[\Delta]$.

5.4.1 Continuum-continuum transitions

Let us adopt the following notation

$$\mathcal{I}_{pp'}(\varphi)=\mathcal{I}_{(E,s)(E',s')}(\varphi)\equiv\tilde{\mathcal{I}}_{ss'}(\theta_E,\theta_{E'},\eta_E,\eta_{E'},\varphi)\ . \tag{5.4.1}$$

We define

$$\mathcal{S}_{ss'}(\theta,\theta',\eta,\eta',\varphi)=l^2\cosh\theta\cosh\theta'\left|\tilde{\mathcal{I}}_{ss'}(\theta,\theta',\eta,\eta',\varphi)\right|^2 \tag{5.4.2}$$

and we introduce the transformations $\mathcal{T}_1$ et $\mathcal{T}_2$ according to

$$\left[\mathcal{T}_1\mathcal{S}_{ss'}\right](\theta,\theta',\eta,\eta',\varphi)=\mathcal{S}_{ss'}(-\theta,-\theta',\eta,\eta',\varphi)\ , \tag{5.4.3}$$

$$\left[\mathcal{T}_2\mathcal{S}_{ss'}\right](\theta,\theta',\eta,\eta',\varphi)=\mathcal{S}_{ss'}(\theta,\theta',\eta,\eta',-\varphi)\ . \tag{5.4.4}$$

In the calculation of the noise due to CC transitions, we will need to calculate

$$\sum_{s,s'=1..4} \mathcal{S}_{ss'} = \{1 + \mathcal{T}_1 + \mathcal{T}_2 + \mathcal{T}_1\mathcal{T}_2\} \sum_{s'=1..4} \mathcal{S}_{1s'} \ , \tag{5.4.5}$$

where we have used the relations (5.2.2). Some algebraic manipulations yield

$$\sum_{s'=1..4} \mathcal{S}_{1s'}(\theta,\theta',\eta,\eta',\varphi) = \frac{\sinh^2\theta\,\sinh^2\theta'}{Q(\theta,\varphi)\,Q(\theta',\varphi)}\,T\left[\cosh\theta\cosh\theta' + \eta\eta'\rho(\varphi)E_A^2(\varphi)\right] \ , \tag{5.4.6}$$

where the ρ function is defined as

$$\rho = 1 - (1-\varepsilon)\frac{1-T}{T}\,\frac{1-E_A^2}{E_A^2} \ , \tag{5.4.7}$$

and where $\varepsilon = 1$ in a TS-TS junction and $\varepsilon = -1$ in a S-S junction (it appears in calculations as $\varepsilon = f(-\varphi)/f(\varphi) = g(-\theta)/g(\theta)$). Note that ρ is simply 1 in the topological case. The sum (5.4.6) is invariant under $\mathcal{T}_1$ and $\mathcal{T}_2$ transformations so that

$$\sum_{s,s'=1..4} \mathcal{S}_{ss'} = 4 \sum_{s'=1..4} \mathcal{S}_{1s'} \ . \tag{5.4.8}$$

Then we can write the contribution to the noise due to CC transitions as follows

$$S_{CC}(\omega,\varphi) = \frac{2}{d_\star}\,\frac{T}{\pi}\int \mathrm{d}E\, n(E)\left[1-n(\omega+E)\right]\left[E(\omega+E)+\rho(\varphi)E_A^2(\varphi)\right] R\left[E,E_A(\varphi)\right] R\left[\omega+E,E_A(\varphi)\right] \tag{5.4.9}$$

where we define

$$R(E_1,E_2) = \Theta\left(|E_1|-1\right)\mathrm{sign}(E_1)\,\frac{\sqrt{E_1^2-1}}{E_1^2-E_2^2} \ . \tag{5.4.10}$$

In the zero temperature limit, the occupation factor $n(E)\left[1-n(\omega+E)\right]$ is either 0 or 1: it is 1 when $E<0$ and $\omega+E>0$ so that

$$\int \mathrm{d}E\, n(E)\left[1-n(\omega+E)\right] \quad \underset{\beta\gg 1}{\to} \quad \int_{-\omega}^{0} \mathrm{d}E \tag{5.4.11}$$

The quantity $R(E,E_A)R(\omega+E,E_A)$ which appears in the integrand (5.4.9) does not vanish only if $E<-1$ and $\omega+E>1$ so that there is a cut-off $S_{CC}(\omega<2,\varphi)=0$ and

$$S_{CC}(\omega,\varphi) \underset{\beta\gg 1}{\sim} \Theta(\omega-2)\,\frac{2}{d_\star}\,\frac{T}{\pi}\int_{1-\omega}^{-1} \mathrm{d}E\,\left[E(\omega+E)+\rho(\varphi)E_A^2(\varphi)\right] R\left[E,E_A(\varphi)\right] R\left[\omega+E,E_A(\varphi)\right] \equiv S^\star_{CC}(\omega,\varphi) \ . \tag{5.4.12}$$

Fig. 5.8 displays the noise maps for different transparencies and in both TS-TS and S-S junctions. There is little dependence on the phase φ, at least for sufficiently large ω, while the magnitude seems to be affected by the transparency in a quasi linear way despite the non trivial dependences on φ and T introduced by E_A (and ρ in the BCS case) which appear in the integrand (5.4.12).

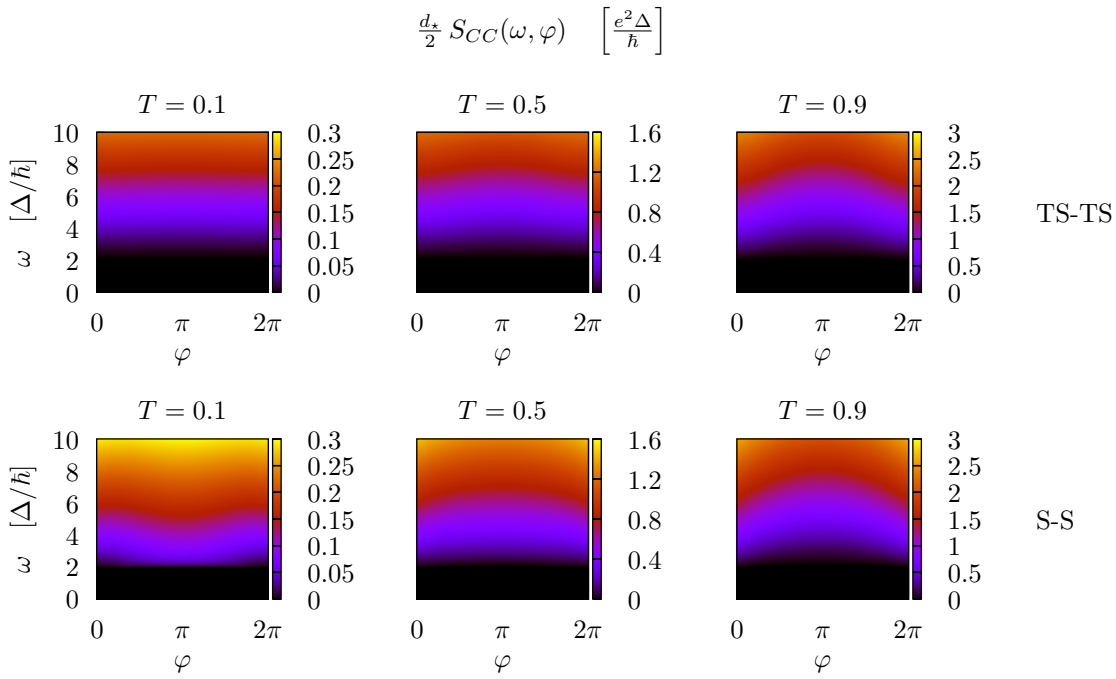

Figure 5.8: Noise $S_{CC}(\omega, \varphi)$ (due to continuum-continuum transitions) in both TS-TS and S-S junctions and for three different transparencies.

In the six first panels of Fig. 5.9, constant φ cuts are displayed with different energy evolutions depending on the phase difference. Nevertheless, in a TS-TS junction, lowering transparency reduces Andreev energy variations ($E_A(\varphi) \to 0$) and the noise is therefore essentially phase independent (constant φ cuts collapse on a single curve). The threshold $\omega = 2\,[\Delta]$ is clearly noticeable in Fig. 5.9.

Behavior near the threshold $0 < \omega - 2 \ll 1$

Just above this threshold, we can derive that the dependence is quadratic. Indeed, since

$$R(1+\epsilon, E_A) \underset{\epsilon\to 0^+}{\sim} \frac{\sqrt{2\epsilon}}{\kappa^2}\ , \tag{5.4.13}$$

we can prove that

$$\frac{d_\star}{2}\, S^\star_{CC}(2+\delta,\varphi) \underset{\delta\to 0^+}{\sim} \frac{T}{\pi}\,\frac{2}{\kappa^2(\varphi)}\left[1-\rho(\varphi)E_A^2(\varphi)\right]\int_0^\delta \mathrm{d}\epsilon\,\sqrt{\epsilon(\delta-\epsilon)}\ . \tag{5.4.14}$$

Then we use the antiderivative

$$\int^u \mathrm{d}v\,\sqrt{v(x-v)} = \frac{1}{4}\left((2u-x)\sqrt{u(x-u)} + x^2\tan^{-1}\left[\sqrt{\frac{u}{x-u}}\right]\right) \tag{5.4.15}$$

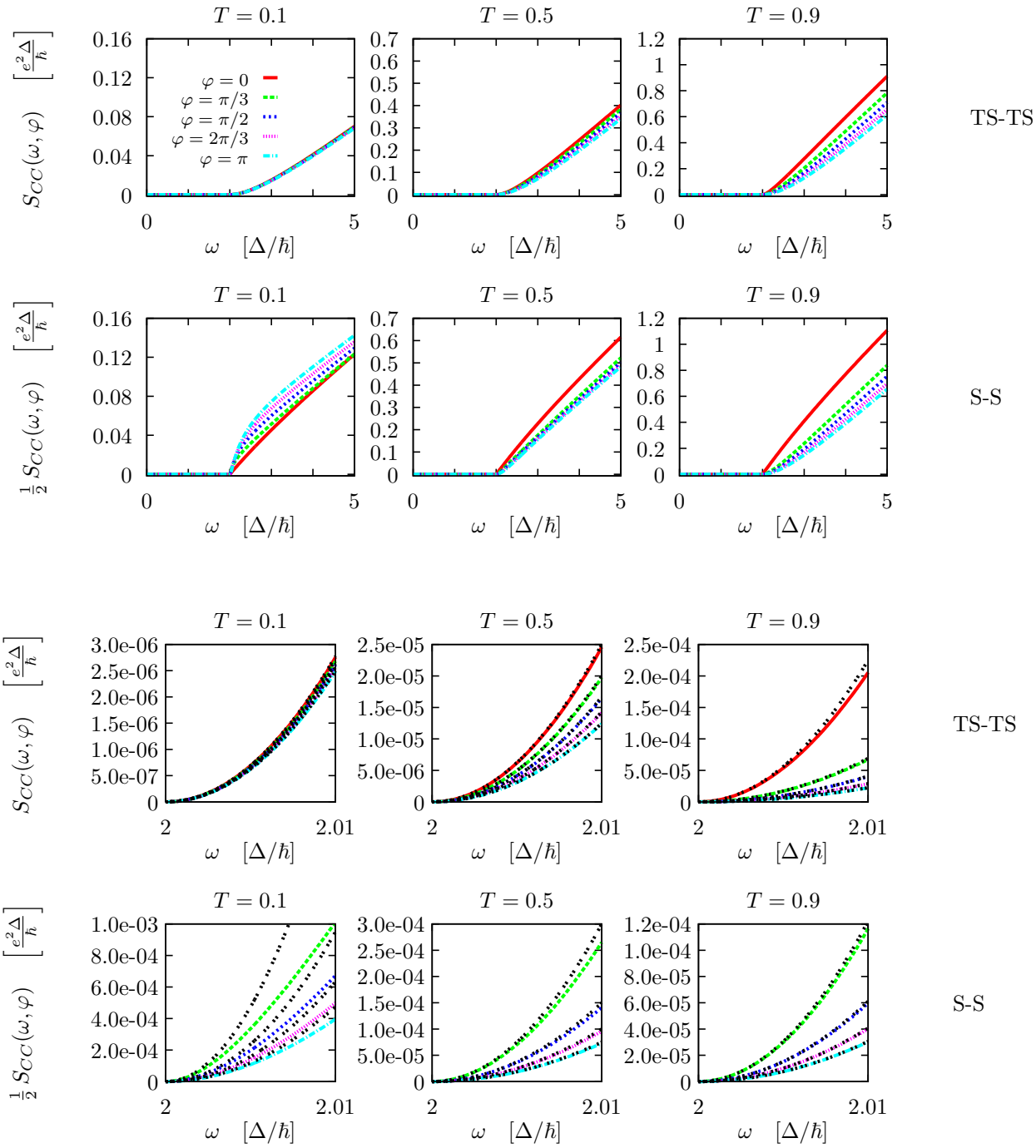

Figure 5.9: Constant φ cuts (the key is given in the first panel) of the noise $S_{CC}(\omega,\varphi)$ (Fig. 5.8). The six last panels are enlargements just above the threshold $2\,[\Delta]$. The black lines are the approximations (5.4.16) (in a S-S junction, this approximation is not valid for $\varphi = 0$).

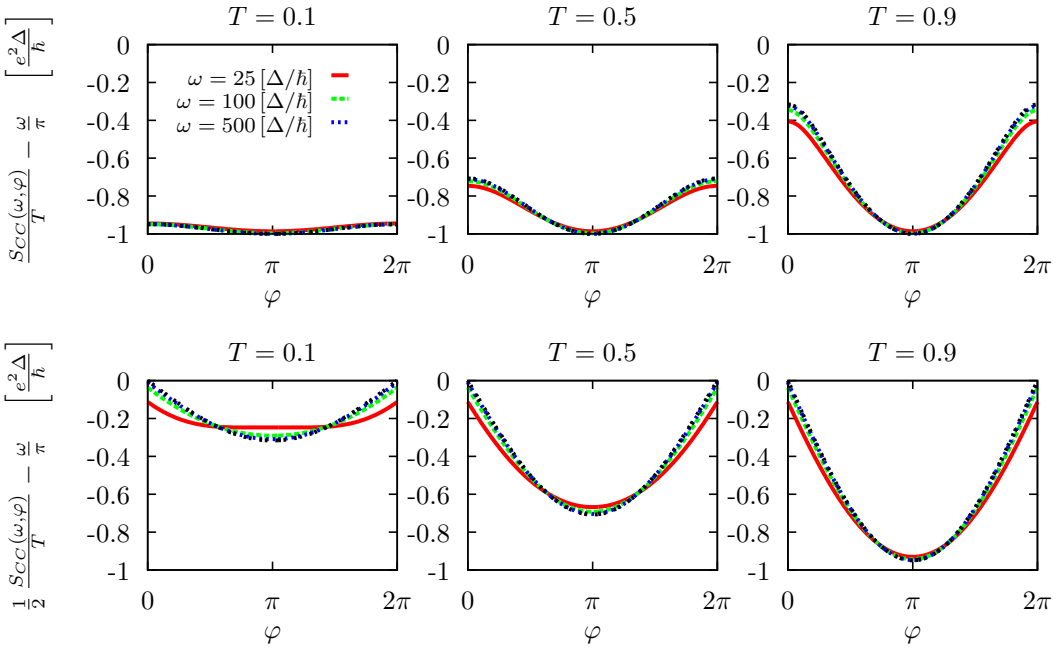

Figure 5.10: Constant ω cuts (the key is given in the first panel) of the noise $S_{CC}(\omega,\varphi)$ (Fig. 5.8), renormalized by the transparency T and for which the linear predominant term at large energies has been substracted. The black lines are the high energy expectations according to (5.4.25) that is $-\kappa(\varphi)$.

in order to establish the following approximation:

$$\frac{d_\star}{2}\, S^\star_{CC}(\omega,\varphi) \underset{\omega\to 2^+}{\sim} \frac{T}{4}\,\frac{1-\rho(\varphi)E_A^2(\varphi)}{\kappa^4(\varphi)}\,(\omega-2)^2 \ . \tag{5.4.16}$$

In the topological case, formula (5.4.16) can be further simplified into

$$S^\star_{CC}(\omega,\varphi)|_{\text{TS-TS}} \underset{\omega\to 2^+}{\sim} \frac{T}{4\,\kappa^2(\varphi)}\,(\omega-2)^2 \ . \tag{5.4.17}$$

This approximation is compared to the numerical results in the six last panels of Fig. 5.9. It is very accurate in a TS-TS junction (except for parameters such that $\kappa \to 0$, *i.e.* for $T \to 1$ and $\varphi \to 0$). In the BCS case, this is not valid for $\varphi = 0$ whatever the transparency since the κ function vanishes. For a given phase $\varphi \neq 0$ in a S-S junction, the parabolic approximation (5.4.16) has a more restricted domain of validity for small transparency since the κ function is proportional to $\sqrt{T}$. Whatever the set of parameters such that the approximation (5.4.16) is valid, this is responsible for a smooth cut-off (since there is zero slope at threshold).

Remark: For $\varphi = 0$ in a S-S junction, we have a linear behavior. Indeed, on can easily prove

that

$$S^{\star}_{CC}(2+\delta,\varphi=0)|_{\text{S-S}} \underset{\delta\to 0^+}{\sim} \frac{T}{\pi}\,\delta\int_0^{\delta}\mathrm{d}\epsilon\,\frac{1}{\sqrt{\epsilon(\delta-\epsilon)}}\ . \tag{5.4.18}$$

Then, using the antiderivative

$$\int^{u}\mathrm{d}v\,\frac{1}{\sqrt{v(x-v)}}=2\tan^{-1}\left[\sqrt{\frac{u}{x-u}}\right]\ , \tag{5.4.19}$$

we get

$$S^{\star}_{CC}(\omega,\varphi=0)|_{\text{S-S}} \underset{\omega/\Delta\to 2^+}{\sim} T\,(\omega-2)\ . \tag{5.4.20}$$

Behavior at large energies $\omega \gg 1$

We can prove that (5.4.12) diverges at high energy and the dominant term is

$$\frac{d_\star}{2}\,S^{\star}_{CC}(\omega,\varphi) \underset{\omega\gg 1}{\sim} \frac{T}{\pi}\int_{1-\omega}^{-1}\mathrm{d}E\,P\left[E,E_A(\varphi)\right]P\left[\omega+E,E_A(\varphi)\right]\ , \tag{5.4.21}$$

where we introduce

$$P(E_1,E_2)=E_1R(E_1,E_2)\ . \tag{5.4.22}$$

We can have an approximation of this integral by cutting the interval in two equal parts and approximating $P(E,E_A)$ on the first subinterval and $P(\omega+E,E_A)$ on the second one by their limits 1

$$\int_{1-\omega}^{-1}\mathrm{d}E\,P(E,E_A)P(\omega+E,E_A)=\int_{1-\omega}^{-\frac{\omega}{2}}\mathrm{d}E\,P(\omega+E,E_A)+\int_{-\frac{\omega}{2}}^{-1}\mathrm{d}E\,P(E,E_A)\ . \tag{5.4.23}$$

Indeed, we know the antiderivative of $P(x,y)$ considered as a function of x:

$$L(x,y)=\int^{x}\mathrm{d}x_1\,P(x_1,y)=\sqrt{x^2-1}-\sqrt{1-y^2}\,\tan^{-1}\left[\sqrt{\frac{x^2-1}{1-y^2}}\right]\quad\text{for}\quad x\geqslant 0\ . \tag{5.4.24}$$

We obtain

$$\frac{d_\star}{2}\,S^{\star}_{CC}(\omega,\varphi) \underset{\omega\gg 1}{\sim} T\left[\frac{\omega}{\pi}-\kappa(\varphi)\right]+\mathcal{O}\left(\frac{1}{\omega}\right)\ . \tag{5.4.25}$$

In Fig. 5.10, we verify the validity of this expansion by substracting the expected linear term and checking that the result is compatible for sufficiently high energies with the $\kappa(\varphi)$ profile, given in Fig. 5.1. We see that the convergence is slower in the BCS case and for small transparency: κ takes lower values (and even vanishes for $\varphi=0$).

5.4.2 Andreev-continuum transitions

In a very similar way with what has been done in the previous section, we adopt the following notation

$$\mathcal{I}_{p\sigma}(\varphi) = \mathcal{I}_{(E,s)\sigma}(\varphi) \equiv \tilde{\mathcal{I}}_{s\sigma}(\theta_E, \gamma_\sigma(\varphi), \eta_E, \sigma, \varphi) \tag{5.4.26}$$

and we define

$$\mathcal{S}_{s\sigma}(\theta, \gamma, \eta, \sigma, \varphi) = l \cosh\theta \left|\tilde{\mathcal{I}}_{s\sigma}(\theta, \gamma, \eta, \sigma, \varphi)\right|^2 \ . \tag{5.4.27}$$

Then, we get

$$\sum_s \mathcal{S}_{s\sigma}(\theta, \gamma(\varphi), \eta, \sigma, \varphi) = \frac{\kappa(\varphi)\sinh^2\theta}{Q(\theta,\varphi)} T\left[\cosh\theta + \sigma\eta\,\rho(\varphi)E_A(\varphi)\right] \ , \tag{5.4.28}$$

where the ρ function has already been encountered in the calculation of the noise due to CC transitions and is defined in Eq. (5.4.7). Let us define

$$\mathcal{M}_\sigma(E,\varphi) = \sum_s \mathcal{S}_{s\sigma}(\theta_E, \gamma(\varphi), \eta_E, \sigma, \varphi) = \frac{\kappa(\varphi)(E^2-1)}{E^2 - E_A^2(\varphi)} T\left[E + \sigma\,\rho(\varphi)E_A(\varphi)\right]\mathrm{sign}(E) \ . \tag{5.4.29}$$

Then we obtain the contribution due to AC transitions as

$$S_{AC}(\omega,\varphi) = \frac{1}{d_\star}\sum_{\sigma=\pm} n\left[\sigma E_A(\varphi)\right]\left(1 - n\left[\omega + \sigma E_A(\varphi)\right]\right) Q_\sigma\left[\omega + \sigma E_A(\varphi), \varphi\right] \ . \tag{5.4.30}$$

The function Q_σ is given by

$$Q_\sigma(\omega,\varphi) = \frac{\Theta\left(|\omega|-1\right)}{\sqrt{\omega^2-1}}\sum_\epsilon \mathcal{M}_{\epsilon\sigma}(\epsilon\omega,\varphi) = 2T\,\kappa(\varphi)\left[\omega + \sigma\rho(\varphi)E_A(\varphi)\right] R\left[\omega, E_A(\varphi)\right] \ , \tag{5.4.31}$$

where the R function has already been introduced in (5.4.10). In the topological case, we can further simplify this expression according to

$$Q_\sigma(\omega,\varphi)|_{\text{TS-TS}} = 2T\,\kappa(\varphi)\,\Theta\left(|\omega|-1\right)\mathrm{sign}\,\omega\,\frac{\sqrt{\omega^2-1}}{\omega - \sigma E_A(\varphi)} \ . \tag{5.4.32}$$

In a S-S junction with zero phase difference, this noise contribution vanishes as the Andreev levels are expelled to the continuum. In the zero temperature limit, noise is obtained only for positive frequencies, there is a cut-off $S^\star_{AC}[\omega < 1 - E_A(\varphi), \varphi] = 0$ and

$$\begin{aligned} S_{AC}(\omega,\varphi) \underset{\beta\gg1}{\sim} \frac{2}{d_\star} T\,\kappa(\varphi)\,\Theta(\omega)\Big\{ & n\left[-E_A(\varphi)\right] R\left[\omega - E_A(\varphi), E_A(\varphi)\right]\left(\omega - \left[1+\rho(\varphi)\right]E_A(\varphi)\right) \\ & + n\left[E_A(\varphi)\right] R\left[\omega + E_A(\varphi), E_A(\varphi)\right]\left(\omega + \left[1+\rho(\varphi)\right]E_A(\varphi)\right)\Big\} \equiv S^\star_{AC}(\omega,\varphi) \ . \end{aligned} \tag{5.4.33}$$

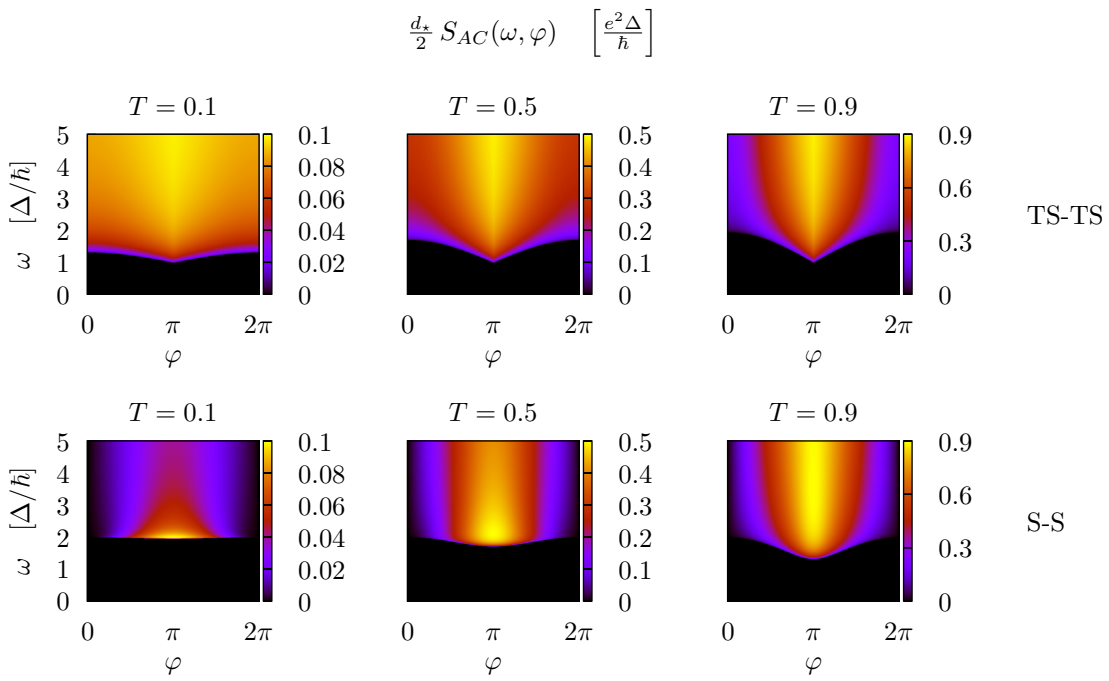

Figure 5.11: Noise $S_{AC}(\omega,\varphi)$ (due to Andreev-continuum transitions) in both TS-TS and S-S junctions and for three different transparencies.

In the topological case, we can further simplify the last expression according to

$$S^{\star}_{AC}(\omega,\varphi)|_{\text{TS-TS}} = \frac{T\,\kappa(\varphi)}{\omega}\Big\{ n\left[-E_A(\varphi)\right]\Theta\left(\omega-\left[1+E_A(\varphi)\right]\right)\sqrt{\left[\omega-E_A(\varphi)\right]^2-1} \\ +n\left[E_A(\varphi)\right]\Theta\left(\omega-\left[1-E_A(\varphi)\right]\right)\sqrt{\left[\omega+E_A(\varphi)\right]^2-1}\Big\}\,. \tag{5.4.34}$$

As long as the Andreev energy remains large compared to the temperature β^{-1} the noise reduces to the first term. In this approximation, there is a cut-off $S^{\star}_{AC}[\omega<1+E_A(\varphi),\varphi]=0$ and

$$S^{\star}_{AC}(\omega,\varphi) \underset{\beta E_A(\varphi)\gg 1}{\sim} \frac{2}{d_\star}\Theta\left(\omega-\left[1+E_A(\varphi)\right]\right)\frac{T\,\kappa(\varphi)}{\omega}\sqrt{\left[\omega-E_A(\varphi)\right]^2-1}\,\frac{\omega-\left[1+\rho(\varphi)\right]E_A(\varphi)}{\omega-2E_A(\varphi)} \equiv S^{\star\star}_{AC}(\omega,\varphi)\,. \tag{5.4.35}$$

In the topological case, we can further simplify the last expression according to

$$S^{\star\star}_{AC}(\omega,\varphi)|_{\text{TS-TS}} = \Theta\left(\omega-\left[1+E_A(\varphi)\right]\right)\frac{T\,\kappa(\varphi)}{\omega}\sqrt{\left[\omega-E_A(\varphi)\right]^2-1}\,. \tag{5.4.36}$$

For a S-S junction with finite transparency $T<1$ (more precisely if we do not have $1-T\ll 1$), the Andreev energy has a non vanishing minimum and we can do the last approximation. In the topological case, the Andreev energy vanishes in $\varphi=\pi$ and we get

$$S^{\star}_{AC}(\omega,\varphi=\pi)|_{\text{TS-TS}} = T\,\frac{\Theta(\omega-1)}{\omega}\sqrt{\omega^2-1}\,. \tag{5.4.37}$$

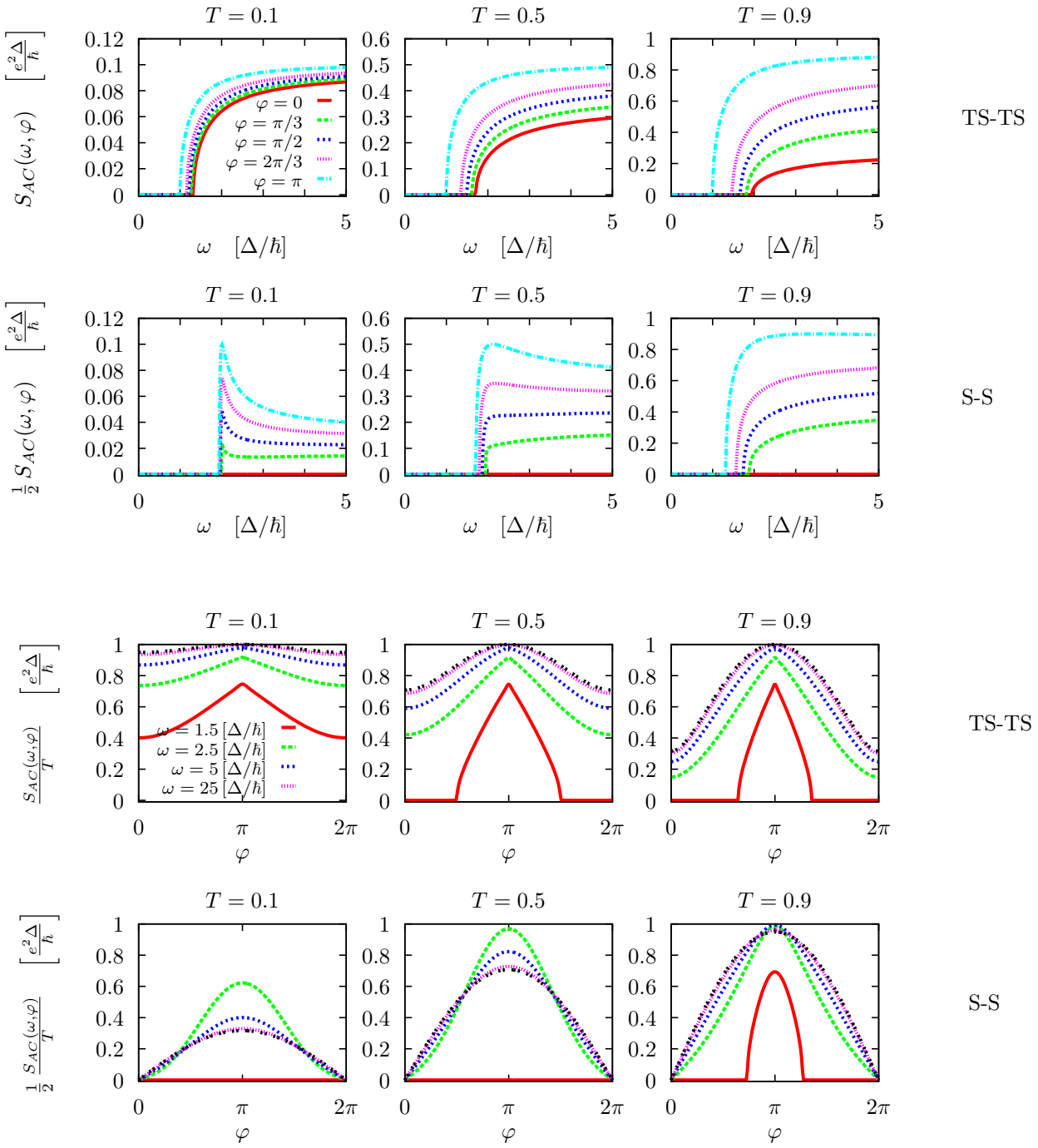

Figure 5.12: Cuts of the noise $S_{AC}(\omega,\varphi)$ given in Fig. 5.11. The six first panels give constant φ cuts (the key is given in the first of these panels). The six last panels give constant ω cuts (the key is given in the first of these panels). The black curve is the high energy limit (5.4.38).

Around the value $\varphi = \pi$, more precisely as long as the Andreev energy $E_A(\varphi)$ is not large compared to the temperature β^{-1}, we have to conserve the full expression (5.4.34).

Fig. 5.11 displays the noise maps for different transparencies and in both TS-TS and S-S junctions. Fig. 5.12 propose constant φ cuts (six first panels) and constant ω cuts (six last panels).

- On Fig. 5.11, the thresholds clearly reproduce the Andreev energy profiles (given in Fig. 5.1). This is especially noticeable because of the infinite slope due to the square root in (5.4.35) and the constant φ cuts of Fig. 5.12 show these sharp thresholds. On the constant ω cuts of Fig. 5.12, the influence of the threshold can be noticed for the value $1 < \omega_0 = 1.5 < 2$: the cut-off could be below (first panel) or above (fourth and fifth panels) ω_0 whatever φ or the cut-off can be crossed for a given φ_0 according to $\omega_0 = 1 + E_A(\varphi_0)$ (other panels).

- Constant ω cuts of Fig. 5.12 provide another signature for a TS-TS junction when looking at finite energies $\omega \gtrsim \Delta$ and turning the phase difference across $\varphi = \pi$: there is a cusp reminiscent of the Andreev energy singular vanishing (when considering $E_A(\pi \pm \delta\varphi) = \varepsilon_\pm$ such that $\varepsilon_\pm \ll 1$ and $\beta\varepsilon_\pm \gg 1$, the local slopes on both sides involve the Andreev energy in a linear way).

- For sufficiently large energies, the φ cuts reach a finite limit which depends on φ according to
$$\frac{d_\star}{2}\, S^\star_{AC}(\omega,\varphi) \underset{\omega\gg 1}{\sim} T\,\kappa(\varphi) + \mathcal{O}\left(\frac{1}{\omega}\right) . \tag{5.4.38}$$
The constant ω cuts confirm this expectation as they converge to the $\kappa(\varphi)$ profiles (given in Fig. 5.1).

5.4.3 Total non-resonant noise

Let us consider the total non-resonant finite frequency noise (out of $\omega = \pm\omega_{AA}$ with $\omega_{AA} = 2E_A$)

$$S_{\rm nr} = S_{CC} + S_{AC} . \tag{5.4.39}$$

In the zero temperature limit, there is a cut-off $S_{\rm nr}(\omega < 1 - E_A(\varphi), \varphi) = 0$ and for energies lower than $\omega_{CC} = 2\,[\Delta]$ only AC transitions contribute to the non-resonant noise, that is

$$S_{\rm nr}(\omega,\varphi) \underset{\beta\gg 1}{\sim} S^\star_{\rm nr}(\omega,\varphi) = S^\star_{\rm CC}(\omega,\varphi) + S^\star_{\rm AC}(\omega,\varphi) \tag{5.4.40}$$

$$= \Theta(\omega-2) S^\star_{\rm CC}(\omega,\varphi) + \Theta\left(\omega - [1 - E_A(\varphi)]\right) S^\star_{\rm AC}(\omega,\varphi) . \tag{5.4.41}$$

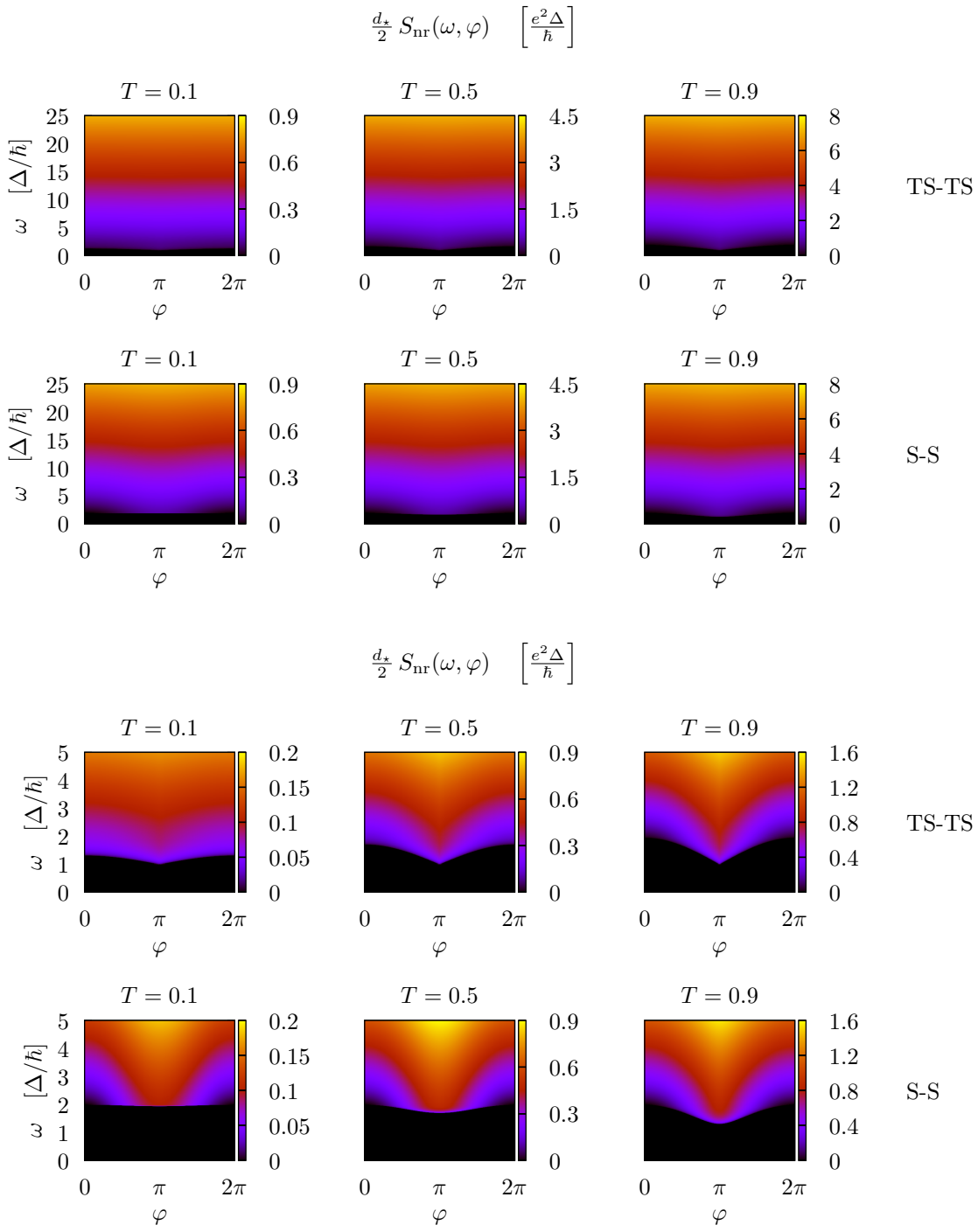

Figure 5.13: Noise $S_{\rm nr}(\omega,\varphi)$ in both TS-TS and S-S junctions and for three different transparencies. The six first panels give a large energy overview while the six last panels give an enlargement around the gap region.

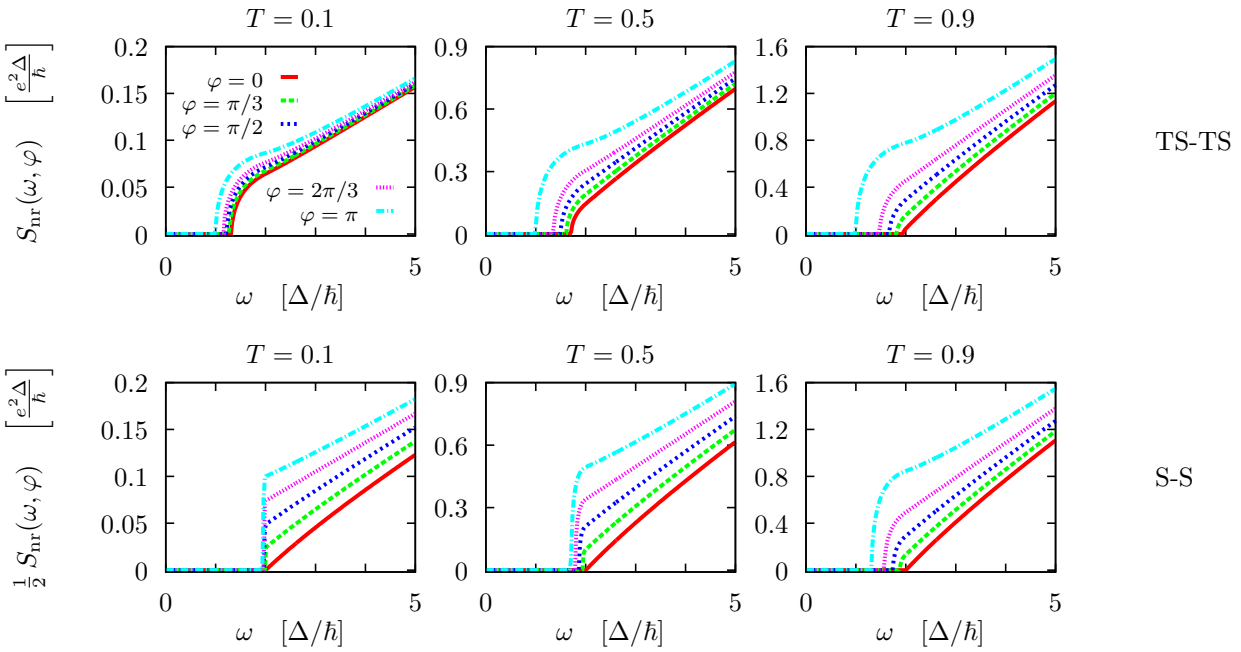

Figure 5.14: Constant φ cuts (the key is given in the first panel) of the noise $S_{\rm nr}(\omega,\varphi)$ given in Fig. 5.13.

If moreover, the Andreev energy remains large compared to the temperature β^{-1}, there is a new cut-off $S_{\rm nr}(\omega < \omega_{AC}(\varphi),\varphi) = 0$ with $\omega_{AC} = 1 + E_A$ and

$$S^{\star}_{\rm nr}(\omega,\varphi) \underset{\beta E_A(\varphi)\gg 1}{\sim} S^{\star\star}_{\rm nr}(\omega,\varphi) = S^{\star}_{\rm CC}(\omega,\varphi) + S^{\star\star}_{\rm AC}(\omega,\varphi) \tag{5.4.42}$$

$$= \Theta(\omega-2)S^{\star}_{\rm CC}(\omega,\varphi) + \Theta\left(\omega - [1+E_A(\varphi)]\right) S^{\star\star}_{\rm AC}(\omega,\varphi)\ . \tag{5.4.43}$$

For sufficiently high energies, the contribution due to CC transitions predominates and as the result of summing the equivalents (5.4.25) and (5.4.38), we find

$$S^{\star}_{\rm nr}(\omega,\varphi) \underset{\omega\gg 1}{\sim} \frac{T\omega}{\pi} + \mathcal{O}\left(\frac{1}{\omega}\right)\ . \tag{5.4.44}$$

In Fig. 5.13, the non-resonant noise is given as a map in the (φ,ω) plane for different transparencies and in both TS-TS and S-S junctions. On a large scale of energies, as proposed by the six first panels, there seems to be little dependence on the phase φ, while the transparency seems to only affect the magnitude in agreement with (5.4.44). An enlargement around the gap region is proposed in the six last panels where we see a stronger dependence on the φ parameter. The (sharp) cut-off reproduces the Andreev energy profile (see Fig. 5.1). The transcient regime

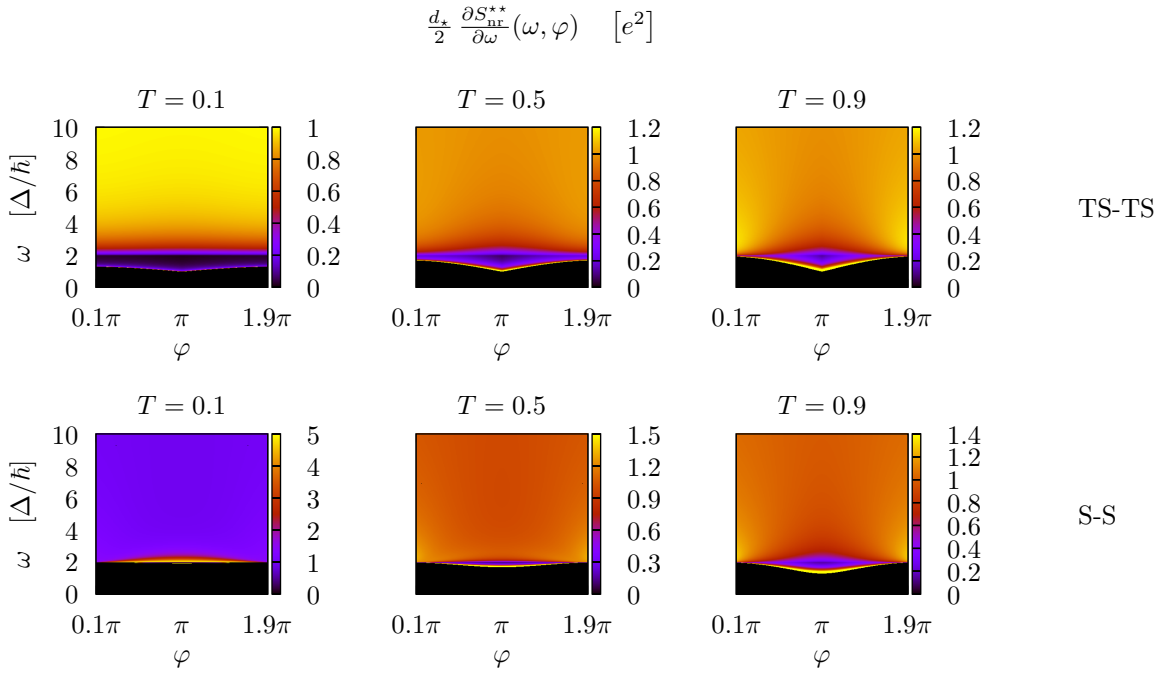

Figure 5.15: Partial derivative of the noise $S^{\star\star}_{\rm nr}(\omega,\varphi)$ with respect to the energy ω, for the three different transparencies of Fig. 5.13. Because of numerical issues, the calculations have not been done for φ values around 0.

between AC dominated regime (for $1+E_A(\varphi)<\omega\lesssim 2$) and CC dominated regime (for $\omega\gg 2$) is clearly noticeable on constant φ cuts of this map (Fig. 5.14), except in a S-S junction with $\varphi=0$ or $T\to 0$ and in a TS-TS junction with $\varphi=0$ and $T\to 1$ for which the Andreev states are expelled to the continuum (closing the transcient interval). Remark that in a S-S junction with $\varphi=0$, the three frequencies collapse $\omega_{AA}=\omega_{AC}=\omega_{CC}=2\Delta$, both AA and AC noise contributions vanish and rather than inheriting the smooth parabolic cut-off generally obtained for CC transitions, a linear behavior is recovered above the threshold 2Δ. Let us emphasize on the increasing behavior of the noise as a function of the energy ω. This is not evident in the BCS case because of the non-monotonic behavior of the contribution due to AC transitions. Nevertheless, we have no evidence of parameters leading to decreasing behavior (see Fig. 5.15).

Remark: In the expression of the non-resonant noise $S_{\rm nr}$ in a TS-TS junction, the transparency appears as an overall factor and in the Andreev energy expression so that dependences on φ and T for $S_{\rm nr}/T$ can be recast in the Andreev energy dependence (contrary to the case of a S-S junction where $\rho(\varphi)$ given in Eq. (5.4.7) provides another dependence on T). In Fig. 5.16,

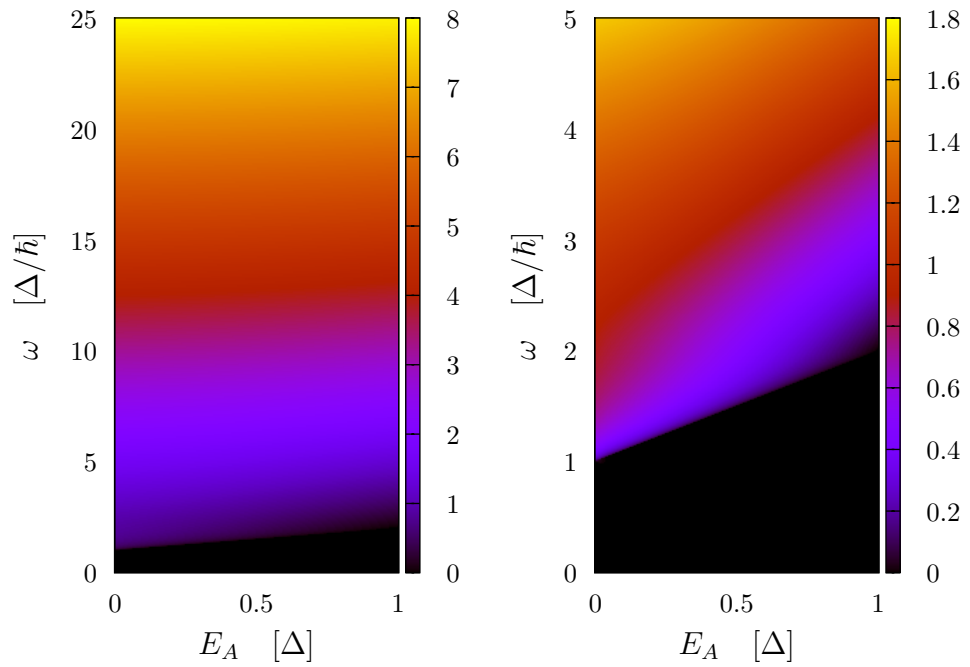

Figure 5.16: Non-resonant noise $S_{\rm nr}/T$ in a TS-TS junction, as a function of E_A and ω. The first panel gives the map on a large scale of energies while the second panel is an enlargement around the gap region.

the map in the (E_A, ω) plane is displayed. Remark that, for a given transparency T, Andreev energies range in $[0, \sqrt{T}]$.

Finite temperature effects

Now let us investigate finite temperature effects. We increase temperature ($\beta^{-1} = 0.1\,[\Delta]$) and display the noise maps around the gap region in the six first panels of Fig. 5.17. The main change is the appearance of noise below the cut-off $1 + E_A(\varphi)$. This is better illustrated in the six last panels of Fig. 5.17 where the relative difference between the two maps is given: the region with the most significant changes is between the curves $1 - E_A(\varphi)$ and $1 + E_A(\varphi)$. Let us also mention the noticeable differences in a TS-TS junction just above the gap and around $\varphi = \pi$: it is the zero of the Andreev energy and this is where the finite values of β cannot reproduce the zero temperature limit.

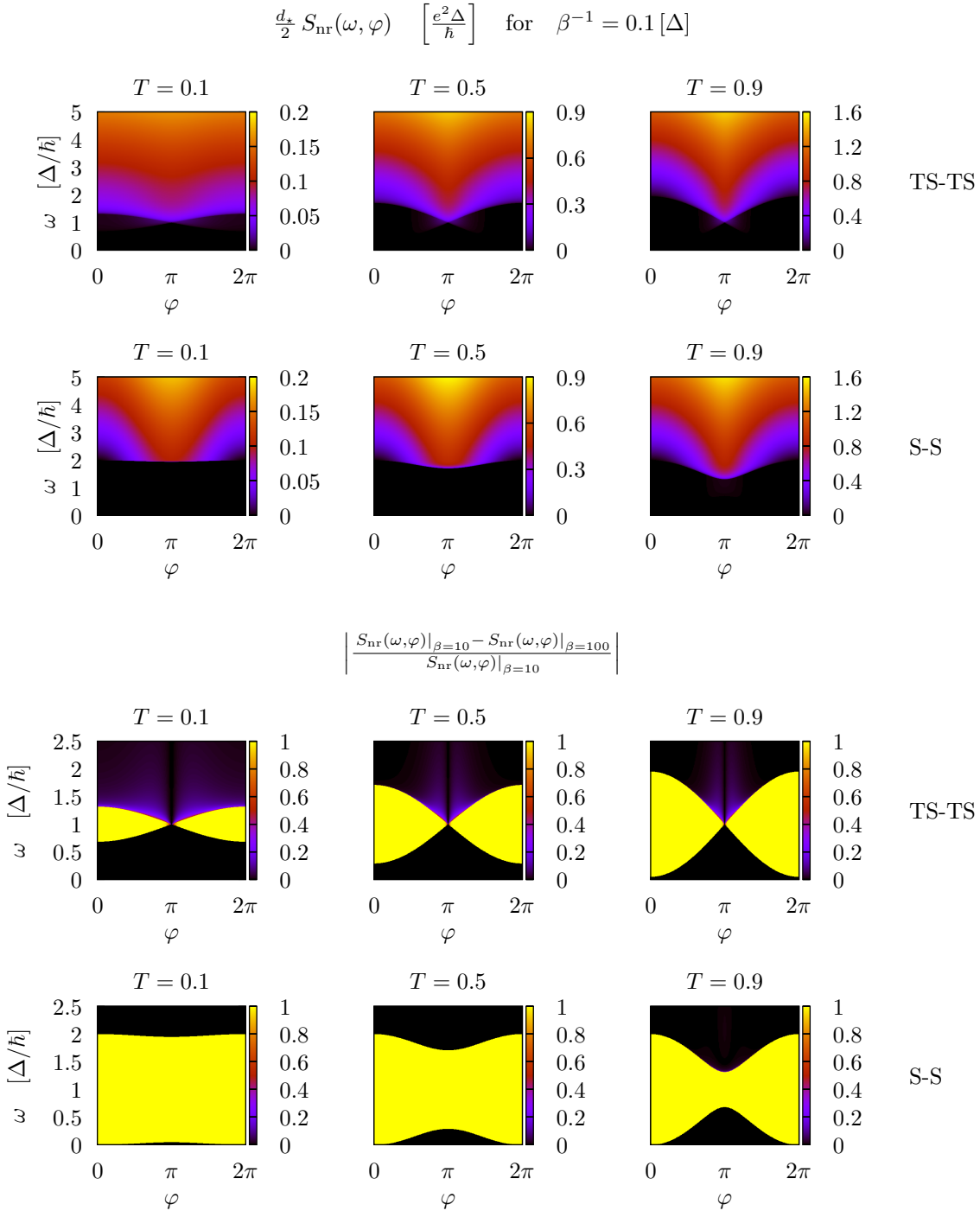

Figure 5.17: Six first panels: noise $S_{\rm nr}(\omega,\varphi)$ around the gap for a finite temperature $\beta^{-1} = 0.1\,[\Delta]$. Six last panels: relative error with the "infinitely small" temperature $\beta^{-1} = 0.01\,[\Delta]$ reference (Fig. 5.13).

5.5 Conclusion and perspectives

More and more convincing signatures compatible with the presence of Majorana fermions in 1D semiconducting wires have been accumulated with recent observations of quantized zero-bias conductance [168,169]. Despite the fact that the confining potential has to be carefully settled in order to avoid spurious non-topological subgap states [189], 2D layouts of 1D p-wave superconductors [152] are still serious candidates to provide the exchange statistics decisive evidence for Majorana fermions. Before the implementation of these networks, quantum transport in 1D systems supporting Majorana fermions, e.g. the junction between 1D topological superconducting wires investigated in this article, deserves deeper study.

We have presented a unified description of S-S and TS-TS junctions in terms of scattering eigenstates. We have shown how Majorana fermions emerge in a TS-TS junction with phase difference $\varphi = \pi$ by explicitely writting the proper linear combinations of (degenerate) zero-energy Andreev bound states. The Josephson current carried by Andreev states can be written in a unified way as the derivative of the Andreev energy $\langle I \rangle \propto \frac{\mathrm{d}E_A}{\mathrm{d}\varphi}$. Transitions inside the Andreev sector are noiseless in the topological case since Andreev states are current eigenstates (a result which is closely related to the emergence of Majorana fermions) in contrast with the BCS case for which a noise resonance at energy $\omega = 2E_A$ is expected for $T < 1$ (finite backscattering). While resonant zero frequency noise is suppressed by lowering temperature in a S-S junction, it is expected to persist in a TS-TS junction operating with $\varphi = \pi$. Transitions which involve continuum states give rise to a non-resonant noise which has been computed. For low temperatures, it exhibits a $\Delta + E_A$ frequency threshold due to AC transitions. CC transitions which occur for energies larger than 2Δ impose an asymptotic linear behavior. A detailed comparison between the two types of junction has been carried out and characteristic features in a TS-TS junction have been highlighted, some of them related to the existence of zero-energy modes in this topologically nontrivial junction.

In the linear response framework, one can adress the issue of computing the current susceptibility which is closely related to the noise $S(\omega)$ studied in this article. Indeed, the imaginary part of the current susceptibility, which gives the linear absorption rate, is proportional to the difference $S(\omega) - S(-\omega)$. In a S-S junction our results coincide with those of Ref. [190]. More interestingly, the noise calculations can be straightforwardly used for computing the current susceptibility in a TS-TS junction. The characteritic features detailed in the main text of this article for the noise will be recovered for the imaginary part of the susceptibility. Let us mention

that dynamic current susceptibility has recently been proposed as a probing tool for the presence of Majorana bound states in a superconduting ring geometry [191]. One can also adress the study of Andreev level qubit [182] population dynamics. In a conventional Andreev qubit, long-lived quasiparticles can be trapped [192], a phenomenon known as quasiparticle poisoning. Within our framework, using the calculations of current matrix elements, one can compare the transition rates between quasiparticle states due to the coupling of the junction to its environment (external circuit, phonons) calculated in Ref. [184], with those calculated in a topological Andreev qubit. When considered as a function of Andreev energy, the latter are simply given by the $T \to 1$ limiting case given in Ref. [184] renormalized by an overall multiplication with $T/2$. Indeed since $d_\star S_{\rm nr}$ in both S-S and TS-TS junctions coincide in the limit $T = 1$ and since $(S_{\rm nr}/T)|_{\text{TS-TS}}$ considered as function of E_A and ω does not depend anymore on T (as mentioned in the previous section), we get

$$\begin{aligned} S_{\rm nr}(E_A,\omega)|^{T}_{\text{TS-TS}} &= T\ S_{\rm nr}(E_A,\omega)|^{T=1}_{\text{TS-TS}} \\ &= \frac{T}{2}\ S_{\rm nr}(E_A,\omega)|^{T=1}_{\text{S-S}} \ . \end{aligned} \tag{5.5.1}$$

The same argument holds for the squared current matrix elements involved in the transition rates of Ref [184]. Stationary occupation probabilities can be computed by adapting the calculation of Ref. [185].

Conclusion

The first part of this thesis concerns the study of hybrid devices including superconducting materials which are microscopically well described within the BCS framework. A key feature of such materials is the possibility to pair electrons in so-called Cooper pairs which constitute entangled states in both spin and momentum degrees of freedom. Cooper pairs are the charge carriers of the (phase-driven) DC Josephson current which flows accross a junction between two superconductors. Andreev reflection is the key mechanism for the subgap charge transfer at the boundary of a superconductor. Within this scenario, the constituent electrons of a Cooper pair can exit a superconducting material. This is at the origin of the concept of an electron entangler since these electrons can be injected in two spatially separated normal conductors through Crossed Andreev Reflection (CAR) resulting in Cooper pair splitting.

The first device studied in **Chapter 2** consists of a Josephson junction between two superconductors with two nanowire/nanotube quantum dots in between. Such a system can provide an equilibrium signature for Cooper pair splitting. Indeed, if a magnetic flux threads the area enclosed by dots and superconductors, the Aharonov-Bohm oscillations of the critical current give information about the nonlocal CAR processes which can occur at the two interfaces and responsible for Cooper splitting and recombination. This setup constitutes an alternative to the early non-equilibrium proposals relying on superconductor-normal junctions arranged in a fork geometry where the splitting of a Cooper pair originated from the injecting superconducting lead is probed by measuring crossed correlations between the currents in the outgoing normal branches. Motivated by the experimental achievements of large couplings between superconductors and dots, the calculation has taken into account these couplings in a non-perturbative way within the path integral formulation of statistical mechanics. The Coulomb on-site repulsion on the quantum dots is treated using a Hubbard-Stratonovich transformation followed by a saddle-point approximation. A splitting efficiency has been defined so that the experimental parameters

optimizing Cooper pair splitting can be indicated to the experimentalist. More precisely, gate voltages can be used to monitor each dot energy so that an even or odd mean occupancy is recovered on the dot together with a 0 or π phase behavior for the associated single Josephson junction, respectively. Among all phase associations, a double Josephson junction constituted of two parallel π junctions provides the best platform for Cooper pair splitting whatever the transparency regime.

The second device studied in **Chapter 3** consists of a three-terminal Josephson junction where a central superconductor is coupled to two lateral superconducting reservoirs *via* nanowire/ nanotube quantum dots. In a Josephson junction between two superconductors, if a voltage is applied, Cooper pairs oscillate between the two reservoirs and consequently an alternative current occurs with a Josephson frequency proportional to the voltage drop. In a three-terminal Josephson junction, several voltage drops and consequently different Josephson frequencies coexist. However, if the central electrode is grounded while the lateral gates are biased with commensurate voltages, then a DC Josephson current is recovered which translates the effective transport of Cooper pairs. The simplest case corresponds to opposite voltages and the production of two entangled Cooper pairs split by double CAR, the so-called quartet state. A path integral approach within the Keldysh formalism is adopted to compute non-perturbatively out-of-equilibrium current and noise and a frequency expansion relying on the voltage commensurability is conveniently used. Numerical results for the quartet resonance are given within the resonant dots regime and the metallic junction regime. The zero-frequency crossed correlations of the currents flowing in the lateral leads are positive in the resonant dots regime while they are negative in the metallic junction regime except for fine-tuned values of phase and voltage. Correlations are suppressed (when compared to the current) at low voltage in the latter case while giant phase-sensitive Fano factors persist in the former case.

The second part of this thesis comes within the scope of the recent enthusiasm for condensed matter realizations of Majorana fermions moslty aroused by the promises of fault-tolerant topological quantum computation. More and more convincing signatures compatible with the presence of Majorana zero-energy modes have been accumulated in the early implementations of the clever proposals based on semiconducting nanowires. Transport properties in systems supporting such excitations can bring supplementary evidences.

In **Chapter 5**, Josephson current and thermal noise have been computed for a junction between conventional superconductors and a junction between topological superconductors (hosting zero-energy quasiparticules with Majorana properties) within a unified framework based on the

Bogoliubov - de Gennes scattering approach, the nature of the superconductors in contact being encoded in the matching condition. This unified treatment allows a systematic study of the two systems and characteristic signatures of a topological junction have been highlighted, some of them being related to the emergence of Majorana zero-energy modes.

Bibliography

[1] Supriyo Datta. Electronic Transport in Mesoscopic Systems. Cambridge Studies in Semiconductor Physics and Microelectronic Engineering. Cambridge University Press, 1995.

[2] B. J. van Wees, H. van Houten, C. W. J. Beenakker, J. G. Williamson, L. P. Kouwenhoven, D. van der Marel, and C. T. Foxon. Quantized conductance of point contacts in a two-dimensional electron gas. Phys. Rev. Lett., 60:848–850, Feb 1988.

[3] R. Landauer. Spatial variation of currents and fields due to localized scatterers in metallic conduction. IBM Journal of Research and Development, 1(3):223–231, July 1957.

[4] Y. Aharonov and D. Bohm. Significance of electromagnetic potentials in the quantum theory. Phys. Rev., 115:485–491, Aug 1959.

[5] R. A. Webb, S. Washburn, C. P. Umbach, and R. B. Laibowitz. Observation of $\frac{h}{e}$ aharonov-bohm oscillations in normal-metal rings. Phys. Rev. Lett., 54:2696–2699, Jun 1985.

[6] K. v. Klitzing, G. Dorda, and M. Pepper. New method for high-accuracy determination of the fine-structure constant based on quantized hall resistance. Phys. Rev. Lett., 45:494–497, Aug 1980.

[7] M. Z. Hasan and C. L. Kane. Colloquium: Topological insulators. Rev. Mod. Phys., 82:3045–3067, Nov 2010.

[8] P. W. Anderson. Absence of diffusion in certain random lattices. Phys. Rev., 109:1492–1505, Mar 1958.

[9] M. Tinkham. Introduction to Superconductivity: Second Edition. Dover Books on Physics. Dover Publications, 2004.

[10] J. Bardeen, L. N. Cooper, and J. R. Schrieffer. Theory of superconductivity. Phys. Rev., 108:1175–1204, Dec 1957.

[11] A. Einstein, B. Podolsky, and N. Rosen. Can quantum-mechanical description of physical reality be considered complete? Phys. Rev., 47:777–780, May 1935.

[12] Alain Aspect, Philippe Grangier, and Gérard Roger. Experimental tests of realistic local theories via bell's theorem. Phys. Rev. Lett., 47:460–463, Aug 1981.

[13] JOHN S. BELL. On the problem of hidden variables in quantum mechanics. Rev. Mod. Phys., 38:447–452, Jul 1966.

[14] A. F. Andreev. The thermal conductivity of the intermediate state in superconductors. Soviet Physics JETP, 19:1228, 1964.

[15] B.D. Josephson. Possible new effects in superconductive tunnelling. Physics Letters, 1(7):251 – 253, 1962.

[16] T.M. Klapwijk, G.E. Blonder, and M. Tinkham. Explanation of subharmonic energy gap structure in superconducting contacts. Physica B+C, 109:1657 – 1664, 1982.

[17] T. Jonckheere, J. Rech, T. Martin, B. Douçot, D. Feinberg, and R. Mélin. Multipair dc josephson resonances in a biased all-superconducting bijunction. Phys. Rev. B, 87:214501, Jun 2013.

[18] Mahn-Soo Choi, C. Bruder, and Daniel Loss. Spin-dependent josephson current through double quantum dots and measurement of entangled electron states. Phys. Rev. B, 62:13569–13572, Nov 2000.

[19] R. Jacquet, J. Rech, T. Jonckheere, A. Zazunov, and T. Martin. Cooper pair splitting and recombination in a nanosquid geometry at high transparency. Phys. Rev. B, 92:235429, Dec 2015.

[20] N. Read and Dmitry Green. Paired states of fermions in two dimensions with breaking of parity and time-reversal symmetries and the fractional quantum hall effect. Phys. Rev. B, 61:10267–10297, Apr 2000.

[21] A.Yu. Kitaev. Fault-tolerant quantum computation by anyons. Annals of Physics, 303(1):2 – 30, 2003.

[22] Liang Fu and C. L. Kane. Superconducting proximity effect and majorana fermions at the surface of a topological insulator. Phys. Rev. Lett., 100:096407, Mar 2008.

[23] Yuval Oreg, Gil Refael, and Felix von Oppen. Helical liquids and majorana bound states in quantum wires. Phys. Rev. Lett., 105:177002, Oct 2010.

[24] Roman M. Lutchyn, Jay D. Sau, and S. Das Sarma. Majorana fermions and a topological phase transition in semiconductor-superconductor heterostructures. Phys. Rev. Lett., 105:077001, Aug 2010.

[25] J. B. Ketterson and S. N. Song. Superconductivity. Cambridge University Press, 1999.

[26] Leon N. Cooper. Bound electron pairs in a degenerate fermi gas. Phys. Rev., 104:1189–1190, Nov 1956.

[27] N. N. Bogoljubov. On a new method in the theory of superconductivity. Il Nuovo Cimento, 7:794–805, March 1958.

[28] J.G. Valatin. Nuovo Cimento, 7:843, 1958.

[29] G. E. Blonder, M. Tinkham, and T. M. Klapwijk. Transition from metallic to tunneling regimes in superconducting microconstrictions: Excess current, charge imbalance, and supercurrent conversion. Phys. Rev. B, 25:4515–4532, Apr 1982.

[30] P.W. Anderson. Theory of dirty superconductors. Journal of Physics and Chemistry of Solids, 11(1):26 – 30, 1959.

[31] Pierre-Gilles de Gennes. Superconductivity of Metals and Alloys. Advanced book classics. Advanced Book Program, Perseus Books, 1999.

[32] H. Pothier, S. Guéron, D. Esteve, and M. H. Devoret. Flux-modulated andreev current caused by electronic interference. Phys. Rev. Lett., 73:2488–2491, Oct 1994.

[33] A.J. Leggett. Lecture notes: Superconductivity, Ancient and Modern, Part 1. 2015.

[34] L.D. Landau and E.M. Lifshitz. Quantum Mechanics: Non-Relativistic Theory. Course of Theoretical Physics. Elsevier Science, 1981.

[35] C J Lambert, V C Hui, and S J Robinson. Multi-probe conductance formulae for mesoscopic superconductors. Journal of Physics: Condensed Matter, 5(25):4187, 1993.

[36] I.O. Kulik. Macroscopic quantization and the proximity effect in s-n-s junctions. JETP, 30:944, 1970.

[37] Richard Feynman. Le cours de physique de Feynman : mécanique quantique. Dunod, Paris, 2000.

[38] B. D. Josephson. The discovery of tunnelling supercurrents. Rev. Mod. Phys., 46:251–254, Apr 1974.

[39] Vinay Ambegaokar and Alexis Baratoff. Tunneling between superconductors. Phys. Rev. Lett., 10:486–489, Jun 1963.

[40] Vinay Ambegaokar and Alexis Baratoff. Tunneling between superconductors. Phys. Rev. Lett., 11:104–104, Jul 1963.

[41] L.N. Bulaevskii, V.V. Kuzii, and A.A. Sobyanin. Superconducting system with weak coupling to the current in the ground state. JETP Lett., 49:659, 1989.

[42] L. I. Glazman and K. A. Matveev. Resonant josephson current through kondo impurities in a tunnel barrier. JETP Lett., 25:290, 1977.

[43] S. A. Kivelson and B. Z. Spivak. Aharonov-bohm oscillations with period hc/4e and negative magnetoresistance in dirty superconductors. Phys. Rev. B, 45:10490–10495, May 1992.

[44] A. V. Rozhkov and Daniel P. Arovas. Josephson coupling through a magnetic impurity. Phys. Rev. Lett., 82:2788–2791, Mar 1999.

[45] J. A. van Dam, Y. V. Nazarov, E. P. A. M. Bakkers, S. De Franceschi, and L. P. Kouwenhoven. Supercurrent reversal in quantum dots. Nature, 442:667, 2006.

[46] Gerald B. Arnold. Superconducting tunneling without the tunneling hamiltonian. ii. subgap harmonic structure. Journal of Low Temperature Physics, 68(1):1–27, Jul 1987.

[47] E. Scheer, P. Joyez, D. Esteve, C. Urbina, and M. H. Devoret. Conduction channel transmissions of atomic-size aluminum contacts. Phys. Rev. Lett., 78:3535–3538, May 1997.

[48] J. C. Cuevas, A. Martín-Rodero, and A. Levy Yeyati. Hamiltonian approach to the transport properties of superconducting quantum point contacts. Phys. Rev. B, 54:7366–7379, Sep 1996.

[49] B. N. Taylor and E. Burstein. Excess currents in electron tunneling between superconductors. Phys. Rev. Lett., 10:14–17, Jan 1963.

[50] J. R. Schrieffer and J. W. Wilkins. Two-particle tunneling processes between superconductors. Phys. Rev. Lett., 10:17–20, Jan 1963.

[51] M. Octavio, M. Tinkham, G. E. Blonder, and T. M. Klapwijk. Subharmonic energy-gap structure in superconducting constrictions. Phys. Rev. B, 27:6739–6746, Jun 1983.

[52] K. Flensberg and J. Bindslev Hansen. Subharmonic energy-gap structure and heating effects in superconducting niobium point contacts. Phys. Rev. B, 40:8693–8699, Nov 1989.

[53] D. Averin and A. Bardas. ac josephson effect in a single quantum channel. Phys. Rev. Lett., 75:1831–1834, Aug 1995.

[54] E. N. Bratus', V. S. Shumeiko, and G. Wendin. Theory of subharmonic gap structure in superconducting mesoscopic tunnel contacts. Phys. Rev. Lett., 74:2110–2113, Mar 1995.

[55] N. van der Post, E. T. Peters, I. K. Yanson, and J. M. van Ruitenbeek. Subgap structure as function of the barrier in atom-size superconducting tunnel junctions. Phys. Rev. Lett., 73:2611–2613, Nov 1994.

[56] E. N. Bratus', V. S. Shumeiko, E. V. Bezuglyi, and G. Wendin. dc-current transport and ac josephson effect in quantum junctions at low voltage. Phys. Rev. B, 55:12666–12677, May 1997.

[57] J. C. Cuevas, A. Martín-Rodero, and A. Levy Yeyati. Shot noise and coherent multiple charge transfer in superconducting quantum point contacts. Phys. Rev. Lett., 82:4086–4089, May 1999.

[58] J.-P. Cleuziou, W. Wernsdorfer, V. Bouchiat, T. Ondarcuhu, and M. Monthioux. Carbon nanotube superconducting quantum interference device. Nature Nanotechnology, 1:53, 2006.

[59] R. S. Deacon, A. Oiwa, J. Sailer, S. Baba, Y. Kanai, K. Shibata, K. Hirakawa, and S. Tarucha. Cooper pair splitting in parallel quantum dot josephson junctions. Nature Communications, 6:7446, 2015.

[60] Z. Wang and X. Hu. Interference and switching of josephson current carried by nonlocal spin-entangled electrons in a squid-like system with quantum dots. Phys. Rev. Lett., 106:037002, Jan 2011.

[61] H. Pan and T. Lin. Control of the supercurrent through a parallel-coupled double quantum dot system. Phys. Rev. B, 74:235312, Dec 2006.

[62] G. Falci, D. Feinberg, and F. W. J. Hekking. Correlated tunneling into a superconductor in a multiprobe hybrid structure. Europhys. Lett., 54(2):255–261, 2001.

[63] J. M. Byers and M. E. Flatté. Probing spatial correlations with nanoscale two-contact tunneling. Phys. Rev. Lett., 74:306–309, Jan 1995.

[64] G. Deutscher and D. Feinberg. Coupling superconducting-ferromagnetic point contacts by andreev reflections. Applied Physics Letters, 76:487, 2000.

[65] D. Beckmann, H. B. Weber, and H. v. Löhneysen. Evidence for crossed andreev reflection in superconductor-ferromagnet hybrid structures. Phys. Rev. Lett., 93:197003, Nov 2004.

[66] Feinberg, D. Andreev scattering and cotunneling between two superconductor-normal metal interfaces: the dirty limit. Eur. Phys. J. B, 36(3):419–422, 2003.

[67] R. Mélin and D. Feinberg. Sign of the crossed conductances at a ferromagnet/superconductor/ferromagnet double interface. Phys. Rev. B, 70:174509, Nov 2004.

[68] S. Russo, M. Kroug, T. M. Klapwijk, and A. F. Morpurgo. Experimental observation of bias-dependent nonlocal andreev reflection. Phys. Rev. Lett., 95:027002, Jul 2005.

[69] P. Cadden-Zimansky and V. Chandrasekhar. Nonlocal correlations in normal-metal superconducting systems. Phys. Rev. Lett., 97:237003, Dec 2006.

[70] S. Oh and J. Kim. Entanglement of electron spins in superconductors. Phys. Rev. B, 71:144523, Apr 2005.

[71] T. Martin. Les Houches Session LXXXI. Elsevier, 2005.

[72] E. M. Purcell. The question of correlation between photons in coherent light rays. Nature, 178:1449, 1956.

[73] T. Martin. Wave packet approach to noise in n s junctions. Physics Letters A, 220(1):137 – 142, 1996.

[74] Guido Burkard, Daniel Loss, and Eugene V. Sukhorukov. Noise of entangled electrons: Bunching and antibunching. Phys. Rev. B, 61:R16303–R16306, Jun 2000.

[75] M. Büttiker. Scattering theory of current and intensity noise correlations in conductors and wave guides. Phys. Rev. B, 46:12485–12507, Nov 1992.

[76] M. P. Anantram and S. Datta. Current fluctuations in mesoscopic systems with andreev scattering. Phys. Rev. B, 53:16390–16402, Jun 1996.

[77] Torrès, J. and Martin, T. Positive and negative hanbury-brown and twiss correlations in normal metal-superconducting devices. Eur. Phys. J. B, 12(3):319–322, 1999.

[78] G. Bignon, M. Houzet, F. Pistolesi, and F. W. J. Hekking. Current-current correlations in hybrid superconducting and normal-metal multiterminal structures. Europhys. Lett., 67(1):110–116, 2004.

[79] Lesovik, G. B., Martin, T., and Blatter, G. Electronic entanglement in the vicinity of a superconductor. Eur. Phys. J. B, 24(3):287–290, 2001.

[80] Nikolai M. Chtchelkatchev, Gianni Blatter, Gordey B. Lesovik, and Thierry Martin. Bell inequalities and entanglement in solid-state devices. Phys. Rev. B, 66:161320, Oct 2002.

[81] Patrik Recher, Eugene V. Sukhorukov, and Daniel Loss. Andreev tunneling, coulomb blockade, and resonant transport of nonlocal spin-entangled electrons. Phys. Rev. B, 63:165314, Apr 2001.

[82] Olivier Sauret, Denis Feinberg, and Thierry Martin. Quantum master equations for the superconductor quantum dot entangler. Phys. Rev. B, 70:245313, Dec 2004.

[83] Olivier Sauret, Thierry Martin, and Denis Feinberg. Spin-current noise and bell inequalities in a realistic superconductor-quantum dot entangler. Phys. Rev. B, 72:024544, Jul 2005.

[84] D. Chevallier, J. Rech, T. Jonckheere, and T. Martin. Current and noise correlations in a double-dot cooper-pair beam splitter. Phys. Rev. B, 83:125421, Mar 2011.

[85] J. Rech, D. Chevallier, T. Jonckheere, and T. Martin. Current correlations in an interacting cooper-pair beam splitter. Phys. Rev. B, 85:035419, Jan 2012.

[86] L Hofstetter, S. Csonka, J. Nygard, and C. Schonenberger. Cooper pair splitter realized in a two-quantum-dot y-junction. Nature, 461:960, 2009.

[87] L. Hofstetter, S. Csonka, A. Baumgartner, G. Fülöp, S. d'Hollosy, J. Nygård, and C. Schönenberger. Finite-bias cooper pair splitting. Phys. Rev. Lett., 107:136801, Sep 2011.

[88] L. G. Herrmann, F. Portier, P. Roche, A. Levy Yeyati, T. Kontos, and C. Strunk. Carbon nanotubes as cooper-pair beam splitters. Phys. Rev. Lett., 104:026801, Jan 2010.

[89] J. Schindele, A. Baumgartner, and C. Schönenberger. Near-unity cooper pair splitting efficiency. Phys. Rev. Lett., 109:157002, Oct 2012.

[90] A. Das, Y. Ronen, M. Heiblum, D. Mahalu, A. V. Kretinin, and H. Shtrikman. High-efficiency cooper pair splitting demonstrated by two-particle conductance resonance and positive noise cross-correlation. Nature Communications, 3:1165, 2012.

[91] J. Wei and V. Chandrasekhar. Positive noise cross-correlation in hybrid superconducting and normal-metal three-terminal devices. Nat Phys, 6:494, 2010.

[92] Patrik Recher and Daniel Loss. Superconductor coupled to two luttinger liquids as an entangler for electron spins. Phys. Rev. B, 65:165327, Apr 2002.

[93] Cristina Bena, Smitha Vishveshwara, Leon Balents, and Matthew P. A. Fisher. Quantum entanglement in carbon nanotubes. Phys. Rev. Lett., 89:037901, Jun 2002.

[94] Sauret, O., Feinberg, D., and Martin, T. Electron teleportation with quantum dot arrays. Eur. Phys. J. B, 32(4):545–548, 2003.

[95] Olivier Sauret, Denis Feinberg, and Thierry Martin. Electron spin teleportation current through a quantum dot array operating in the stationary regime. Phys. Rev. B, 69:035332, Jan 2004.

[96] Kittel C. Introduction to Solid State Physics. John Wiley & Sons, Inc.

[97] J. F. Cochran and D. E. Mapother. Superconducting transition in aluminum. Phys. Rev., 111:132–142, Jul 1958.

[98] H. A. Leupold and H. A. Boorse. Superconducting and normal specific heats of a single crystal of niobium. Phys. Rev., 134:A1322–A1328, Jun 1964.

[99] S. J. Tans, M. H. Devoret, H. Dai, A. Thess, R. E. Smalley, L. J. Geerligs, and C. Dekker. Individual single-wall carbon nanotubes as quantum wires. Nature, 386:474, 1997.

[100] J.W. Negele and H. Orland. Quantum many-particle systems. Frontiers in physics. Addison-Wesley Pub. Co., 1988.

[101] J. Zinn-Justin. Intégrale de chemin en mécanique quantique: introduction. Savoirs actuels. Série Physique. EDP Sciences, 2003.

[102] A. Popoff. Transport in nantrostructrures in the presence of electronic corrrelations: equilibrium and non equilibrium currents. PhD thesis, Université de la Méditerranée - Aix-Marseille II, 2008.

[103] J. Rech, T. Jonckheere, T. Martin, B. Douçot, D. Feinberg, and R. Mélin. Proposal for the observation of nonlocal multipair production. Phys. Rev. B, 90:075419, Aug 2014.

[104] F. D. M. Haldane. Scaling theory of the asymmetric anderson model. Phys. Rev. Lett., 40:416–419, Feb 1978.

[105] F. Siano and R. Egger. Josephson current through a nanoscale magnetic quantum dot. Phys. Rev. Lett., 93:047002, Jul 2004.

[106] Mahn-Soo Choi, Minchul Lee, Kicheon Kang, and W. Belzig. Kondo effect and josephson current through a quantum dot between two superconductors. Phys. Rev. B, 70:020502, Jul 2004.

[107] Axel Freyn, Benoit Douçot, Denis Feinberg, and Régis Mélin. Production of nonlocal quartets and phase-sensitive entanglement in a superconducting beam splitter. Phys. Rev. Lett., 106:257005, Jun 2011.

[108] A. H. Pfeffer, J. E. Duvauchelle, H. Courtois, R. Mélin, D. Feinberg, and F. Lefloch. Subgap structure in the conductance of a three-terminal josephson junction. Phys. Rev. B, 90:075401, Aug 2014.

[109] Sylvie Duhot, Fran çois Lefloch, and Manuel Houzet. Cross correlation of incoherent multiple andreev reflections. Phys. Rev. Lett., 102:086804, Feb 2009.

[110] M. Houzet and P. Samuelsson. Multiple andreev reflections in hybrid multiterminal junctions. Phys. Rev. B, 82:060517, Aug 2010.

[111] N. M. Chtchelkatchev, T. I. Baturina, A. Glatz, and V. M. Vinokur. Synchronized andreev transmission in sns junction arrays. Phys. Rev. B, 82:024526, Jul 2010.

[112] E. V. Bezuglyi, E. N. Bratus', V. S. Shumeiko, G. Wendin, and H. Takayanagi. Circuit theory of multiple andreev reflections in diffusive sns junctions: The incoherent case. Phys. Rev. B, 62:14439–14451, Dec 2000.

[113] B. Kaviraj, O. Coupiac, H. Courtois, and F. Lefloch. Noise correlations in three-terminal diffusive superconductor–normal-metal–superconductor nanostructures. Phys. Rev. Lett., 107:077005, Aug 2011.

[114] R Mélin, D Feinberg, H Courtois, C Padurariu, A Pfeffer, J E Duvauchelle, F Lefloch, T Jonckheere, J Rech, T Martin, and B Doucot. D.c. josephson transport by quartets and other andreev resonances in superconducting bijunctions. Journal of Physics: Conference Series, 568(5):052006, 2014.

[115] J. C. Cuevas and H. Pothier. Voltage-induced shapiro steps in a superconducting multiterminal structure. Phys. Rev. B, 75:174513, May 2007.

[116] Sidney Shapiro. Josephson currents in superconducting tunneling: The effect of microwaves and other observations. Phys. Rev. Lett., 11:80–82, Jul 1963.

[117] Roman-Pascal Riwar, Driss M. Badiane, Manuel Houzet, Julia S. Meyer, and Yuli V. Nazarov. Reprint of : Cross-correlations of coherent multiple andreev reflections. Physica E: Low-dimensional Systems and Nanostructures, 82:92 – 98, 2016. Frontiers in quantum electronic transport - In memory of Markus Büttiker.

[118] Régis Mélin, Moïse Sotto, Denis Feinberg, Jean-Guy Caputo, and Benoît Douçot. Gate-tunable zero-frequency current cross correlations of the quartet state in a voltage-biased three-terminal josephson junction. Phys. Rev. B, 93:115436, Mar 2016.

[119] J. Rammer and H. Smith. Quantum field-theoretical methods in transport theory of metals. Rev. Mod. Phys., 58:323–359, Apr 1986.

[120] A. Zazunov, R. Egger, C. Mora, and T. Martin. Superconducting transport through a vibrating molecule. Phys. Rev. B, 73:214501, Jun 2006.

[121] T. Jonckheere, A. Zazunov, K. V. Bayandin, V. Shumeiko, and T. Martin. Nonequilibrium supercurrent through a quantum dot: Current harmonics and proximity effect due to a normal-metal lead. Phys. Rev. B, 80:184510, Nov 2009.

[122] Yonatan Cohen, Yuval Ronen, Jung-Hyun Kang, Moty Heiblum, Denis Feinberg, Régis Mélin, and Hadas Shtrikman. Nonlocal supercurrent of quartets in a three-terminal josephson junction. Proceedings of the National Academy of Sciences, 2018.

[123] Jason Alicea. New directions in the pursuit of majorana fermions in solid state systems. Reports on Progress in Physics, 75(7):076501, 2012.

[124] Martin Leijnse and Karsten Flensberg. Introduction to topological superconductivity and majorana fermions. Semiconductor Science and Technology, 27(12):124003, 2012.

[125] C.W.J. Beenakker. Search for majorana fermions in superconductors. Annual Review of Condensed Matter Physics, 4(1):113–136, 2013.

[126] T D Stanescu and S Tewari. Majorana fermions in semiconductor nanowires: fundamentals, modeling, and experiment. Journal of Physics: Condensed Matter, 25(23):233201, 2013.

[127] Ramón Aguado. Majorana quasiparticles in condensed matter. La Rivista del Nuovo Cimento, 40:523, 2017.

[128] Steven R. Elliott and Marcel Franz. Colloquium: Majorana fermions in nuclear, particle, and solid-state physics. Rev. Mod. Phys., 87:137–163, Feb 2015.

[129] Michael E. Peskin and Daniel V. Schroeder. An Introduction to quantum field theory. Addison-Wesley, Reading, USA, 1995.

[130] W. Pauli. Relativistic field theories of elementary particles. Rev. Mod. Phys., 13:203–232, Jul 1941.

[131] The quantum theory of the electron. Proceedings of the Royal Society of London A: Mathematical, Physical and Engineering Sciences, 117(778):610–624, 1928.

[132] E. Schrödinger. An undulatory theory of the mechanics of atoms and molecules. Phys. Rev., 28:1049–1070, Dec 1926.

[133] P. A. M. Dirac. A theory of electrons and protons. Proceedings of the Royal Society of London A: Mathematical, Physical and Engineering Sciences, 126(801):360–365, 1930.

[134] E. Majorana. Teoria simmetrica dell'elettrone e del positrone. Nuovo Cim, 14:171, 1937.

[135] Frank T. Avignone, Steven R. Elliott, and Jonathan Engel. Double beta decay, majorana neutrinos, and neutrino mass. Rev. Mod. Phys., 80:481–516, Apr 2008.

[136] W. H. Furry. On transition probabilities in double beta-disintegration. Phys. Rev., 56:1184–1193, Dec 1939.

[137] S. R. Elliott, A. A. Hahn, and M. K. Moe. Direct evidence for two-neutrino double-beta decay in ^{82}Se. Phys. Rev. Lett., 59:2020–2023, Nov 1987.

[138] Anthony J. Leggett. A theoretical description of the new phases of liquid ^{3}He. Rev. Mod. Phys., 47:331–414, Apr 1975.

[139] R. Balian and N. R. Werthamer. Superconductivity with pairs in a relative p wave. Phys. Rev., 131:1553–1564, Aug 1963.

[140] T. Senthil and Matthew P. A. Fisher. Quasiparticle localization in superconductors with spin-orbit scattering. Phys. Rev. B, 61:9690–9698, Apr 2000.

[141] C. Chamon, R. Jackiw, Y. Nishida, S.-Y. Pi, and L. Santos. Quantizing majorana fermions in a superconductor. Phys. Rev. B, 81:224515, Jun 2010.

[142] C. W. J. Beenakker. Annihilation of colliding bogoliubov quasiparticles reveals their majorana nature. Phys. Rev. Lett., 112:070604, Feb 2014.

[143] F. D. Parmentier, E. Bocquillon, J.-M. Berroir, D. C. Glattli, B. Plaçais, G. Fève, M. Albert, C. Flindt, and M. Büttiker. Current noise spectrum of a single-particle emitter: Theory and experiment. Phys. Rev. B, 85:165438, Apr 2012.

[144] Bocquillon Erwann, Freulon Vincent, Parmentier François D., Berroir Jean-Marc, Plaçais Bernard, Wahl Claire, Rech Jérome, Jonckheere Thibaut, Martin Thierry, Grenier Charles, Ferraro Dario, Degiovanni Pascal, and Fève Gwendal. Electron quantum optics in ballistic chiral conductors. Annalen der Physik, 526(1-2):1–30.

[145] A Yu Kitaev. Unpaired majorana fermions in quantum wires. Physics-Uspekhi, 44(10S):131, 2001.

[146] Catherine Kallin. Chiral p-wave order in sr 2 ruo 4. Reports on Progress in Physics, 75(4):042501, 2012.

[147] Gregory Moore and Nicholas Read. Nonabelions in the fractional quantum hall effect. Nuclear Physics B, 360(2):362 – 396, 1991.

[148] D. A. Ivanov. Non-abelian statistics of half-quantum vortices in p-wave superconductors. Phys. Rev. Lett., 86:268–271, Jan 2001.

[149] Chetan Nayak, Steven H. Simon, Ady Stern, Michael Freedman, and Sankar Das Sarma. Non-abelian anyons and topological quantum computation. Rev. Mod. Phys., 80:1083–1159, Sep 2008.

[150] N. B. Kopnin and M. M. Salomaa. Mutual friction in superfluid ^{3}He: Effects of bound states in the vortex core. Phys. Rev. B, 44:9667–9677, Nov 1991.

[151] G. E. Volovik. Fermion zero modes on vortices in chiral superconductors. Journal of Experimental and Theoretical Physics Letters, 70(9):609–614, Nov 1999.

[152] Jason Alicea, Yuval Oreg, Gil Refael, Felix von Oppen, and Matthew P. A. Fisher. Non-abelian statistics and topological quantum information processing in 1d wire networks. Nature Physics, 7:412, 2011.

[153] Jay D. Sau, Roman M. Lutchyn, Sumanta Tewari, and S. Das Sarma. Generic new platform for topological quantum computation using semiconductor heterostructures. Phys. Rev. Lett., 104:040502, Jan 2010.

[154] Jason Alicea. Majorana fermions in a tunable semiconductor device. Phys. Rev. B, 81:125318, Mar 2010.

[155] V. Mourik, K. Zuo, S. M. Frolov, S. R. Plissard, E. P. A. M. Bakkers, and L. P. Kouwenhoven. Signatures of majorana fermions in hybrid superconductor-semiconductor nanowire devices. Science, 336(6084):1003–1007, 2012.

[156] Liang Fu and C. L. Kane. Josephson current and noise at a superconductor/quantum-spin-hall-insulator/superconductor junction. Phys. Rev. B, 79:161408, Apr 2009.

[157] A. Cook and M. Franz. Majorana fermions in a topological-insulator nanowire proximity-coupled to an s-wave superconductor. Phys. Rev. B, 84:201105, Nov 2011.

[158] T.-P. Choy, J. M. Edge, A. R. Akhmerov, and C. W. J. Beenakker. Majorana fermions emerging from magnetic nanoparticles on a superconductor without spin-orbit coupling. Phys. Rev. B, 84:195442, Nov 2011.

[159] M. Wimmer, A. R. Akhmerov, M. V. Medvedyeva, J. Tworzydło, and C. W. J. Beenakker. Majorana bound states without vortices in topological superconductors with electrostatic defects. Phys. Rev. Lett., 105:046803, Jul 2010.

[160] Anindya Das, Yuval Ronen, Yonatan Most, Yuval Oreg, Moty Heiblum, and Hadas Shtrikman. Zero-bias peaks and splitting in an al–inas nanowire topological superconductor as a signature of majorana fermions. Nature Physics, 8:887, 2012.

[161] H. O. H. Churchill, V. Fatemi, K. Grove-Rasmussen, M. T. Deng, P. Caroff, H. Q. Xu, and C. M. Marcus. Superconductor-nanowire devices from tunneling to the multichannel regime: Zero-bias oscillations and magnetoconductance crossover. Phys. Rev. B, 87:241401, Jun 2013.

[162] M. T. Deng, C. L. Yu, G. Y. Huang, M. Larsson, P. Caroff, and H. Q. Xu. Anomalous zero-bias conductance peak in a nb–insb nanowire–nb hybrid device. Nano Letters, 12(12):6414–6419, 2012.

[163] A. D. K. Finck, D. J. Van Harlingen, P. K. Mohseni, K. Jung, and X. Li. Anomalous modulation of a zero-bias peak in a hybrid nanowire-superconductor device. Phys. Rev. Lett., 110:126406, Mar 2013.

[164] Leonid P. Rokhinson, Xinyu Liu, and Jacek K. Furdyna. The fractional a.c. josephson effect in a semiconductor–superconductor nanowire as a signature of majorana particles. Nature Physics, 8:795, 2012.

[165] Ching-Kai Chiu, Jay D. Sau, and S. Das Sarma. Conductance interference in a superconducting coulomb blockaded majorana ring. Phys. Rev. B, 97:035310, Jan 2018.

[166] Esben Bork Hansen, Jeroen Danon, and Karsten Flensberg. Probing electron-hole components of subgap states in coulomb blockaded majorana islands. Phys. Rev. B, 97:041411, Jan 2018.

[167] S. M. Albrecht, A. P. Higginbotham, M. Madsen, F. Kuemmeth, T. S. Jespersen, J. Nygård, P. Krogstrup, and C. M. Marcus. Exponential protection of zero modes in majorana islands. Nature, 531:206, 2016.

[168] Fabrizio Nichele, Asbjørn C. C. Drachmann, Alexander M. Whiticar, Eoin C. T. O'Farrell, Henri J. Suominen, Antonio Fornieri, Tian Wang, Geoffrey C. Gardner, Candice Thomas,

Anthony T. Hatke, Peter Krogstrup, Michael J. Manfra, Karsten Flensberg, and Charles M. Marcus. Scaling of majorana zero-bias conductance peaks. Phys. Rev. Lett., 119:136803, Sep 2017.

[169] H. Zhang, C.-X. Liu, S. Gazibegovic, D. Xu, J. A. Logan, G. Wang, N. van Loo, J. D. S. Bommer, M. W. A. de Moor, D. Car, R. L. M. Op het Veld, P. J. van Veldhoven, S. Koelling, M. A. Verheijen, M. Pendharkar, D. J. Pennachio, B. Shojaei, J. S. Lee, C. J. Palmstrøm, E. P. A. M. Bakkers, S. Das Sarma, and L. P. Kouwenhoven. Nature, 556:74, 2018.

[170] Martin Greiter, Vera Schnells, and Ronny Thomale. The 1d ising model and the topological phase of the kitaev chain. Annals of Physics, 351:1026 – 1033, 2014.

[171] Linhu Li, Chao Yang, and Shu Chen. Topological invariants for phase transition points of one-dimensional z2 topological systems. The European Physical Journal B, 89(9):195, 2016.

[172] Mikio Nakahara. Geometry, Topology and Physics.

[173] Linhu Li, Chao Yang, and Shu Chen. Topological invariants for phase transition points of one-dimensional z2 topological systems. Eur. Phys. J. B, 89:195, 2016.

[174] R. Jackiw and C. Rebbi. Solitons with fermion number 1/2. Phys. Rev. D, 13:3398–3409, Jun 1976.

[175] C.L. Kane. Chapter 1 - topological band theory and the 2 invariant. In Marcel Franz and Laurens Molenkamp, editors, Topological Insulators, volume 6 of Contemporary Concepts of Condensed Matter Science, pages 3 – 34. Elsevier, 2013.

[176] A. Furusaki and M. Tsukada. A unified theory of clean josephson junctions. Physica B, 165-166:967, 1990.

[177] C. W. J. Beenakker and H. van Houten. Josephson current through a superconducting quantum point contact shorter than the coherence length. Phys. Rev. Lett., 66:3056–3059, Jun 1991.

[178] C. W. J. Beenakker. Universal limit of critical-current fluctuations in mesoscopic josephson junctions. Phys. Rev. Lett., 67:3836–3839, Dec 1991.

[179] A. Martín-Rodero, A. Levy Yeyati, and F. J. García-Vidal. Thermal noise in superconducting quantum point contacts. Phys. Rev. B, 53:R8891–R8894, Apr 1996.

[180] A. Zazunov, R. Egger, and A. Levy Yeyati. Low-energy theory of transport in majorana wire junctions. Phys. Rev. B, 94:014502, Jul 2016.

[181] V. S. Shumeiko, G. Wendin, and E. N. Bratus'. Resonance excitation of superconducting bound states in a tunnel junction by an electromagnetic field: Nonlinear response of the josephson current. Phys. Rev. B, 48:13129–13132, Nov 1993.

[182] A. Zazunov, V. S. Shumeiko, E. N. Bratus', J. Lantz, and G. Wendin. Andreev level qubit. Phys. Rev. Lett., 90:087003, Feb 2003.

[183] A. Zazunov, V. S. Shumeiko, G. Wendin, and E. N. Bratus'. Dynamics and phonon-induced decoherence of andreev level qubit. Phys. Rev. B, 71:214505, Jun 2005.

[184] D. G. Olivares, A. Levy Yeyati, L. Bretheau, Ç. Ö. Girit, H. Pothier, and C. Urbina. Dynamics of quasiparticle trapping in andreev levels. Phys. Rev. B, 89:104504, Mar 2014.

[185] A. Zazunov, A. Brunetti, A. Levy Yeyati, and R. Egger. Quasiparticle trapping, andreev level population dynamics, and charge imbalance in superconducting weak links. Phys. Rev. B, 90:104508, Sep 2014.

[186] Roman-Pascal Riwar, Manuel Houzet, Julia S Meyer, and Yuli V Nazarov. Control of andreev bound state population and related charge-imbalance effect. Journal of Physics: Condensed Matter, 27(9):095701, 2015.

[187] J.J. Sakurai. Modern Quantum Mechanics. Addison-Wesley Publishing Company, 1994.

[188] A.A. Abrikosov, L.P. Gorkov, and I.E. Dzyaloshinski. Methods of Quantum Field Theory in Statistical Physics. Dover Publications, 1963.

[189] Tudor D. Stanescu and Sankar Das Sarma. Building topological quantum circuits: Majorana nanowire junctions. Phys. Rev. B, 97:045410, Jan 2018.

[190] F. Kos, S. E. Nigg, and L. I. Glazman. Frequency-dependent admittance of a short superconducting weak link. Phys. Rev. B, 87:174521, May 2013.

[191] Mircea Trif, Olesia Dmytruk, Hélène Bouchiat, Ramón Aguado, and Pascal Simon. Dynamic current susceptibility as a probe of majorana bound states in nanowire-based josephson junctions. Phys. Rev. B, 97:041415, Jan 2018.

[192] M. Zgirski, L. Bretheau, Q. Le Masne, H. Pothier, D. Esteve, and C. Urbina. Evidence for long-lived quasiparticles trapped in superconducting point contacts. Phys. Rev. Lett., 106:257003, Jun 2011.